Single-molecule-based imaging study of EGFR receptor nano-organization regulation : to pathophysiological mechanisms in kidney diseases

Thi Thuy Hoang

Thi Thuy Hoang. Single-molecule-based imaging study of EGFR receptor nano-organization regulation : to pathophysiological mechanisms in kidney diseases. Molecular biology. Université Paris-Saclay, 2022. English. NNT : 2022UPAST012 . tel-03675257

HAL Id: tel-03675257
https://theses.hal.science/tel-03675257v1

Submitted on 23 May 2022

Single-molecule-based imaging study of EGFR receptor nano-organization regulation : application to pathophysiological mechanisms in kidney diseases

Thèse de doctorat de l'université Paris-Saclay

École doctorale n° 573 interfaces : matériaux, systèmes, usages (INTERFACES)
Spécialité de doctorat : Ingéniérie des systèmes complexes
Graduate School : Sciences de l'ingénierie et des systèmes. Référent : CentraleSupélec

Thèse préparée dans le Laboratoire d'Optique et Biosciences (École Polytechnique, INSERM, CNRS), sous la direction de **Antigoni ALEXANDROU**, Directrice de Recherche, et la co-direction de **Nicolas OLIVIER**, chargé de recherches et **Cedric BOUZIGUES**, Maître de conférences

Thèse soutenue à Palaiseau, le 14 Janvier 2022, par

Thi Thuy HOANG

Composition du Jury

Francois TREUSSART Professeur, Université Paris-Saclay	Président
Mathieu COPPEY Directeur de Recherche, Institut Curie	Rapporteur & Examinateur
Pierre-Emmanuel MILHIET Directeur de Recherche, Université de Montpellier	Rapporteur & Examinateur
Cécile LEDUC Chargée de Recherche, Institut Jacques Monod	Examinatrice
Olivia LENOIR Chargée de Recherche, Université de Paris	Examinatrice
Antigoni ALEXANDROU Directrice de Recherche, Ecole Polytechnique	Directrice de thèse
Nicolas OLIVIER Chargé de Recherche, Ecole Polytechnique	Co-directeur de thèse
Cédric BOUZIGUES Maître de Conférences, Ecole Polytechnique	Co-directeur de thèse

THESE DE DOCTORAT

NNT : 2022UPAST012

Dedication

To my mother

Acknowledgements

First of all, I would like to thank all the jury members, the reviewers Dr. Pierre Emanuel MILHIET, and Dr. Mathieu COPPEY, the jury president, Prof. François TREUSSART, and the examiners Dr. Cécile LEDUC and Dr. Olivia LENOIR who accepted to review my thesis, attend to my thesis defense, and gave me a lot of insight. Especially, I would like to express my special thanks to Dr. P.E. MILHET, Dr. COPPEY, and Prof. TREUSSART who patiently read and evaluated my thesis.

Secondly, I would like to express my deep and sincere gratitude to my research supervisors: Antigoni, Nicolas, and Cédric. Without all of you, my work couldn't even begin nor have been finished.

Antigoni, no words could express my gratitude to you. You are the best supervisor I could have. You listened and understood all my problems, all the mistakes I have made. I remembered when I was working late during the pregnancy, you were so patient to wait for me to finish the experiment. When I made a mistake about the experiments, you just told me to repeat them. When I told you that I was pregnant you said you saw me like your daughters and respected all the decisions that I wanted to make. Thank you for all the love that you have for our petit Léo also. Thank you for staying up until 3 a.m. to correct all the grammatical errors in my thesis. Thanks for the fruitful discussions during this time.

Nicolas, I would like to express my deepest gratitude to you. Thank you for your presence to rescue me from the darkest time of my research life. Your passion, intelligence, and your work have reawakened my love of science. Thank you for understanding me, even when I didn't finish the whole French sentence.

Cedric, thank you for all your ideas that blew my mind when we were discussing. Thank you for all the jokes that you made for everyone.

Next, I want to thank the director of the lab, Dr. François HACHE for accepting me to do my Ph.D. at the LOB.

Furthermore, I would like to thank all the collaborators involved in my Ph.D. project. First of all, I would like to thank Dr. Pierre-Louis THARAUX and Dr. Eric RUBINSTEIN for providing us with the parietal epithelial cells (wild-type PEC and shCD9 PEC) and CD9 antibodies, respectively, used in the experiments. Secondly, I would like to thank Dr. Thierry GACOIN and Rabei MOHAMMEDI for the nanoparticle synthesis and for their help with the nanoparticle functionalization. The completion of my dissertation would not have been possible without the support from Dr. Yann Lanoiseleée and Dr. Denis Grebenkov for the tracking analysis. Moreover, I would like to extend my sincere thanks to Dr. Jean-Baptiste Masson for the fruitful discussion and support.

Life can not be smooth without true friends or colleagues. I would like to thank first the

members of my research group. I would like to express my gratitude to Rivo, Chao, Pascal, Fanny, Maxime, and Ravi for helping me with the experiments. Thank you for being there whenever I needed help. Thank you for being my friends and listening to my problems, giving me wise advice. Especially, thank you Pierre for teaching me to use the confocal microscope.

I would like to thank all other members of the lab and my friends in the office. Thank you for organizing the many wine soirées for me to cry out the stress: Bahar (your jokes are so funny), Lien, Dale, Josephine (ma douce lapine), Julia, Paul (my special friend), Chlotilde, XiuJun, Vincent, Yoan, Margaux, Marco, Lipsa, Olga... I would like also to thank all other members of the laboratory for being so kind to me. After leaving the lab, maybe I will forget how to analyze my old data but I would never forget you.

I also want to thank all my Vietnamese friends in X, Paris-Saclay, and Toulouse for helping us during my thesis. Last but not least, I would like to show my love to my petite family and my big family. Chuc, thank you for holding me tight when life is dark or bright. Hau, you have taught me so many things that I never thought of. Chi, thank you for always loving me and forgiving all my mistakes. Me, thank you for loving me until your last breath.

Contents

List of Abbreviations

0.1 List of Acronyms

AAV	ANCA-associated vasculitis	25
ACR	Urine albumin to creatinine ratio	52
ANCA	Anti-neutrophil cytoplasmic antibody	25
Anti-GBM	Anti-glomerular basement membrane disease	24
aPECs	Activated PECs	29
BBM	Bowman's basement membrane	32
BCR	B-cell receptor	44
cPECs	Cuboidal PECs	20
CTGF	Connective tissue growth factor	32
CHO	Chinese hamster ovary	40
CH	Constant heavy chain	100
CL	Constant light chain	100

MSD	Mean square displacement	61
NA	Numerical aperture	62
NOS	Not-otherwise-specified	28
NTS	Nephrotoxic serum	51
PAINT	Point Accumulation for Imaging in Nanoscale Topography	68
PALM	Photoactivated localization microscopy	62
PAG1	Glycosphingolipid-enriched microdomains 1	44
PA-FPs	Photoactivated fluorescent proteins	69
PEC	Parietal epithelial cell	19
PR3	Proteinase 3	25
PDGF	Platelet-derived growth factor	32
PODXL	Podocalixin	53
PSF	Point spread function	88
QDs	Quantum dots	78
RPGN	Rapidly Progressive Glomerulonephritis	24
sdAb	Single-domain antibody	100
SIM	Structured illumination microscopy	62

Introduction

The cell membrane is a sophisticated structure where lipids and proteins organize optimally to maintain cell function and signaling. The Epidermal Growth Factor Receptor (EGFR) is an important protein in the cell membrane which is involved in many cell activities such as cell division, cell proliferation, and even cell death. There is a large number of research studies investigating the nature of EGF receptor confinement by using different techniques, but until now it is still controversial where EGF receptors are located. EGF receptors in the membrane are found mostly to be located in cholesterol- and sphingolipid-enriched membrane nanodomains. CD9, on the other hand, is a membrane protein that is a member of the tetraspanin family and plays a crucial role in cell adhesion and cell fusion, and forms another type of membrane nanodomain enriched in tetraspanin and cholesterol.

My thesis is the continuation of work done by two previous Ph. D. students, Chao Yu and Hélène Lazareth, who investigated EGFR confinement in Madin-Darby Canine Kidney (MDCK) and CD9 involvement in kidney disease in glomerular parietal epithelial cells (PEC), respectively [1, 2]. By using single-particle tracking and hydrodynamic force in a microchannel, C. Yu found out that EGF receptors in MDCK are located in cholesterol- and sphingomyelin-enriched nanodomains. Furthermore, she also observed that EGF receptors bind directly to the actin cytoskeleton in addition to being confined in these nanodomains. H. Lazareth, on the other hand, studied the involvement of CD9 in inflammatory kidney diseases, by inhibiting the tetraspanin CD9 expression in parietal epithelial cells (PEC) of the kidney glomeruli by shRNA, and observed partial protection of mouse models for Rapidly Progressive Glomerulonephritis (RPGN) and other inflammatory kidney diseases. In previous work at the Paris Cardiovascular Research Center, Bollée et al. used an EGFR inhibitor to also improve the survival of a moused model of RPGN [3].

In this context, the goal of my thesis was to understand the connection between EGF receptors and CD9 proteins and to answer the question of why both proteins are involved in kidney disease and through which molecular mechanisms. To this end, I used single-molecule tracking and super-resolution microscopy. My work was conducted mainly in the laboratory "Optique et Biosciences" at Ecole Polytechnique, also affiliated to CNRS and INSERM. Different tasks in the thesis were done in collaboration with other labs. Through our collaboration with the team of Pierre-Louis Tharaux at the Paris Cardiovascular Research Center, we could have access to primary cultures of parietal epithelial cells both wild-type and stable CD9-depleted cells using the shRNA technique as well as to the know-how in kidney diseases. The nanoparticle synthesis and functionalization were conducted in collaboration with the group of Thierry Gacoin in the laboratory ”Physique de la Matière Condensée” also at Ecole Polytechnique. The analysis of the single-particle tracking data was done in collaboration with Yann Lanoiselée at the University of Birmingham and Denis Grebenkov at the laboratory ”Physique de la Matière Condensée”. The CD9 protein antibody was generously provided by Eric Rubinstein of the Institut André Lwoff.

Outline

The main purpose of the thesis was to discover a potential link between epidermal growth factor receptors (EGFR) and CD9 proteins in parietal epithelial cells that are both involved in the development of inflammatory kidney diseases. Our main hypothesis was that EGF receptors could be located in CD9 tetraspanin-enriched membrane nanodomains. Besides that, the nature of the confinement of EGF receptors in different cell types is also discussed.

Chapter 1 introduces the kidney structure, kidney function, inflammatory kidney diseases, and the role of parietal epithelial cells in maintaining kidney function and their involvement in inflammatory kidney diseases.

Chapter 2 is an overview of cell membrane organization and different models to describe the cell membrane architecture.

Chapter 3 reviews various microscopy techniques used to study the cell membrane and biological samples in general.

Chapter 4 examines the localization and clustering of EGFR and CD9 in the parietal epithelial cell membrane using the dSTORM super-resolution single-molecule localization technique and provides evidence for the molecular mechanism of the involvement of EGFR and CD9 in kidney disease and the link between the two membrane molecules.

Chapter 5 investigates the nature of EGF receptor confinement in different cell types by using single-molecule tracking and a new model to analyze the motion of the receptor which alternates between free and confined motion.

Chapter 1

Introduction to Kidney

Contents

> ”We are all made from star dust and we will all return to star dust, like a cosmic palindrome.”
>
> A.S.KING

1.1 Kidney

The kidney is a pair of bean-shaped and reddish-brown organs located in retroperitoneal space.

In our daily life, we intake different substances, some are toxic, others may exceed our daily needs of the body. Therefore, to maintain the level of substances circulating in the body and to avoid an accumulation of unused or toxic substances, the kidney has to filter out the soluble molecules in the blood, control the volume of body fluids, balance the blood osmolality inside the body, balance the acid-base concentrations, adjust the electrolyte concentrations, and remove toxins. Furthermore, kidneys also have an important role in converting vitamin D into its activated form - calcitriol that the body could use [4].

1.1.1 Kidney Structure

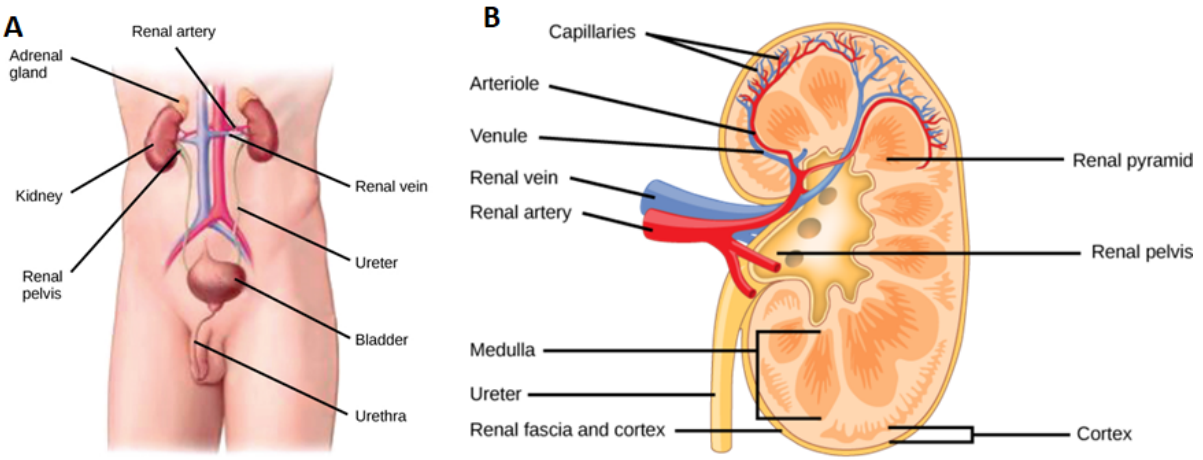

Figure 1.1: (A)The kidney position inside the human body. (B) The anatomy of the kidney. Figure from [5].

The kidney contains two main parts: the outer renal cortex and the inner renal medulla as shown in Figure 1.1 B. The blood is filtered in the kidney entering by the renal artery and, after being filtered in the kidney, the blood returns to the blood mainstream by the renal vein. The renal medulla is the innermost part of the kidney [6].

Nephrons and blood filtering process in the kidney

The blood filtering happens in nephrons which are the microscopic and functional units of the kidney. In the human kidney, there are about one million nephrons and, for each individual, the number of nephrons ranges approximately from 200,000 to over 2.5 million which is age-related and also disease dependent [7].

Each nephron is composed of a renal corpuscle and a renal tubule (Figure 1.2). The renal corpuscle consists of a tuft of capillaries called a glomerulus and an encompassing Bowman's capsule [9]. There are four main steps in blood filtering. The blood filtering occurs in the glomerulus. First of all, the blood enters the glomerulus through the afferent arteriole and is filtered in the glomerulus by hydrostatic pressure. The small molecules (water, ions, glucose, amino acids) are filtered while the large molecular weight, molecules remain in the blood and circulate back to the bloodstream via the efferent arteriole. The second step is reabsorbing of the soluble molecules: the filtered fluids called ultrafiltrate exit by the peritubular capillaries where the soluble molecules like salts and glucose are reabsorbed. After that, in the secretion process, the molecules are secreted from the renal tubular cell back to the ultra-filtrate. The last step of the process is excretion. The ultra-filtrate is transported to the collecting duct tube where a part of reabsorbing occurs and the fluids with waste become urine [10] (Figure 1.2 and 1.3).

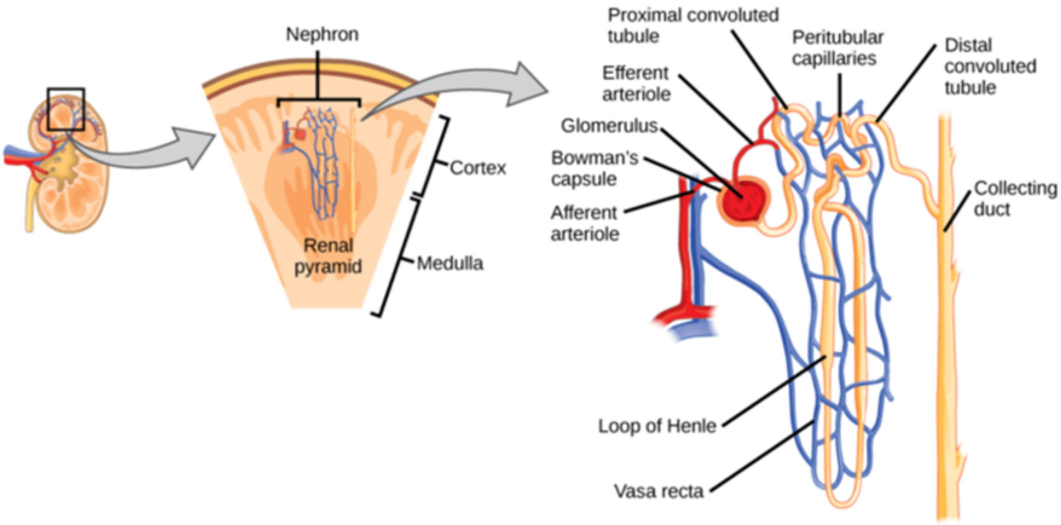

Figure 1.2: The nephron is located inside the kidney and is the smallest unit of filtration. The blood is filtered in the glomerulus and the urine and waste products go to the bladder by going through the tubule to the collecting duct. Figure from [8].

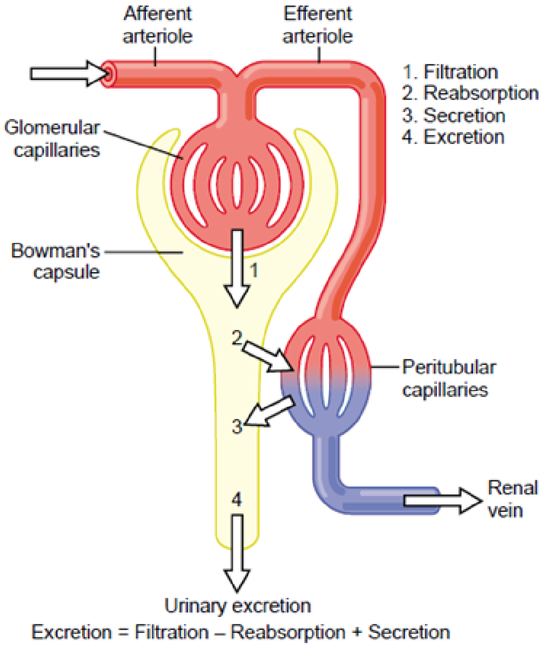

Figure 1.3: Scheme of four main blood filtering processes and urine formation in the nephron. Figure from [11].

Glomerulus and glomerular filtration barrier

As mentioned above, the glomerulus is a microscopic filter of the nephrons. The afferent arteriole after entering the kidney nephron is nested inside the glomerulus and forms a cup-like sac located at the beginning of each nephron, called a glomerular capsule. The blood is filtered at the glomerulus. The glomerulus can filter the blood because of its unique cell structure which is made of three different layers which constitute the Glomerular filtration barrier (GFB) [10] (Figure 1.4).

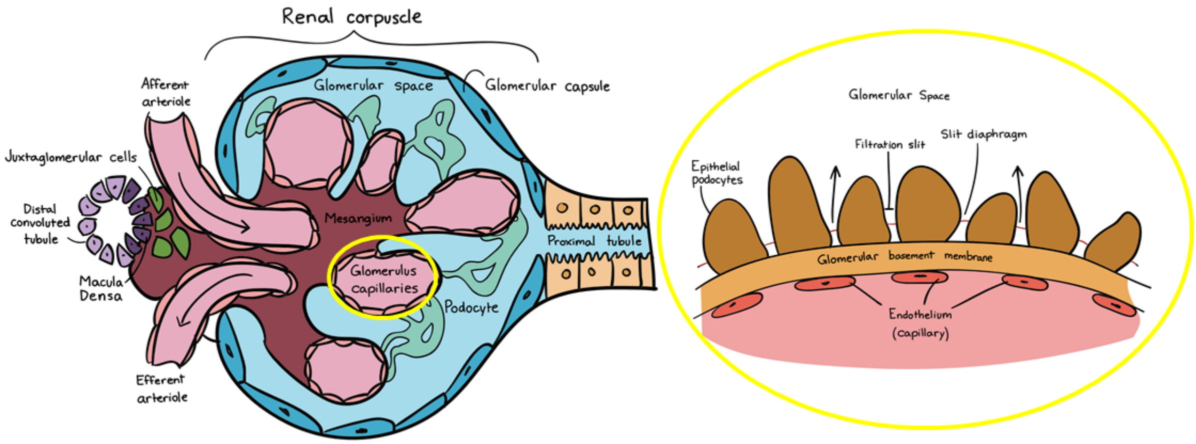

Figure 1.4: Scheme of the glomerulus (left) and the three different layers of glomerular filtration barrier (GFB) (right). Figure from [12].

Endothelium

The first cell layer is composed of endothelial cells (Figure 1.4). This layer forms pores called fenestrations with 70 to 100 nm in diameter. This unique structure of the endothelial layer acts as a simple filtration barrier that helps the glomerulus filter the small soluble molecules while not allowing the blood cells and large proteins to pass through the membrane.

Glomerular basement membrane (GBM)

The glomerular basement membrane is the second layer that is located between the endothelium and the epithelial podocytes. The GBM is a specialized extracellular matrix, that consists of laminin, type IV collagen, nidogen, and heparan sulfate proteoglycan. The glomerular basement membrane has a thickness of 305-330 nm in humans and is negatively charged [13].

Epithelium-Podocytes

The epithelium layer of the glomerular capillary is composed of podocytes which are renal specialized cells. These podocytes in humans as well as in mice wrap around the glomerular basement membrane via cytoplasmic pedicles (Foot processes (FP)) and form slits of about 40 nm between them [14, 15]. The podocyte cells are also negatively charged like the GBM and the endothelial layer (Figure 1.5).

Blood enters the glomerulus capillaries carrying soluble molecules and proteins. Under hydrostatic pressure, the blood is forced through the glomerular filtration barrier where water and small soluble plasma molecules pass through. The big and negatively charged proteins such as albumin remain in the blood with blood cells; only a small fraction of these molecules are leaked out to the Bowman's space [16] (Figure 1.5).

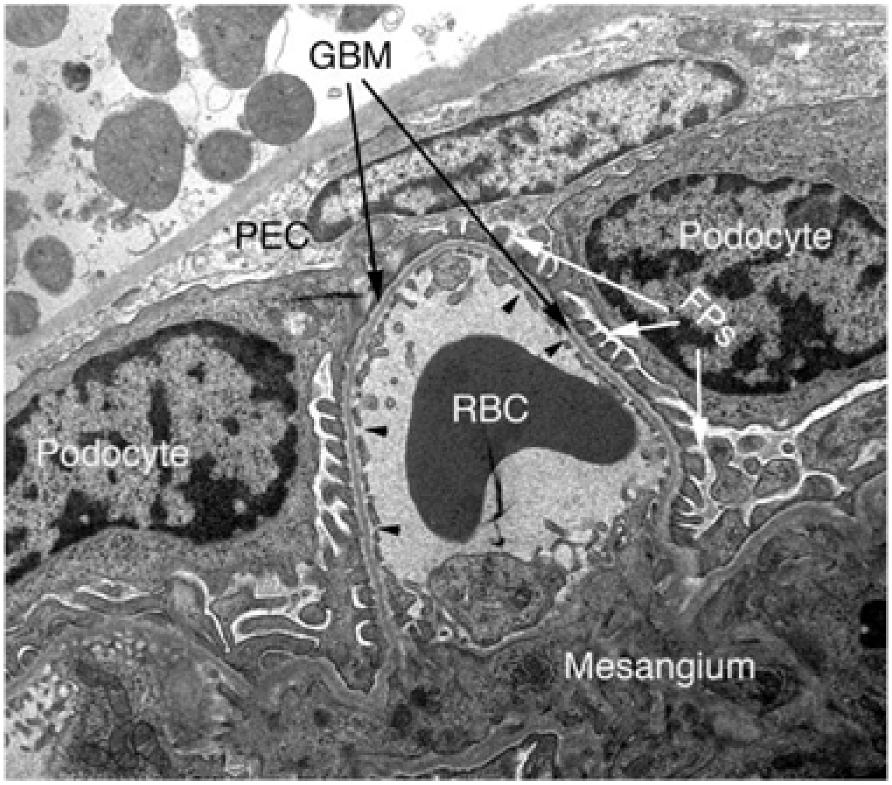

Figure 1.5: The structure of the glomerular capillary loop is revealed by TEM. A red blood cell is inside the capillary. The endothelial cells form fenestrations (see black arrowheads) on the wall of the capillary. The glomerular basement membrane (GBM) is a thin layer between the endothelium and the podocyte foot processes (FPs) (see white arrow). The mesangium contains mesangial cells and their associated matrix. A Parietal epithelial cell (PEC) lie on the Bowman's capsule. Figure extracted from [17].

1.1.2 Parietal Epithelial Cells

The ultrafiltrate including water and the molecules passing the filtration barrier reaches the Bowman's space where a monolayer of parietal epithelial cells (PECs) are located (Figure 1.4). PECs and podocytes share a common lineage from the same mesenchyme until the S-shaped stage of glomerulogenesis. After the S-shaped stage, the two cell lines express different marker proteins for their functional purposes. In mature PECs and podocytes, these markers are different and can be used to distinguish the two cell types. Unlike endothelial cells and podocytes, which are located in the filtration barrier of the glomerulus, PECs are located on the Bowman's capsule and are less studied as the primary factor for kidney disease. As discussed below, however, PEC cells participate directly in the pathogenesis of different glomerular diseases. Therefore, it is important to know the structures, as well as the characteristics of PECs in normal and disease conditions [18].

There are different types of PECs in the glomerulus. Based on their structures, they can be divided into three sub-populations as shown in Figure 1.6:

- Flat parietal epithelial cell (fPECs) are the most common PECs that lies mostly in the Bowman's capsule. In normal conditions, they are the most abundant of all types of PECs.

- Intermediate PECs (iPECs) are located at the tubular orifice which makes bridges between fPECs and the cuboidal PECs a third subgroup of PECs. The iPECs have more cytoplasm compared to fPECs.

- Cuboidal PECs (cPECs) are located on the most proximal part of the proximal tubule and may also line parts of the Bowman's capsule. The cPECs have a more voluminous cytoplasm compared to iPECs and fPECs and have a cuboidal shape [19].

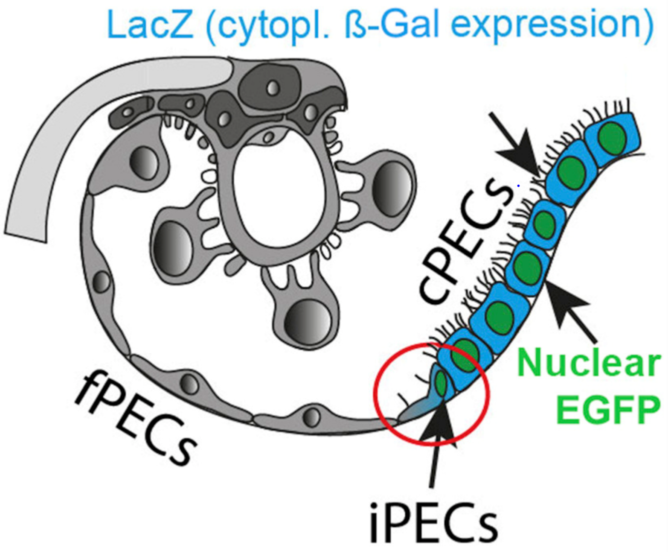

Figure 1.6: Scheme of different types of PECs: flat PECs, intermediate PECs and cuboidal PECs in the Bowman's capsule and proximal tubule. Figure from [19].

The proteins expressed by PECs based on their specific functions are listed below:

Junctional proteins

During their development, PECs express junctional proteins including tight junction proteins and adhesion proteins like cadherins. The tight junction proteins expressed in PECs are claudin-1, -2, and -3, zonula occludens-1(ZO-1), and occludin [20–22]. By using immunostaining of kidney sections, Ohse et al. found out that the claudin-1 and ZO-1 and occludin are expressed in PECs and podocytes in adult kidneys [23]. The tight junction proteins are necessary for connections between PECs and the Bowman's capsule (Figure 1.7).

Transcription factors

The transcription factors are proteins that bind to a specific region of DNA to regulate specific protein expression. In PECs, transcription factors for controlling the expression of junction proteins (cadherin) are expressed [24]. PAX family including PAX 2 and PAX 8 are also expressed in PECs. The PAX2 is a transcription factor that regulates the genes controlling cell proliferation, cell growth, and cell survival [25]. The PAX 8, another member of the PAX family, was also found to be expressed exclusively in PECs [23].

Enzymes and ubiquitin-related proteins

Enzymes including endopeptidases are present in PECs. The endopeptidases are proteolytic peptidases that break peptide bonds of nonterminal amino acids [25]. In mice and rat PECs, the neutral endopeptidase CD10 is expressed. In contrast, these proteins are not expressed in adult human PECs, only in podocytes [26, 27]. Another enzyme Aldh1a1 that helps convert vitamin A into retinoic acid is also expressed in PECs in physiological as well as in pathological conditions.

Protein gene product 9.5 (PGP9.5), a ubiquitin-related protein was detected in rat [28], mouse [22] and human [29] PECs.

Antioxidants

J.E Wiggins showed that antioxidant ceruloplasmin is more expressed when the mouse is aging. Because biological aging is accelerated by high-calory intake, increased free radical production, therefore, the cells require more antioxidants to neutralize the free radicals [30].

Intermediate filament proteins

Intermediate filaments including keratin, desmin, vimentin have a tubular structure associated with other cell components like membranes, cytoskeletons, and other proteins. Cytokeratin is an intermediate filament protein that associates with itself to create a bundle with a radius of around 50 nm and spread in the cytoplasm of the cell. Among the different intermediate filament proteins, cytokeratin 8 and 18 are found to be expressed in PECs [25]. Other intermediate filaments like desmin and vimentin are only expressed in podocytes but not in PECs [31].

Extracellular matrix proteins

Fraser syndrome 1 (FRAS1) is also found in PECs. The FRAS1 is known as a protein associated with the PEC basal membrane and helps the adherence to the lamina densa [32].

Membrane proteins

Membrane proteins are also found to be present in the membrane of normal PECs tetraspanin CD9 [2], EGF receptors [3, 33, 34] and transferrin (see also Chapter 4). These proteins have important functions in cell signaling, cell migration, and cell adhesion. More details about EGFR and CD9 their involvement in kidney disease will be discussed in chapter 2. CD44 expression also is identified as the activation of PECs during the proliferation and invasion [35].

Function of PEC

Permeability Barrier

First of all, the PEC layer serves as the final filtration barrier before the ultrafiltrate reaches the tubule. Using transmission electron microscopy, Webber et al. found out that

PECs have many junctions like desmosomes, intermediate junctions, and tight junctions that could help form a filtration layer in the Bowman's capsule [36]. The study indicated that PECs were able to uptake an enzyme called horseradish peroxidase through intercellular clefts. Based on that, they suggest that PECs could act as a permeability barrier and for transcellular transport. Furthermore, Ohse et al. also indicated that in anti-GBM disease, the number of tight junctions in PECs was significantly reduced compared to normal PECs. In their study, they also found that the loss of tight junction proteins also increased in the anti-GBM disease model in mice [23]. Figure 1.7 demonstrates the filtration barrier of PECs.

Contractility

PECs lie on the Bowman's capsule and possess filaments in the basal membrane regions. Therefore, Webber et al. tested the hypothesis that they are involved in a contractile function [37]. If the contraction is observed, it might indicate active participation of this layer of cells in the process of glomerular filtration since by contracting they might modify both the volume and the pressure within the Bowman's space. After injecting histamine, acetylcholine, or adrenaline into rats or kidney tissue sections, they observed the shape of PECs changed. However, there was no involvement of filaments at the basal membrane where they are believed to have a contractile function as their primary structural role.

Mechanosensation

In PECs, chemical and mechanical sensors in particularly cilia are present in PECs revealed by electron microscopy in 1977 by Arakawa et al. [38]. One side membrane of PECs is exposed to the Bowman's space and the flow of ultrafiltrate. Therefore, using their cilia, PECs may have a mechano-sensing function [39].

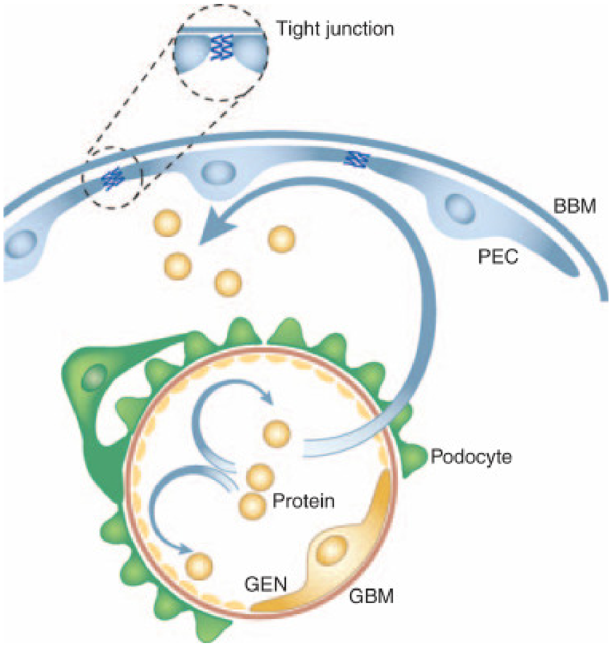

Figure 1.7: Scheme of tight junctions that are created by PEC cells. Figure from [18].

1.2 Kidney diseases

1.2.1 Extracapillary Glomerulonephritis

The extracapillary glomerulonephritis is known as Rapidly Progressive Glomerulonephritis (RPGN) or crescentic glomerulonephritis and was first described by Volhard and Fahr in 1914. It is characterized by a rapid loss of kidney function and leads to a patient's death within several months [40]. Mostly parietal epithelial cells in Bowman's capsule proliferate abnormally and migrate into the urinary space leading to the formation of a crescent with multiple layers of epithelial cells. The crescent formation takes up more than 50% of the glomeruli in the kidney. The RPGN is a rare disease but extremely lethal. The incidence and prevalence of the disease depend on its causes [41].

Causes and Clinical Presentation

The extracapillary glomerulonephritis that appears in the vascular system was divided into three main groups based on their immunopathological characteristics: anti-neutrophil cytoplasmic antibody (ANCA)-associated vasculitis, Anti-glomerular basement membrane disease (Anti-GBM), and immune complex renal diseases (Figure 1.8).

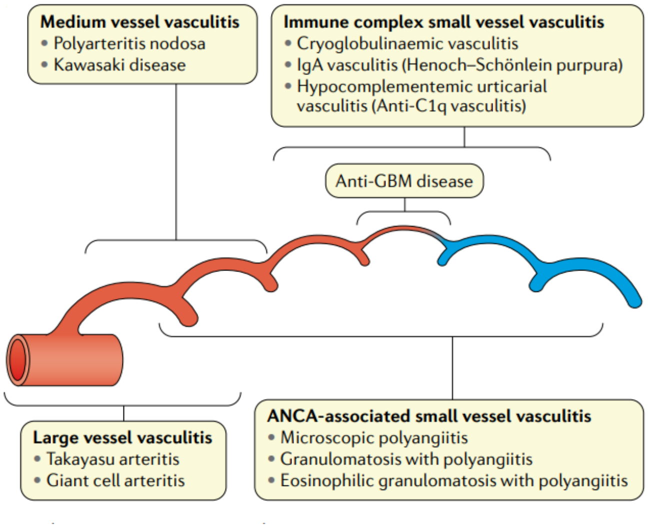

Figure 1.8: The definition of vasculitis by the Chapel Hill nomenclature. Figure extracted from [42].

ANCA-Associated Vasculitis

ANCA-associated vasculitis (AAV) is a pauci-immune or a systemic small vessel vasculitis. AAV is the most common cause of extracapillary glomerulonephritis, making up 60% of cases [43, 44]. Anti-neutrophil cytoplasmic antibody (ANCA) is known as a group of autoantibodies against an antigen in neutrophils, the myeloperoxidase or Proteinase 3 (PR3). Neutrophils after being activated by ANCA are involved in inflammation and harm blood vessels. They normally damage small blood vessels but can affect also other types of vessels [45, 46]. The mechanism of pathogenic ANCAs is shown in Figure 1.9.

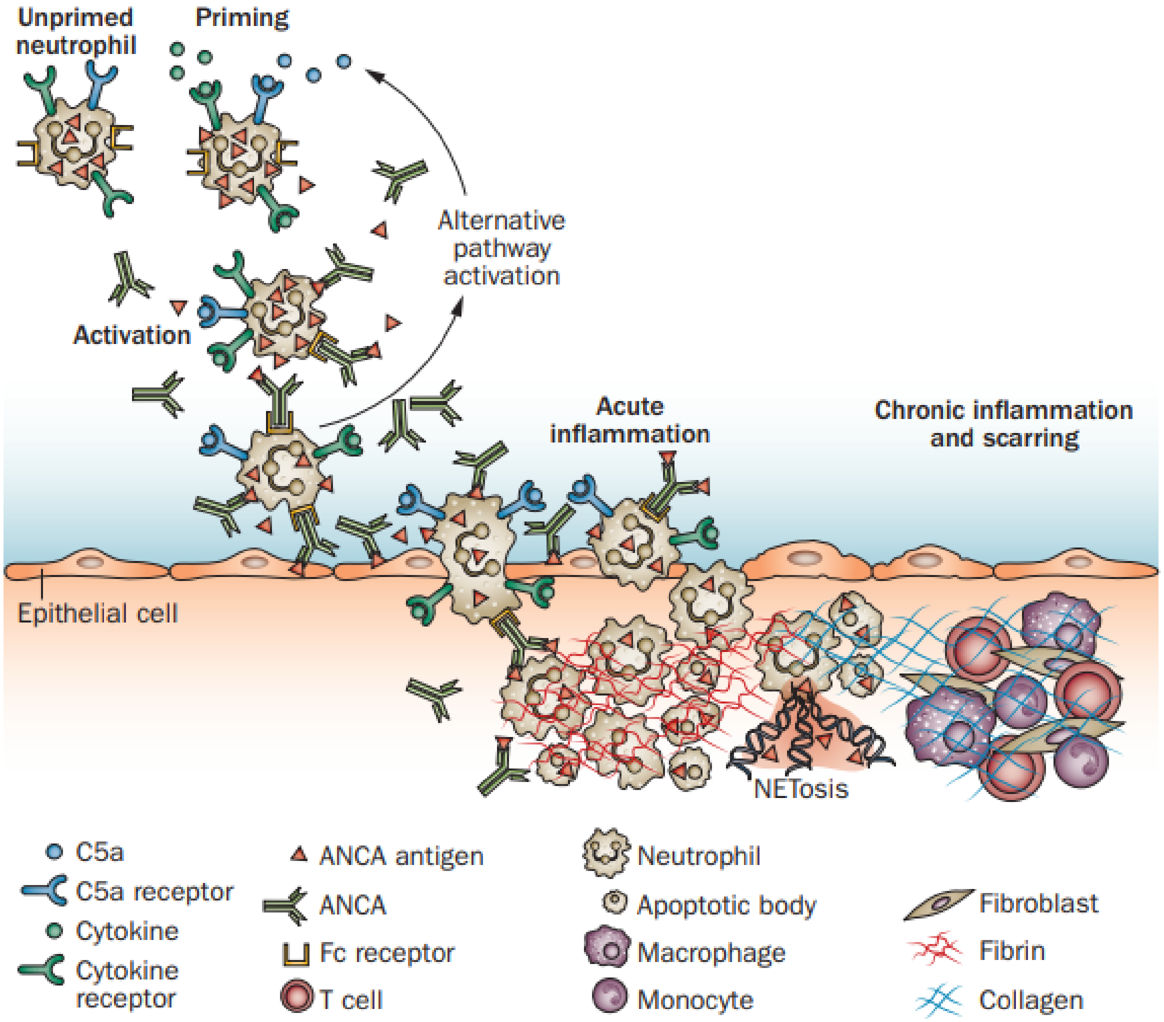

Figure 1.9: The pathogenic ANCAs. The neutrophils(or monocytes) are activated by ANCAs in the presence of cytokines or C5a fragments. In the presence of cytokines or C5a, the antigens (MPO and PR3) of ANCA are released to the environment by neutrophils and then react with ANCA. The ANCA bound to antigens binds to Fc receptors of the neutrophil membrane which leads to neutrophil activation. The activated neutrophils then cause further activation by producing C5a. C5a and ANCA create an inflammatory amplification loop. The C5a fragments then attract and produce more neutrophils. The neutrophils again are activated by ANCA and produce more C5a. Destructive factors released by activated neutrophils and generated by complement activation cause inflammatory injury to vessel walls. Figured extracted from [45].

Anti-glomerular Basement Membrane Disease

Anti-GBM antibody disease is a rare autoimmune disorder characterized by circulating autoantibodies directed against specific antigenic targets within the glomerular and alveolar basement membranes. The anti-GBM disease is also called Goodpasture's Syndrome named after Dr. Ernest Goodpasture, who identified the syndrome in 1919 during an influenza pandemic in a patient who died from pulmonary hemorrhage and renal failure [47, 48]. However, until 1964, with the development of immunofluorescence techniques, the antibodies of the anti-GBM antibodies were able to detect anti-GBM antibodies in kidney tissue [49]. The anti-BGM antibodies may result in glomerular necrosis and crescent formations. The GBM consists of collagen type IV. The anti-GBM antibodies attack the collagen a3 chain and the domain NC1 of the collagen in the GBM of glomeruli. The crescents formed in anti BGM are different from those in AVV. In anti-GBM disease, the crescent may include a mixture of cellular, fibro-cellular and fibrous crescents [48] (see Figure 1.10).

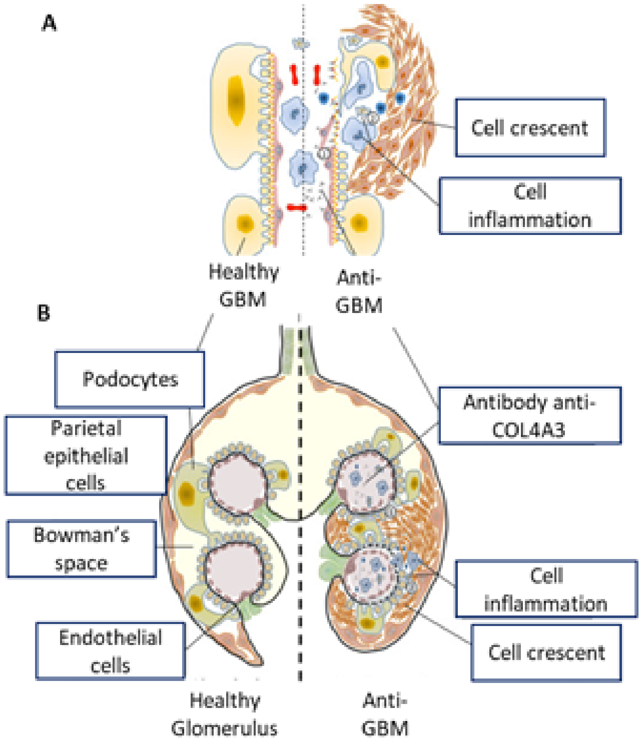

Figure 1.10: The crescent in anti-GBM disease. Schematic representation of the involvement of the glomerular basement membrane (A) within the renal glomerulus (B) Left: the healthy GBM and glomerulus, Right: the GBM and glomerulus in anti-GBM disease with formations of cell and fiber crescents. Figure adapted from [50]

Immune Complex Small Vessel Vasculitis

The immune complex vasculitis is common among three different types of small vessel vasculitis. The immune complex includes cryoglobulinaemic vasculitis, IgA vasculitis, and hypocomplementemia urticarial vasculitis [51] (see Figure 1.8).

1.2.2 Focal and Segmental Glomerulosclerosis

Focal segmental glomerulosclerosis (FSGS) is a common form of kidney disease. Focal segmental glomerulosclerosis accounts for approximately 20% of cases of the nephrotic syndrome in children and 40% of such cases in adults, with an estimated incidence of 7 per 1 million [52, 53]. The cardinal feature is progressive glomerular scarring. Early in the disease course, glomerulosclerosis is both focal, involving a minority of glomeruli, and segmental, affecting a portion of the glomerular globe [54].

FSGS is classified into two types based on the disease cause: primary FSGS and secondary FSGF. The primary FSGS is an idiopathic form because the cause is not known. It has been proposed that FSGS may be mediated by circulating permeability factors. The secondary FSGS is caused by another disease or a drug. For example, it can be caused by viruses or specific mutations. FSGS can be drug-induced involving heroin, interferon-α, interferon-β, and interferon-γ, lithium, pamidronate, sirolimus, calcineurin-inhibitor nephrotoxicity, or anabolic steroids. FSGS can have several different appearances or variants when they are seen under the microscope. A classification of histologic variants recognizes tip lesson, perihilar, cellular, and collapsing disease variants and applies to both primary and secondary focal segmental glomerulosclerosis [54, 55].

The lesions can be classified and ranked following the Columbia classification that suggests a hierarchy of lesions for diagnosis: collapsing variant, tip lesion, cellular variant, perihilar variant, and lastly, Not-otherwise-specified (NOS) [56, 58]. The cellular lesion is perhaps the most difficult lesion to identify reproducibly and shows segmental endocapillary hypercellularity occluding lumens with or without foam cells and karyorrhexis [59]. Some biopsies will show multiple morphologic lesions. In the NOS, segmental sclerosis/segmental destruction of capillary loops with the increase of extracellular matrix. The specific segmental damage cannot be determined. In the tip variant, the glomerular scarring and damage occur in the portion of the glomerular tuft juxtaposed to the tubular pole. Abnormalities include adhesion to the Bowman's capsule at the tip, hypercellularity, the presence of foam cells, and/or sclerosis [59, 60]. Similar to NOS, the perihilar variants show segmental sclerosis and destruction of capillary loops with matrix increase. However, the segment is located near the hilum. The hilum is the location where the blood enters and exits the glomerulus [61]. The collapsing variant is considered the most rapidly progressive form of FSGS. The collapsing variant shows segmental or global mesangial consolidation and loss of endocapillary patency in association with extracapillary epithelial hypertrophy and/or proliferation.

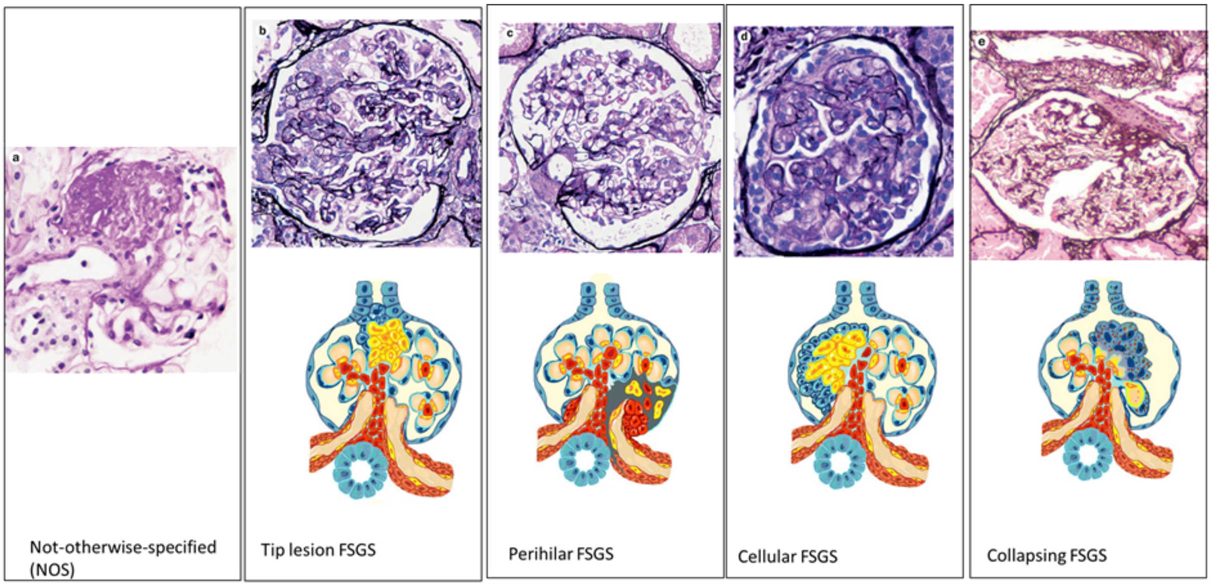

Figure 1.11: The Columbia classification of FSGS. From left to right: Not-otherwise-specified, (b)tip lesion FSGS, (c) perihilar FSGS, (d) cellular FSGS, (e) collapsing FSGS. Figure adapted from [56, 57].

Microcystic tubular dilation is frequently present [62, 63].

1.3 PEC involvement in kidney diseases

As mentioned in the previous section, in the RPGN, there is no primary involvement of PECs in kidney disease. However, the crescent formation due mainly to PEC proliferation and migration indicates the participation of PECs directly in the pathogenesis of different glomerular diseases. Below, there is a list of PEC responses to injury.

Activated PECs form early cellular crescents

Activated PECs (aPECs) have larger cytoplasm, can migrate and proliferate and produce more matrix than fPECs. In aPECS, CD4 protein is known as a specific marker to distinguish between aPECs and other cell types. In the glomerulus, monocytes and macrophages also express CD4, therefore, to distinguish aPECs from those cells, the shapes, as well as locations of the cells or double specific staining for these cells, are also considered [64–66]. The mechanism and signaling pathways of PEC activation and proliferation are not fully understood. By partially depleting PECs, Sicking et al. indicated that it could induce activation of the rest of the PEC population. After being activated, the PECs proliferated and migrated into the Bowman's space and formed cellular crescents leading to periglomerular infiltration. It was also observed that there was no adhesion between the glomerular tuft and the Bowman's capsule. Therefore, the authors concluded against the hypothesis that adhesion was needed to form cellular crescents [67].

Proliferation of activated PECs involved in early crescent formation

When PECs are mature, in non-pathological conditions, their proliferation rate is relatively low [68]. The turnover rate of PECs is similar to that of endothelial and mesangial cells in glomerulus about, 1% per day [69]. Even though they share the same epithelial cell lineage with PECs, the podocyte turnover rate is not detected after the capillary loop stage. The early cellular crescents in the RPGN diseases are mainly formed by activated PECs and activated podocyte proliferation. The cellular composition of crescents appears to change over time, with proliferating glomerular epithelial cells predominating in the early stages of crescent formation [70]. In the later stages, infiltrating macrophages, lymphocytes, and myofibroblasts are numerous, especially when the Bowman's capsule is ruptured [71, 72].

Following FSGS induction in Thy1.1 mice, cuboidal PECs and iPECs expressed the highest levels of proliferation and activation markers in the glomerulus. Taken together, studies on glomerular crescents have shown that the PECs can become a highly activated cell type that proliferates and plays an active role in the formation and progression of crescents [19].

Apoptosis

To maintain the number of PECs in the glomerulus after proliferation, PECs set up apoptosis, the programmed cell death [73]. When PECs are dead, the proliferating cells in the crescents are replaced by scar tissue. Therefore, the cellular crescents become fibrous crescents [74]. Furthermore, the PECs were also found in patient urine. Therefore, it is believed that cell detachment is also one of the factors to reduce the number of PECs [75]. In the review by Ohse et al., they concluded that a decrease in PEC numbers through apoptosis and/or detachment occurs after injury. However, it is still a controversial topic [18].

Epithelial-Mesenchymal Transition

An Epithelial-mesenchymal transition (EMT) is a biological process in which polarized epithelial cells normally interact with the basement membrane via their basal surface lose their cell polarity and cell-cell adhesion to assume a mesenchymal cell phenotype. The mesenchymal cells have higher migration rates and invasiveness [76, 77]. Studies suggest that EMT in the kidney underlies scarring. Recent evidence supports EMT occurring in PECs. The distinct markers of epithelial cells and mesenchymal cells are normally used to study EMT. Ng et al. [78] and Fujigakiet al.[79] found out that there is an increase in α-smooth muscle actin in PECs in the experimental models of the crescentic GN model. Shimizu et al. showed the involvement of integrin-linked kinase (ILK) in the process of PEC EMT *in vitro* and *in vivo* [74]. T.Ohse et al. showed that increased levels of SNAIL can cause loss of claudins and occludin in cultured PECs exposed to TGF-β [18].

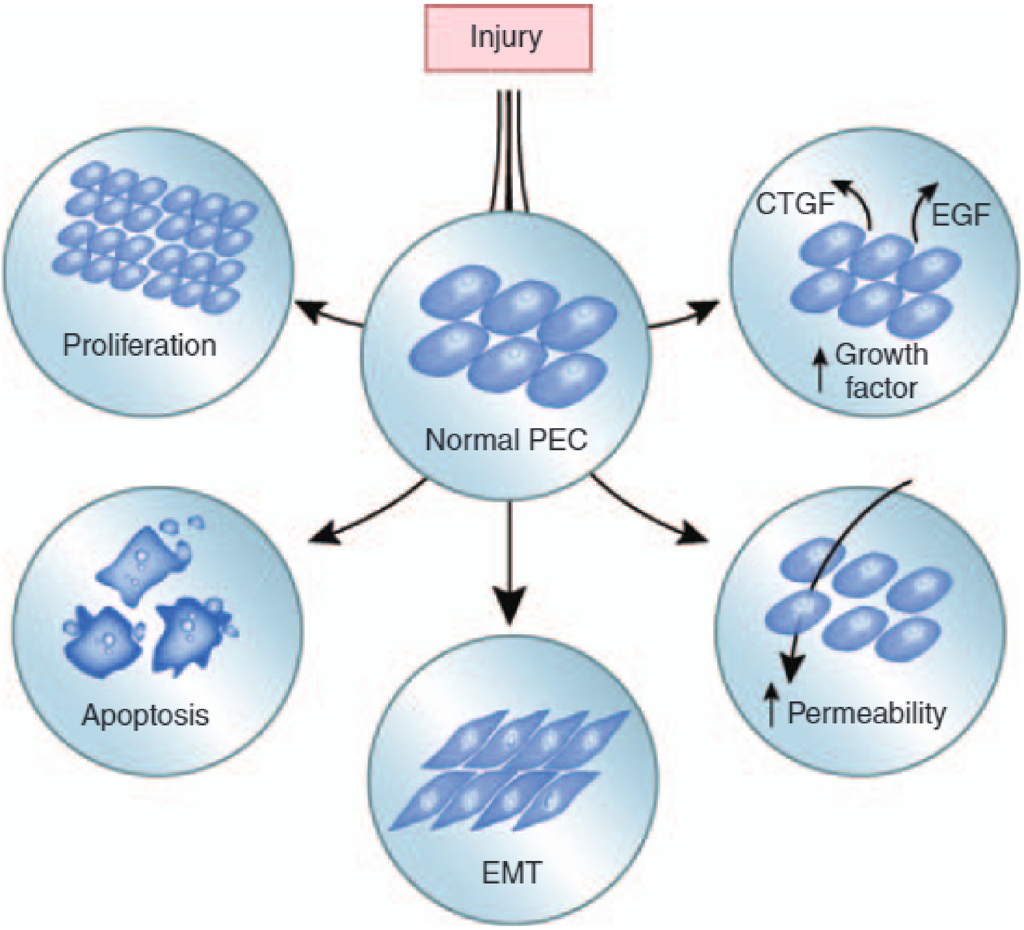

Figure 1.12: Summary of PEC response to kidney injury. The figure adapted from [18].

Increase in Kidney Permeability

The permeability function of PECs is not fully understood. Kriz et al. [80] showed that in rat models of spontaneous FSGS if the monolayer structure of PECs is disrupted, there is an influence in urine flow. Tracer studies using lissamine green and ferritin were administered by intravenous injection and were subsequently traced histologically in serial kidney sections. The results showed misdirected filtration into the periglomerular area. Based on the study, they proposed a model where a new urinary space between the tubular epithelium and the tubular basement membrane was initiated by the loss of PECs and adhesion of the glomerular tuft to the Bowman's basement membrane (BBM).

However, T. Ohse et al. showed in a mouse model with an anti-GBM disease that PECs and BBM form a secondary barrier to the urinary filtrate due to their tight junction proteins. They found that even after a decrease in the number of tight-junction proteins after induced injury, the monolayer of PEC is intact and still leads to misdirect urine into the periglomerular area [23].

The two groups were using different kidney disease models and also different tracers and detection systems. Therefore, there is more research needed to further understand the permeability roles of PECs in kidney diseases.

PECs acquire many characteristics of podocytes after injury

Podocytes are located on the last layer of the filtration barrier of the glomerulus, they play an important role in maintaining the filtration barrier function. The loss of podocytes initiates the progression of glomerulosclerosis [81]. Podocytes are highly differentiated post-mitotic cells that cannot divide. Therefore, the body needs to find a way to replace the loss of podocytes to maintain their numbers in the glomerulus. Recently, several studies have reported the possibility that PECs serve as local progenitor cells. In their study, Appel et al.[82] performed PEC tracing studies in transgenic mice that express inducible lacZ mainly in PECs. lacZ is a gene that encodes β-galactosidase (LacZ), an intracellular enzyme that cleaves the disaccharide lactose into glucose and galactose. LacZ was induced in PECs with doxycycline on postnatal day 5, and the distribution of labeled cells was examined at different dates during the mouse development. Interestingly, labeled cells were found in the glomerular tuft, and nephrin was co-expressed with lacZ in these cells. The number of labeled cells in glomerular tuft increased over time. From this study, they concluded that PECs serve as podocyte progenitor cells during nephrogenesis. Moreover, Sagrinati et al. [83] identified multipotent progenitor cells on the Bowman's capsule in the human kidney based on hematopoietic stem cell marker expression. Isolated stem cells showed an ability to differentiate into multiple glomerular cell types, including podocytes under appropriate cell culture conditions [83, 84].

Increase in growth factors

Several growth factors, such as Connective tissue growth factor (CTGF), Platelet-derived growth factor (PDGF), transforming growth factor-beta TGF-β, Heparin-binding epidermal growth factor-like growth (HB-EGF), Epidermal Growth Factor (EGF), are expressed at higher levels in PECs while PECs respond to the injury and proliferate to form crescents [85]. CTGF which is known as a connective tissue growth factor (CCN2) is a cellular matrix protein of the CCN family of extracellular matrix-associated heparin-binding proteins. CTGF has important roles in many biological processes, including cell adhesion, migration, proliferation, angiogenesis, skeletal development, and tissue wound repair. In their study, they investigated the level of expression of CTGF in human renal biopsies of different renal diseases using *in situ* hybridization to detect the corresponding mRNA. CTGF is more highly expressed in disease PECs than in PEC in normal conditions and is also found in the extra capillary and severe mesangial proliferative lesions of crescentic glomerulonephritis, IgA nephropathy, focal and segmental glomerulosclerosis, and diabetic nephropathy. Their results indicate that CTGF may be a common growth factor involved in the physiological response to the kidney injury and perhaps affects other cells in a paracrine manner [86].

Fujigaki et al. showed a correlation between the expression of PDGF-B and its receptor PDGFR in crescent formation in anti-GBM disease. The expression of PDGF-B and PDGFR in PECs was significantly higher in anti-GBM disease rats compared to normal rats [87].

1.4 Summary

In this chapter, I present an overview of the kidney structure and the mechanisms of some inflammatory kidney diseases. In the kidney, the nephron is the smallest filtration unit inside which the glomerulus is located. The blood that enters the glomerulus through the afferent arteriole is firstly filtered in the glomerular filtration barrier. After this filtration step, the blood circulates back to the blood vessels through the efferent arteriole while water and small molecules reach the Bowman's space.

The parietal epithelial cells (PEC) that lie on the Bowman's space are involved in the filtration process of the kidney but also in the invasion of the Bowman's space which degrades the glomerular filtration function and in the crescent formation in kidney diseases. Growth factors are much more highly expressed in PECs during kidney disease than in PECs in healthy kidneys. After kidney injury, PEC cells are activated and proliferate to form cellular crescents. PEC cells also set up apoptosis of the proliferating PECs in the crescents which then become scar tissue.

Chapter 2

Membrane Organization

Contents

> ”The beauty of a living thing is not the atoms that go into it, but the way those atoms are put together.”
>
> Carl Sagan

2.1 Cell Membrane Structure and Composition

The cell membrane is an essential component of the cell that encloses the cell cytoplasm and other parts of the cell. In animal cells, there is no cell wall, so, the membrane plays as a barrier that protects the other cell components from the outer environment by their unique semipermeable property, where it allows only certain molecules to cross the membrane while preventing others to enter and exit the cell. The simplest model of the cell membrane is the Fluid Mosaic Model proposed by Singer and Nicholson in 1972. It postulates that the membrane is composed of a sea of lipids and proteins moving freely inside the lipid sea [88, 89]. After decades of research, there are different models which are proposed to explain different properties of the membrane and its components. These models will be discussed in section 2.2 while section 2.3 addresses the involvement of EGFR and CD9 in kidney disease.

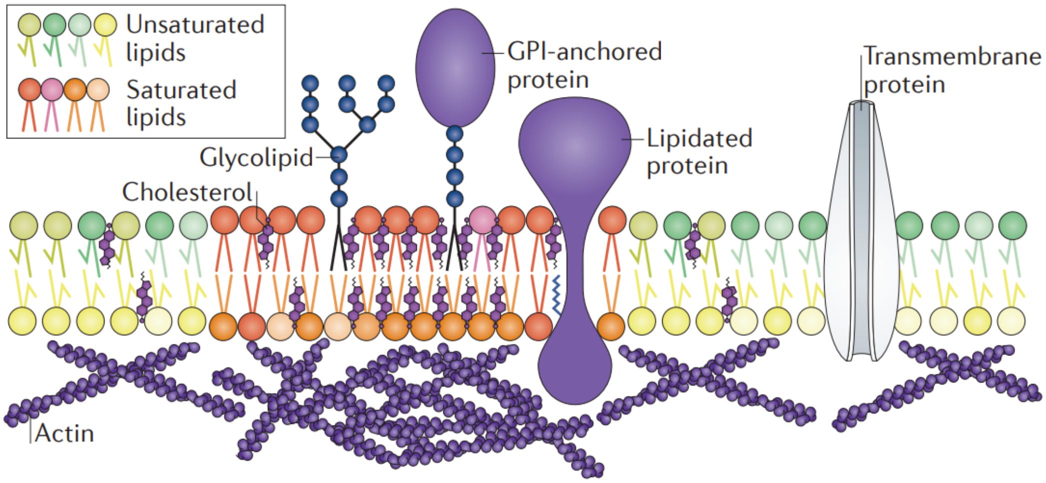

Figure 2.1: Membrane organization. The cell membrane is composed of a lipid bilayer and proteins diffusing inside the lipid bilayer. Some proteins are confined in cell membrane domains called rafts, others are localized outside rafts. Figure from [90].

2.1.1 Lipids

The cell membrane is made of lipids, proteins, and carbohydrates. Lipids take up around 50% of membrane mass and other parts are made up mostly proteins (around 42%) and carbohydrates (2% to 8%) [91]. As shown in figure 2.1, the cell membrane consists of different types of lipids. Because of their amphiphilic properties, lipids spontaneously form a bi-layer membrane where the hydrophilic heads are exposed to outer space and the cytoplasm while the hydrophobic tails are pulled out of the waterside and spontaneously point toward each other. Moreover, because of the amphiphilic property, the lipid bi-layers are more stable in closed form to avoid exposure of the hydrophobic tails to water [92].

There are different types of lipids in the cell membrane. The most abundant lipids that are found in the membrane are phospholipids which are unsaturated lipids. They have one hydrophilic head and two hydrophobic tails. One of the hydrophobic tails is saturated and the other is unsaturated and contains one or more cis-double bonds in the carbon chain. The unsaturation degree and the length of the carbon chain are important to determine the fluidity of the membrane. (Figure 2.3 A). Because of the kinked effect created by the unsaturated cis-form of phospholipids, it is more difficult for these lipids to be compacted together.

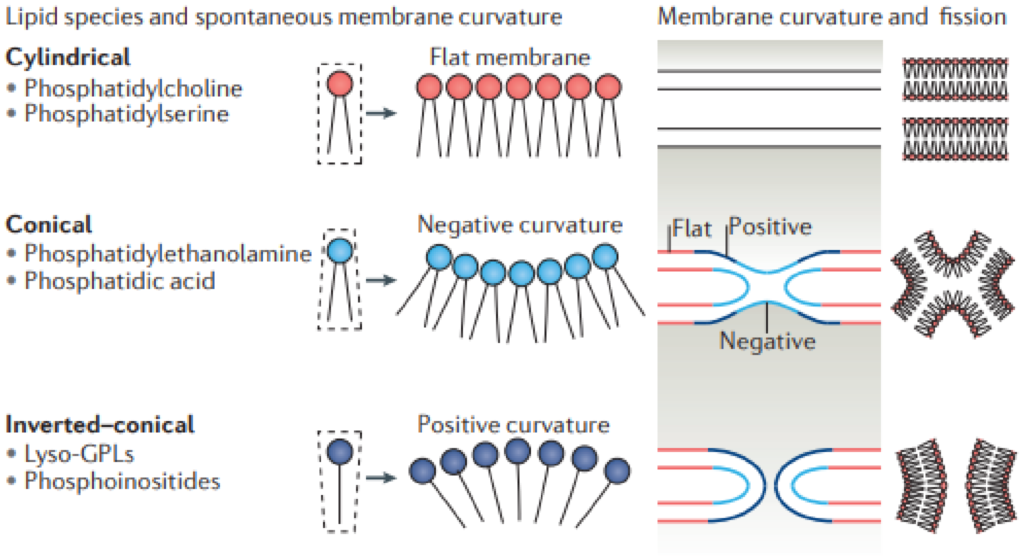

Figure 2.2: Lipids have different ratios of amphiphilic heads and hydrophobic tails, the ratios of these lipids create lipids in three forms: cylindrical, conical, and inverted-conical. These forms can affect the membrane spontaneous curvature. Figure extracted from [93].

Other types of lipids found in the cell membrane are sphingolipids that have a saturated carbon chain. Unlike phospholipids, because of their saturated chains, they can form highly ordered and highly compact domains. These domains have been called raft domain in the cell membrane and (Figure 2.3 B) [94, 95] will be discussed in more detail in the following section.

Cholesterol is a member of the sterol family, built from four linked hydrocarbon rings (Figure 2.3 C). A hydrocarbon tail is linked to the steroid at one end, and a hydroxyl group is attached at the other end. Cholesterol itself is not able to form lipid bilayers but instead inserts itself mainly into domains to make the domains more rigid. The incorporation of cholesterol into the membrane helps enhance membrane rigidity. The composition of cholesterol changes in cell types. For example, cholesterol takes up to 25% in the nerve cell membrane while it is absent in some intracellular membranes [96].

The glycolipids, as their name implies, are sugar-containing lipids anchored to the extracellular side of the membrane. The carbohydrate chain is exposed at the extracellular surface while the hydrocarbon chain inserts itself into the membrane bilayer [95, 97].

2.1.2 Proteins

While lipids play an important role in forming and remaining the structure and stability of the membrane, proteins in the membrane participate in membrane functions. Depending on their binding positions to the membrane, they could be categorized as integral and peripheral proteins. The integral α-helical proteins include at least one hydrophobic tail(α-helical domains) which could integrate into the hydrophobic part of the membrane lipids while the hydrophilic part is exposed to the extracellular environment or inward to the cytoplasm. The membrane proteins could have one or several α-helical domains. If the integral protein

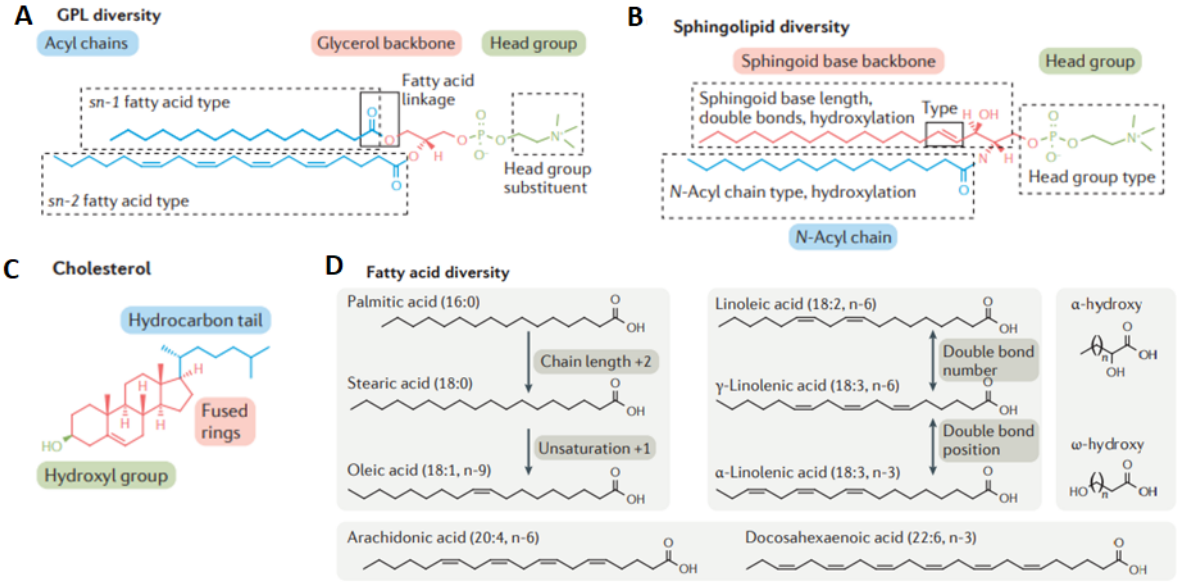

Figure 2.3: (A) Glycerophospholipids are the most abundant lipids in the cell membrane. They have a glycerol backbone with fatty acids and a head group consisting of phosphate and alcohol. (B) Sphingolipids have two different types of tails: hydroxylation(N-acyl chain) and unsaturated tails. The head group of sphingolipids defines their names. (C) Cholesterols have ring structures with hydroxyl heads and a short hydrocarbon tail. (D) Fatty acids have a variety of different chain lengths, levels of unsaturation, and positions of double bonds. Figure extracted from [93].

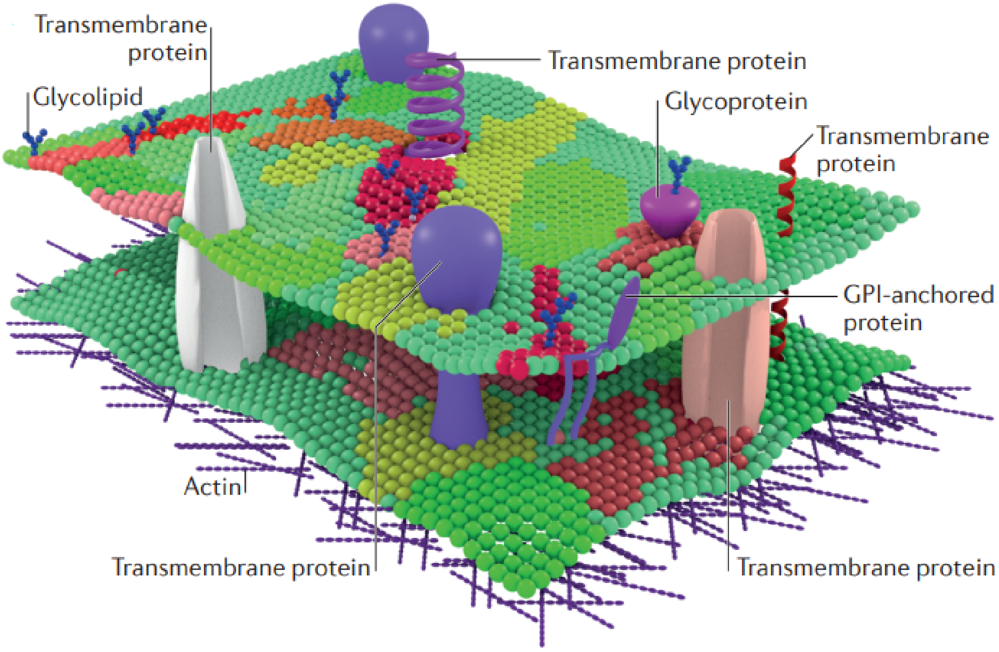

Figure 2.4: Different types of proteins in the cell membrane. Figure from [90].

stretches from one side of the membrane to other side, it is called a transmembrane protein. In the outer membrane of Gram-negative bacteria such as E. coli, porins are present which are a class of transmembrane proteins whose structure is made of a beta-barrel pore. The porins in the outer membrane of an E. coli cell provide channels for the passage of disaccharides, phosphate, and similar molecules. Proteins containing seven membrane-spanning α helices form a major class that includes bacteriorhodopsin and many cell-surface receptors.

The peripheral membrane proteins are anchored on the interface between the lipid-water interface. They can interact through one of their structural domains with integral membrane proteins or with the polar head groups of membrane phospholipids by electrostatic interactions, non-specific hydrophobic interactions, or using a cascade of binding events of other cytosolic proteins. Because they are not inserted into the hydrophobic part of the lipid bilayers as integral proteins, therefore, they have high mobility and can be involved in signaling processes and interactions with other membrane proteins. Carbohydrates are attached to some proteins to form glycoproteins. Glycoproteins are formed by covalent binding between carbohydrates and proteins. Glycoproteins which are mostly integral proteins are also known as Glycosylphosphatidylinositol (GPI) anchors. GPI-anchor proteins are attached to a GPI complex molecular group via an amide linkage to the protein's C-terminal carboxyl group [98].

2.1.3 Carbohydrates

While lipids and membrane proteins are studied intensively in recent years, carbohydrates are less studied. The carbohydrates cover the external surface of the cell membrane. They bind to lipids and proteins to form glycolipids and glycoproteins, respectively. The glycoproteins were introduced in section **Proteins** (Figure 2.4). Because they locate in the outer space of the cell, the carbohydrates have essential roles in cell-cell interactions and pathogen bindings [99].

2.2 Cell Membrane Models

2.2.1 Raft Model

In 1972, Singer and Nicholson proposed the Fluid Mosaic Model that describes the cell membrane as composed of a lipid bilayer that contains proteins moving freely inside it [88]. However, as we discussed in section 2.1.1, the lipid bilayers of the membrane contain different lipid molecules. The heterogeneous lipid compositions are believed to lead to the formation of domains enriched in certain types of molecules. The regions where cholesterol and sphingolipids are packed together are called cholesterol- and sphingolipid-enriched domains or lipid rafts. These domains are highly ordered and more compact. The size of the lipid rafts may vary from one cell type to the other and its value ranges from 20 nm to 200 nm [100].

The first experiment that led to the hypothesis of the lipid raft existence is the discovery of a non-insoluble membrane domain in Triton X-100 at low temperature. The rafts are not only enriched in cholesterol and sphingolipids but also contain different proteins such as transmembrane proteins or GPI-anchored proteins [101, 102] (Figure 2.5).

However, the method of using non-ionic detergents for determining the nature of a domain has been criticized. In 2003, Shogomori et al. showed that the different conditions of detergent used in dissolving the raft could lead to different results in the protein composition of the raft. Other experiments also found out that Triton X-100 can create highly packed domains from an initial homogeneous solution of lipids in a membrane model [104]. Recently, lipid rafts are considered as domains enriched in sphingolipids, sterols like cholesterol, and GPI-anchored proteins. However, there are many controversial results on the composition of these raft domains in the cell membrane [105]. By using nanoscale secondary ion mass spectrometry (nanoSIM), Frisz et al. found that the domains in fibroblast cell membrane were enriched in sphingolipids but not enriched in cholesterol [106]. The results on raft domains found in different cells with various techniques also raise the question about the size of the raft domains [103]. Suzuki et al. used gold nanoparticle-labeled GPI-anchored proteins and found using the Stimulation-induced temporary arrest of lateral diffusion (STALL) a domain size of 50 nm in the human epithelial cell line T24 [107]. Using a combination of advanced microscopy and spectroscopy to study the GPI-anchored proteins in COS-7 cells, the GPI-anchored proteins were observed to be dynamically compartmented within domains smaller than 120 nm [108]. In COS-7 cells, the raft domains are cholesterol- and sphingolipid-dependent. The nanocluster formation of GPI-anchored proteins in the Chinese hamster ovary (CHO) was also revealed by high spatial and temporal resolution FRET. The GPI-anchored receptors were found to be located in clusters of 10 nm in size which are cholesterol and actin-dependent [109].

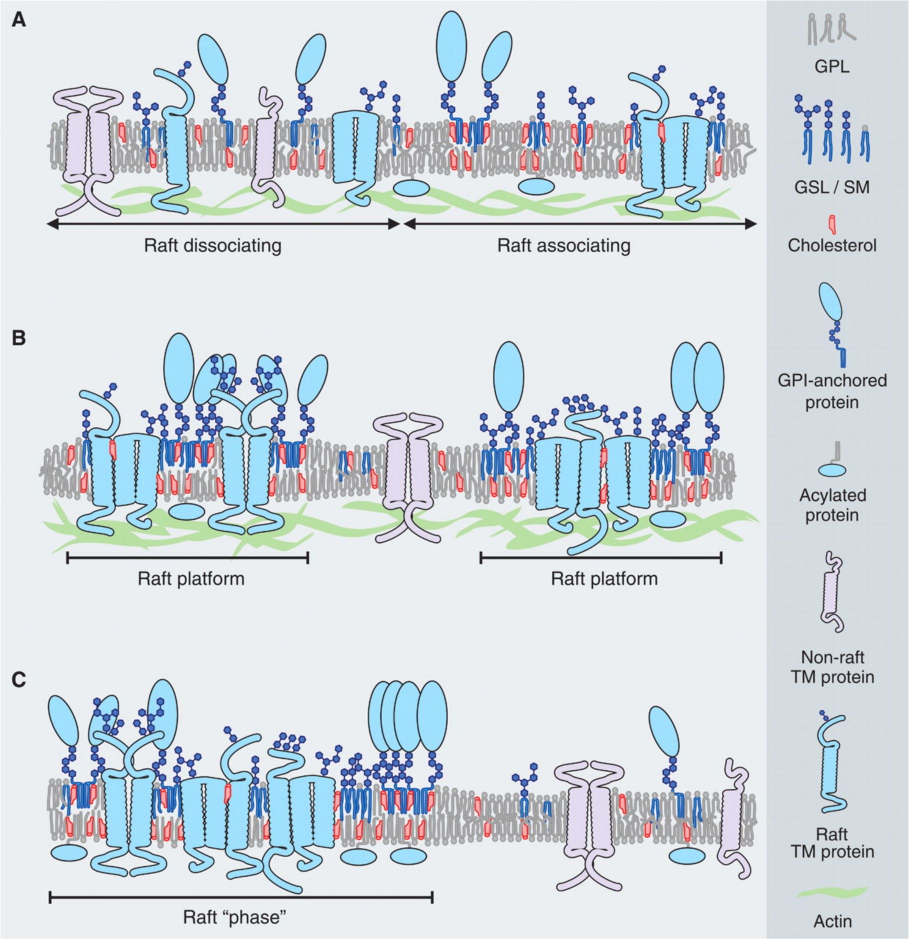

Figure 2.5: (A) The raft domain where the cholesterols and sphingolipids assembly can be modulated by GPI-anchored proteins or transmembrane proteins, acylated cytosolic effectors, or actin cytoskeletons. Some proteins (non-raft proteins) do not associate with the raft domains. (B) The raft domains are considered to facilitate cell functional activities like ligand binding events, synapse formation, protein oligomerization. (C) The raft phase can be formed at physiological temperatures when specific lipid-protein interactions are included. Figure from [103].

2.2.2 Picket and Fence Model

The picket and fence model was first introduced by A.Kusumi et al. while they were studying transmembrane proteins by single molecular tracking using gold nanoparticle labels [110]. Based on the tracking experiments, they proposed a model where the proteins stay a certain time confined in one domain before hopping to an adjacent domain. In the picket-fence model, the diffusing transmembrane proteins are considered to be freely moving in the membrane but their cytoplasmic domain collides with the skeleton mesh (the fence) just under the membrane (Figure 2.6 a). These collisions produce temporary confinement of the proteins inside one domain determined by the skeleton-meshwork before hopping above the actin filament occurs and diffusion continues another domain. The transmembrane proteins tracked include transferrin receptor, a2-macroglobulin receptor, the anionic channel protein band 3, E-cadherin, and its mutants, as well as a G protein-coupled receptor (GPCR), the m-opioid receptor, as test molecules. Interestingly, using molecular tracking of phospholipids in the membrane, they also found that the phospholipids were not freely moving in the cell membrane but had limitations in their motion similar to those studied transmembrane proteins even though the phospholipids tracked were located in the extracellular leaflet o the bilayer not directly in contact with the skeleton in the cytoplasm [110]. That can be explained by the motion of the phospholipids being limited by the membrane ”picket”. The pickets in the cell membrane are proteins that bind to the cortical actin cytoskeleton and form a barrier that affects the diffusion of other receptors. Spencer et al. found that CD4 binds to actin skeletons via ezrin as a picket while the hyaluronic acid acts as a fence. The extracellular domain of CD4 binds to hyaluronan to form a pericellular coat. The motion of phagocytic receptors is affected by this picket fence and the pericellular coat [111]. Proteins tethered to the actin cytoskeleton are discussed in more detail in the next section.

Furthermore, images of the cytoskeleton underlying the cell membrane were taken by using electron microscopy which revealed its patterns and structures. These patterns with periodic strips of around 5 nm indicated that most of the skeletons were formed by actin filaments. The mesh sizes created by these actin filaments in different cell types also have similar to the domain size determined by tracking phospholipids [113, 114] (Figure 2.7).

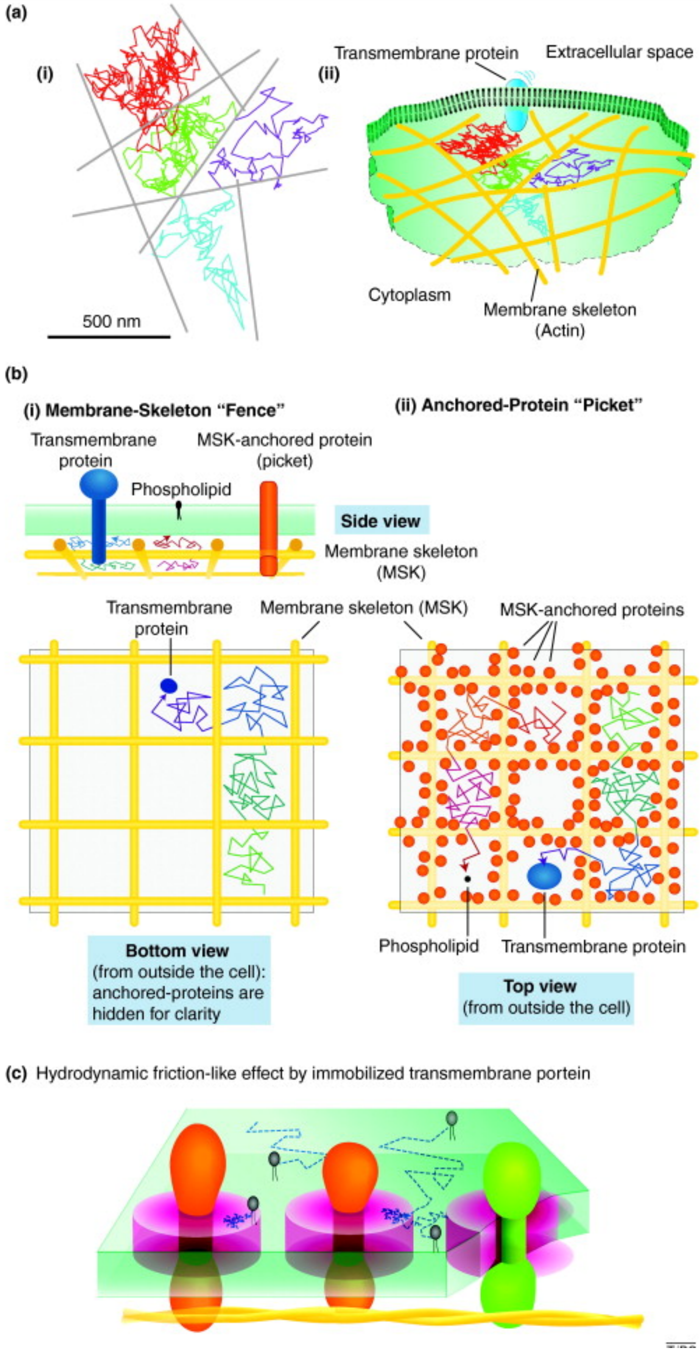

Figure 2.6: Fence and Picket Model. (a) The actin filaments act as a fence that limits the mobility of the transmembrane receptors. (b) In the picket model, the transmembrane proteins bound to actin filaments are considered as pickets. The phospholipids or other transmembrane proteins diffuse and collide with these pickets. (c) Due to the hydrodynamic friction between the moving molecules and picket proteins, the motion of diffusing molecules is slower. Figure from [112].

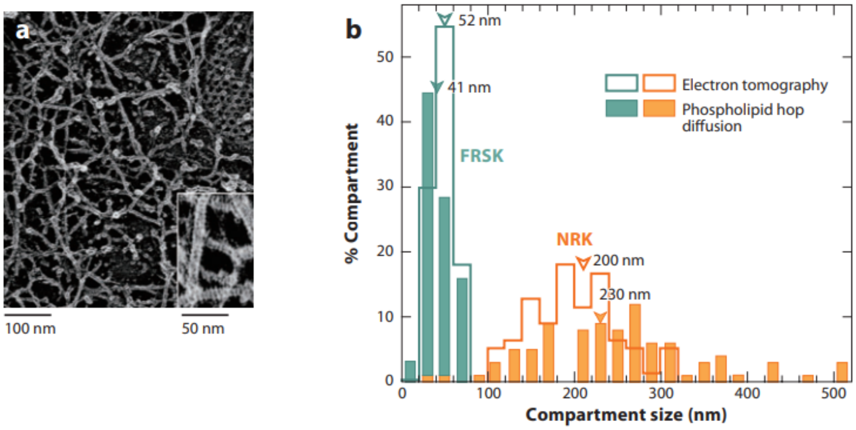

Figure 2.7: Fence and Picket Model. (a) The compartment size and structure of actin meshwork were revealed by electron tomography. (b) The comparison between the compartment size by electron tomography and tracking of phospholipid hop diffusion. Figure from [113, 114].

2.2.3 Tethered Proteins

The confinement of membrane proteins may also be due to the tethering to the cytoskeleton. The membrane proteins can be attached to the cytoskeleton via other proteins such as Erzin or the filament A. The movement of proteins tethered to the actin filaments is elastic around the anchor point, therefore, they seem to be confined in a small round domain [115]. Verkman et al. tracked the epithelial Cystic fibrosis transmembrane conductance regulator (CFTF) Cl- channel and found out that the confinement is elastic and is well described by a spring-like potential. The confinement of the transmembrane protein was also actin-dependent. Therefore, they proposed the hypothesis that the protein is tethered to the membrane actin network [116].

The tethered proteins were also observed in B-cells where the phosphoproteins associated with Glycosphingolipid-enriched microdomains 1 (PAG1) associate with actin filaments via ezrin. Upon activation of B-cell receptor (BCR) by antigens, there were changes in both the organization and composition of raft domains and reorganization of actin filaments. (Figure 2.8). Indeed, after antigen binding to BCR, the BCR is translocated into the raft region and localizes the same domain as PAG1. (Figure 2.8). The lipid raft also coalesced and become larger after the activation [117, 118].

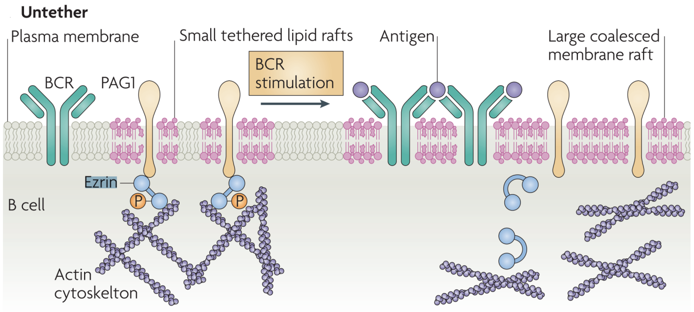

Figure 2.8: Left: Before antigen-binding event, the membrane rafts are tethered to the actin cytoskeleton via the association of phosphoprotein associated with glycosphingolipid-enriched microdomains 1 (PAG1) and phosphorylated ezrin. Right: The activation of B-cell receptor (BCR) by antigen binding leads to dephosphorylation and conformation change of ezrin. This results in the dissociation between actin filaments and PAG1 and the formation of a larger coalesced membrane raft. Figure from [118].

2.2.4 Tetraspanin enriched microdomains (TEM)

Tetraspanins are transmembrane proteins with four loops crossing the cell membrane, which plays important role in cell adhesion, cell secretion, and endocytosis. Tetraspanins can interact with other tetraspanins as well as different proteins and lipids in the membrane. They can interact with cholesterol and gangliosides to form platforms where specific proteins are concentrated. These domains are called Tetraspanin-Enriched Domains (TEM). The size of TEM can range from 200 nm to 400 nm in diameter. Even though the tetraspanin domains share some common features with lipid rafts, they have some different characteristics that distinguish them from lipid rafts: they are not dissolved by Triton-X100 at low temperature and do not associate with caveolin or glycosylphosphatidylinositol-anchored proteins [119]. The comparison of TEMs and rafts is shown in the box below.

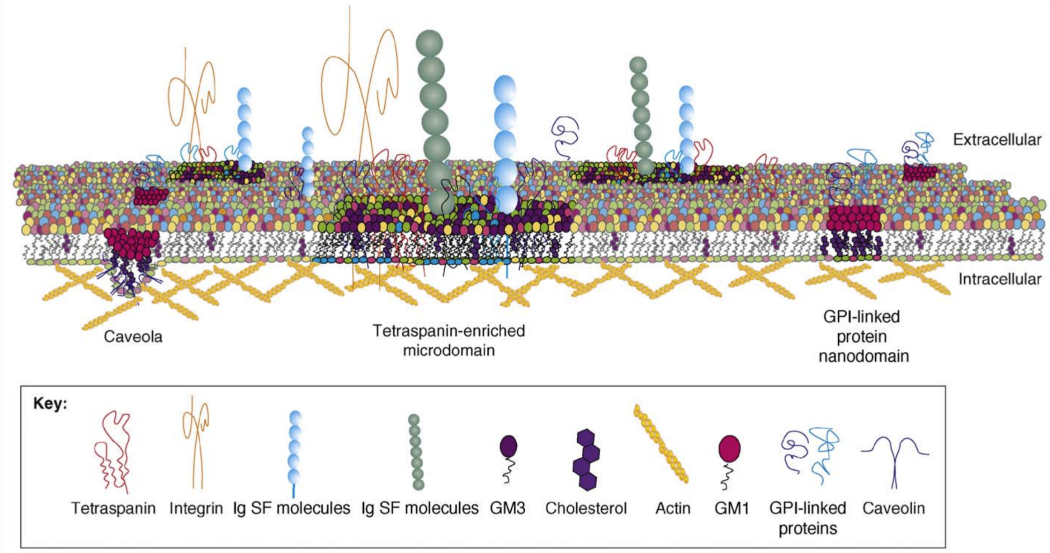

Figure 2.9: Tetraspanins and other domains in the cell membrane. Figure from [120].

Comparison between TEMs and Rafts. Box adapted from [119]

Temperature
TEMs are maintained at 37°C while rafts are disrupted [119].

Effect of Cholesterol Depletion
TEMs remain intact or only partially disrupted after cholesterol depletion while rafts are disrupted after cholesterol depletion [121, 122].

Detergents
At low temperature, TEMs are dissolved mostly by 1% Triton X whereas lipid rafts are insoluble in 1% Triton. TEMs are also dissolved in other non-ionic detergents like Brij and CHAPS [122].

Protein Palmitoylation
Palmitoylation is the covalent attachment of fatty acids to the residues of proteins, most membrane proteins. Palmitoylation enhances the hydrophobicity of proteins. Palmitoylation of TEM proteins does not enhance insolubility or decrease the density. In contrast, the palmitoylation of raft proteins promotes insolubility [123–125].

Domain Components
In TEMs, the most common partners of tetraspanins are integrins (Figure 2.9). Other proteins like junction protein claudin-1 are also found associated with teraspanins [126]. In contrast, GPI-linked proteins, caveolin and Src-family kinases are found to be located in rafts but not in TEMs [127, 128].

By using the super-resolution technique (STED), the details of the size and density of tetraspanin domains were also revealed [129]. Not all the tetraspanin family members are in the same domain. Zuidscherwoude et al. studied the confinement domains where the different tetraspanin family members were located: CD53, CD37, CD81, and CD82 [129]. The CD53 proteins are located in the smallest domains while the CD37 proteins are localized in the largest domain among these four tetraspanin confining domains. The CD81 and CD82 domains, and the majority of the CD37 domains are around 100 nm - 150 nm in size (Figure 2.10). The CD37 and CD53 clusters are located relatively close to the CD81 or CD82 clusters.

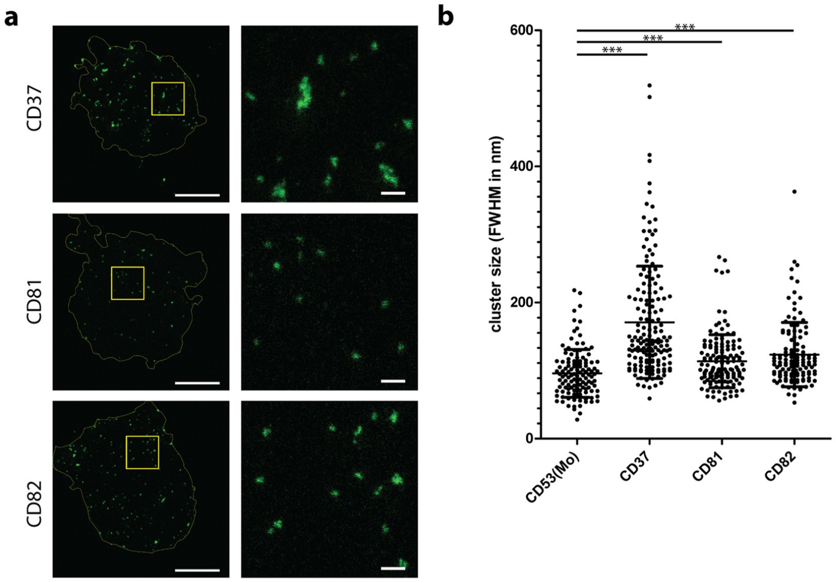

Figure 2.10: (a) The distribution of CD37, CD81, and CD82 proteins in the cell membrane of a JY B cell. (b) The cluster size of CD53, CD37, CD81, and CD82. Figure from [129].

2.3 Epidermal Growth Factor Receptors

The epidermal growth factor receptors (EGFR) belong to the ErbB family of receptor tyrosine kinases (RTK). There are four members of ErbB family: EGFR (ErbB1, HER1)[130], ErbB2 (HER2, neu in rodents)[131] ErbB3 (HER3) [132]and ErbB4 (HER4)[133]. EGFR are transmembrane proteins with an extracellular N-terminal domain containing four subdomains, a transmembrane, intracellular domains including the juxtamembrane domain, the tyrosin kinase N and C-lobes, and the C-terminal tail [134, 135] (Figure 2.11). The extracellular domain of EGFR includes four subdomains,[136] they are illustrating as in Figure: L1 and L2 are ligand bind regions, CR1 and CR2 are cysteine-rich subdomains [135, 137]. EGFR can be activated by the binding of EGF or other ligands to the regions L1 and L2 of the extracellular domains [138, 139]. After ligand binding, the EGFR conformation changes, the regions CR1 and CR2 of the extracellular domain can interact with other EGFR or other members of the ErbB family to create a homodimer or a heterodimer, respectively [137, 140]. Note that the HER2 even without ligand binding is already in the conformation that can interact with other ligand-bound receptors [139] (Figure 2.11).

Multiple signal transduction pathways lie downstream of activated EGFRs and have been reviewed [141]. EGFR activation can lead to multiple signal transduction pathways that are involved cell survival, cell proliferation, cell migration, cell polarity, and adhesion. Furthermore, EGFR deficiency or overexpression is involved in many diseases. The overexpression of EGFR can be associated with different kinds of cancer including adenocarcinoma of the lung, anal cancers, glioblastoma, and epithelial tumors of the head and neck [141].

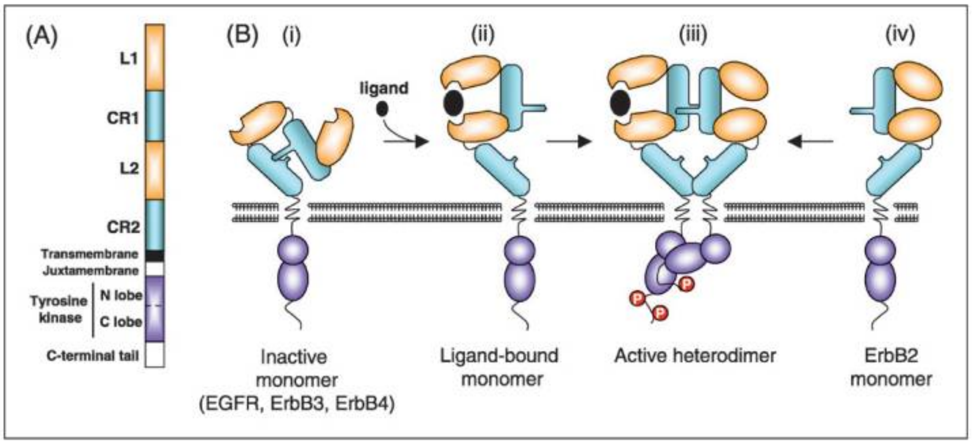

Figure 2.11: (A) The structure of EGFR: from top to bottom: the ligand-binding region 1 (L1), the enriched cystein subdomain (CR1), ligand binding 2 (L2), the cystein-rich subdomain (CR2), the transmembrane region, juxtamembrane region, the tyrosin kinase domain: N lobe and C lobe, and the C-terminal tail. (B) Steps in receptor activation: (i) Inactive form of EGFR, ErbB3, and ErbB4. (ii) Conformational changes after ligand binding to the regions L1 and L2 of receptors. (iii) Interactions between cystein-rich subdomains of 2 receptors to form an activated dimer. (iv) The HER2, even without ligand binding, is already in a conformation that can interact with other ligand-bound receptors. Figure from [141].

EGFRs are involved in many cellular activities and many cancer diseases. Therefore, they have been studied extensively in cancer and biophysical research. Using dSTORM, J. Gao et al. have shown that the average size of EGFR clusters is about 200 nm [142]. Using two-color dSTORM, they also found out that EGFR are partially overlapped with lipid rafts.

By using single-molecule tracking as well as super-resolution microscopy (sequential dSTORM), it has been shown that EGFR activation is clathrin-pathway dependent [143]. Furthermore, by using 2-color molecule tracking and 2-color super-resolution, this group also found that in mutant EGFR, the mutants can form a stable dimers without ligand binding process [144].

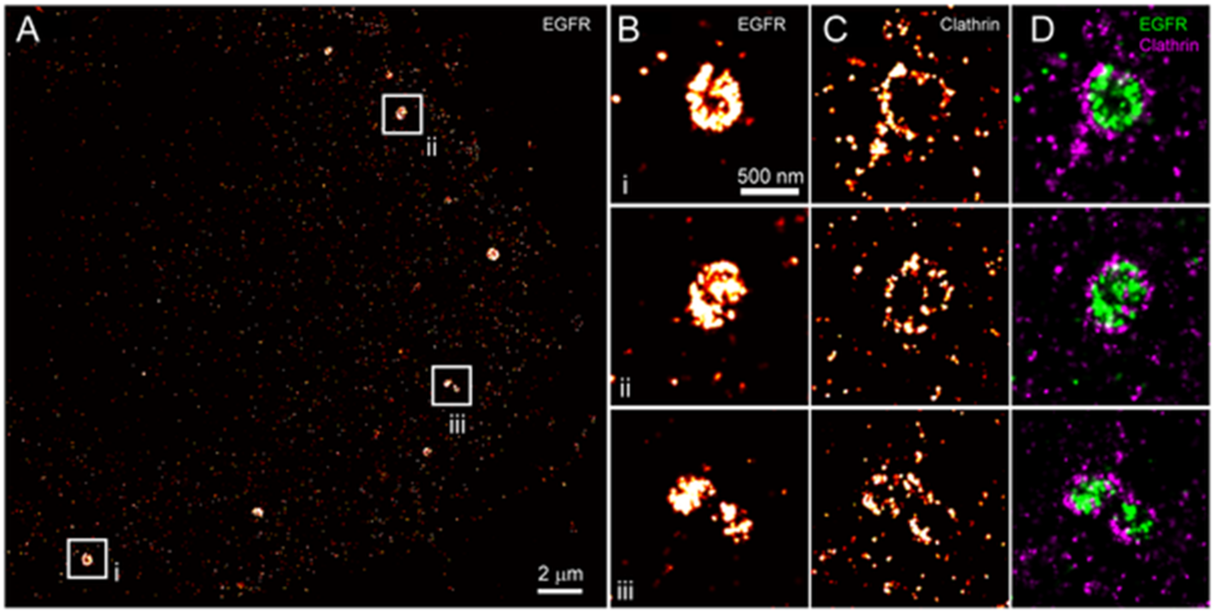

Figure 2.12: (A) The distribution of EGFR after activation by EGF in the HeLa cell membrane. EGF was labeled with Alexa 647. (B) Zoom into the aggregation regions of EGFR i, ii, and iii. (C) When the Alexa 647 fluorophore labeling EGFR was photodestructed, the clathrin molecules were labeled with anti-clathrin-AF647. The clathrin-coated pit was formed around a EGFR cluster. (D) The overlay image of EGFR and clathrin (EGFR in green, clathrin in magenta). Figure from [143]

2.4 The CD9 tetraspanin Protein

CD9 is a member of the tetraspanin protein family, it is also called Tspan 29. Similar to other tetraspanin members, as mentioned in section 2.2.4, it has four transmembrane domains crossing the membrane [145, 146]. Tetraspanins are structurally characterized by containing four transmembrane domains including a small extracellular loop (SEL or EC1), a large extracellular loop (LEL or EC2), and short intracellular N- and C-terminal tails as shown in Figure 2.13, [147, 148]. The tetraspanin family can be distinguished from other transmembrane proteins with four transmembrane domains by the shared overall structure and by the presence of conserved amino acid residues (Cysteine-cysteine-glycine motif) (Figure 2.13). CD9 has four cysteine residues within LEL.

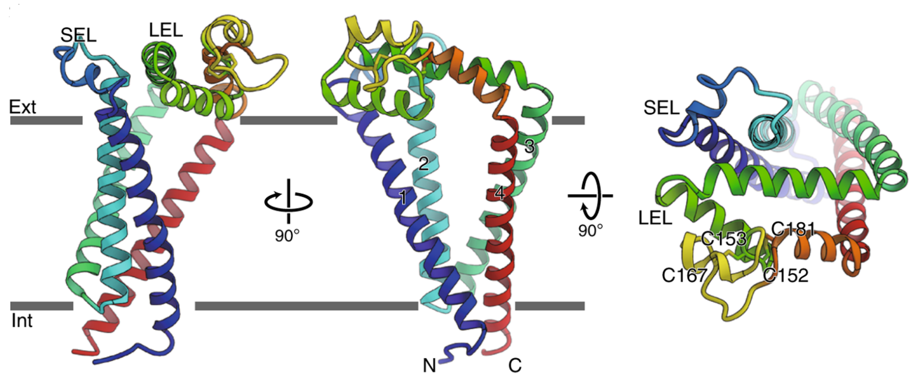

Figure 2.13: Structure of the CD9 protein. Tetraspanin proteins are composed of four transmembrane domains (numbered 1,2,3,4), of two extracellular loops, a small extracellular loop (SEL or CE1), and a large extracellular loop (LEL or CE2), and of N- and C- terminal tails. The cysteine residues in CD9 are Cys152-Cys181 and Cys153-Cys167 which form disulfide bonds. Figure from [149].

CD9 is associated with different cellular activities including motility, proliferation, differentiation, fusion, and adhesion. Because CD9 is involved in various cellular activities, it plays an essential role in many physiological and pathological processes, including sperm-egg fusion, neurite outgrowth, myotube formation, viral infections, tumorigenicity, and metastasis. Furthermore, CD9 is also a component of TEM and has either direct or indirect interactions with other membrane proteins such as metalloproteinases, ion channels, transporters, signaling transducers, and cytoskeletal linkers, or it may act as receptors for cytokines. CD9 can potentially alter the activity of these molecules through different mechanisms such as their selective confinement in TEMs, which would hinder their access to their cognate substrates or binding of their extracellular or intracellular ligands [150].

The CD9 protein has been studied in particular by the P.-E. Milhiet group in the human prostatic carcinoma cell line (PC3). They not only investigated the dynamics of the CD9 protein but also showed the distribution of CD9 proteins in the cell membrane and its interaction with other tetraspanin proteins. CD9 proteins are more concentrated in zones called CD9-enriched zones together with CD81. While in this cell type, they are not located in the same area as CD55 and CD46. CD55 is a GPI-anchored protein that is known to be located in raft domains while CD46 is a type I membrane protein excluded from rafts.

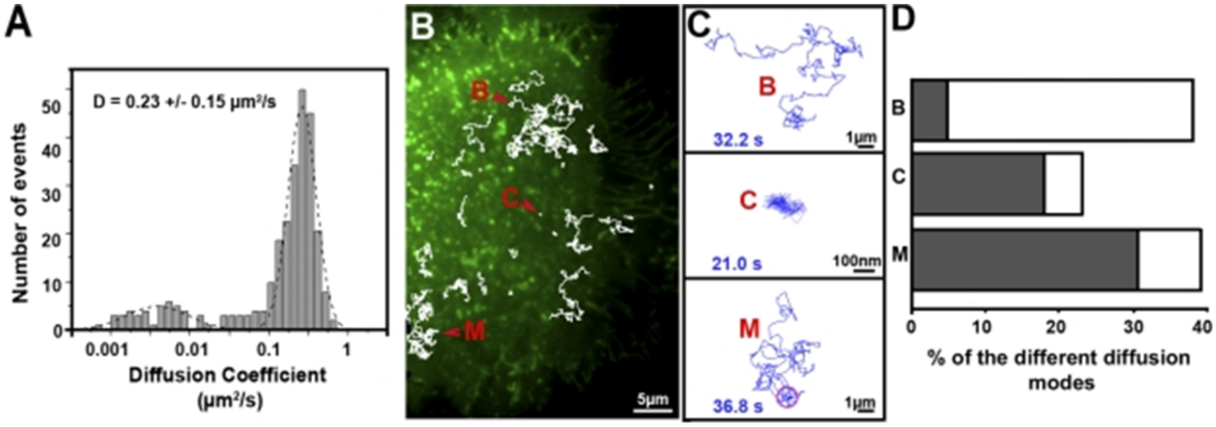

Figure 2.14: (A) The diffusion coefficient distribution of CD9 proteins in the PC3 cell membrane. The first Gaussian fits the diffusion distribution of confined CD9 molecules, whereas the second Gaussian fits the diffusion distribution of free CD9. (B) and (C) Three modes of CD9 diffusion on the cell membrane, where the trajectory labeled B shows free motion, the trajectory labeled C shows confined motion and the trajectory labeled M displays alternation between free and confined motion of CD9. (D) The percentage of free, confined, and alternating diffusion modes of CD9 proteins in PC3 cell line. Figure from [151].

Moreover, by using single-molecule tracking, they have shown that CD9 is dynamic and possesses three different modes of movement. CD9 can be confined in a region or can be freely diffusing in the membrane or may alternate between confined and free states (Figure 2.14).

2.5 EGFR and CD9 are involved in renal diseases

As discussed in section 1.3, the crescent formation in the RGPN disease is caused by the proliferation of epithelial cells and infiltration of inflammatory cells. HB-EGF which is a ligand of EGF receptors is found to be expressed during inflammatory and pathological processes [152]. Bollée et al. conducted a study on the roles of HB-EGF and EGFR in an anti-GBM Nephrotoxic serum (NTS)-induced mouse model of RPGN. HB-EGF is induced not only in the mouse model of RPGN but also in human renal biopsies [3]. In the study, the proHB-EGF mRNA was measured by real-time PCR in kidneys. After 8 days of NTS injection, the proHB-EGF mRNA in the RPGN model mouse was found to be three times higher than in the control case. Not only the proHB-EGF expression was higher, but they also revealed that the phosphorylation of EGFR increased as the result of EGFR activation by HB-EGF (Figure 2.15). 8 days after NTS injection, the level of pEGFR was almost 2.5 times higher than in the control case. In contrast, in mice with HB-EGF deficiency or treated with EGFR inhibitor AG1478, the phosphorylation of EGF receptors remained low.

The crescent formation is due to epithelial cells and inflammatory cells including podocytes. Bollée et al. also revealed that HB-EGF induced a migratory phenotype in podocytes. Furthermore, inhibition of *Egfr* gene or blockade of the EGFR kinase activity in podocytes can prevent renal failure [3].

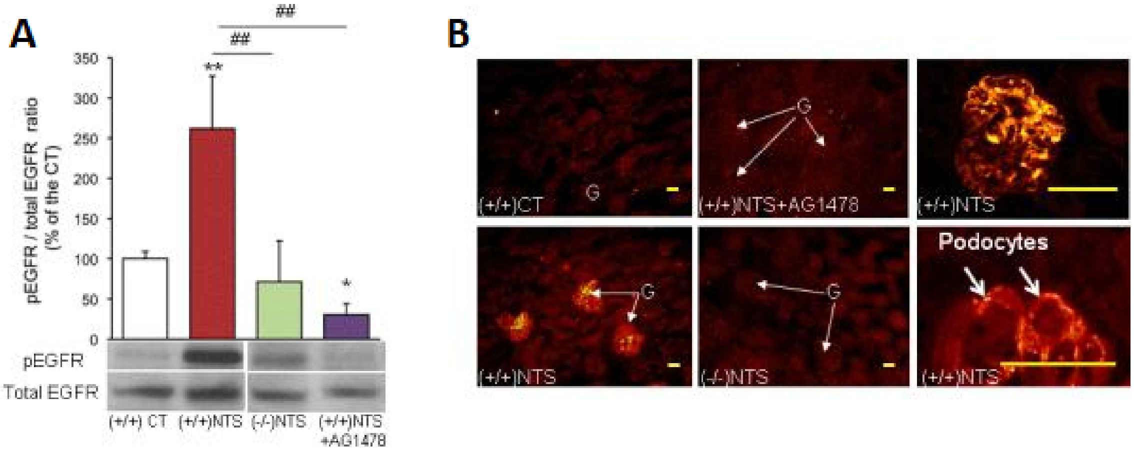

Figure 2.15: (A) The phosphorylation level of EGFR (pEGFR) revealed by Western blot in control mice, RPGN mouse model after 8 days of NTS injection, HB-EGF-deficient RPGN mouse and in a RPGN mouse model treated with EGFR inhibitor AG1478. Values are mean ± s.e.m. (n = 6–8 per group). $*P < 0.05$ versus controls at baseline; $**P < 0.01$ versus controls at baseline; $P < 0.01$ versus mice treated with vehicle only.(B) Immunofluorescence staining for pEGFR in renal cortex after 8 days of NTS injection. Scale bar (orange), 50 μm CT: control,(+/+) NTS: RGPN mice injected with NTS, (-/-) NTS: HB-EGF-deficient mice injected with NTS, (+/+) NTS+AG1478 the RPGN model injected with inhibitor EGFR AG1478. Pec: parietal glomerular epithelial cells; G: glomerulus. Figure from [3].

In more recent work, Lazareth et al. also studied the role of CD9 proteins in migration and proliferation of parietal epithelial cells and glomerular disease [2]. Similar to the HB-EGF expression increase in podocytes, CD9 is overexpressed in PEC in necrotizing crescentic glomerulonephritis (CGN) and FSGS mouse models compared to the control mouse group (Figure 2.16). *Cd9* mRNA increases about 1.5 times with respect to the control case after 4 days of NTS injection.

Similar to the inhibition of *EGFR* gene, the global depletion of CD9 also protects from renal failure. To determine the kidney failure level, the ratio between urine albumin and creatinine was calculated. In normal kidney conditions, large proteins like albumin leaking into urine are negligible, while creatinine is a waste product that is filtered by the kidney into the urine. The Urine albumin to creatinine ratio (ACR)urine albumin to creatinine ratio (ACR) is normally used to determine kidney disease. After 5 and 21 days of NTS injection, the ACR in genetic CD9 depletion mice remains low while the ACR in NTS-injected mice increases significantly (Figure 2.17 A). Moreover, there was no crescent formation in the kidney when removing globally CD9 from mice (Figure 2.17 B, C).

EGFR and CD9 are involved in many cell activities and functions, their association has been studied widely in cancer research. Murayama et al. [153] found in ensemble measurements that CD9 colocalizes with EGFR in a gastric cancer cell line and that CD9 also enhances the internalization of EGFR and the signaling process of EGF-EGFR.

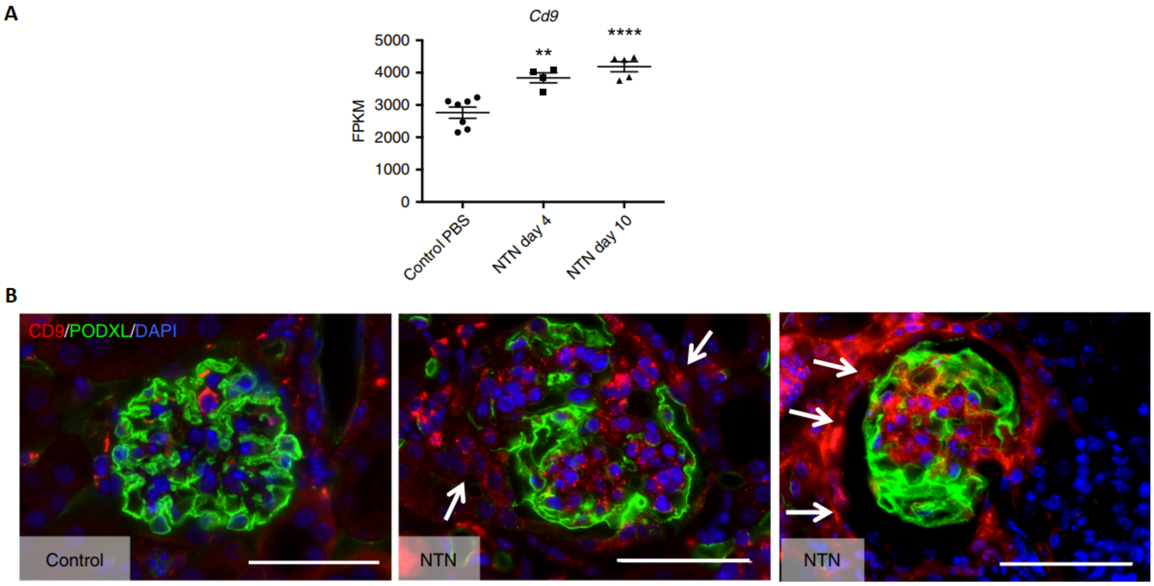

Figure 2.16: (A) *Cd9* mRNA expression in control mice and after 4 days and 10 days of NTS injection, respectively. (B) Immunofluorescence staining of CD9 (red) in murine kidney section, Podocalixin (PODXL) (green), DAPI (blue) in control mice and NTS injected mice. test: $**P < 0.01; ****P < 0.0001$. The CD9 expression increases in the ensemble glomerular cells including PECs and podocytes. Scale bar, 50 µm. Figure from [2].

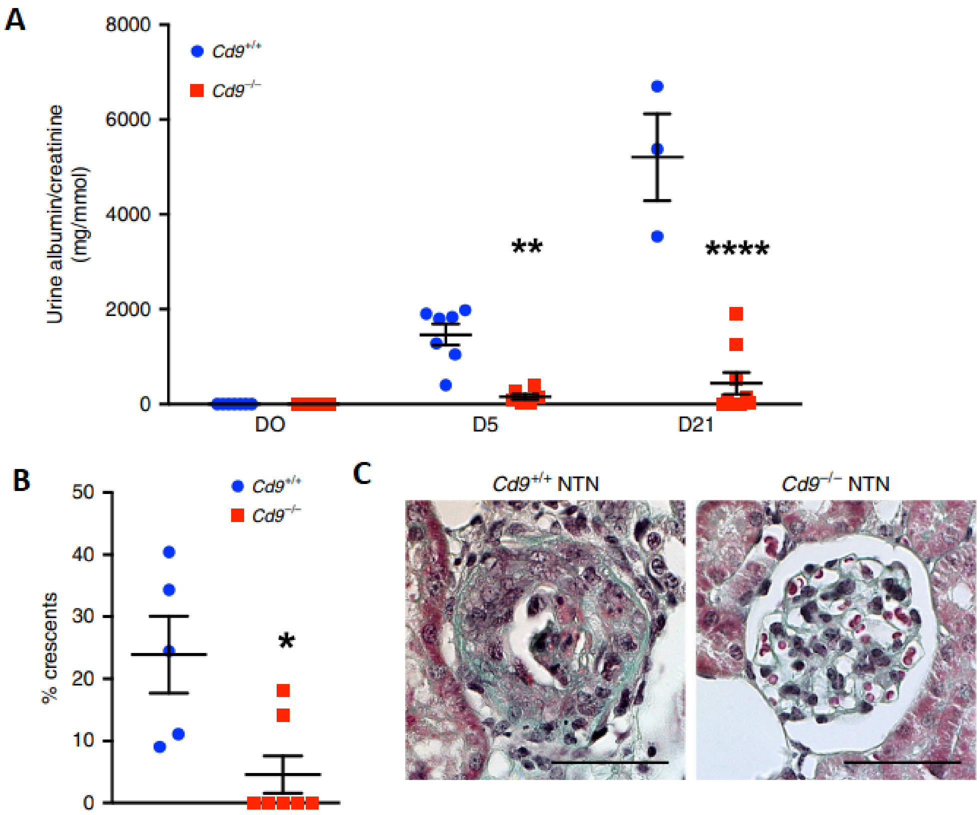

Figure 2.17: (A) Urine albumin to creatinine ratio in two groups of nephrotoxic serum-induced necrotizing crescentic glomerulonephritis mice (CGN) without and with CD9 depletion. t-test: $*P < 0.5; **P < 0.01; ****P < 0.0001$. (B) The percentage of crescent formation after 21 days of NTS injection. (C) Masson's trichrome staining on kidney sections of two groups of mice after 10 days of NTS injection. Scale bar, 50 µm. Figure from [2].

2.6 Summary

While the first chapter introduces the big picture of kidney disease and cellular involvement in kidney disease, the second chapter briefly summarizes the membrane organization and the molecular mechanisms involved in some renal diseases.

The membrane is not a simple lipid bilayer inside which the membrane proteins move freely; most membrane proteins are organized into different nanodomains. These domains can be enriched in some specific kind of lipid such as cholesterol and sphingolipids, (rafts, where GPI-anchored proteins are found) or can be enriched in tetraspanin proteins and integrins (tetraspanin-enriched membrane domains, TEM). The organization of the membrane is also affected by the underlying actin cytoskeleton and by protein tethering to the actin filaments (picket-and-fence model).

The proteins in the cell membrane play essential roles in cell signaling and cell interactions. EGFR and C9 are two transmembrane proteins that are related to severe kidney diseases. The blockage of EGFR or the depletion of CD9 proteins can globally improve the course of rapidly progressive glomerulonephritis (RPGN) in mouse models [2, 3].

Therefore, in my thesis, I am going to investigate the relationship between these two membrane proteins in parietal epithelial cells and the molecular mechanisms leading to their role in kidney disease. Our hypothesis is that, although EGFR is typically found in raft domains in several cell types, they may be confined in tetraspanin-enriched domains in parietal epithelial cells. Indeed, this would explain the role of CD9 in kidney disease.

Chapter 3

Methods to Study Membrane Organization

Contents

> ”La lumière n’est perceptible que si
> elle elle interagit avec un objet: comble
> des paradoxes, la lumière qui nous
> éclaire et nous permet de voir le
> monde est, en elle-même, invisible.”
>
> Xuan-Thuan TRINH

As discussed in the previous chapter, the cell membrane has a complex organization. It is important to understand its organization, the interactions between proteins and proteins, lipids and proteins, lipids and lipids, and the functions of these components. Many techniques have been employed to study the membrane organization. In this chapter, these different techniques will be discussed.

3.1 Single particle imaging and tracking

3.1.1 Principle of Single Particle Tracking

In Single-particle tracking (SPT), the molecules of interest are labeled by fluorescent molecules or nanoparticles. The motions of these molecules are observed during a certain period, the tracking of all molecular positions, and, subsequently, of all transitions from one position to the next as a function of time yields the trajectory of the molecule. Figure 3.1 shows the principle of SPT. From the trajectory of the tracked molecules, information about the molecules can be extracted such as the molecule diffusivity, confinement area, the forces acting on the molecule, interactions between different molecules.

The SPT can overcome the problem of the optical diffraction limit by localizing the emitters with sub-diffraction precision. The optical diffraction limit of microscopy is defined as $d = \frac{\lambda}{2NA}$, where d is the smallest distance between two particles that can be resolved, NA is the numerical aperture, and λ is the incident wavelength. Therefore, in SPT the labeling concentration with the fluorescent molecules is kept low to avoid overlap between them. There are some techniques developed to distinguish also overlapping emitters, but they require more analysis and yield a lower resolution. The point spread function (PSF) normally are fitted with an Airy disk or with a 2D-Gaussian function. The shape of the PSF can be fitted with high precision and accuracy methods such as the Richards-Wolf model and the Gibson Lanni model [154, 155]. However, these methods are more computationally demanding. The simplest model used to determine PSF is a 2D-Gaussian model. Figure 3.2 shows the comparison between using Airy disk and Gaussian fitting to the PSF (Equation 3.1). The ring structure of the Airy disk PSF is not captured by Gaussian fitting. However, isotropic emitters in the focal plane have the highest intensity concentrated in the central lobe, and, the ring intensity is not distinguishable on top of the background signal (Figure 3.2 D). Furthermore, using Gaussian fitting reduces the computational cost.

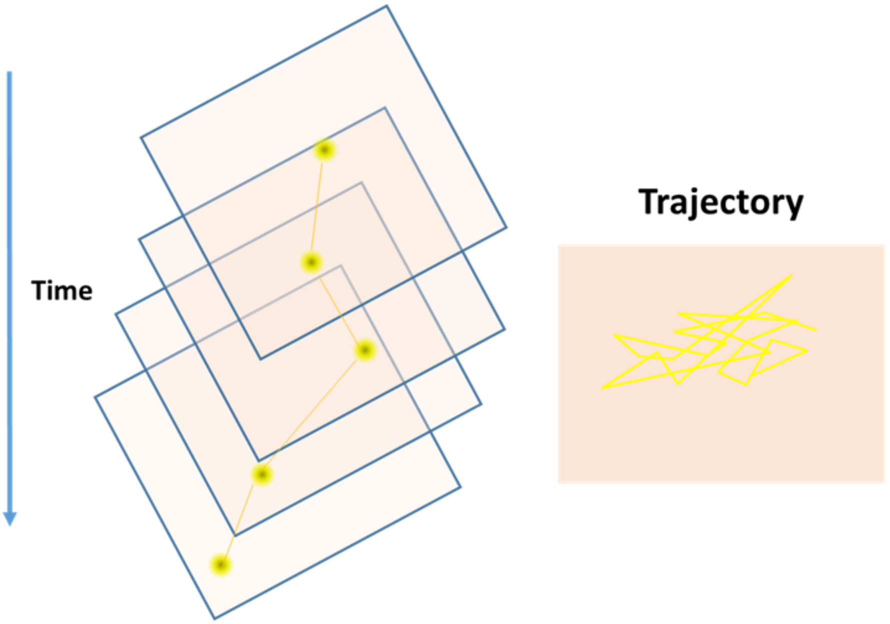

Figure 3.1: Single particle tracking principle.

$$PSF_{Gaussian} = A\exp(-\frac{x^2+y^2}{2\delta_{xy}^2}) \tag{3.1}$$

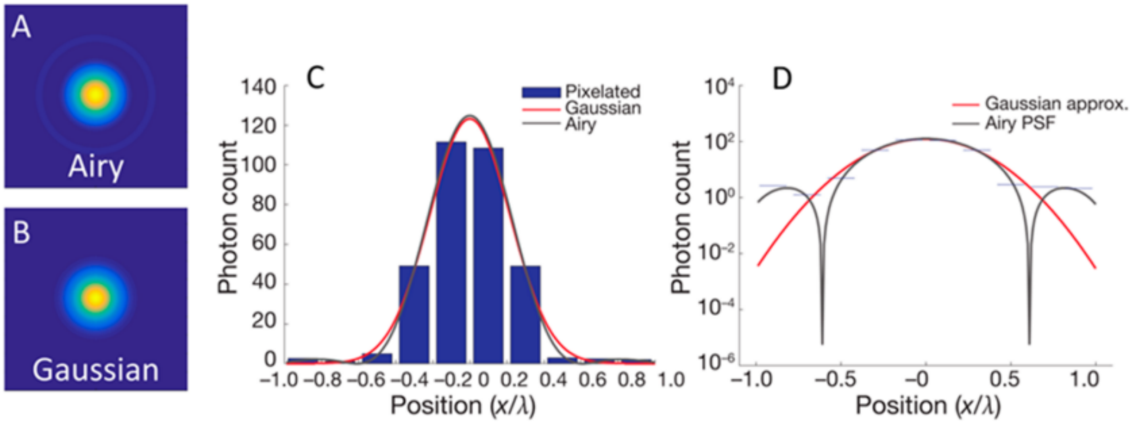

Figure 3.2: The point spread function models by (A) Airy disk and (B) 2D-Gaussian function. (C) Pixelated image is fitted with Airy and Gaussian function. (D) Pixelated image fitted with Airy and Gaussian function in logarithmic scale. Figure from [156]

The precision of the molecule localization is as the localization error of the center of the Gaussian fitting. The localization precision depends on the number of detected photons.

3.1.2 Single Particle Tracking Probes

Organic Dyes

SPT probes are fluorescent proteins, organic fluorescent molecules, or luminescent nanoparticles. The probes used in SPT require high photostability and brightness. The most common probes used in single-particle tracking are organic fluorophores, such as the cyanine family, the Alexa family or Rhodamine [157]. The fluorescent dyes can be attached directly to lipids to make lipid compounds such as Rhodamine-DPPE, Bodipy-Cholesterol, etc. However, changes at the lipid head or tails to attach the fluorescent molecules can change the properties of lipids [158]. When labeling proteins, fluorescent dyes are normally coupled to antibodies that increase the size of the complex. Therefore, care must be taken to avoid modifying the motions of the proteins of interest. However, compared to the nanoparticle size and weight, the fluorescent dyes are the smallest probes, smaller also than fluorescent proteins. One main disadvantage of fluorescent molecules is that they are easily photobleached. Therefore, the tracking duration is short compared to what can be obtained with nanoparticle labels.

Quantum Dots

Quantum Dots also are used in SPT due to their high photostability properties. Quantum dot size determines the emission properties: when the inorganic core size is larger, the emission shifts to red. The quantum dot cores are small from 2 nm to 10 nm. However, to maintain the colloidal stability of quantum dots in an aqueous solution, a water solubilization layer is added that increases the size to about 15 nm - 30 nm [159]. One disadvantage of using QDs is that their size is relatively large compared to the size of the target molecules which can modify the trajectory of the labeled proteins. Another difficulty of using QDs in tracking is the requirement to control the number of functionalization/biomarkers (ex: Fab fragments) on the surface of QDs. When the number of recognition molecules on the surface is too high, it can lead to the crosslinking of target molecules. Moreover, quantum dots are blinking during the tracking experiments due to surface defects that can temporarily trap an electron or a hole and stop the quantum dot from emitting light due to the presence of non-radiative Auger processes [160]. There are methods to analyze the disrupted trajectories to apply for quantum dot blinking problems but this complexifies the analysis.

Rare-Earth-Doped Oxide Nanoparticles

The rare-earth-doped nanoparticles have high photostability without blinking. Therefore, they are suitable for longer tracking experiments [161–163]. Moreover, they can be easily used in gated detection because they have a long radiation lifetime. However, the main disadvantage of rare-earth-doped oxide is the excitation in UV and near UV region, therefore, it can cause light toxicity to living cells. In our experiment, we use 30-nm europium-doped yttrium vanadate nanoparticles for tracking. The ideal ratio between the targeted protein and an antibody fragment on the surface of the nanoparticle is 1:1. However, it is difficult to achieve this ratio while obtaining labeling efficiency. Therefore, in our experiment, we used the ratio 1:3 between nanoparticle and ligands of targeted proteins to get the optimal labeling efficiency while avoiding the crosslinking effect.

Other nanoparticles are also used in single-particle tracking experiments such as gold nanoparticles, diamond nanoparticles [164, 165].

3.1.3 Mean Square Displacement Analysis

SPT is considered a method that combines spatial and temporal resolution. To understand the motion of the tracked molecules, the Mean square displacement (MSD) that describes the square displacement over a period of time-averaged over the whole trajectory is calculated [166]:

Brownian motion

$$< r^2 >= 4Dt \tag{3.2}$$

Anomalous Diffusion

$$< r^2 >= 4Dt^\alpha \tag{3.3}$$

Directed motion with diffusion

$$< r^2 >= 4Dt + (vt)^2 \tag{3.4}$$

Corralled or confined motion

$$< r^2 >=< r_c^2 > [1 - A_1 \exp -(\frac{4A_2Dt}{< r_C^2 >})] \tag{3.5}$$

The 2D Brownian motion is created by a collision of particles with the molecules, the MSD of the Brownian motion is represented as in equation 3.2. When molecules move in a more complicated environment, the linear relationship between the MSD and time is broken (equation 3.3 with $\alpha < 1$), the molecule diffusion becomes anomalous [167]. When the molecules move towards a direction, the motion is called directed motion. The MSD of directed motion is written in equation 3.4, the second term on the equation on the right with the speed v adds the active motion to the random term [168]. The corralled or confined motion is observed in many cell component motions, for example, many proteins in the cell membrane are observed to be confined in a small domain. The MSD of the confined motion is written in equation 3.5.

3.2 Introduction to Super-Resolution Microscopy

Single-molecule tracking (SMT) is a powerful technique but it also has limitations. In order to observe single-molecule tracking without overlapping emission of fluorophores, the label density in SMT has to below. Therefore, we lose information about the density distribution of the molecules studied. To overcome this problem, we use single-molecule localization microscopy to study the density of EGFR and its distribution at the cell membrane. In this chapter, I will first describe different super-resolution imaging techniques:

1. Ensemble techniques: Stimulated emission depletion microscopy (STED) & Structured illumination microscopy (SIM).

2. Techniques based on molecule localization: Stochastic optical reconstruction microscopy (STORM) and Photoactivated localization microscopy (PALM).

Then, I will focus on STORM blinking principles and describe the image analysis for molecular localization and clustering. The diffraction limit of resolution was recognized by Abbe in the 19th century. He showed that the spatial resolution of an optical microscope is limited by the diffraction of light [169]. The resolution depends on wavelength, the refractive index of the medium between the image lens and the sample, the Numerical aperture (NA). The resolution limitation is defined by equation 3.6:

$$d = \frac{\lambda}{2n\sin(\theta)} = \frac{\lambda}{2NA} \tag{3.6}$$

Where λ is the observation wavelength of the system, n is the refractive index of the medium, and θ is the maximum half-angle of the light that can enter the imaging lens with respect to the perpendicular to the lens. $NA = n\sin(\theta)$ is defined as the numerical aperture of the optical system. In an optical microscope, the wavelength ranges approximately from 400 nm to 800 nm and samples are typically imaged in water immersion ($n = 1.33$, $NA \approx 1.2$) or oil immersion imaging systems ($n = 1.51$, $NA \approx 1.4$). Therefore, in the best-case scenario, the diffraction limit can reach around 150 nm.

Many techniques have been developed recently to overcome this resolution limit and they are called super-resolution microscopy techniques. The different super-resolution microscopy methods are summarized in Figure 3.3.

3.3 Deterministic/ensemble Super Resolution techniques

Both structured illumination (SIM) and stimulated emission depletion (STED) microscopy use illumination patterns to get resolution beyond the diffraction limit, but use very different physical processes. While SIM uses a periodic pattern that interferes with the sample structure to create Moiré fringes, STED uses a hole pattern and stimulated emission to get a smaller effective PSF. The details of the two methods are discussed in the following sections.

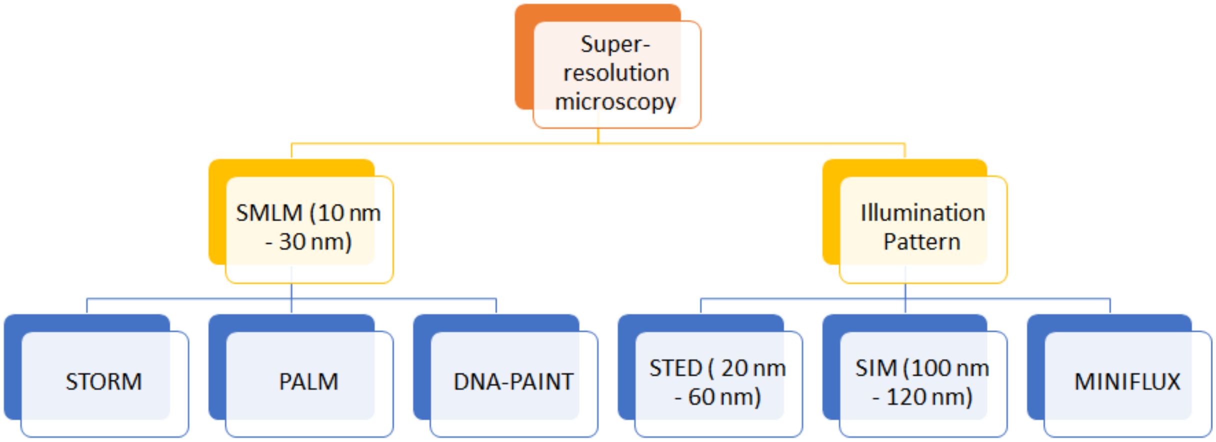

Figure 3.3: Non exhaustive overview of super resolution microscopy techniques.

3.3.1 Structured illumination (SIM) microscopy

As indicated in the technique name, in structured illumination microscopy, a known structured pattern is imaged onto the object to image. The known structured excitation pattern of light then interferes with the unknown sample structure patterns to yield an effect known as the Moiré effect. Different images are acquired, then these images are deconvolved to obtain the super-resolution images of the sample. The final sample image can obtain resolution two times smaller than the resolution limited by the diffraction limit. In Fourier space, the diffraction limit acts as a low pass filter where the low-frequency signals can pass while the high-frequency signals can't propagate [170]. The concept of SIM is shown in Figure 3.4.

SIM is a strong microscopy technique that provides higher resolution than confocal microscopy or wide-field microscopy. Moreover, it does not require specific fluorophores or special imaging mediums for the experiment. The technique has low phototoxicity and is suitable for multicolor imaging. Compare to other single-molecule localization microscopy techniques, it is faster. Therefore, it can be used for live and 3D imaging. However, the resolution of SIM is lowest around 100 nm, this resolution is much higher than other super-resolution techniques about 10 nm to 50 nm.

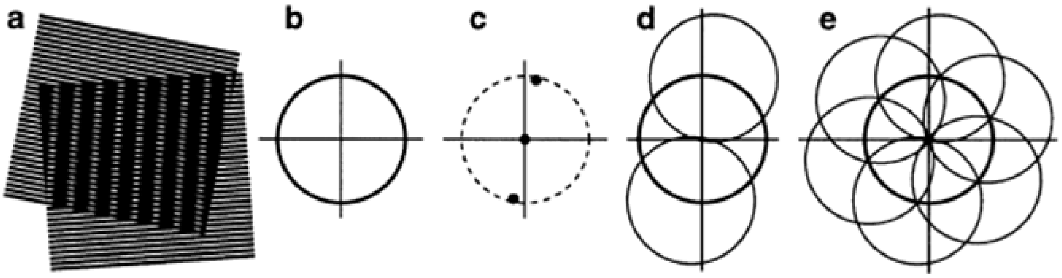

Figure 3.4: The concept of SIM. (a) The Moiré fringes (the darker stripes) are created by the interference of 2 striped patterns, the excitation pattern, and the emission pattern due to the sample structure, Fourier Space: (b) In conventional microscopy, in Fourier space, the observation region is defined by a circle. Areas outside of the circle can not be observed. (c) The sinusoidal pattern typically used for the excitation of the sample can be represented as 3 dots in reciprocal space and dots represent the observable region limited by the diffraction limit. (d) The sample is illuminated with a striped pattern, it creates the Moiré fringes and, in the Fourier space, the observable region is extended. (e) By using different orientations and phases of the pattern, the resolution of the image can be twice better than in standard wide-field striped conditions. Figure from [170]

.

3.3.2 Stimulated emission depletion (STED) microscopy

In STED, microscopy fluorescent molecules are first excited by a pulsed laser and are promoted from the ground state to an excited state. Then by using a second laser pulse the fluorescence of molecules outside of the central region is depleted via stimulated emission [171, 172]. To achieve the depletion at the periphery, the intensity of the second pulse laser has to be at a saturation level where all the fluorescence around the focal point is suppressed while maintaining the center fluorescence. By doing that, only a small fraction of fluorescence at the center is kept which leads to an effective PSF. This PSF is much smaller compared to the conventional PSF.

Compare to SIM, STED obtains two times higher resolution. The technique is fast, it can be used for live imaging. However, because of high-intensity laser used in STED, it has high phototoxicity to the cells.

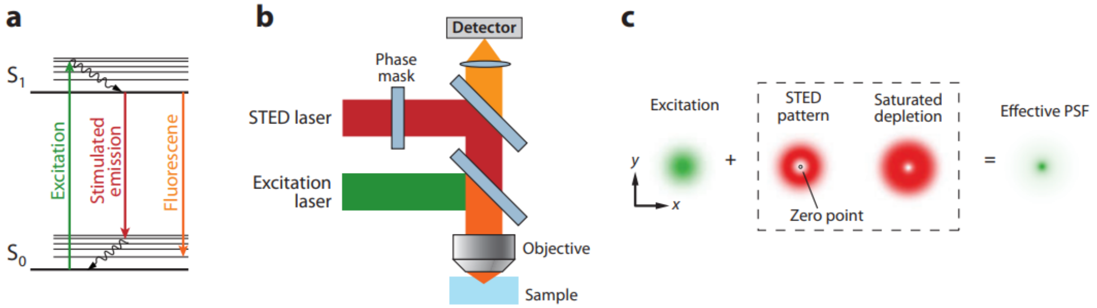

Figure 3.5: Principle of STED excitation and emission (a) The Jablonski diagram of the transitions of fluorophores in STED. The molecules absorb a photon and go from the S0 ground state to an excited state (S1). The second STED laser is red shifted to be compatible with the emission photons and promote the Stimulated Emission process. (b) Scheme of a STED setup: the first laser excites fluorescence molecules, the STED laser is red shifted and passes through a phase mask to create a pattern where the center point has no intensity. (c) PSF pattern of molecules with fluorescence only and combined with STED saturated depletion to create a smaller effective PSF. Figure from [172]

.

3.4 Super-resolution techniques based on single-molecule localization

The principle of Single-Molecule Localization Microscopy (SMLM) is presented in Figure 3.6, the first step is to label proteins of interest with a fluorophore (dyes, nanoparticles, or tagging the proteins with FPs). After the samples are labeled, they are put under the microscope for imaging. Depending on the fluorophore, different buffer solutions (STORM) or excitation approaches (PALM, DNA-PAINT) can be used for the imaging, the main objective is to obtain the excitation and emission of only a small fraction of fluorophores for a given period. In the next step, a series of images are recorded as in one frame only small subsets of fluorophores are excited. The localization of molecules is determined from thousands of images and then combined to form the final images. Therefore, the resolution between molecules is determined by the uncertainty of the localization in low-density images. Therefore, the resolution is much lower than in conventional microscopy. Before the image is analyzed, it is processed to correct drift or reduce problems created by the fluorophore blinking process. Then the last step which is called the post-processing step is to analyze the information obtained by the super-resolution images [173].

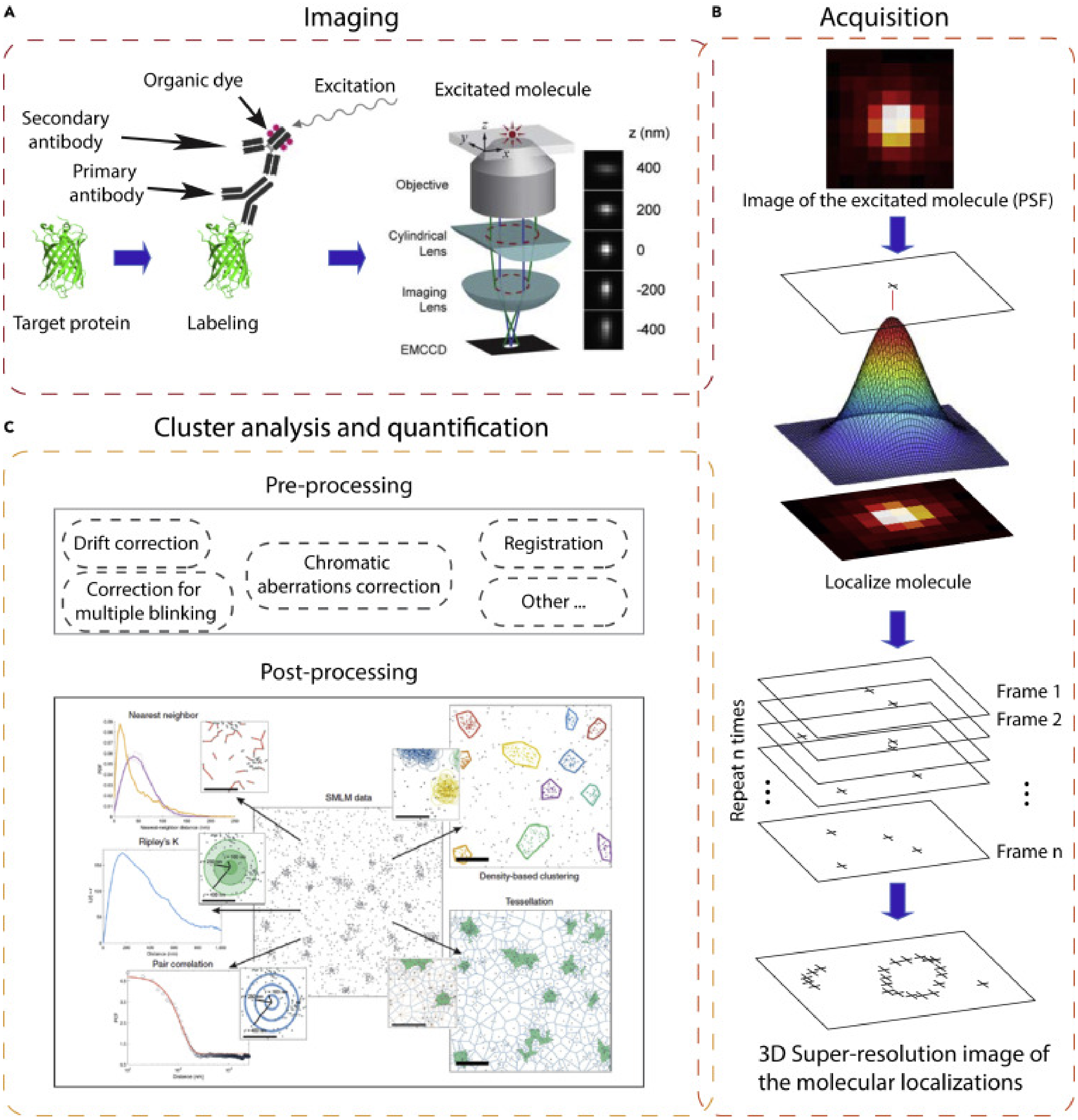

Figure 3.6: Pipeline for SMLM. (A) Sample labeling process and image acquisition in SMLM. This image shows an adaption that enables z-resolution in addition to x- and y-resolution. (B) Localization of molecules by fitting PSF with Gaussian and creation of a super-resolution image. (C) The pre-processing and post-processing to characterize the protein organization. Figure from [173].

3.4.1 DNA-PAINT

The technique called Point Accumulation for Imaging in Nanoscale Topography (PAINT) was first introduced by Sharonov et al. [174] in 2006. In principle, it is based on the diffusion and interactions of the fluoroscopes with the measured subjects. The fluorophores are captured on camera only if they attach temporarily to the target subjects. The rest of the time, they are out of focus or diffuse too quickly to be measured. Then similar to single-molecule tracking, fluorescent spots are fitted with high precision, these molecule localizations are considered as their actual location. The interaction is unknown and not specific, it could be electrostatic force or hydrophobic interaction.

To obtain more specific binding to target molecules, a variant of this technique was proposed, DNA-PAINT, where a DNA-dye (imager) construct is used to transiently attach to the complementary DNA (docking) of target molecules. The docking DNA strands are connected to antibodies of the target molecules [175, 176]. When the imagers bind to the docking molecules, they diffuse slowly and emit enough photons in a single location to be detected by the camera as a bright emitting spot. Otherwise, they are not detectable because they diffuse too fast to give rise to a localized signal. The binding time is the time during which the imagers remain attached to the complementary DNA branch. This time depends on the stability of the dsDNA that is formed which, in turn, depends on the length of the DNA branches, GC-base content, temperature, and concentration of salt in the buffer solution [176].

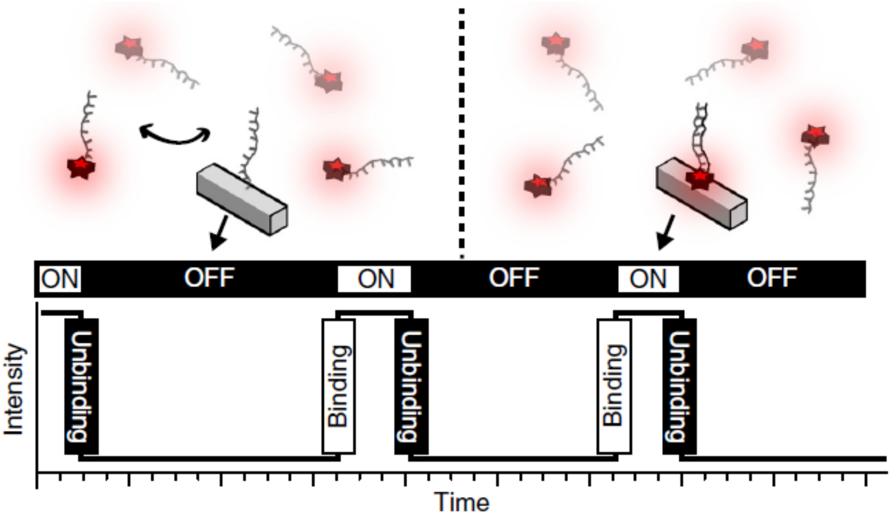

Figure 3.7: The mechanism of the DNA-PAINT technique. Fluorophores are in "off" state when they are not bound to a substrate and are floating by diffusion in the solution. When they are bound to the complementary DNA branch labeling the target molecule, they are imaged. Figure from [176]

As with other single-molecule localization microscopy techniques, DNA-PAINT has both advantages and disadvantages. The principle of DNA-PAINT is based on the transient attachment of DNA to their complementary branch so that, after measurement, the imagers can be washed away and other imagers can be added to label multiple compartments in biological objects. This method is called Exchange-PAINT, and it can be performed for up to ”9 colors”. In order to design these experiments, the docking branches (9 base pairs) are designed by changing the sequence of DNA bases in the branch to obtain a new docking chain. In fact in the experiment, 9 base pair imager strands were labeled with the same fluorophores (Cy3b) [177].

For other super-resolution techniques, it remains a challenge to quantitatively measure molecules of interest. Here in DNA-PAINT techniques, R. Jungmann et al. introduced the qPAINT method in 2016 to quantify the number of docking sites [178]. By exploiting the information on the kinetics of DNA binding and unbinding processes, the concentration of imagers, and the frequency of on-off state of fluorophores. Compared to dSTORM, the DNA-PAINT also doesn't need specific environments like oxygen scavenging molecules, enhancement of molecule fluorescence, and pH control [179]. By adjusting the binding time to collect higher numbers of photons, a more precise localization of molecules could be obtained.

However, the method also has its own drawbacks. First, because of a high concentration of non-bound imagers, there is a high background signal contributing to the images. Therefore, there is a limited number of setups that can be used to measure DNA-PAINT signals, a system like light-sheet microscopy or Total internal reflection imaging (TIR). Secondly, due to the introduction of DNA strands in imaging solution, DNA-PAINT is only suitable for fixed cell experiments or imaging membrane structures in living cells [176].

3.4.2 Photo-activated Localization Microscopy (PALM)

PALM that is short for Photoactivated Localization Microscopy is a super-resolution microscopy technique similar to dSTORM. The method was first developed by E. Betzig in 2006 [180]. Thanks to this, E. Betzig was awarded the Nobel Prize in 2010 in chemistry along with Stefan Hell and William Moerner for their contributions in developments in super-resolution microscopy. PALM relies on the stochastic activation, localization, and bleaching of single photoswitchable molecules. Even though PALM and STORM have the same principle in imaging and analyzing data, STORM uses organic dyes in suitable buffer solution to favor the blinking process while PALM uses Photoactivated fluorescent proteins (PA-FPs) controlled by a Ultraviolet (UV) laser.

3.4.3 Stochastic Optical Reconstruction Microscopy (STORM)

In 2006, the first paper was published by Rust. et al [181] and described the principle of Stochastic Optical Reconstruction Microscopy (STORM). The authors used Cy5 as a blinking molecule and Cy3 as a supporter for Cy5 blinking. Cy5 first was turned off in a dark state by illuminating with a powerful red laser then back to the fluorescent state with a green laser. Two years later, Heilmann et al.[182] showed that conventional fluorophores could be used without using supporting molecules [181]. Therefore, the method was called direct STORM or dSTORM. In STORM experiment, we use a specific buffer that is favorable for blinking process of the dyes including a primary thiol as reducing agents (β-mercaptoethanol and β-mercaptoethylamine) and oxygen scavenging agents like glucose oxydase/catalase [181] to reduce photobleaching,[182], sulfite [183] and COT to increase the brightness [179] in Tris-HCl(pH = 7.5) buffer.

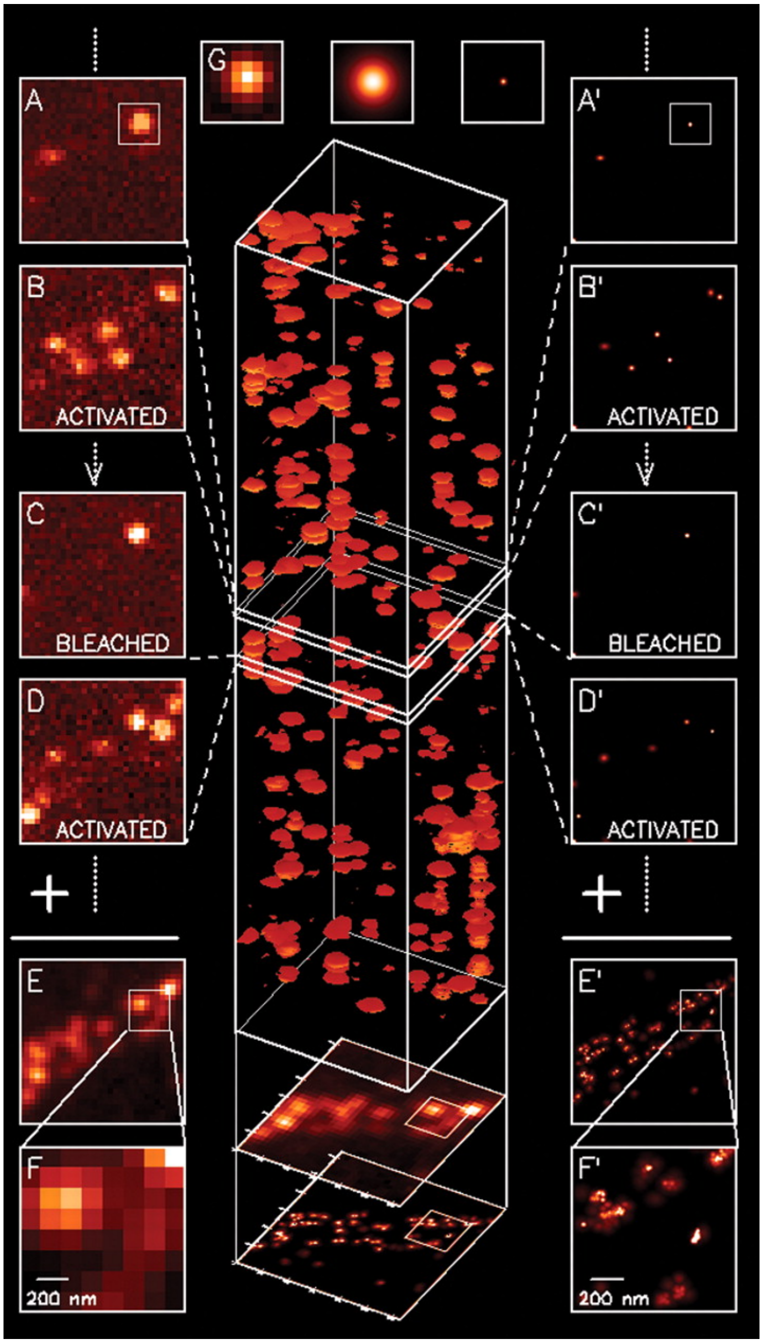

Figure 3.8: Principle of PALM. (A), (B) The photoactivated fluorescent proteins (PA-FP) are activated by a pulse laser at 40 nm. (C),(D) The molecules are bleached by the laser then reactivated by the laser. The process of activation and bleaching of PA-FP is repeated until most of PA-FP is depleted. (E), (F) The sum of all molecule images if they are limited by the diffraction limit. (G) In PALM, the molecule positions are found by fitting the PSF of the emission. (A′), (B′), (C′), (D′) The reconstructed images from emission points in (A), (B), (C), (D) respectively. (E′), (F′) The summary of all the positions in serial image frames which give the super-resolution image. The resolution is now determined by the uncertainties of the localization fitting. Scale: 1 × 1 in (F) and (F), 4 × 4 elsewhere. Figure from [180]

3.4.4 Probes for Single-Molecule Localization Microscopy

Requirements for SMLM probes

In order to get good localization precision, the fluorophores need to emit enough photons. The higher the number photons emitted, the better localization precision of fluorophores that can be achieved [184]. The error of the position of fluorophores fitted by a Gaussian is shown in equation:

$$\sigma = \sqrt{\frac{s^2}{N} + \frac{\frac{a^2}{12}}{N} + \frac{4\sqrt{\pi}s^3b^2}{aN^2}} \tag{3.7}$$

Where σ is the standard deviation, N is the number of photons captured by the camera, a is the pixel size of the imaging detector, and b is the standard deviation of the background noise. The background noise is composed of background auto-fluorescence and detector noise. The first and second terms on the right-hand side are respectively related to the photon shot noise and the finite pixel size of the detector while the last term refers to the effects of background noise on the localization of a fluorophore. When the background noise is negligible, the Equation 3.7 becomes:

$$\sigma \approx \frac{s}{\sqrt{N}} \tag{3.8}$$

In addition, in order to obtain better-reconstructed images, the fluorescent molecules should not stay in the "on" state too long. The duty cycle is the ratio of time a fluorescent molecule resides in the "on" state divided by the time that molecule stays in the "off" state. If the duty cycle is high, and there is an overlap between fluorescent molecules and it is difficult to separate them. Therefore, the localization precision of molecules is less precise in the case of a high duty cycle. Furthermore, in order to identify single emitters in those images, more computationally intensive and time-consuming methods are needed.

Another factor affecting the quality of the final image is the switching times of fluorophores between the "on" state and the "off" state before bleaching permanently. Therefore, it leads to multiple localizations of the same molecule and requires post-processing steps to correct (see Chapter 4).

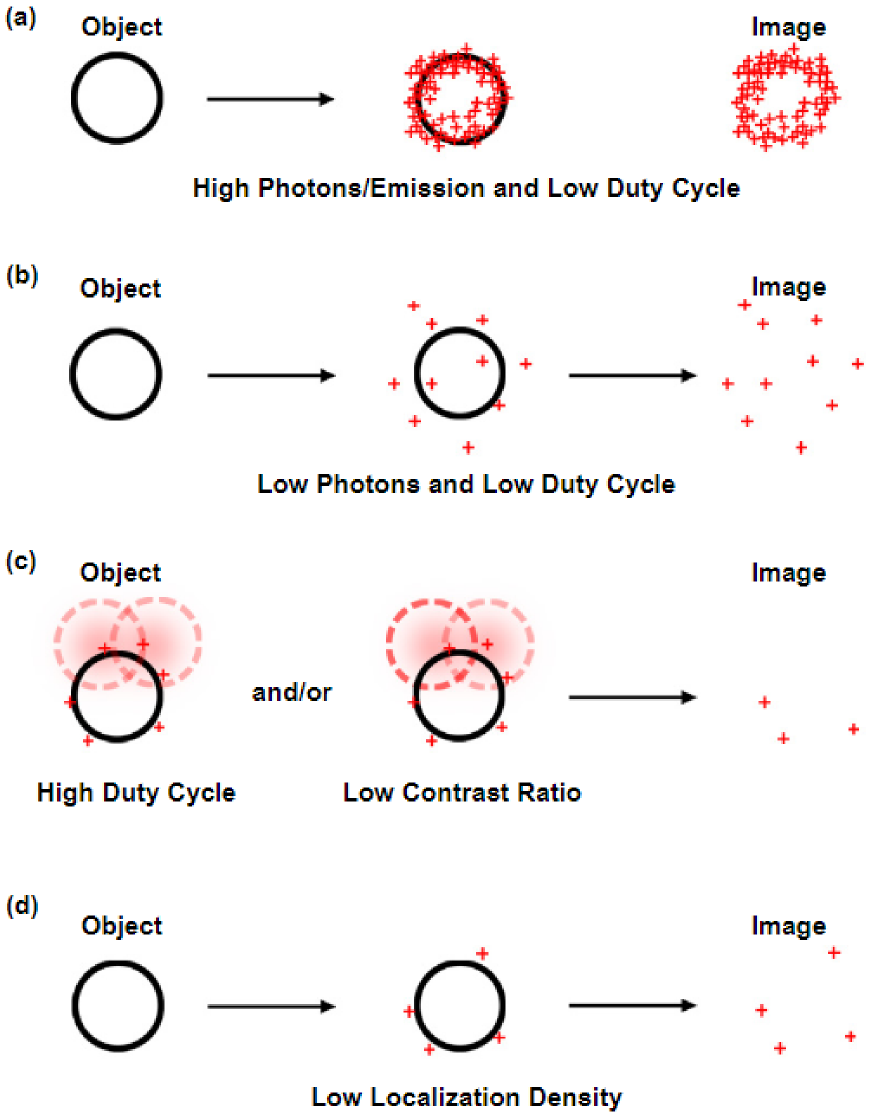

Figure 3.9: Properties of fluorescent probes affect the constructed image. (a) The best dye has a high photon emission while having a low duty cycle. The reconstructed image of the observed object will have good quality. (b) When probes have low photons and low duty cycle, there fewer signals, and the object is poorly imaged. (c) Probes have a high duty cycle and/or low contrast ratio create the overlap of fluorescent emission which lowers the identified locations. (d) When the object has low efficient labeling, it leads to a low number of identified locations. Figure from [185]

Organic Dyes

Principle of dye blinking

Principle of **Cyanine** family blinking.

Upon illumination by laser light, electrons in molecules can go to **an excited state** then go to the low level of excited state by vibrational relaxation (ps). They can go back to the ground state by fluorescence emission. The process is fast, the lifetime of the excited state is short, typically in the ns scale. Back to the ground state, electrons can absorb light again and experience many cycles until they are bleached. In the excited state, they can also transfer into a triplet state with a longer lifetime and return to the ground state by phosphorescence, non-radiative decay, or be quenched by oxygen present in the solution. By adding primary thiol, the Cy5 family molecules react with primary thiol (Figure 3.10). The thiol reacts with the polymethine bridge show the bridge in the figure 3.11 and disrupts the conjugated electron system of the molecules thus creating a dark state. The Cy3 has a shorter bridge that does not blink by adding thiols but Cy5.5 has one more ring and is switchable by using thiol molecules [186].

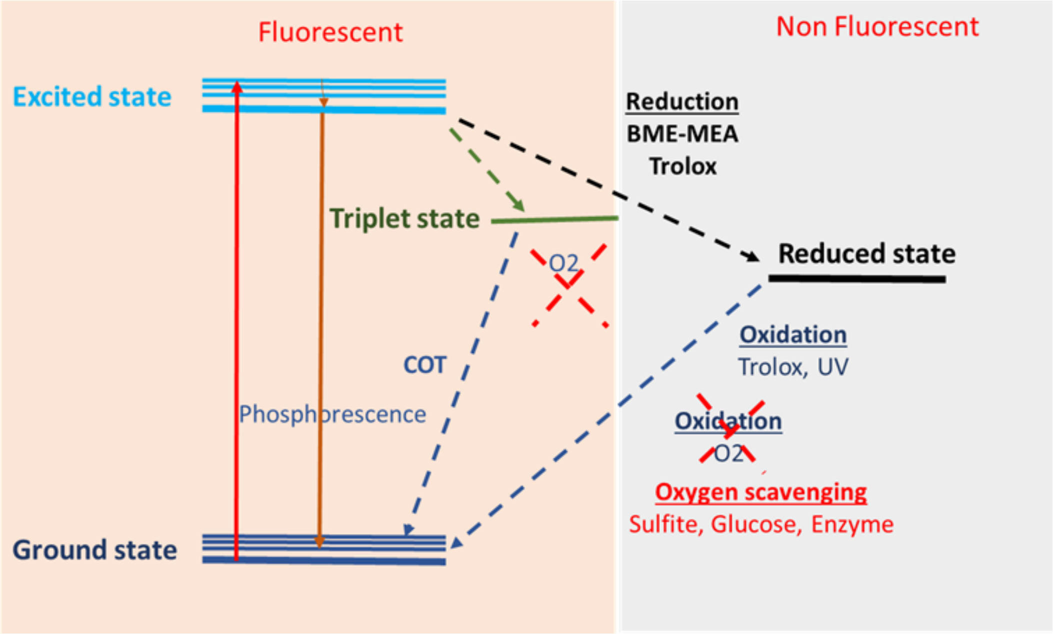

Figure 3.10: Blinking mechanism of Cy5 family. Figure adapted from[179].

Organic dyes have been used widely in single-molecule localization microscopy. The most popular class of organic dyes are cyanines including Cy5, Cy5.5, and Cy7. Their structures are close to that of Alexa 647. Because of its fluorescent properties, high-intensity emission, low duty cycle, and a high number of switching cycles, Cy5 is considered one of the best fluorophores besides Alexa 647 [187]. In 2011, Dempsey et al. evaluated 26 different

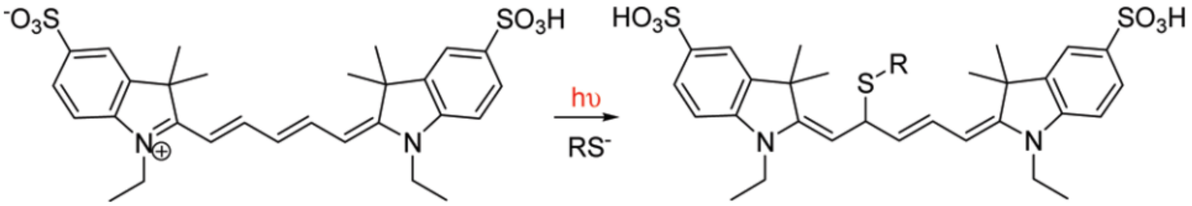

Figure 3.11: Mechanism of Cy5 fluorophore blinking in low oxygen environment in a STORM experiment. The thiol (RS-) reacts with the bridge of Cy5 and breaks its conjugated electron system and creates the dark state of Cy5. Figure from [186]

.

commercial dyes divided into three main groups with distinctive spectrum to compare their properties that are important for use in SMLM applications. These properties include duty cycle, number of emitted photons, number of cycles before photobleaching. Taking into account also other studies, the properties of different dyes are summarized in Table 3.1. The dyes were placed in different buffer solutions, the buffer solution used in these experiments from upper row to lower row are deoxygenation (glucose oxidase with catalase) and thiols (MEA and βME), deoxygenated solution, and MVAA (methyl viologen and ascorbic acid), deoxygenated solution plus TCEP and MVAA, only deoxygenated solution without thiols or tris(2-carboxyethyl)phosphine (TCEP) and aqueous solution. From the study, Dempsey et al. concluded that the properties of dyes strongly depend on the composition of buffer solutions. In general, the fluorophores blink and fluorescent the best in deoxygenated buffers where they are not rapidly quenched by oxygen. Furthermore, by adding a moderate amount of MEA and βME to the solutions, we can enhance the blinking cycles and number of photons. However, if the optimal amount of MEA is exceeded, it leads to a lower number of switching cycles, or lower number of photons, or both.

Organic Dye	λ ex(nm)	λem(nm)	λ on/off	ϵ	Q.Y	D.C	n.o.p	n.c	refs
BS:	GLOX,	βME	MEA						
Alexa 647^{a,f}	650	665	405/647	239000	0.33	$1.2e^{-3}$	5202	26	[188]
Alexa 750^{a,f}	749	775	405/750	240000	0.12	$1e^{-4}$	703	6	[188]
ATTO 488^{a,f}	501	523	405/488	90000	0.8	$2.2e^{-3}$	1110	49	[188]
BODIPY $FL^{a,g}$	503	523	405/448	80000	0.97	$1.8e^{-2}$	756	3.4	[189, 190]
$Cy3B^{a,f}$	559	570	405/561	130000	0.67	$4e^{-4}$	2057	5	[188]
Dyomics 654^{a,f}	654	675	405/647	220000	NR	$1.8e^{-3}$	3014	19	[188]
$DyLight^{a,g}$	752	778	405/750	220000	NR	$2e^{-4}$	749	6	[188]
ER-Tracker $Red^{a,h}$	587	615	405/561	64300	NR	$3e^{-4}$	820	28	[191]
$SiR^{a,h}$	645	662	NR/640	100000	0.39	NR	630	NR	[192]
BS:	GLOX,	MVAA							
ATTO 488^{b,g}	501	523	405/488	90000	0.8	$2e^{-3}$	e^4	1	[188, 193]
$Cy3B^{b,g}$	559	570	405/561	130000	0.67	$3e^{-3}$	e^5	1	[188, 193]
BS:	GLOX	TCEP	MVAA						
Alexa 647^{c,f}	650	665	405/647	239000	0.33	$1.3e^{-4}$	2400	NR	[188, 193]
Alexa 750^{c,f}	749	775	405/750	240000	0.12	$4e^{-4}$	2800	NR	[188, 194]
BS:	only GLOX								
PA-JF 549^{d,h}	561	571	405	101000	0.88	$1e^{-5}$	$1.9e^4$	1	[195, 196]
PA-JF 646^{d,h}	637	664	405	152000	0.54	$1.6e^{-6}$	NR	1	[195, 196]
BS:		Aqueous	Solution						
amino-$DCDHF^{e,i}$	594	613	405/561	130000	0.67	NR	$2.3e^6$	5	[188]
$DTE^{e,f}$	488	582	375/488	37300	0.45	$4e^{-4}$	200-300	14	[197]
$HMSiR^{e,g}$	650	672	NR	100000	0.39	NR	2600	> 20	[198]
OA-2 $(open)^{e,j}$	532	650	355/532	83000	0.02	NR	222	NR	[199]
MC $(open)^{e,j}$	532	665	UV/532	52000	0.17	NR	630	NR	[192]

Note: λex, excitation wavelength; λem, emission wavelength; λon/off, wavelengths for switching the fluorescence on and off, respectively; ϵ, extinction coefficient; Q.Y, fluorescence quantum yield; D.C duty cycle, the fraction of time spent in the on the state before photobleaching; n.o.p number of photons, number of detected photons per localization event; the number of cycles, number of switching cycles; refs, journal references for published data. Superscripted ae indicate the composition of the imaging cocktail: (a) deoxygenated + thiol; (b) deoxygenated + MVAA (methyl viologen and ascorbic acid) where fluorophores had been previously reduced with NaBH4; (c) deoxygenated + TCEP + MVAA; (d) deoxygenated; and (e) no additives to the aqueous buffer. Superscripted fj indicate the specimen used for fluorophore characterizations: (f) fixed cells; (g) antibody adsorbed to coverglass; (h) live cells; (i) fluorophores immobilized in poly(methyl methacrylate) (PMMA) (for quantum yield measurements) or gelatin (for other measurements); (j) fluorophores on nanoparticles. NR indicates the parameter was not reported.

Table 3.1: Properties of organic fluorophores used in SMLM. Table is adapted from [187]

Fluorescent Proteins

Fluorescent proteins used in SMLM can be divided into three main groups: irreversible photoactivatable, reversible photoactivatable (PA-FPs) and photoshiftable fluorescent proteins (PS-FPs). Irreversible photoactivatable fluorescent proteins (PA-FPs) can be activated by a specific wavelength and once photobleached, they can not go back to the initial state. For example, modified green fluorescent proteins are irreversible photoactivate fluorescent proteins (Figure 3.12 A), they are activated by UV light to go into the bright state; in this state, the proteins can absorb around 500 nm and then emit photons at 517 nm. In contrast, reversible PA-FPs can be in the "on" and "off" states hundreds of times before being photobleached. See in Figure 3.12 B, the example of Dronpa, it can absorb in the UV region at 390 nm but shows no emission. If the fluorophore is activated by a laser at 405 nm or activated thermally, it can turn into a bright state where it can absorb and emit light. This process is reversible, the fluorophore in the bright state can go back to the initial state by using a 488 nm laser. All known PS-FPs are known as irreversible PS-FPs. For example, monomeric Eos can shift its spectra from a green state (absorbs at 506 nm and emits photons at 516 nm) to an orange state (absorbs at 569 nm and emits photons at 581 nm) after exposure to UV (at 405 nm). The process is irreversible, the Eos in the orange state can't go back to the green state (Figure 3.12 C).

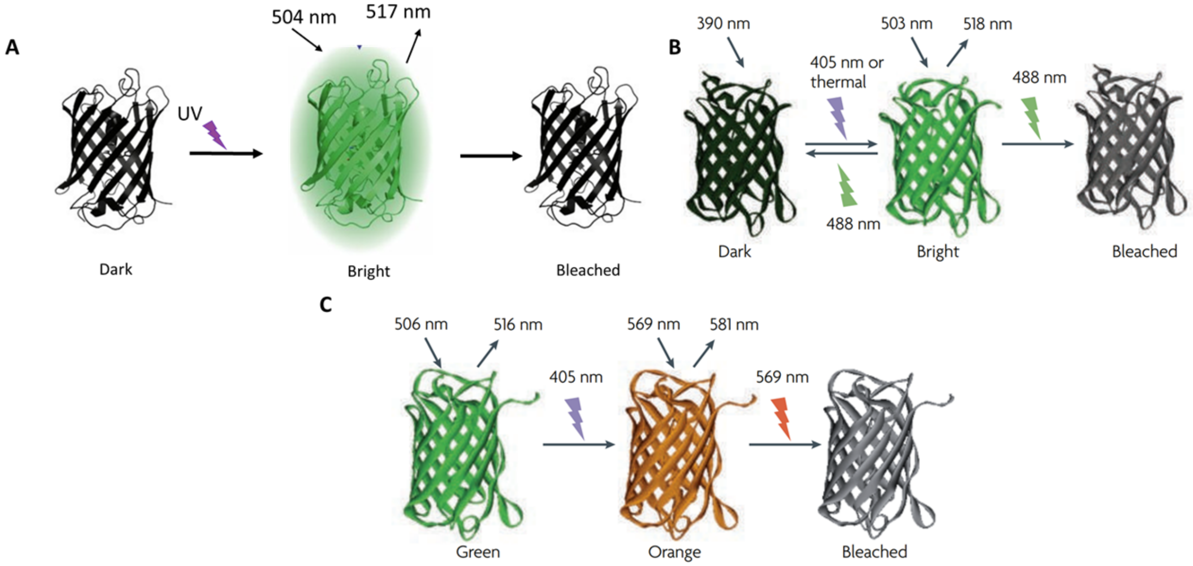

Figure 3.12: Fluorescent Proteins in SMLM. (A) A green irreversible fluorescent protein that can be activated by using a UV laser, absorbs at 504 nm, and emits at 517 nm. (B) A reversible photoactivatable (PA-FPs) protein, Dronpa, can be activated by using a laser at 405 nm or thermally, the activated form of Dronpa can absorb light at 488 nm and emit at 518 nm. (C) A photoshiftable fluorescent protein, mEos can absorb at green (506 nm) emits at 516 nm to change to an orange state (absorbs at 569 nm and emits photons at 581 nm). Figure adapted from [200].

Among fluorescent proteins, the mEos family, mMaple, and Dendra are most popular due to their characteristics with low duty cycle, high on-off contrast, and a high number of the emitted photon. The comparison of properties of different FPs is listed in Table 3.2. One of the problems of FPs like mEos 2 is the protein aggregation on the cell membrane at high concentrations. Therefore, it could affect the interpretation of the results and form false clusters [201]. To overcome this weakness, mEos2 and mEos3.2 were engineered to minimize the aggregation while still maintaining the optical properties of the original proteins. By further mutating surface residues on mEos2 to remove nucleophilic groups, two mutants, mEos4a and mEos4b, were formed. The optical properties of mEos2 are not affected Without the nucleophilic groups. Moreover, these FPs are not involved in cross-linking with aldehydes and OsO4 (the fixation agent used in electron microscopy) to form aggregations. Therefore, the new mutants can be used not only for super-resolution imaging but also are for electron microscopy [202, 203]. The main disadvantage in using photoactivatable FPs is their dual-channel emission property, they are difficult to use in multichannel imaging [187].

FPs	λex(nm)	λem(nm)	λon/off	ϵ	Q.Y	D.C	n.o.p	n.c	refs
Dendra 2	490/553	507/573	405/488	45000/35000	0.5/0.55	$4e^{-6}$	686	2.7	[204–207]
Dronpa	503	518	405/488	95000	0.85	$8e^{-4}$	262	60-70	[200, 206, 208, 209]
Dreiklang	511	529	340/412	83000	0.41	NR	400-700	> 160	[210–212]
mEos2	506/573	519/584	405/573	56000/46000	0.84/0.66	e^{-6}	1000	2.8	[201, 205, 206, 213]
mEos3.2	507/572	516/580	405/572	63400/32200	0.84/0.55	$3e^{-6}$	1000	2.4	[205, 206, 214]
mMaple	489/566	505/583	380/566	15000/30000	0.74/0.56	$2e^{-6}$	1000	3.4	[205, 206, 213]
Mmaple 3	489/566	506/583	405/561	NR	NR	$6e^{-7}$	675	2.8	[206]
PAmCherry1	564	595	370	18000	0.46	$8e^{-6}$	725	1	[205, 206, 215]
PEGFP	504	517	405	17400	0.79	$1.3e^{-3}$	313	NR	[206, 216]

Note: λex (excitation wavelength); λem (emission wavelength); λon/off (wavelengths for switching the fluorescence on and off, respectively); ϵ (extinction coefficient); QY (fluorescence quantum yield); on/off contrast (ratio of intensity of the emissive form to the dark form); D.C duty cycle (fraction of time spent in the on state); n.o.p photons/localization (number of detected photons per localization event); n.c switching cycles (number of switching cycles); N.R. indicates the parameter was not reported.

Table 3.2: Properties of Fluorescent Proteins using in SMLM. Table adapted from [187]

Nanoparticles

Quantum dots (QDs) are semiconductor nanoparticles, having optical and electronic properties that depend on their size and composition. Quantum dots are well known for their high-intensity fluorescence and higher resistance to photobleaching than common dyes and FPs. However, the duty cycles of blinking QDs are high and the switching kinetics are not homogeneous. Therefore, they are not considered ideal probes for single-particle tracking. Instead of using them in SMLM like STORM or PALM, QDs are applicable in **SOFI!** (**SOFI!**) which relies on a statistical analysis of temporal fluctuations of the emission [217]. Furthermore, QDs with CdSe core and ZnS shells with reduced in the thickness [218] or addition of ascorbic acid to the imaging solution [219] were used to improve the blinking rate.

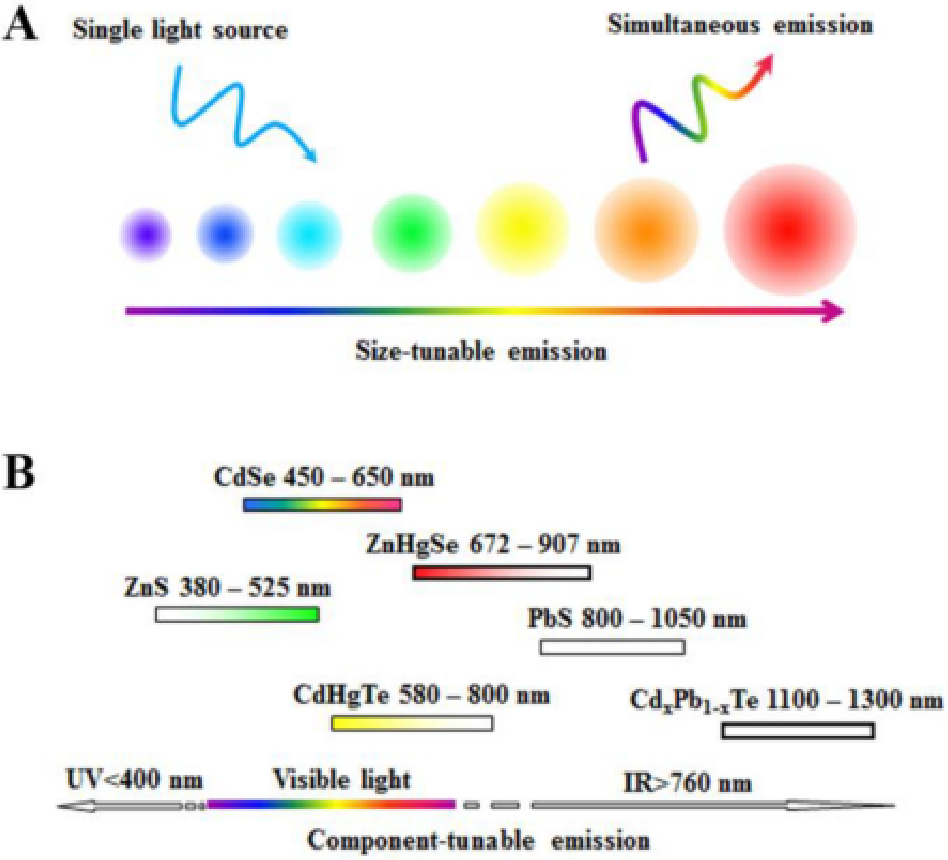

Figure 3.13: Emission spectra of quantum dots based on (A) size (B) composition. Figure from [220]

3.5 Quantification of SMLM data

3.5.1 Analysis of raw SMLM datasets

After acquiring the emission of fluorophores, the first step of SMLM analysis is to determine the fluorophore localization in thousands of frames of images. Similar to single molecular tracking, the fluorophore localizations are considered as the center of fitting Gaussian with PSF of fluorophores emission. In our analysis, we use software implemented in ImageJ called ThunderSTORM to determine the molecule localizations [221]. More details of the analysis will be discussed in Chapter 4.

3.5.2 Introduction

In super-resolution microscopy, final images are a combination of point locations which is different from conventional images where data information is presented as a signal intensity value in each pixel. Therefore, the analysis that is developed to analyze images from conventional microscopy is not suitable to analyze the point cloud information in super-resolution images. Instead, clustering methods are used to analyze super-resolution images.

The proteins in cells can interact with each other to form clusters of dimers or oligomers of proteins. For example, in the cell membrane, as discussed in Chapter 2, proteins may be enriched in certain confinement domain domains (rafts, TEM domains thus leading to protein clusters. The distance of the interactions can thus range from a few nanometers to hundreds of nanometers. Using super-resolution microscopy, we can map the positions of the proteins and show the distance relationship between these molecules. Therefore, clustering methods are employed to analyze SMLM data.

3.5.3 Clustering Analysis Methods for SMLM data

Ripley's Function

Ripley's function is used frequently to analyze the spatial distribution and clusters [222]. In the Ripley function, two properties of distribution are considered, firstly, the density of points and secondly, the expected number of points N within a distance r of another point. The Ripley K function is the second-moment property normalized by the density (or intensity):

$$K(r) = \frac{1}{n}\sum_{i=1}^{n} N_{pi}(r)/\lambda \tag{3.9}$$

Where λ is the density, the number of points per area (N/A), N_{pi} is the number of points around the i^{th} point and the sum is taken over n points.

The L-function was proposed by Besag [223] as normalization for the K function:

$$L(r) = \sqrt{\frac{K(r)}{\pi}} \tag{3.10}$$

The K-function can be further normalized so that the expected value is 0, yielding the so-called H-function [224]:

$$H(r) = L(r) - r \tag{3.11}$$

Ripley's K-function is typically used to compare a given point distribution with a random distribution; i.e., the point distribution under investigation is tested against the null hypothesis that the points are distributed randomly and independently. When the H-function has a negative value, the point distribution is dispersed when the H-function is positive, it indicates a cluster distribution of the points. When the H-function value is 0, the distribution is considered to be a uniform distribution. In recent papers, the authors also used the maximal value of H(r) to determine the cluster size. Kiskowski also found that the maximal value found for the H-function is approximately equal to the cluster radius [225].

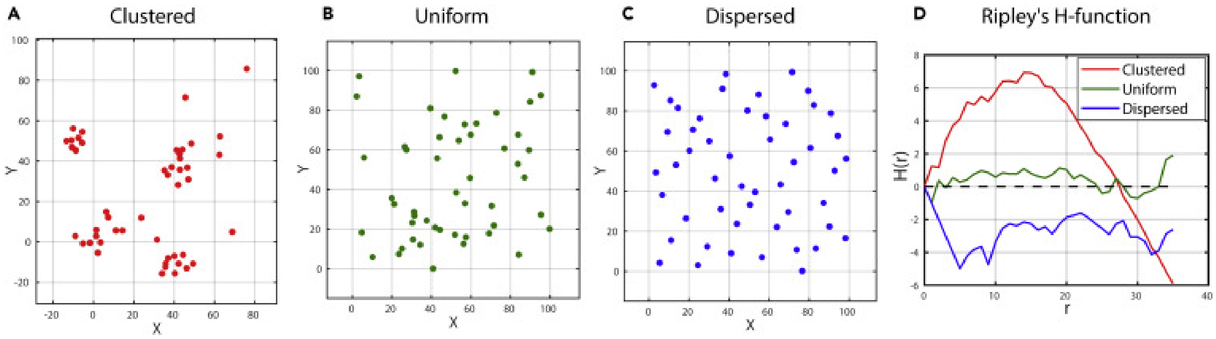

Figure 3.14: H-function values for different distributions: (A) Clustered distribution, (B) Uniform distribution, (C) Dispersed Distribution, (D) H-function graph. Figure from [226].

Correlation-Based Methods

Correlation-based methods including pair correlation, autocorrelation, cross-correlation, colocalization are widely used in SMLM both pre-processing and post-processing quantification [227–229]. In SMLM, one fluorophore may blink multiple times; therefore, it can create false structures or clusters of molecules. In order to address the effect of multiple blinking sequences of a fluorophore, in pre-processing, correlation-based methods are used to analyze and calculate the numbers of neighbors around a point inside a circle with a certain radius. Cross-correlation is also used in finding and correcting mechanical drift in SMLM. Furthermore, a coordinate-based correlation analysis framework developed by S. Malkusch et al. is also used for determining colocalization in two-color SMLM imaging [228].

Density-Based Methods

Density-based methods are popular among data mining and cluster determination methods. The Density-based algorithm for spatial clustering (DBSCAN) is developed by Ester et al. can determine clusters with different shapes and sizes. Furthermore, the method can be used to filter out noise when the input parameters are set appropriately [230].

The method is based on the different densities inside clusters and in the background. The density inside clusters is higher compared to that in the background; therefore, the method uses two parameters to determine if each point belongs to a cluster or not by using a minimum number of points around it (minPts) and a neighborhood radius ϵ. In this method, the center points normally have a higher number of neighbors inside a circle with a certain

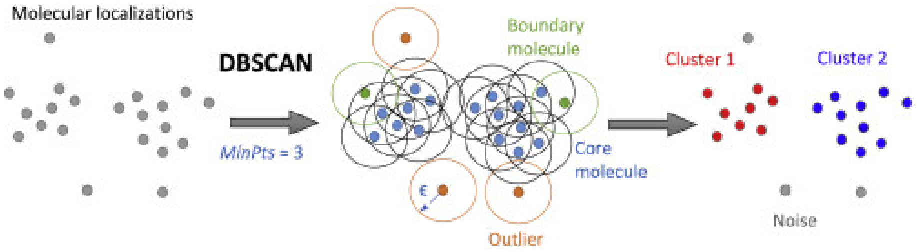

Figure 3.15: DBSCAN method for cluster analysis includes two parameters MinPts and neighborhood radius ϵ to distinguish between points inside clusters and noise. Figure from [173].

radius while the outermost points have fewer neighbors. When the core point is determined, expand the cluster by adding all directly reachable to the cluster. Therefore, the minimum number of neighbors has to be set to be a small value. The method works the best when the density inside clusters and outside is very different. However, in SMLM, DBSCAN has disadvantages in analyzing the SMLM images because the method is purely based on density. For example, in SMLM, one fluorophore blinks multiple times; therefore, using DBSCAN can determine the artifactual nano-clusters created by the blinking effect. Furthermore, DBSCAN is based on arbitrarily choosing two parameters. Moreover, DBSCAN calculates all pairwise distances of the data set, so the run time scales with the number of points n [173, 231]. Therefore, it takes hours to finish SMLM analysis. To overcome these drawbacks, a Fast optimized cluster algorithm for localization (FOCAL) [231]. In FOCAL, a grid was developed to optimize the runtime for clustering compared to DBSCAN. Furthermore, only one parameter, the density threshold (minL) in FOCAL needs to be optimized rather than two parameters in the case of DBSCAN. A 3DFOCAL was also developed to analyze 3D SMLM data [232]. However, FOCAL has difficulties when working with small cluster sizes. The grids need to be small leading to longer time analysis. Moreover, when dealing with high noise or high density and overlapped clusters, FOCAL also shows weaknesses.

Graph-Based Methods

Graph-based methods or graph theory methods are mathematical structures used to model relations between objects or an ensemble of interactions of a system. In a graph, the objects are represented as nodes or points that are connected by lines to show their interactions (lines) [233]. A complete graph organizes the points into different modules, clusters, or communities. Graph-based methods have plenty of applications from real-world problems such as computer science, linguistics, and social science to fundamental research in chemistry, physics, mathematics and biology [234–239]. Recently, a graph-based method (unsupervised learning method) was used for identifying the structure of caveolae and cav1 scaffolds from SMLM images [240, 241]. From 3D dSTORM images of Cav1 in Hela cell membranes, Khater et al. used a pipeline to filter noise and multiple blinking effects of fluorophores and to then segment these cloud points into blobs [240].

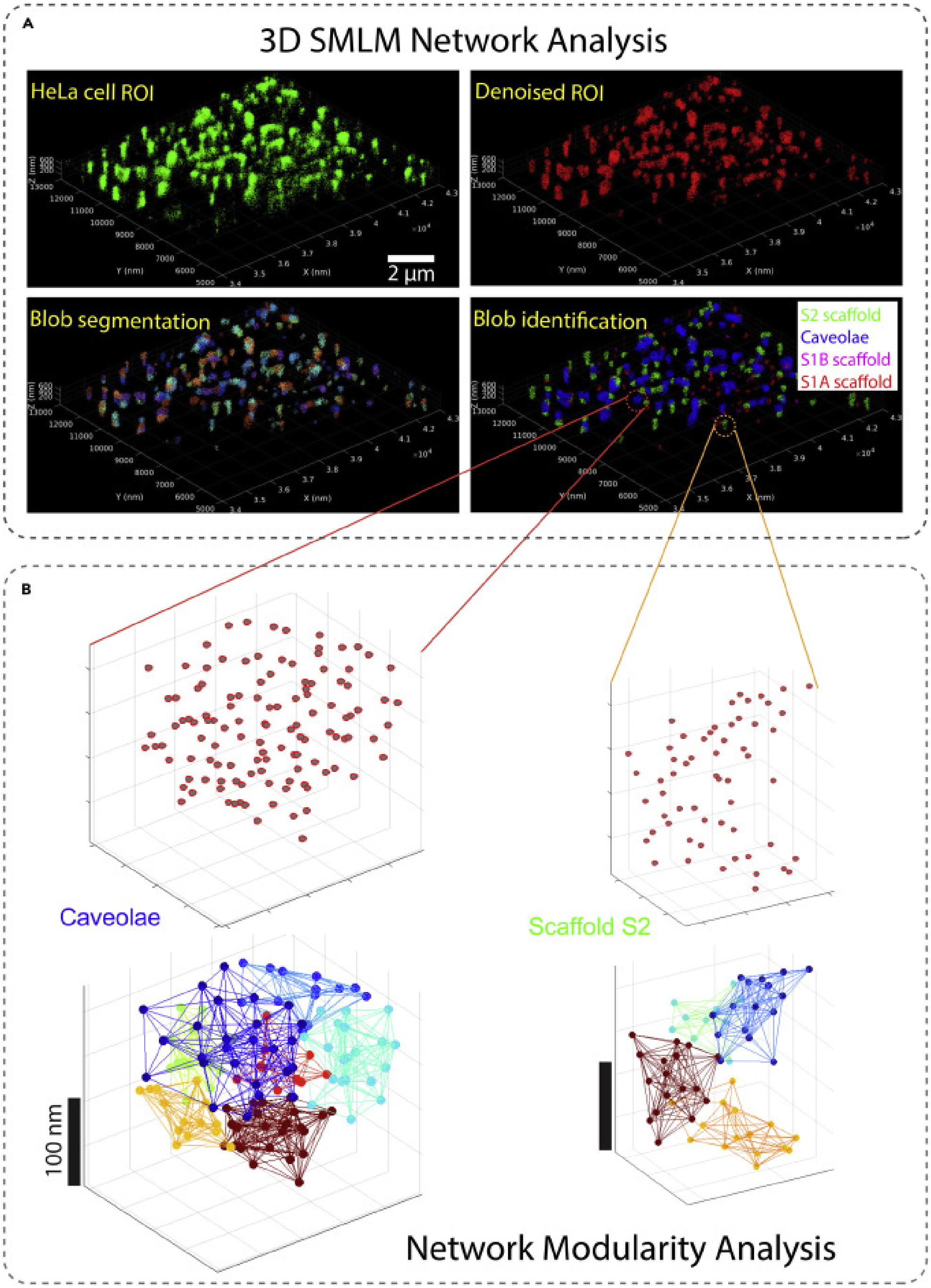

Figure 3.16: Graph-base method used in segmentation of SMLM data. (A) A pipeline analysis to remove noise and segment blobs. (B) The module network created by a graph-based method to distinguish different Cav1 structures. Figure from [173].

3.6 Conclusion

In this chapter, different microscopy techniques have been discussed. Each method has advantages and disadvantages. Compared to conventional microscopy, super-resolution techniques can yield a resolution down to 10 nm to 20 nm, which reveals many important biological structures. Structured-Illumination microscopy (SIM) provides the highest resolution among super-resolution techniques, a resolution of about 100 nm. Stimulated-emission depletion microscopy (STED) provides higher resolution than SIM but requires a second intense laser for the depletion step that is harmful to the cells. Photoactivated localization microscopy (PALM) and stochastic optical reconstruction microscopy (STORM) is based on the same principle of turning fluorescent labels ”on” and ”off”: while in PALM fluorescent proteins with a photoactivation property are used to obtain the ”on” and ”off” states, STORM uses fluorescent organic dyes in an oxygen-scavenging and reducing environment to obtain the desired blinking effect. DNA-PAINT is similar to PALM and STORM but requires more complicated sample preparation steps.

In this thesis, we chose the STORM method to study the EGF receptor and CD9 protein organization in the cell membrane, as described in the following chapter (Chapter 4), because of the following advantages: The sample preparation steps are simple and the organic dyes have high fluorescence yield and intensity, which is beneficial for the resolution of the image. Indeed, STORM provides a high resolution of about 10 nm to 20 nm which is much smaller than the typical membrane nanodomain sizes of about 200 nm that we want to resolve. However, the oxygen-depleted and reducing environment used in STORM is more suitable for fixed samples. Therefore, to compensate for this weakness of STORM, we also used single-molecule tracking to study the dynamics of EGF receptors (Chapter 5).

Chapter 4

EGFR and CD9 organization in cell membrane

Contents

> “A scientist in his laboratory is not a mere technician: he is also a child confronting natural phenomena that impress him as though they were fairy tales.”
>
> Marie Curie

In this chapter, I am going to present the results of our STORM experiments on the EGFR and CD9 distribution in the PEC cell membrane. But first, I will describe our STORM data analysis and the verifications I performed to confirm its validity: the first step of the analysis is to determine the localization of all the molecules (section 4.1.2). The detection of the molecules is done by using a plug-in in ImageJ called ThunderSTORM [221] which involves a pre-processing and a post-processing step. The effects of pre-processing and post-processing parameters on the number of molecule localizations are discussed in detail in the next section. After obtaining the molecule localizations and filtering away the non-specific labeling or low-signal molecules, we use a tesselation method called SR-tesseler to identify and quantify clusters in the protein distribution [242]. After describing all the analysis steps for my STORM experiments and verifying that the analysis parameters do not influence the obtained results, I will describe first the one-color imaging results that show the distribution of EGFRs in the PEC and shCD9 PEC cell membrane and the distribution of EGFRs and CD9 in the PEC membrane. In the last part, I will first present the problems that we needed to solve to realize two-color dSTORM experiments and analysis. Then the overlap between CD9 and EGFR clusters as compared to the overlap between transferrin receptors (used as reference molecules for which no overlap is expected) and EGFR will be discussed in the last section.

4.1 STORM Data Analysis

4.1.1 Molecule localization

In conventional microscopy techniques such as in wide-field or confocal microscopy, all fluorophores emit light at the same time. Therefore, their emissions are overlapped (Figure 4.1) and yield a blurry image. In contrast, in SMLM, only a subset of fluorescent molecules is active in a given camera frame. Therefore, their fluorescent emissions are not overlapped. After acquiring the emission of fluorophores, the first step of SMLM analysis is to determine the fluorophore localization in thousands of images. Similar to single-molecule tracking, the fluorophore localizations are considered to be at the center of a fitted 2D Gaussian. Figure 4.1 describes the principle of molecule localization in a super-resolution image. The hidden feature is revealed by the sum of all blinking fluorescent localizations after they are determined.

To localize the position of fluorophores, we used a plug-in of ImageJ called ThunderSTORM [221]. The pipeline of single-molecule localization by ThunderSTORM is demonstrated in Figure 4.2 and Box.

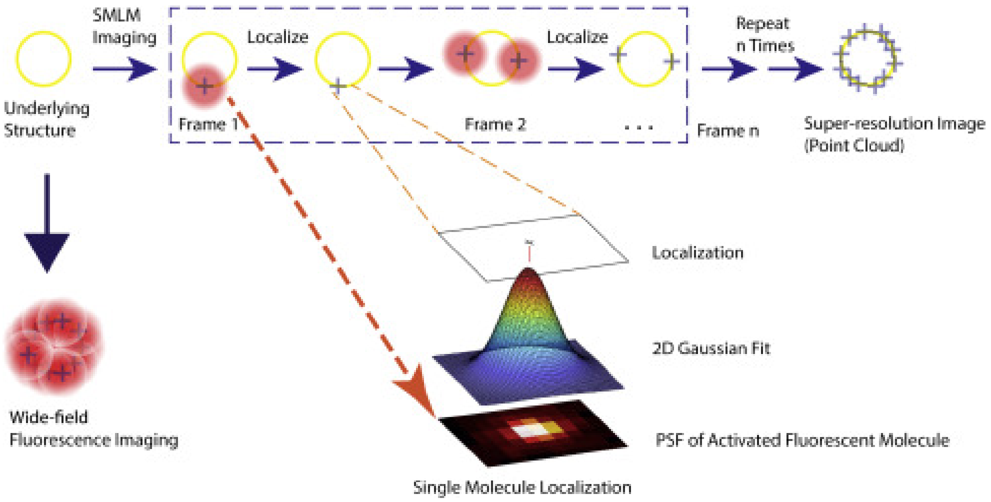

Figure 4.1: Single Molecule Localization. The underlying structures are revealed by single molecule localization by fitting fluorescence emission with a 2D Gaussian. Figure from [173]

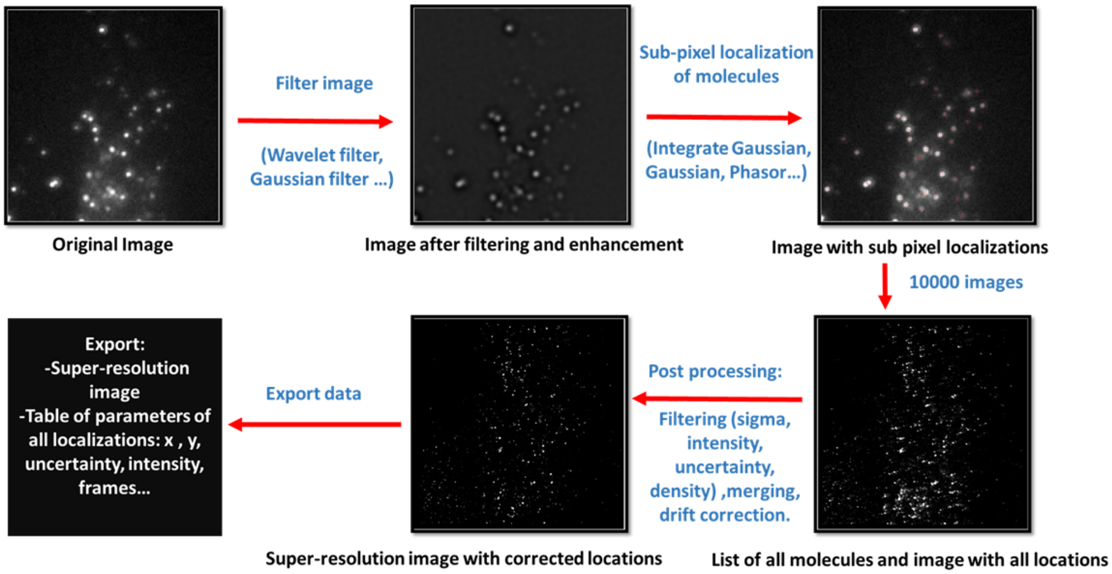

Figure 4.2: Data processing pipeline for single-molecule super-resolution imaging using the Thunderstorm plug-in in FIJI. The original images with background noise and autofluorescence are first filtered. The program gives multiple choices for the filtering steps. For example, we can choose to use a Wavelet filter or Gaussian filter to enhance the images. The second step is to detect molecules in filtered images by comparing their intensity to the intensity in their neighborhood. The precise position of molecules is next determined using a fitting with integrated Gaussian, Gaussian, or phasor method. The outputs after this step are a table with localized positions and the information of localized molecules such as sigma, position uncertainty, intensity, and a summary image of all the localizations. After that, all the localized molecules undergo post-processing steps to eliminate, for example, low-intensity spots, too high or too low sigma values, too high uncertainty, etc. Figure adapted from [221]

Molecule localization using ThunderSTORM

The first step in the localization of fluorescent molecules is to detect the molecules by filtering the image. ThunderSTORM provides several methods such as low-pass or band-pass filter or wavelet filter. In our case, the wavelet filter was the one used in all the analyses. After image filtering, the next step in ThunderSTORM is to detect molecules. In order to find a molecule, the intensity of each pixel in the filtered image is compared to a threshold value. The threshold can be, for example, the standard deviation of the intensity values from the first wavelet filtering level. The intensity is also compared to the intensity of 4- or 8-connected neighbors and if it is higher, the point is accepted as a candidate molecule for further processing. The last part is to fit the detected molecules to get a sub-pixel accurate position. The program also provides many different methods for 2D fitting the Point spread function (PSF) such as fitting with 2D or 3D Gaussian, or integrated Gaussian, Phasor-based localization 2D or 3D.... The post-processing step is discussed in the next section [221].

The next step is to select the molecules detected with high precision and in the focal plane. When the fluorophores are out of the focal plane, their PSF is broader than that of molecules at the focal plane. The sigma value is related to the FWHM of the PSF:

$$\sigma = \frac{FWHM}{2\sqrt{2ln2}} \tag{4.1}$$

where

$$FWHM = \frac{\lambda}{2NA} \tag{4.2}$$

The NA of the Olympus oil-immersion objective used is 1.49. Therefore, the approximate relationship between sigma and wavelength can be represented as follows:

$$\sigma \sim \frac{\lambda}{5.9} \tag{4.3}$$

For example, if we use Alexa 647, the emission is around 700 nm, and the sigma of the Gaussian fitting of the PSF is around 108 nm. We, therefore, eliminate molecules with sigma values larger than 200 nm and smaller than 100 nm. We also eliminate the points with low intensity and high localization uncertainty. Figure 4.3 demonstrates how the localization points are selected after the localization process. The first step is to eliminate the molecules with too large sigma (so only the points in the focal plane are selected for the next step) or too small sigma (these points are artifacts). Secondly, the points with low intensity are also removed (these points are typically due to noise). Then, in order to remove fluorophores due to nonspecific binding, a density filter was sometimes applied. In density filtering, the program checks all the points and numbers of neighbors in a circle with a defined radius R. If the molecule has a higher number of neighbors than a defined threshold, the molecules are kept. Otherwise, they are considered as isolated molecules due to nonspecific binding and are removed. Figure 4.4 left demonstrates the filter process to remove isolated molecules.

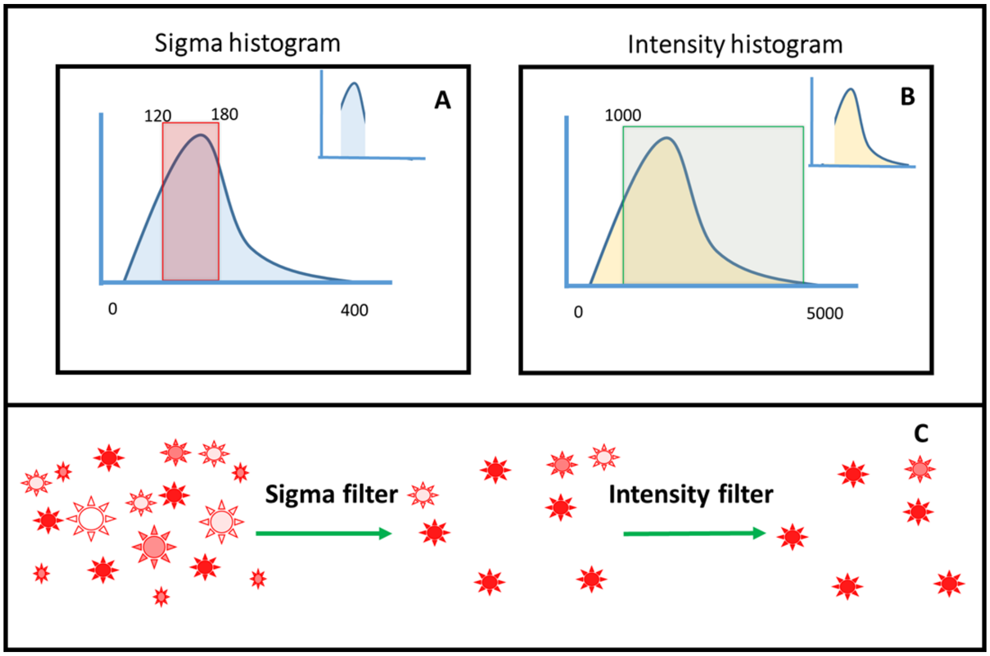

Figure 4.3: :Sigma and intensity filter in post-processing data after localizing molecule positions. (A) The sigma histogram of all molecules, and the window selection of molecules with appropriate sigma. (B) The intensity of molecules before and after filtering and corresponding window selection. (C) The diagram shows molecule selection using sigma and the intensity filter of molecules.

During dSTORM acquisition, one fluorophore can appear in multiple consecutive images. Therefore, in order to not over-count the number of fluorophores, a merging process was used. In merging, molecules in sequential images found inside a circle with a threshold radius R_0 are merged into one molecule (Figure 4.4 Right).

Mechanical drift is also one of the problems in SMLM. Because the time required to acquire all the images is long, the mechanical drift is significant in SMLM. Therefore, we used the correlation-based method that is implemented in ThunderSTORM to correct the drift.

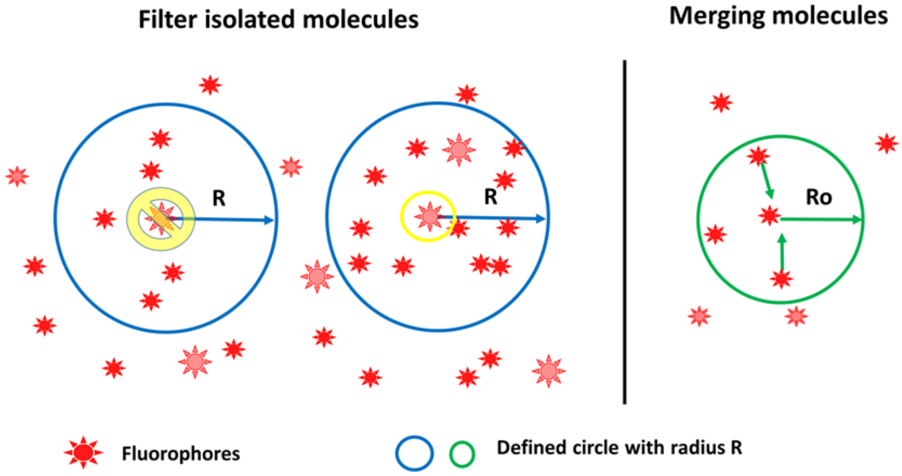

Figure 4.4: Density filtering of isolated fluorophores and merging identical fluorophores seen in sequential images. Left: The molecules with higher or equal numbers of neighbors than a defined threshold inside a circle with radius R are kept. Otherwise, they are removed. Right: Merging molecules is applied when these molecules are inside a circle with a defined radius in two consecutive frames.

4.1.2 Pre-processing and Post-processing

Effect of pre-processing parameters on the number of molecule localizations

In single-molecule localization techniques, the number of localizations depends on the parameters selected for the pre-processing and post-processing. In pre-processing, the wavelet filter was used in all the analyses. To detect the approximate molecule localizations, we used the local maximum method which requires the definition of a threshold. The local maximum method was run for different values of the peak intensity threshold (PIT): 40, 60, and 100. When the PIT is chosen to be low at 40, the program detects weak intensity spots as shown in Figure 4.5 A. These detection spots may be false and due to the noise in the image. In contrast, if the peak intensity is chosen to be too high, the program ignores spots with medium intensity as shown in Figure 4.5 C. Therefore, a PIT value equal to 60 was chosen to analyze the detected localizations of EGFR molecules labeled with polyclonal secondary antibodies in PEC and shCD9 PEC cells.

The number of molecule localizations diminishes when the PIT increases as shown in Figure 4.5 D. Figure 4.5 D and E shows that the number of detected localizations diminishes approximately by a factor of two when going from PIT = 40 to PIT = 100.

Table 4.1: Summary of pre-processing analysis for EGFR labeled with polyclonal secondary antibodies.

Pre-processing conditions			
Pre-processing steps	Condition 1	Condition 2	Condition 3
Step 1: Wavelet filter (B-Spline)	Scale: 2.0 Order: 3	Scale: 2.0 Order: 3	Scale: 2.0 Order: 3
Step 2: Local maximum	PIT=40	PIT=60	PIT=100
Step 3: PSF: Integrated Gaussian Fitting method: Maximum likelihood	Fitting radius: 3 pixels Initial sigma: 1.1 pixel	Fitting radius: 3 pixels Initial sigma: 1.1 pixel	Fitting radius: 3 pixels Initial sigma: 1.1 pixel
Number of detected molecules	87385	63859	40802

Table 4.1 sums up the different parameters in pre-processing of EGFR localizations in PEC and shCD9 PEC that lead to a change in the total number of detections.

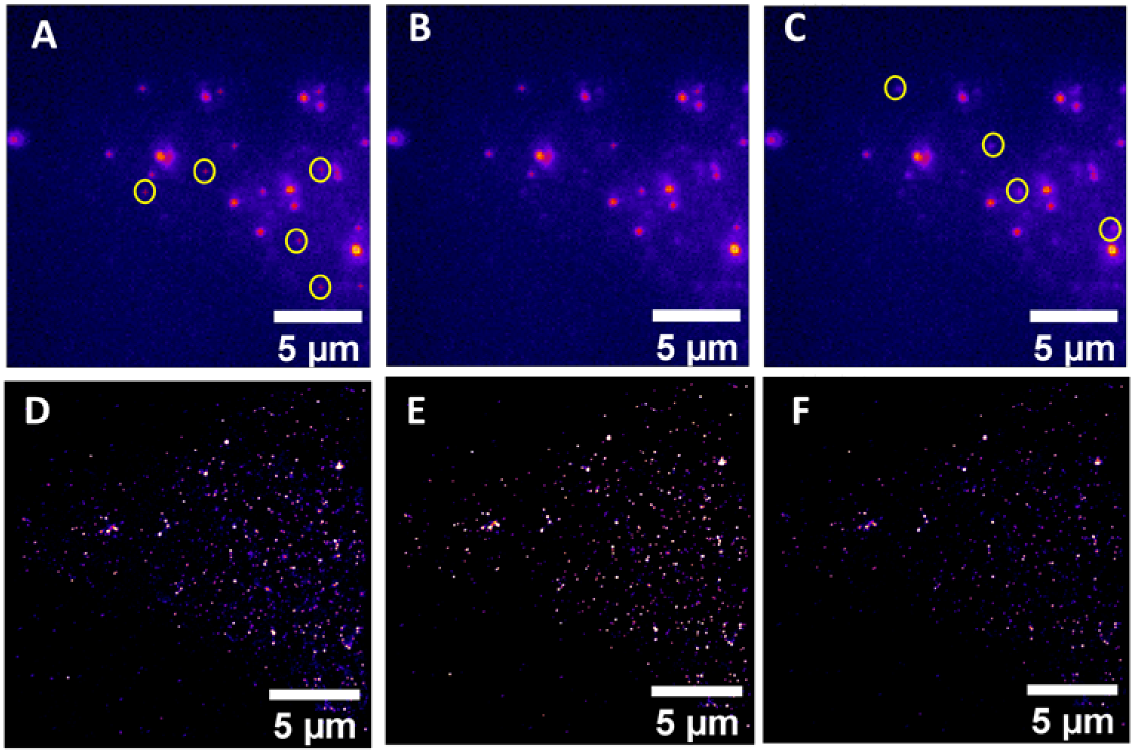

PIT: 40
87385 localizations

PIT:60
63859 localizations

PIT: 100
40802 localizations

Figure 4.5: The number of molecule localizations depends on the peak intensity threshold in the approximate molecule position step of pre-processing using ThunderSTORM. Peak intensity threshold is (A),(D) 40 (B),(E) 60, and (C),(F) 100. Figures (A), (B) and (C) show the molecules determined by different peak intensity value in one frame. Figures (D), (E) and (F) show the sum of all localizations.

Effects of post-processing parameters on the number of molecule localizations

The pre-processing parameters affect the total number of localizations. In our case, the conditions of pre-processing were found to be optimal at PIT = 60. However, the pre-processing step can only be optimized to remove the low-level signals. It does not remove the high-sigma localizations or isolated fluorophores and does not avoid over-counting the number of receptors due to the fact that a single fluorophore may blink several times. Therefore, a post-processing step is necessary for further analysis in single-molecule localization techniques.

Table 4.2: Summary of post-processing analysis for EGFR labeled with polyclonal secondary antibodies.

Post-processing conditions			
Post-processing steps	No filter	σ and uncertainty (3/4)	σ, uncertainty, density & merging (1/2)
Filter	No	100 nm <sigma<200 nm Uncertainty<50 nm	100 nm<sigma<200 nm Uncertainty<50 nm
Density filter	No	No	Neighbors=2 Radius=50.0 nm
Merging	No	No	Off frames=1 Dist=10 nm.
Drift correction	Cross correlation	Cross correlation	Cross correlation

Table 4.2 shows three post-processing conditions used for EGFR labeling with polyclonal secondary antibodies in PEC and shCD9 PEC data. In the first one, there is no filtering or merging; only drift correction was applied to subtract drift from all the localizations. In the second condition, we used a filter for the sigma and uncertainty values of the localizations. The localizations with sigma lower than 100 or higher than 200 or with uncertainty higher than 50 nm were removed. In the third condition, the data undergoes two filtering steps and a merging process. In this condition, the localizations were first filtered by their sigma and uncertainty values; then a density filter was applied. The density filter removed the isolated molecules that have less than 2 neighbors around them in a circle of 50 nm in radius. After

these filter steps, merging was applied to remove the molecules appearing in consecutive frames with a distance lower than 10 nm.

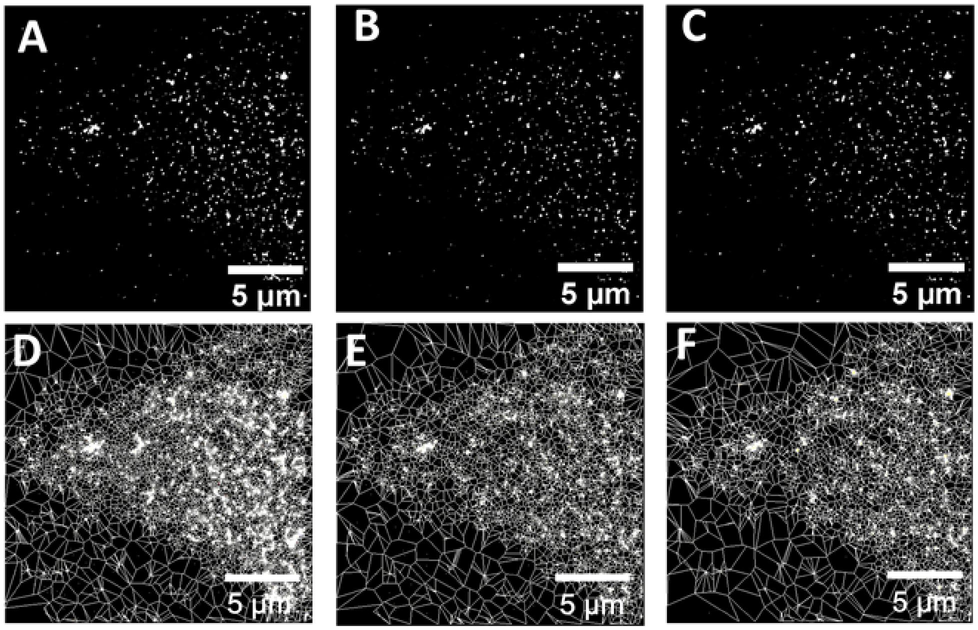

Figure 4.6: The number of molecule localizations using polyclonal antibody labeling changes depending on the different post-processing filter conditions. (A) The molecule localizations in the cell membrane of PEC without post-processing. (B) Molecule localizations after post-processing with parameters lead to retaining three-quarters of the initial molecule localizations. (C) Same as in (B) except that half of the molecule localizations are retained after post-processing. Voronoï segmentation of molecule localizations in the PEC cell membrane for different post-processing conditions: (D) Without post-processing. (E) Three-quarters of molecule localizations are retained after post-processing. (F) Half of the molecule localizations are retained.

Figure 4.6 A-C show the number of detected localizations in the three different conditions of post-processing described above, while Figure 4.6 D, E, and F show the Voronoï diagram of the localizations corresponding to the post-processing conditions in Figure 4.6 A, B, and C, respectively. It can be seen that, after the post-processing step, although the numbers of molecules are reduced by one-fourth and one-half, the main structures and distributions of EGF receptors on the cell membrane remain the same. Therefore, the post-processing that was applied is solid enough to remove molecules due to nonspecific binding or molecules with too low signals and still keep the characteristics of EGF receptor distribution in the cell membrane.

4.1.3 Clustering Analysis

Tessellation method for clustering

After getting the positions of the fluorophores, the next step is to find out the organization of proteins in the cell membrane. To determine the distribution of EGFR and CD9 in the cell membrane, we used a segmentation method based on Voronoï tessellation. The program that we used is called SR-Tesseler and was written by Levet et al. [242].

In the Voronoï method, the molecule sites are considered to be seeds. The space around each seed is divided into several polygons where the seed is at the polygon center. The characteristics of the neighbors around each seed depend on two main factors: the polygon shape and size. While the shape of the polygon depends on the number of surrounding neighbor molecules, the polygon size indicates the density of these neighbors around that seed. The localization density is calculated as the number of seeds divided by the polygon area around those seeds. To determine the cluster organization, after the Voronoï diagram is created, first, several parameters are calculated from all the polygons such as the area of each seed, the density of different rank areas around the seed, the mean distance between the seed and surrounding neighbors, and shape index of the assembly of all polygons of a certain rank. The second step is to define a threshold and choose the polygons of interest that have parameters that are higher than that threshold. For example, in Figure 4.7, polygons with a first-rank density higher than 1.5 times the density of the whole image are chosen. Third, the software computes objects, i. e. clusters, by merging all selected polygons that share common edges and defines object outlines by connecting all localizations belonging to the borders of the objects.

In Figure 4.8 A, the Voronoï diagram shows the EGFR distribution in clusters on the cell membrane of PEC. Figure 4.8 B shows the magnification of one cluster of EGF receptors. Polygons decrease in size from the edge to the center of the cluster. This agrees with data from single-molecule tracking (see Chapter 5), where the confining potential is higher at the outer edge of the cluster than near the cluster center. It leads to polygon areas close to the cluster center being smaller than the polygons of points at the cluster edge. Figure 4.8 C shows that the polygon areas inside the cluster center are more homogeneous. It has been shown that EGF receptors in the cell membrane are located in clusters in many cell types [1]. Here, the data of EGF receptors segmented by the Voronoï method also indicate that EGF receptors in PEC are localized inside clusters where the density of cluster decreases from the center to the vicinity of the receptor confinement domain.

The localizations were further analyzed using the SR-Tesseler program to analyze the cluster properties. Four main parameters were extracted from the tessellation method including the area of clusters, the number of localizations inside clusters, the density of localizations in clusters, and the diameter of clusters.

Figure 4.10 A, B, C, D show the results for the four main parameters of the clusters obtained after different post-processing conditions. It is seen that all main parameters do not change significantly after the post-processing. This also confirms through the visualization of the Voronoï diagram in Figure 4.6 that the main components and structures of receptors

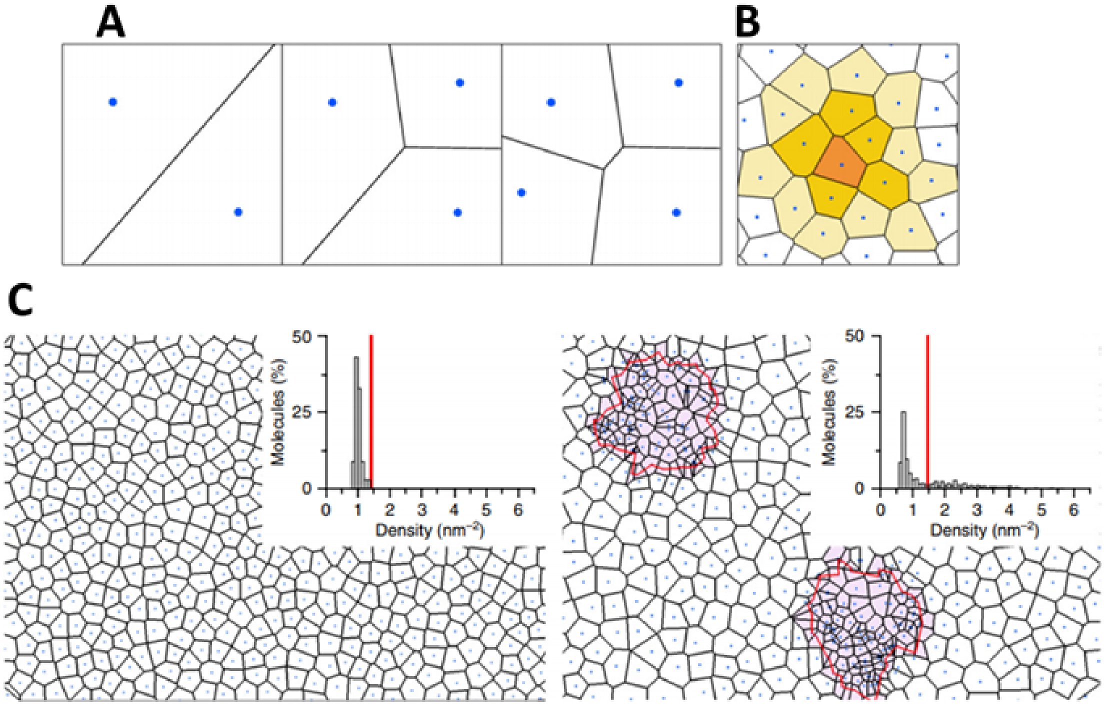

Figure 4.7: Voronoï-based segmentation. (A) Construction of polygons from left to right. The line that divides the space between two seeds is equidistant from the two seeds. When more seeds are added to the space, the previous line is cut by the new line that is created between the old seeds and the new one. The process is repeated until all seeds have been added to the system to create a Voronoï diagram. (B) The polygons around each seed are ranked with respect to their relative position to the polygon where the seed is located (in deepest orange color). The first boundary polygons in medium orange have edges touching an edge of the polygon containing the seed and are termed first-rank polygons. Whereas the polygons in lighter orange have edges touching the first-rank polygons and are designated as second-rank polygons. (C) The clustering of the seeds is based on the density of the first-rank polygons. On the left, in a uniform distribution, no cluster is determined with a threshold that is 1.5 times higher than the localization density of the whole image. While, on the right, the polygons with a density of the first-rank polygons higher than the threshold are selected and all the selected polygons which share common edges are merged to create a cluster. Image extracted from [242].

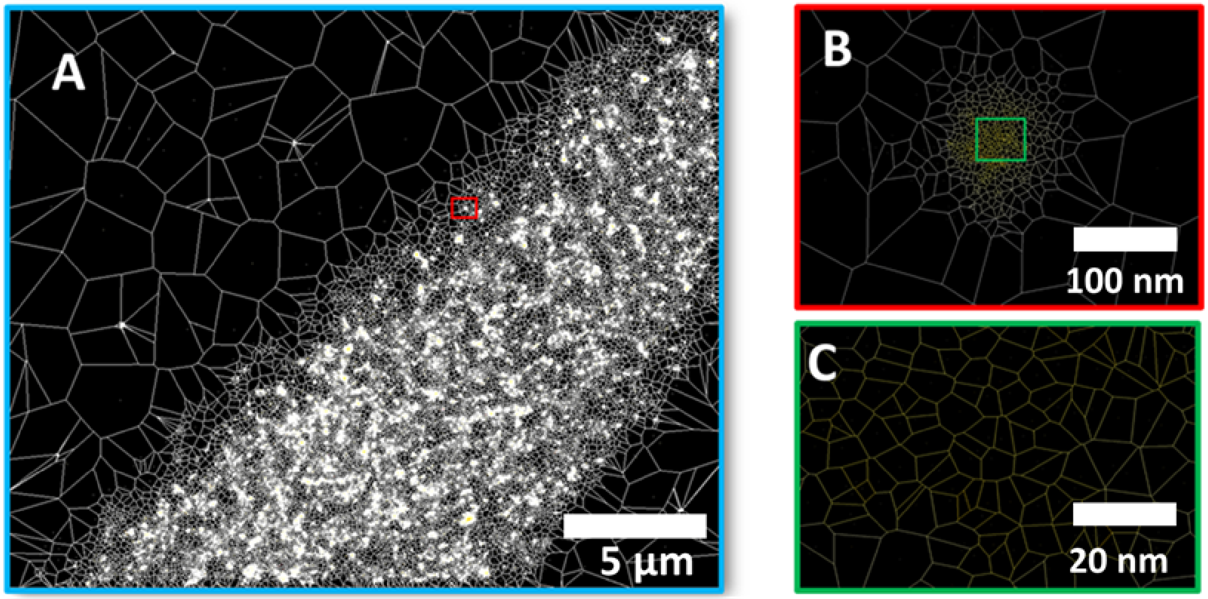

Figure 4.8: The Voronoï based segmentation of EGF receptors on the cell membrane of PEC with three different magnifications. The Voronoï diagram showing (A) the shape of the cell membrane, (B) the cluster, and (C) polygons inside the cluster.

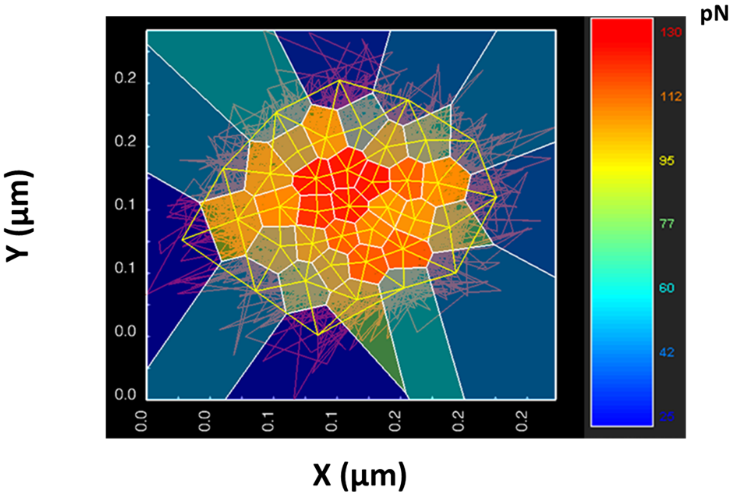

Figure 4.9: Voronoï mesh of EGF receptor trajectory by single molecule tracking in PEC.

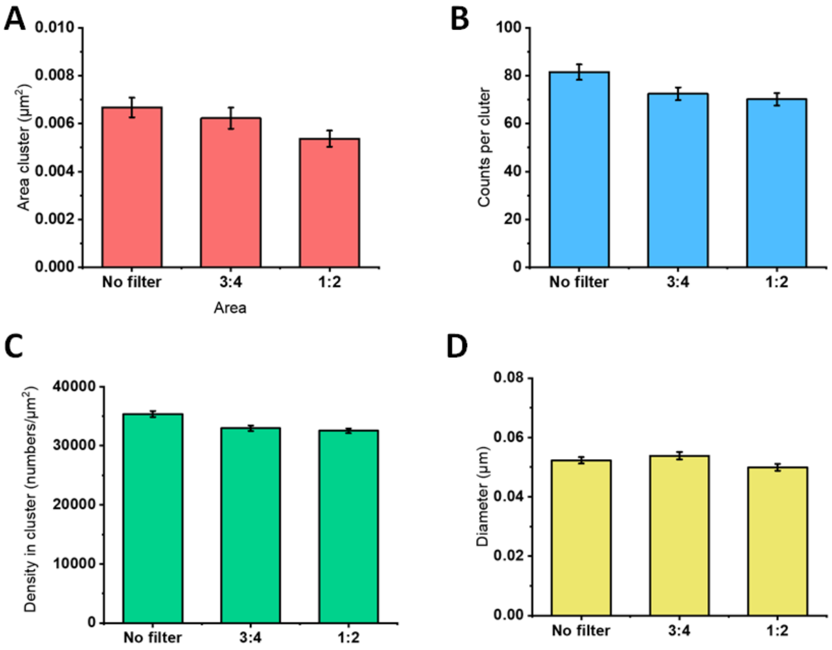

Figure 4.10: EGF receptor localizations in PEC obtained by targeting with polyclonal secondary antibodies. Analysis with different post-processing filter conditions.(A) Cluster area. (B) Number of localization counts per cluster. (C) Density of receptors per cluster area. (D) Diameter of clusters.

remain after the filtering and merging process. For other experiments such as EGF receptors in shCD9 PEC labeled with polyclonal secondary antibodies, EGFR labeled with nanobodies, and CD9 proteins labeled with polyclonal secondary antibodies, the post-processing conditions were also checked and are displayed in Appendix B.

4.2 EGFR localization and distribution in PEC and shCD9 PEC

4.2.1 Difference between labeling with nanobodies and polyclonal secondary antibodies

A nanobody is smaller than a conventional IgG antibody. In common IgG, there are three main parts, Constant heavy chain (CH), Constant light chain (CL), Varying heavy chains (VH). Isolated from conventional antibodies, the Fab fragment which is comprised of VH, VL, and CL can also be used as a smaller unit to bind to antigens. The smallest fragment from conventional IgG is called scFv, includes VL and VH, and can be considered as the smallest intact functional antigen-binding fragment. A nanobody is extracted from a Heavy-Chain antibody (HCab) which does not have CL and VL chains. The Single-domain antibody (sdAb) or nanobody is the smallest unit binding to antigens that can be engineered from HCab produced by cameloids. Nanobodies usually have a molecular weight around 15 kDa while Fab fragments are around 50 kDa [243].

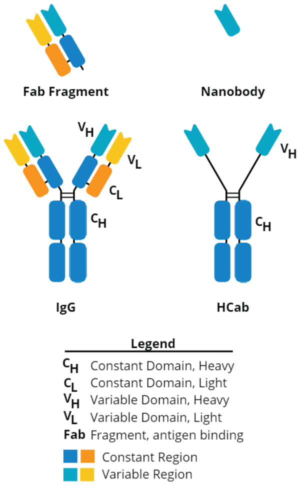

Figure 4.11: Structure of conventional antibody that produces Fab Fragment and nanobody obtained from HCab.

Application of nanobodies: Because nanobodies are small, produced in bacteria, and have high affinity, they are used in many applications in bio-imaging as well as therapeutics [243]. In 2006, Rothbauer et al.[244] showed that they could fuse nanobodies to fluorescent proteins (GFP) to label different compartments in living cells. The fusion of fluorescent proteins and nanobodies is called chromobodies. Furthermore, in SMLM, in previous work, instead of using GFP antibodies to label GFP, nanobodies were used because they have a smaller size than the conventional antibody, and they also have a high affinity to GFP[245]. The fusion of nanobodies to Alexa 647 takes advantage of organic fluorophores with a high photon yield such as Alexa 647. This allowed efficient super-resolution imaging of existing GFP constructs with minimal linkage errors.

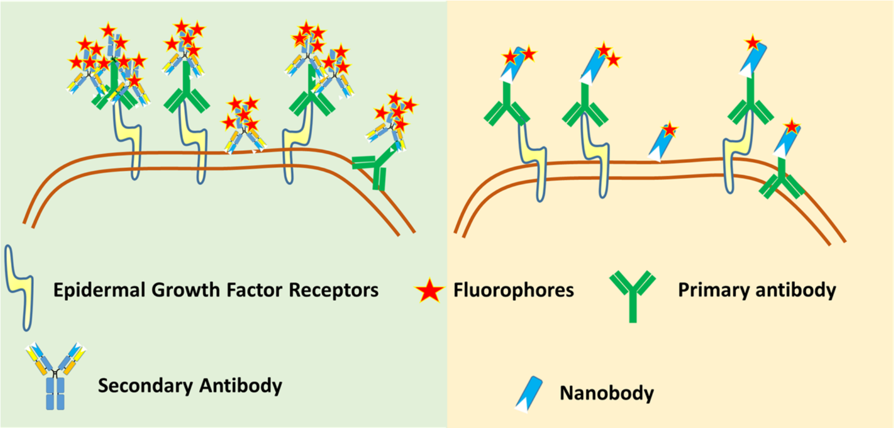

Figure 4.12: Labeling of primary antibodies with polyclonal secondary antibodies vs. labeling of primary antibodies with nanobodies.

In the experiments, fixed cells were incubated first with a primary antibody then with a secondary antibody labeled with an organic fluorophore. For the first series of experiments, the antigen is recognized with a monoclonal primary antibody and then polyclonal secondary antibodies were used because this leads to more fluorophores per receptor and therefore more signals. It is known that multiple polyclonal secondary IgGs can bind to different epitopes of a primary antibody. Furthermore, polyclonal antibodies are large and are typically labeled by multiple fluorophores. In total, the number of fluorophores coupled to a receptor can therefore range from 3 to 20. Hence, using polyclonal secondary antibodies helps enhance the fluorophore signal in the whole system. However, because this amplification effect creates uncertainties in the observed receptor number, we also used labeling of the receptors with nanobodies playing the role of secondary antibodies to obtain more quantitative measurements. The nanobodies we use are known to be labeled by 1 to 2 fluorophores. In our second series of experiments, nanobodies labeled with 1-2 fluorophores were used to bind to EGFR to decrease the uncertainty in the number of fluorophores per receptor.

4.2.2 EGFR distribution in PEC and shCD9 PEC

To understand how removing CD9 proteins affects the distribution of EGF receptors on the cell membrane in PEC at the molecular level, we compared first the characteristics of EGF receptors in PEC and short hairpin CD9 Parietal Epithelial cells (shCD9 PEC). The shCD9 PEC was created by using the short hairpin RNA technique. In short, a short hairpin RNA was inserted in PEC cells to silence the expression of the CD9 gene via RNA interference.

Figure 4.13 and Table 4.3 represent the main parameters of EGF receptor clusters in PEC and shCD9 PEC by using polyclonal secondary antibodies or nanobodies. We can see that the results using polyclonal secondary antibodies or nanobodies to label EGF receptors are consistent in terms of EGFR cluster characteristics in PEC and shCD9 PEC.

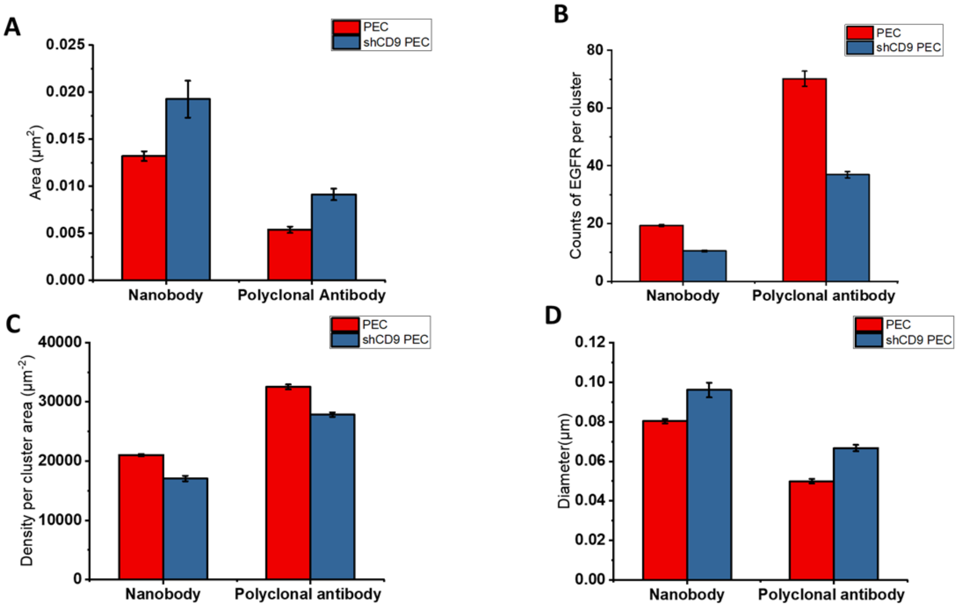

Figure 4.13: EGFR cluster analysis in PEC and shCD9 PEC by using SR-tesselar analysis of the dSTORM data. The parameters are: (A) cluster size (B) fluorophore counts per cluster (C) the molecular density inside the cluster, and (D) cluster diameter.

As we can see in Figure 4.13 A and D, the area and diameter of EGFR clusters in PEC are smaller than those in shCD9 PEC. Using polyclonal secondary antibodies, the area of the EGF receptor domain is found to be larger in PEC than in shPEC, i.e. 0.0053 ± 0.0003 μm^2 in PEC and 0.009 ± 0.002 μm^2 in shCD9 PEC, respectively. By using nanobodies, the area of the EGF receptor domain is also larger in PEC than in shCD9 PEC. We also found that the area when using nanobodies is larger than when using polyclonal secondary antibodies. This may be due to the lower number of fluorescent labels per receptor when using nanobodies which may lead to the algorithm finding a larger cluster area.

Moreover, Figures 4.13 B and C show that both the counts of molecules and the molecule density inside clusters are lower in the case of shCD9 PEC cells compared to PEC. The number of counts per cluster corresponds to the number of receptors per cluster. The mean number of counts in one domain in PEC is 70 ± 3 counts per cluster (using polyclonal secondary antibodies) and 19.3 ± 0.3 receptors per cluster (using nanobodies), whereas in shCD9 PEC the number of receptors is only half of that in PEC 37 ± 1 with polyclonal secondary antibodies, and 10.4 ± 0.3 with nanobodies. As expected, when using nanobody labeling of the receptors, the number of fluorophores per cluster drops. The number of counts per cluster inside a domain using nanobodies is 3.6 times lower than the number using polyclonal secondary antibodies. This is consistent with the estimation of the fluorophore number per receptor in the polyclonal secondary antibody case (5-30) and in the nanobody case (2-4).

By calculating the density of counts in whole cells, we can see that the receptors are mainly located in small domains both in PEC and in shCD9 PEC cells. We noticed that the lack of CD9 does not lead to the presence of EGF receptors outside clusters: the receptors are still confined mostly in clusters with a somewhat bigger size. The average count density in the whole cell is approximately one thousand times lower than inside the cluster. To calculate the density per cell, the cell surface was first identified by using a plug-in of ImageJ, trainable Weka segmentation. We then take the total number of molecule locations after the ThunderSTORM analysis and divide by the cell area.

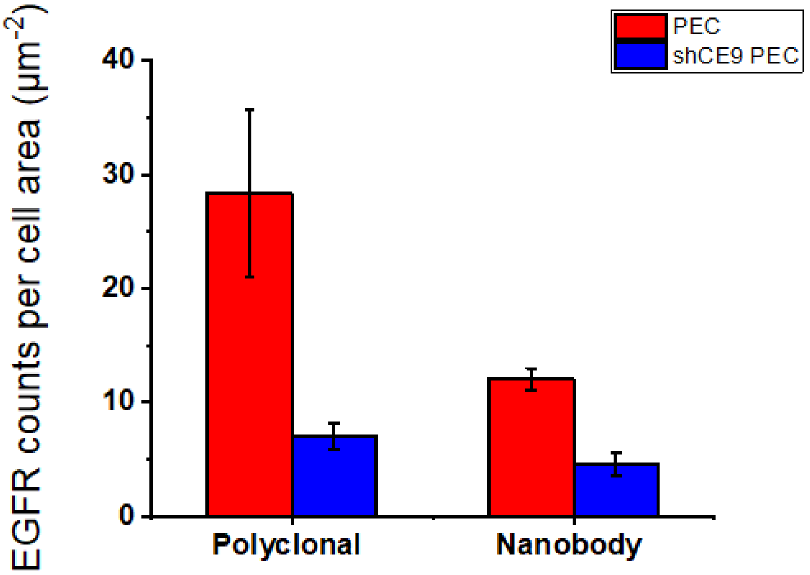

Figure 4.14: Number of EGF receptor counts per cell area in PEC and shCD9 PEC.

Lazareth et al. found using semi-quantitative Western Blot experiments that the depletion of CD9 in PEC cells leads to a reduction in the total number of EGF receptors, as well as in its phosphorylation after HB-EGF stimulation (Figure 4.15) [2]. Our results confirm their finding in a quantitative manner: there are about 4 times fewer EGF receptors in shCD9 PEC compared to PEC cells.

Our finding is compatible with the hypothesis that EGF receptors are located in CD9 tetraspanin-enriched domains. As the depletion of CD9 is expected to decrease the number of tetraspanin-enriched domains in the membrane, we may conjecture that EGR receptors do not find a favorable environment for their insertion in the cell membrane. This may lead

		PEC	shCD9 PEC
Area (μm^2)	Nanobody	0.0132 ± 0.0005	0.019 ± 0.002
	Polyclonal antibody	0.0053 ± 0.0003	0.0091 ± 0.0006
Counts per cluster	Nanobody	19.3 ± 0.3	10.4 ± 0.3
	Polyclonal antibody	70 ± 3	37 ± 1
Count density inside cluster (μm^{-2})	Nanobody	21017 ± 193	17057 ± 450
	Polyclonal antibody	32534 ± 407	27852 ± 375
Diameter (μm)	Nanobody	0.080 ± 0.0001	0.0096 ± 0.0003
	Polyclonal antibody	0.0049 ± 0.0001	0.066 ± 0.001
Count density whole cell (μm^{-2})	Nanobody	12 ± 1	4.5 ± 0.9
	Polyclonal antibody	28 ± 7	7 ± 1

Table 4.3: Summary of EGF receptor distribution on the cell membrane of PEC and shCD9 PEC cells.

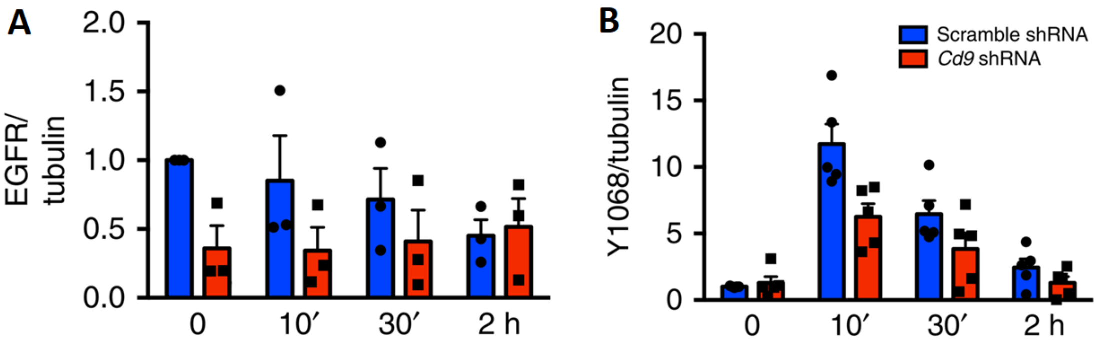

Figure 4.15: Semi-quantitative Western blot analysis of the expression of (A) EGFR, and (B) of phospho-EGFR Y1068 (pEGFR Y1086) in control (scramble Short hairpin RNA (shRNA)) and CD9-depleted (Cd9 shRNA) PEC cells after stimulation with HB-EGF. Figure from [2]

to the receptors being more rapidly internalized into the cytosol and degraded leading to a lower number of receptors in the whole cell in steady-state conditions. Moreover, when CD9 proteins are depleted, we expect the tetraspanin domains to be less compact. This explains why EGF receptors are found in clusters with somewhat larger area in shCD9 PEC than in PEC cells. However, as both the number of counts per cluster and the density of receptors in clusters decrease in PEC depleted of CD9, the result showing an increase of domain size in shCD9 PEC with respect to PEC cells may be an apparent effect due to the lower molecular density. Therefore, we also used single-molecule tracking experiments (see Chapter 5) to confirm this finding.

4.2.3 EGFR and CD9 localization and distribution in PEC

To further investigate the relationship between CD9 proteins and EGF receptors in the cell membrane, we performed STORM imaging of CD9 proteins in PEC. Figure 4.16 shows the comparison of EGF receptor clusters and CD9 clusters. The cluster parameters are similar in the two cases. However, as expected, we do not get the same results for the two receptors. Indeed, we find the CD9 cluster size to be bigger than the EGFR cluster size. This difference may not be significant because the two receptors are different. Therefore, the labeling efficiency of the antibodies is different, and also the number of proteins per cluster is not the same. This means that the number of counts and density of EGF receptors and CD9 proteins are different (Figure 4.16 C, D) and could lead to the cluster size of CD9 proteins seeming different compared to that of EGF receptors, as shown in Figure 4.16 A and D. Indeed, the number of detected CD9 proteins inside clusters are smaller than that of EGF receptors and this may cause the tessellation method to find a larger cluster area.

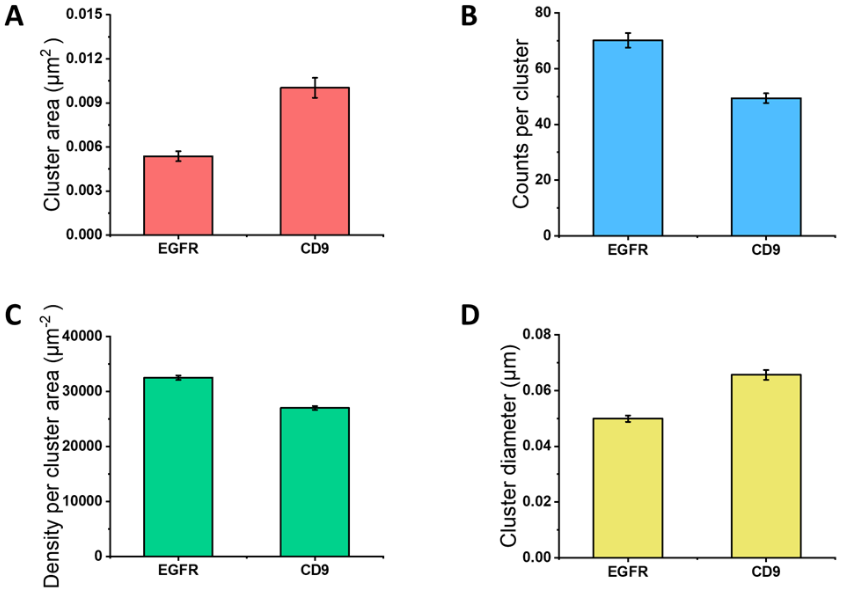

Figure 4.16: EGFR with polyclonal antibody and CD9 protein distribution in PEC cells is revealed by STORM experiments and SR-Tesselar analysis. (A) Cluster area, (B) counts per cluster, (C) cluster density, (d) diameter of receptor clusters calculated from the tessellation technique.

	EGFR	CD9
Area (μm^2)	0.0053 ± 0.0003	0.010 ± 0.0006
Counts per cluster	70 ± 3	49 ± 2
Count density inside cluster (μm^{-2})	32534 ± 407	27041 ± 361
Diameter (μm)	0.0049 ± 0.0001	0.066 ± 0.001

Table 4.4: Summary EGF receptor and CD9 distribution on the cell membrane of PEC.

4.3 2-color dSTORM experiments labeling EGFR and CD9

4.3.1 Problems with the mechanical drift

Mechanical drift causes serious problems not only for long-term single-particle tracking experiments but also in dSTORM. In our dSTORM experiments, the acquisition time for one frame is 50 ms, and one sequence includes between 10000 and 20000 images. Therefore, the mechanical drift is significant and can change the analysis result. In one color dSTORM, typically, drift correction is done by using an algorithm based on image correlation that is implemented in ThunderSTORM (the image reconstruction program). This drift-correction algorithm can be used for single-color imaging, though it is more reliable when applied to data sets with higher density, brighter signal, and lower background signals. However, in two-color imaging in dSTORM, the two corrections are performed independently, resulting in two sharp images but where the drift correction between the two data sets adds a random shift of the first image with respect to the second image.

Figure 4.17 shows the effect of mechanical drift on dSTORM. α-tubulin, one of the main components of microtubules was labeled in COS7 cells with two different dyes: Alexa 647 and CF 750. After the images were reconstructed and overlaid, the microtubule images in the two channels are not superimposed due to the mechanical drift.

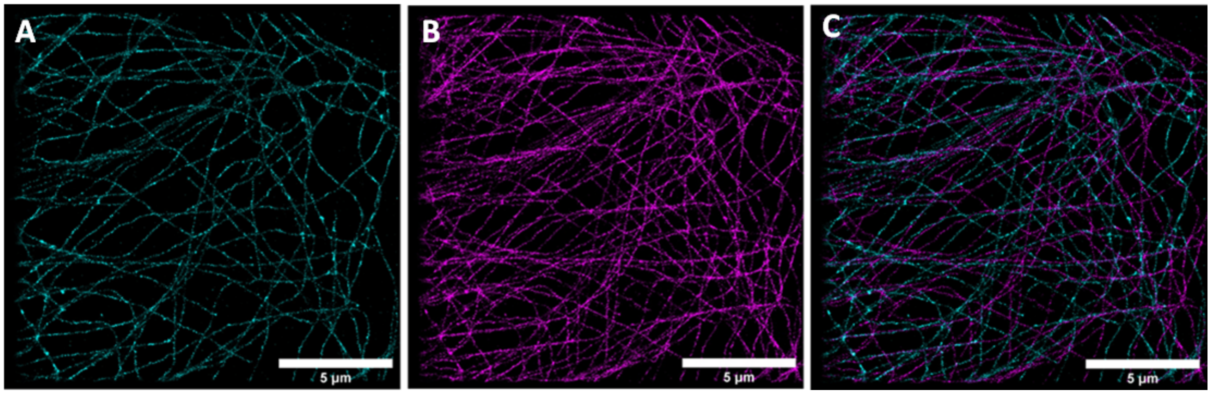

Figure 4.17: Image of microtubules in a COS7 cell. (A) The microtubules were labeled with Alexa 647 (B) The same microtubules were also labeled with CF 750. (C) Overlay of two reconstructed images of the same cell.

Figure 4.18 shows a two-color image of EGFR (red) and CD9 (green) in a PEC cell. The image was created by using the reconstructed images of ThunderSTORM and applying a Gaussian blur (radius = 5). As we can see from the edge of the cell, the green color is shifted towards the bottom and to the right compared to the red color. We then calculated the smallest distance between the cluster centers of CD9 and EGFR and found that it is not centered at 0 but is slightly shifted away from 0 (Figure 4.19).

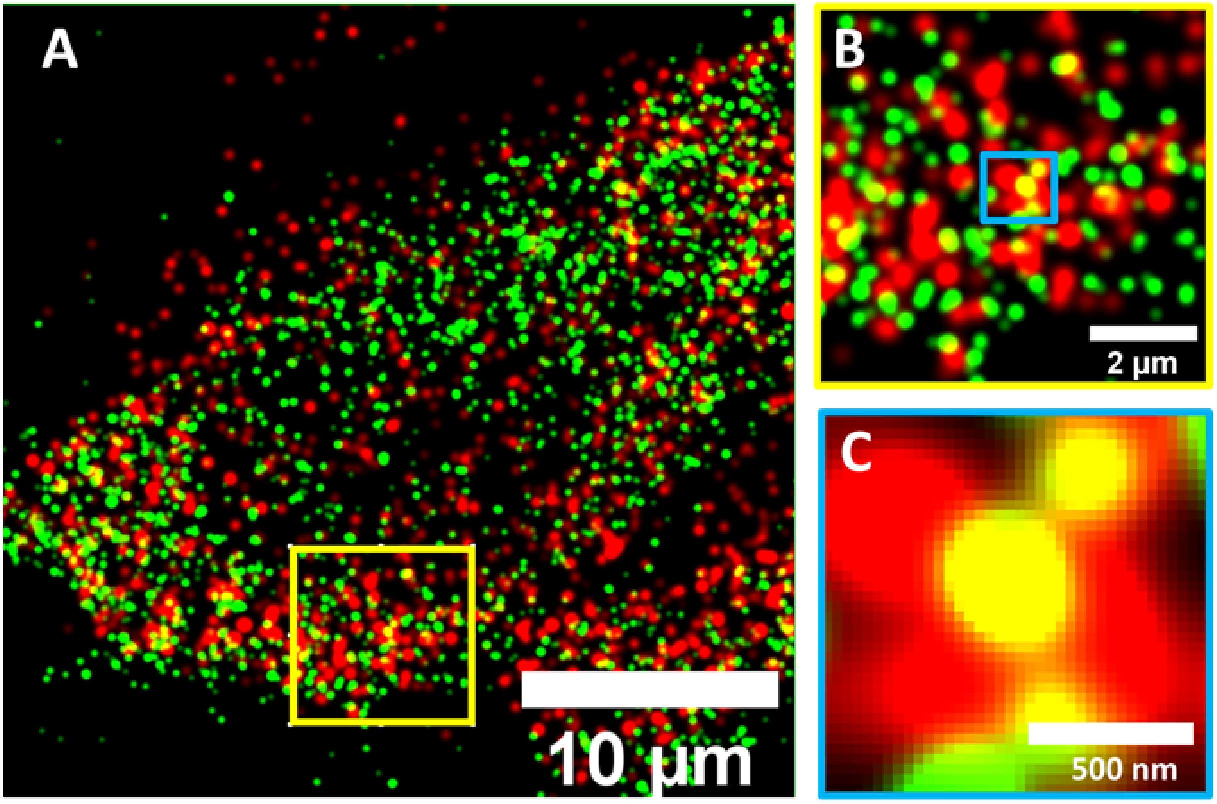

Figure 4.18: 2-color STORM image of EGFR (red) and CD9 (green) in PEC cells. (A) The overlay image of two channels, CD9 and EGFR, with independent drift correction. (B) Zoom-in image of a region where the clusters are clearly seen. (C) Region where the two-color clusters somewhat overlap.

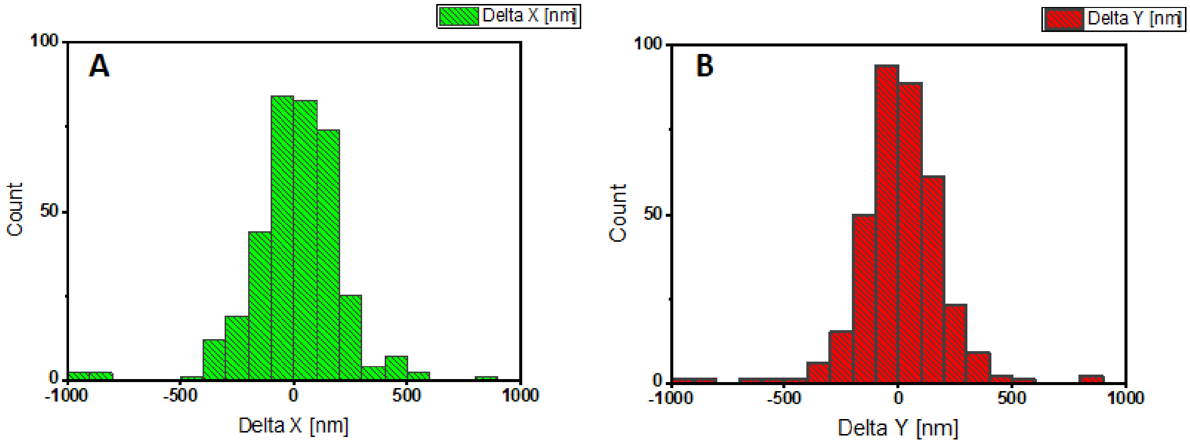

Figure 4.19: Minimum distance between CD9 and EGF receptor cluster centers in (A) X direction and (B) Y direction.

To correct the mechanical drift, we next used fixed fiducial markers that can be used as reference points between the two channels.

4.3.2 Using fixed fiducial markers for the drift correction

To correct the mechanical drift in dSTORM, we used gold nanoparticles which have broad absorption and emission spectrum, as well as stable fluorescence suitable for long-term measurements. However, the exposure of these gold nanoparticles to the imaging solution makes the nanoparticles blink. Therefore, we first spin-coated the gold nanoparticles on the glass coverslips and then coated the coverslips with a thin silicate layer to avoid direct contact between the nanoparticles and the imaging buffer. Figure 4.20 shows the fluorescence intensity of gold nanoparticles excited with 640 nm and 532 nm lasers, respectively. The signal from the nanoparticles is stable and is not bleached even after a long period of time.

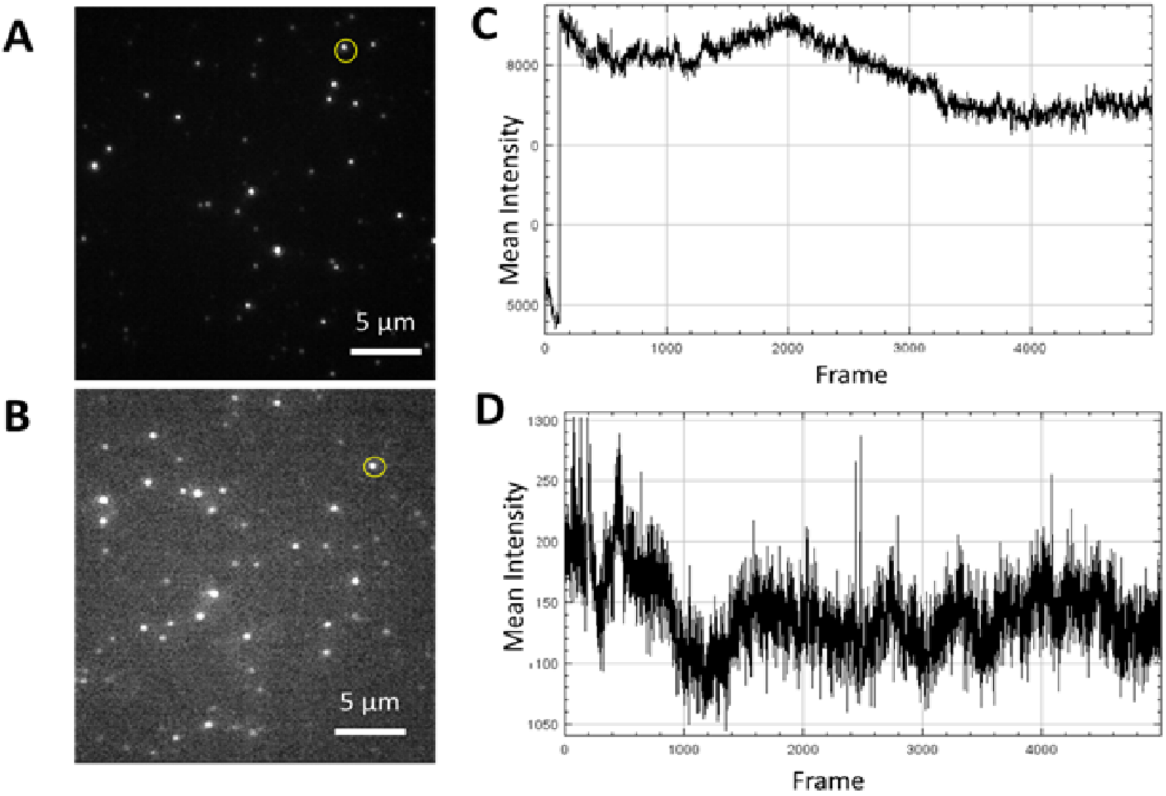

Figure 4.20: The fluorescence of gold nanoparticles was excited at (A) 640 nm and (B) 532 nm. (C) and (D) The intensity profile of gold nanoparticle fluorescence emission during 5000 frames upon 640 and 532 nm excitation, respectively.

Figures 4.21 A and C show the EGFR and CD9 protein distribution on the PEC membrane. Before drift correction, there is almost no overlap between the two protein clusters. However, after subtracting the drift by using the fixed gold nanoparticles on the coverslip surface, there is a partial overlap between the two proteins in the cell membrane. This result provides a further indication that at least a fraction of EGF receptors is located in CD9-enriched nanodomains. As discussed above, this explains why depleting CD9 proteins leads to lower EGFR insertion in the cell membrane, a lower number of EGFR receptors, and a lower level of phosphorylation. Moreover, note that CD9 protein expression is much higher in PEC cells observed in an inflammatory disease mouse model than in PEC cells of healthy mice [2]. Our STORM results confirm the low CD9 expression level in PEC cells isolated from healthy mice observed by Lazareth et al. [2]. This low expression level of CD9 protein also renders their observation in STORM experiments more difficult.

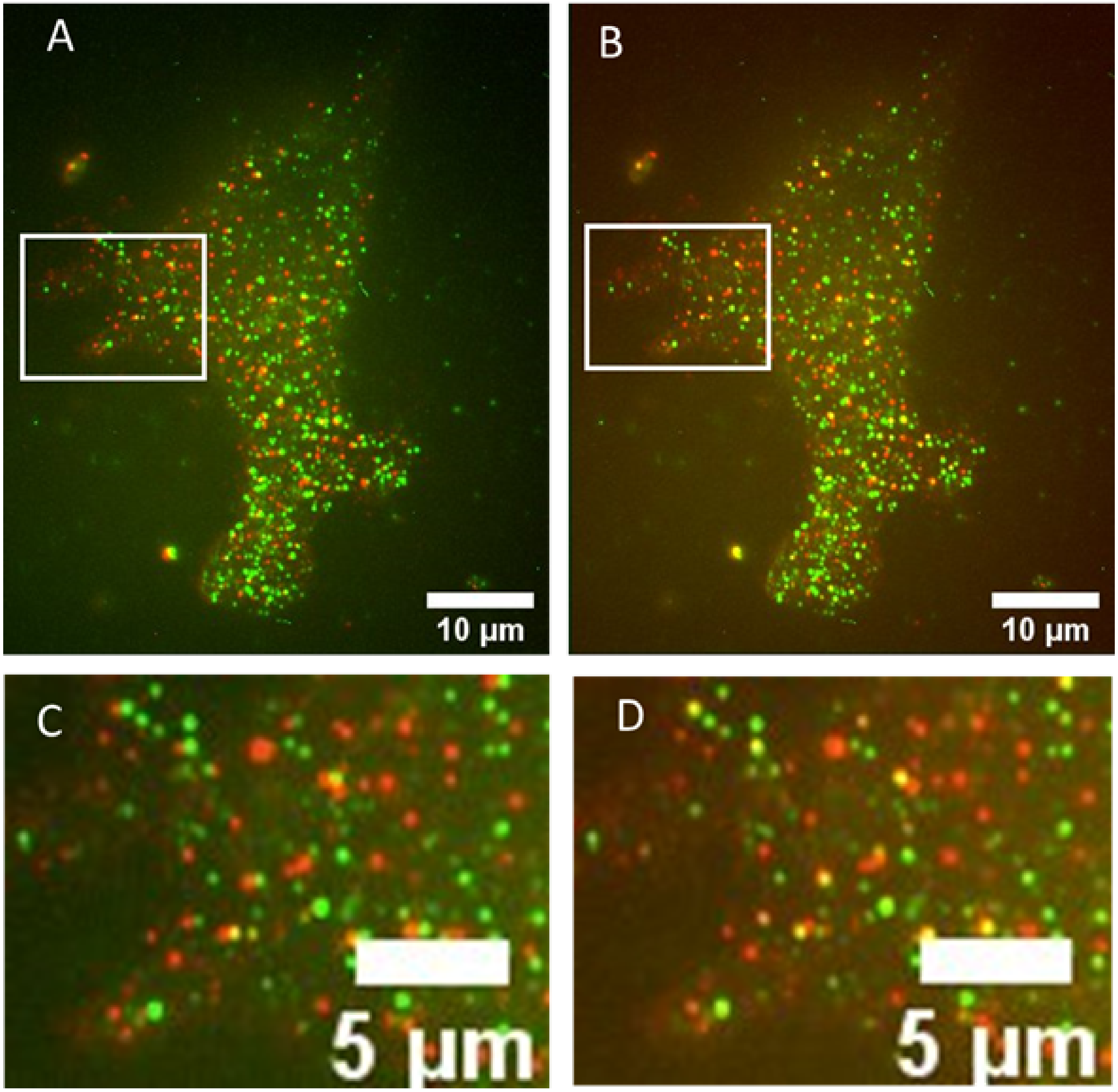

Figure 4.21: EGFR (red) and CD9 protein (green) distribution in PEC cell (A) before drift correction, (B) after drift correction. (C), (D) A region was zoomed in before and after drift correction, respectively.

To compare this partial overlap between EGFR and CD9 clusters with a reference case where we expect negligible overlap, we chose transferrin receptors which are known to localize neither in rafts nor in tetraspanin-enriched domains. The diffusion of transferrin receptors is influenced by the cytoskeleton meshwork underneath the cell membrane as described by the picket-and-fence model [113, 114].

Figure 4.22 A and B show the distribution of EGFR and transferrin receptors in the cell membrane of a PEC cell before and after drift correction, respectively. We can see that both before and after drift correction, the transferrin receptor and EGFR clusters have less overlap compared to CD9 and EGFR clusters. To measure quantitatively how the overlap of CD9 and EGFR clusters compares to the overlap of transferrin receptor and EGFR clusters, we calculated the minimal distance between CD9 clusters and EGFR clusters and the minimal distance between transferrin receptor clusters and EGFR clusters (Figure 4.23).

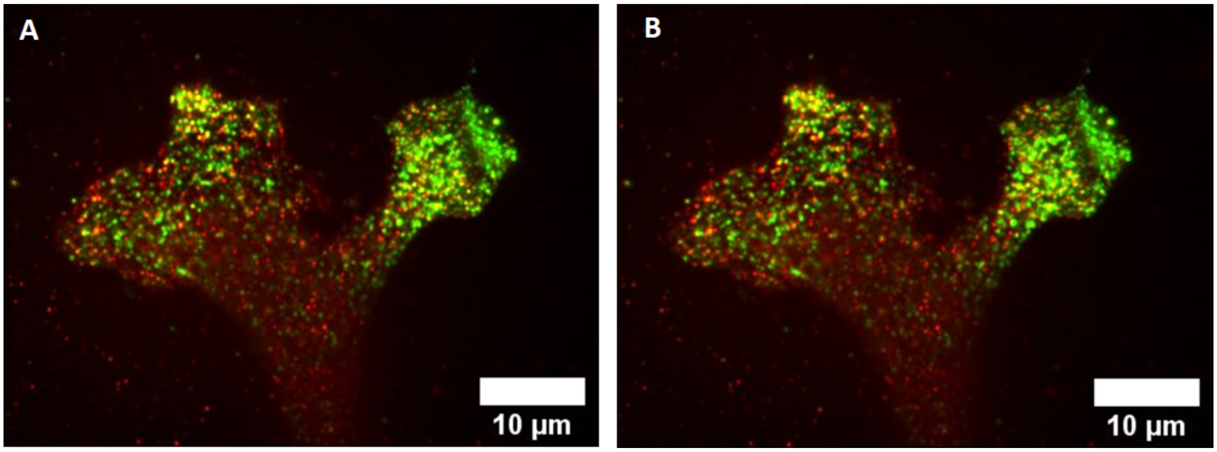

Figure 4.22: EGFR (red) and transferrin receptor (green) distribution in a PEC cell (A) before drift correction, (B) after drift correction.

After calculating the minimal distance, we calculated the percentage of the distances that are smaller than 100 nm (the typical size of the clusters) to determine the percentage of CD9 clusters that show overlap with EGFR clusters and the percentage of transferrin receptor clusters that show overlap with EGFR clusters. Indeed, we considered that two clusters of proteins overlap when the distance between the two cluster centers is smaller or equal to 100 nm.

We can see from Figure 4.24 that there is a higher percentage of overlap between CD9 clusters and EGFR clusters (14.3 ± 2.7 %) than between transferrin receptor clusters and EGFR clusters (2.5 ± 0.8 %).

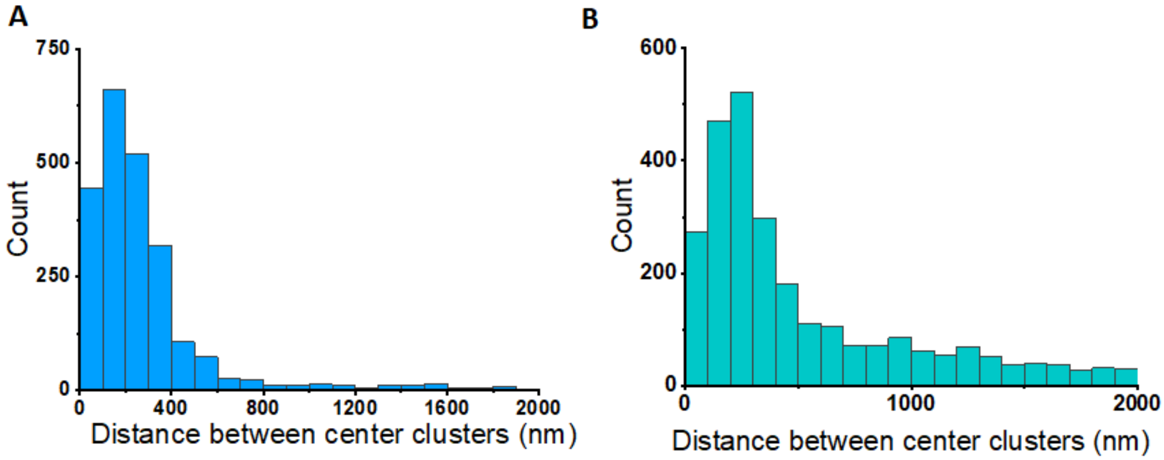

Figure 4.23: The histogram of the distance between (A) CD9 cluster centers and the closest lying EGFR cluster center in PEC cells and (B) between transferrin receptor cluster centers and the closest lying EGFR cluster center.

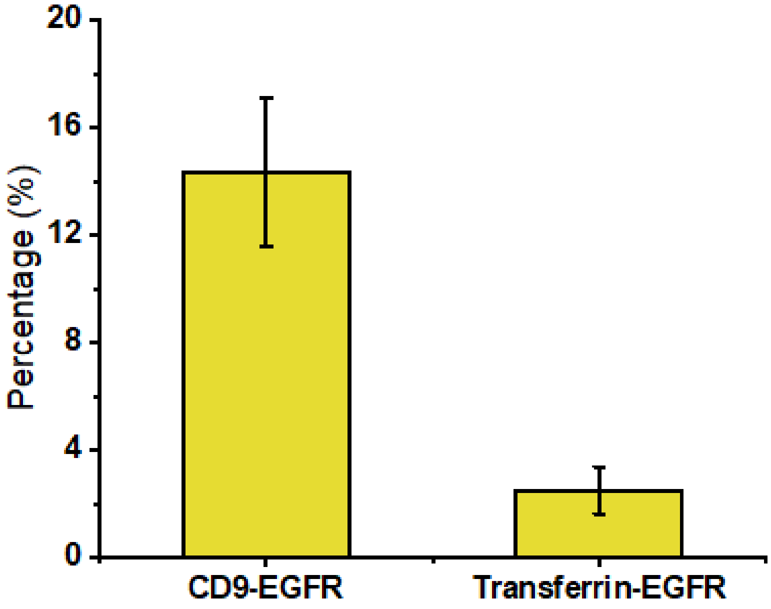

Figure 4.24: The percentage of overlap between CD9 clusters and EGFR clusters and between transferrin receptor clusters and EGFR clusters. We consider that two clusters overlap if the distance between their centers is smaller than 100 nm.

4.3.3 CD9 and EGFR labeling efficiency

Since the one-color experiments and the two-color experiments were done with different protocols, we verified that the results for EGFR were consistent. We, therefore, compared the distribution of CD9 and EGFR obtained from two-color and one-color imaging in PEC. The results from 2-color imaging are slightly different from the results from 1-color STORM measurements. This could be due to the fact that the background noise is higher for 2-color imaging. However, the cluster properties do not change significantly from one-color to two-color imaging experiments.

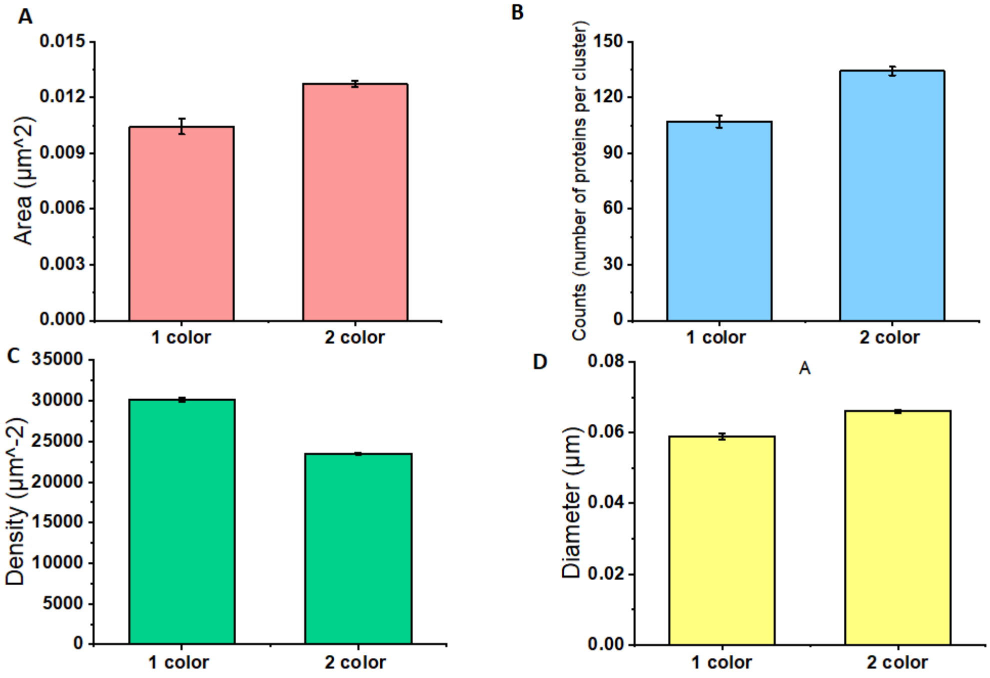

Figure 4.25: EGFR cluster analysis using SR-Tesselation method from 1-color and 2-color imaging data. Four main parameters are shown: (A) mean cluster area, (B) number of counts per cluster, (C) density of counts inside cluster, and (D) diameter of cluster.

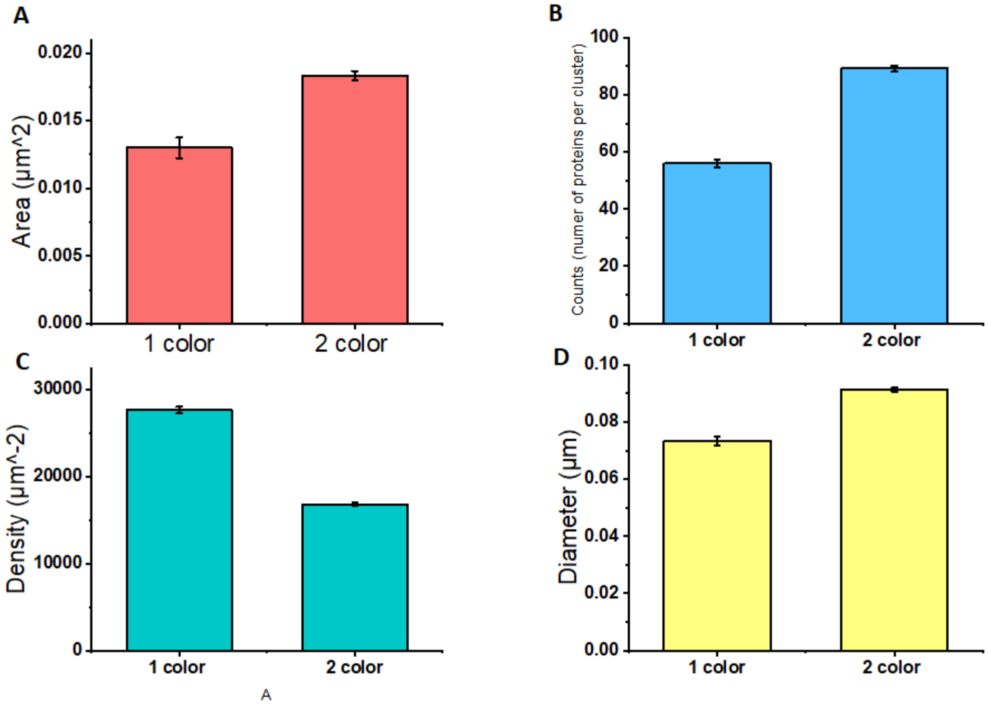

Figure 4.26: CD9 protein distribution analysis in 1-color and 2-color imaging, the clustering was analyzed by using the tessellation method. (A) cluster size, (B) number of counts per cluster (C) density of localizations per cluster and (D) diameter of cluster.

4.4 Discussion and Conclusion

In this chapter, we used STORM to study the organization of EGF receptors and CD9 in PEC and shCD9 PEC cells. In our experiments, we used both polyclonal secondary antibodies for higher signal and nanobodies as secondary antibodies to minimize the uncertainty in the number of fluorophores labeling each EGFR protein. We could thus check that both polyclonal and nanobody secondary antibodies gave similar results. For the analysis, we used the ThunderSTORM plug-in in Fiji to determine the molecule localization. The software provides multiple options for pre-processing and post-processing analysis. Using these pre-processing and post-processing steps, we can eliminate the artifacts created by the measurement that could interfere with the results. We varied the values of the different parameters in the pre-processing and post-processing steps to determine their effects on the results and identify the optimal values of these parameters. The tessellation method was then used to determine the protein clusters from the full set of data points after the molecule localization process. Even though the STORM technique faces difficulties due to problems such as mechanical drift, it is a powerful technique that provides resolution well beyond the limit of diffraction.

From one-color STORM experiments, the distributions of EGFR and CD9 were revealed. The EGF receptors are found to be localized mostly in nanodomains with a mean size of about 100 nm. In CD9-depleted PEC cells, EGFR is confined in nanodomains with a somewhat larger domain size than in PEC cells. Moreover, the absence of CD9 affects both the EGFR membrane organization and population. The number of EGF receptors per nanodomain decreases in shCD9 PEC cells compared to the wild-type PECs. Furthermore, the density of EGF receptors in the nanodomain as well as the average density in the whole-cell diminishes with the depletion of CD9. Similar to EGF receptors, CD9 are located mostly inside the clusters, with lower density than EGF receptors. Note that CD9 in PEC cells from healthy mice is expressed at lower levels than in PEC cells of disease mouse models [2].

Our interpretation of these results is that EGF receptors are, at least partly, confined in CD9 tetraspanin-enriched domains. When CD9 is depleted in shCD9 PEC cells, EGF receptors do not find the appropriate environment to insert themselves in the membrane and are present in lower numbers and density in the cell membrane. Moreover, the EGFR confining domains in shCD9 PEC cells are probably larger due to the much lower number of CD9 proteins available.

This result confirms the semi-quantitative finding of H. Lazareth et al. (2019) that the total population of EGFR and phosphorylated EGFR is lower in shCD9 PEC than in PEC. Indeed, our results also explain why the number of phosphorylated EGFR is lower in CD9-depleted PECs: there is a lower number of EGF receptors per cell, a lower number of EGF receptors in each confinement domain, and a lower density of EGFR inside each confinement cluster. When the number of EGF receptors in the cell membrane is lower, we expect the signaling to be less efficient. Moreover, the activation of EGFR takes place only after receptor dimerization. Therefore, a lower receptor density in the membrane confinement domains means that the dimerization process will be slower. Because EGF receptor activation leads to cell proliferation, cell migration, and cell death, this finding also explains why the course of RPGN improves after globally deleting CD9 in mice.

By using two-color STORM imaging, the relative distribution of EGFR and CD9 in the PEC membrane can be revealed. We find a partial overlap between EGFR and CD9 clusters. An uncertainty remains, however, because, in our analysis, the drift correction is done independently for the images of each color. Therefore, there is a non-zero displacement between the images of the two colors. To circumvent this problem, we introduced gold nanoparticles on the microscope slides as fiducial markers visible in the images of both colors. A thorough analysis of these latter results should confirm and quantify the degree of overlap between CD9 and EGFR clusters and our interpretation of why CD9 depletion affects the population and distribution of EGFR.

Chapter 5

Epidermal growth factor receptor tracking

Contents

> ”The monarchs that fly south will not make it back north. Each departure, then, is final. Only their children return; only the future revisits the past.”
>
> Ocean VUONG

Super-resolution microscopy techniques are powerful techniques for receptor localization and quantification. However, these techniques are more suitable for fixed samples and for non-dynamic systems. Single-molecule tracking is a complementary solution with respect to SMLM suitable for studying the dynamics of receptors in the cell membranes. Therefore, we used single-molecule tracking to investigate the behavior of epidermal growth factor receptors in three types of cells: Vascular smooth muscle cells (VSMC), Parietal epithelial cells (PEC), and short hairpin RNA CD9 parietal epithelial cells (shCD9 PEC). Several controversies have arisen in the field of receptor confinement in the cell membrane. Some of these controversies may be due to the fact that various research teams have worked on different cell types. Indeed, it is possible that the same receptor may be confined in different confinement domains depending on the cell type. Therefore, during my thesis, I investigated this possibility by the tracking of epidermal growth factors (EGFR) in different cell types. To study the nature of EGFR confinement, various treatments were used including disrupting raft domains by removing cholesterol or sphingomyelin lipids and preventing actin polymerization by treating cells with latrunculin B.

5.1 Single-Particle tracking of EGFR

5.1.1 Introduction

Figure 5.1 shows the pipeline of our single-particle tracking experiment and analysis. The details of the experiment and analysis will be discussed in the next section. In short, we used 30-nm europium-doped vanadate nanoparticles coupled to EGF to track EGFR in the MDCK, VSMC, PEC, and shCD9 PEC. The localization of the molecule in each frame is determined by fitting the PSF of the emission by a 2D Gaussian. The confined parts of the trajectory of EGFR are determined manually (in VSMC) or by a Gaussian Mixture Model (PEC and shCD9 PEC) and were then analyzed by Bayesian inference to get information about the diffusivity, the force acting on the receptors, and the confinement area. In addition, a new method was developed in collaboration with Yann LANOISELEE and Denis GREBENKOV to identify the parts of EGFR trajectories that are confined while also obtaining the information about the portions of free motion of the receptors. After splitting the trajectories into confined and free portions using this new algorithm, the confined portions were analyzed to extract the diffusion coefficient and the spring constant of a parabolic confining potential by using an MSD-based method.

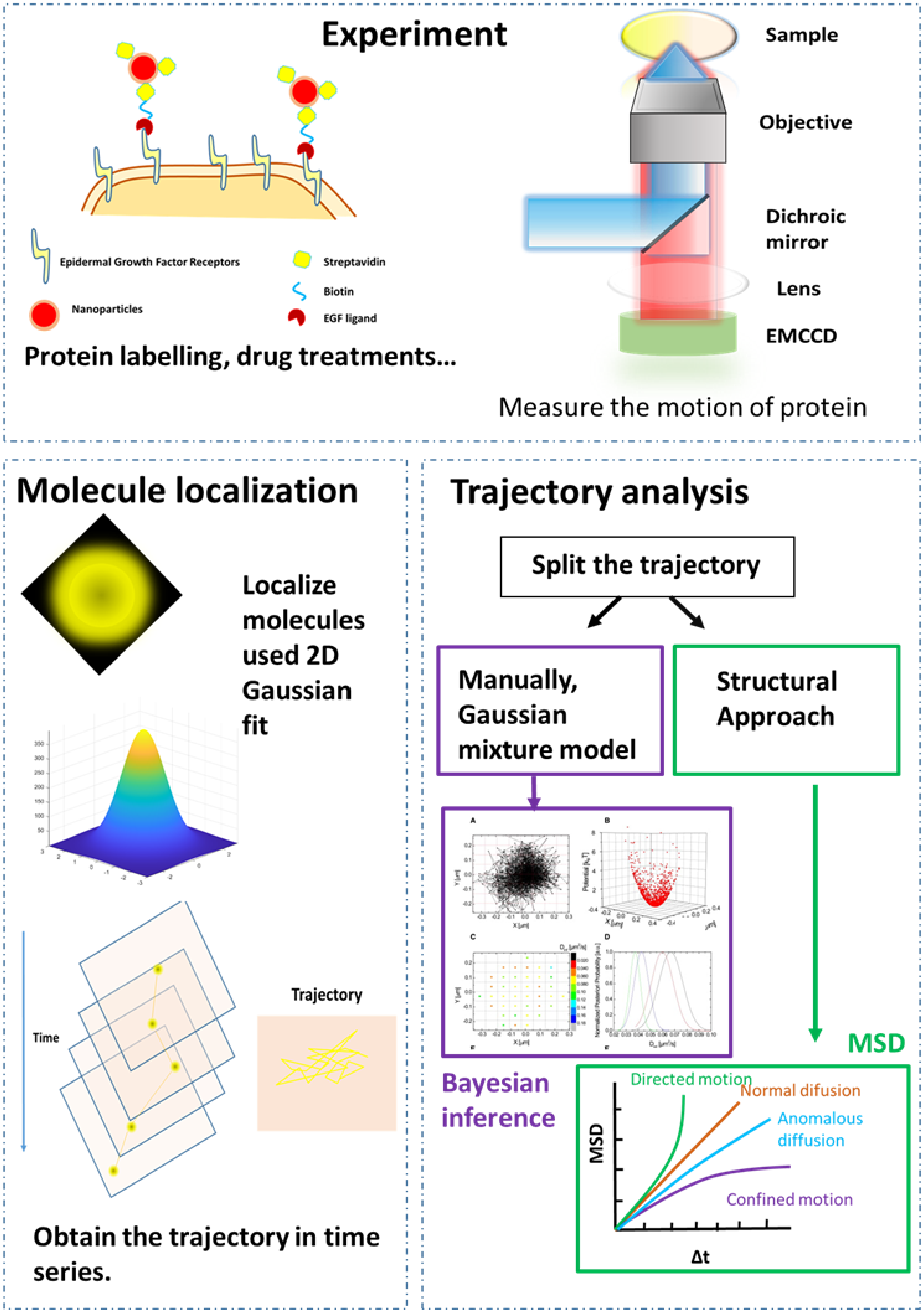

Figure 5.1: The pipeline of the EGFR single-particle tracking experiment and analysis.

5.1.2 EGFR Labeling

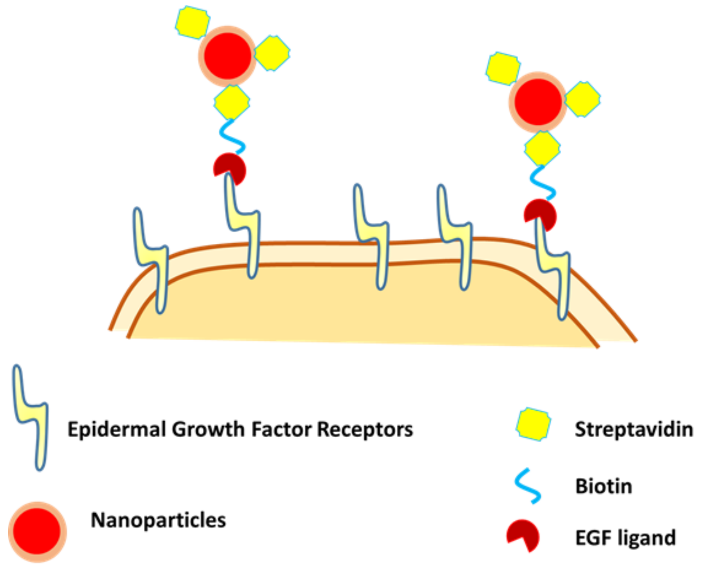

Figure 5.2: EGFR tracking scheme: The EGF receptors are tracked using labeling with NP-streptavidin conjugates bound to biotin-EGF.

Biotinylated epidermal growth factor (biotin-EGF) was incubated with europium-doped yttrium vanadate NPs conjugated with streptavidin (Figure 5.2). The coupling and tracking experimental details are discussed in Appendix A. The EGF-labeled europium nanoparticles were then incubated with cells to bind to EGF receptors. The incubation time was 15 minutes before washing the cells three times with imaging solution (HBBS+ 10% HEPES). During the tracking, the imaging solution was used to minimize the solution auto-fluorescence and to maintain a suitable pH for the cell environment. The ratio of streptavidin and NPs is 20:1, and the ratio of biotin-EGF per NPs is 3:1. The streptavidin to NPs ratio is high to fully cover the surface of NPs to avoid non-specific interactions with the cell membrane while the number of biotin-EGF per NP is lower to avoid cross-linking of proteins in the cell membrane.

5.1.3 Raft Destabilization

To understand the nature of EGFR confinement in VSMC, first, the raft was destabilized by using cholesterol oxidase to transform the cholesterol into cholestenone. Cholesterol oxidase is an enzyme that catalyzes the reaction between cholesterol and oxygen to cholest-4-en-3-one and hydrogen peroxide.

$$Cholesterol + O_2 \rightleftharpoons Cholesten - 4 - en - 3 - one + H_2O_2 \tag{5.1}$$

To understand the nature of EGFR confinement in VSMC, first, the raft was destabilized by using cholesterol oxidase to transform the cholesterol into cholestenone. Cholesterol oxidase is an enzyme that catalyzes the reaction between cholesterol and oxygen to cholest-4-en-3-one and hydrogen peroxide. The process of transformation from cholesterol to cholestenone is less harmful to the cell compared to other methods for cholesterol extraction such as cyclodextrin [246]. Even though using cholesterol oxidase is less efficient in disrupting the raft, it is sufficient to destabilize the highly compact raft by transforming cholesterol into cholestenone. In the experiments, the cells were incubated with 20U/mL cholesterol oxidase for 30 min at 37°C. In previous work, Türkan et al. [247] found that around 30% of the cell cholesterol is changed into cholestenone after applying this cholesterol oxidase concentration in MDCK cells. Moreover, about 90% of the cell's sterol is in the plasma membrane [248]. The removal of cholesterol in the cell membrane in these conditions was sufficient to disrupt raft domains.

The raft domains are also enriched in sphingolipids. Sphingolipids are involved in many cellular activities such as cell differentiation, cell proliferation or cell death [249–251]. Therefore, to examine whether sphingolipids affect the confinement of EGF receptors or not, we used sphingomyelinases to catalyze the hydrolysis of sphingomyelin into ceramide [252].

5.1.4 Actin skeleton disruption

Actin is the most abundant intracellular protein in eukaryotic cells. Actin makes up 10% by weight in muscle cells and about 1 to 5% in other cell types. The actin monomers that are globular monomers are called G-actin. G-actins can polymerize to form a linear polymeric microfilament called F-actin (filamentous). Actin is involved in many cell activities such as cell contraction, cell movement, intracellular transport/trafficking, cell shape change, cytokinesis, cytoplasmic streaming. Furthermore, actin was also found in interaction with receptors in the cell membrane and with the raft domains [1]. In different cell types, the structure of actin filaments is also different. Figure 5.3 shows the F-actin in MDCK, VSMC, and PEC. As expected from the function of the cells, in VSMC cells actin filaments are more organized than in MDCK and in PEC cells. This is due to the important functions of actin in defining cell shape and in implementing muscle contraction in muscle cells.

The polymerized actin is asymmetric, one end is called the pointed end and the other end is called the barbed end. The pointed end is where the leaving of monomers from the actin strand takes place while the barbed end is the end in the growth direction. When the rate of dissociation of monomers at the pointed end is higher than the association rate at the barbed end, the actin filaments are in depolymerization mode and vice-versa. In order to prevent actin polymerization, we used the toxin latrunculin B. Latrunculin B is known to bind to actin monomers and to prevent them from binding to the barbed end leading to actin depolymerization. Latrunculin B was kept in the imaging solution during the tracking process to prevent the actin re-polymerization process.

The effect of latrunculin B on the cell shape and size after 15 minutes of incubation is shown in Figure 5.4. After latrunculin B treatment, the cells contain fewer actin filaments leading to a size decrease. Moreover, the cells become more rounded after treatment. Note that the cell shape and size didn't change after cholesterol oxidase treatment.

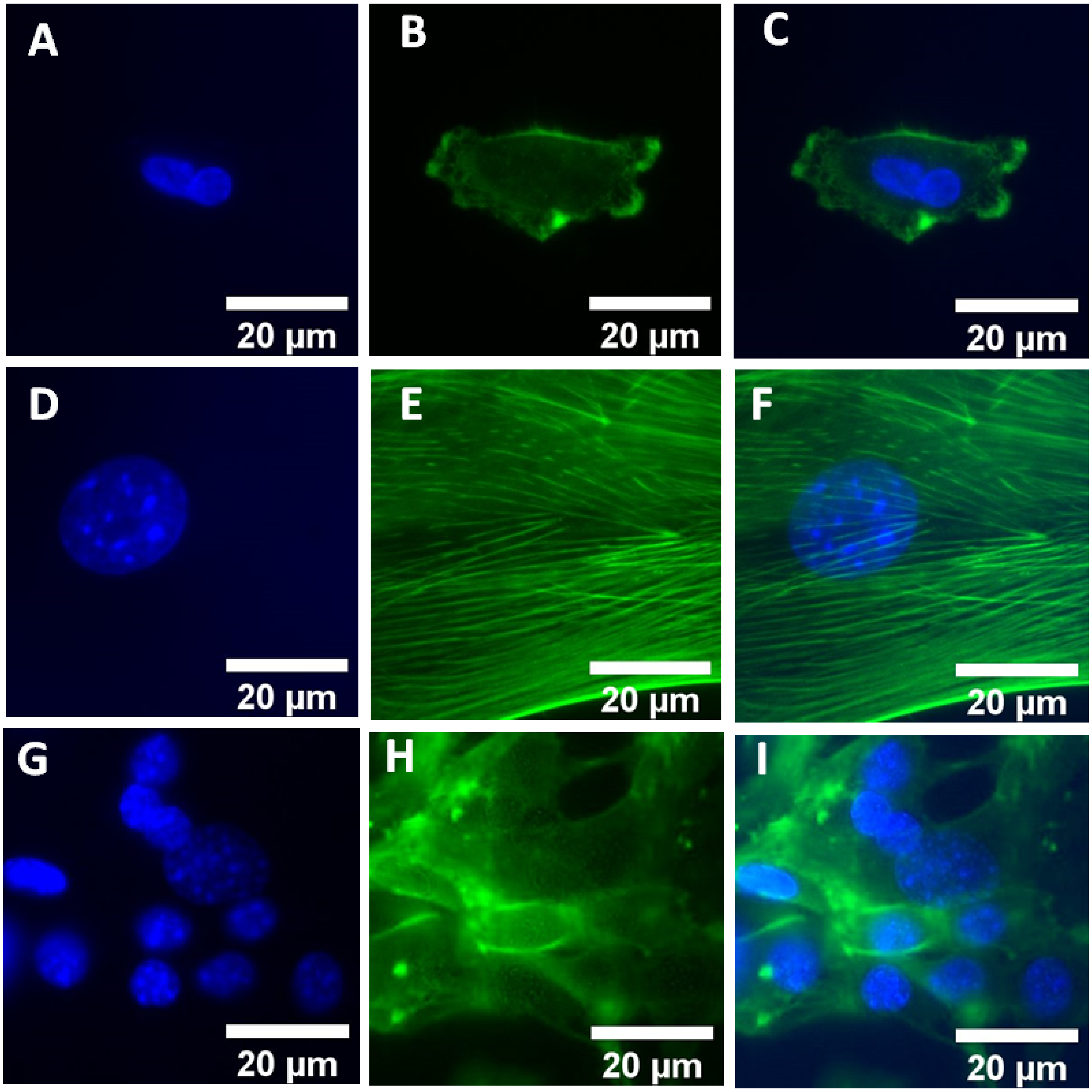

Figure 5.3: Actin skeleton network in MDCK, VSMC, and PEC. (A),(D),(G) The nucleus of MDCK, VSMC, and PEC cells, respectively. (B), (E), (H) Actin filaments of MDCK, VSMC, and PEC, respectively. (C), (F), (I) The overlap of images (A) and (B), images (D) and (E), images (G) and (H), respectively. The actin filaments were labeled with phalloidin and the nucleus was stained with DAPI. The images were taken using wide-field microscopy.

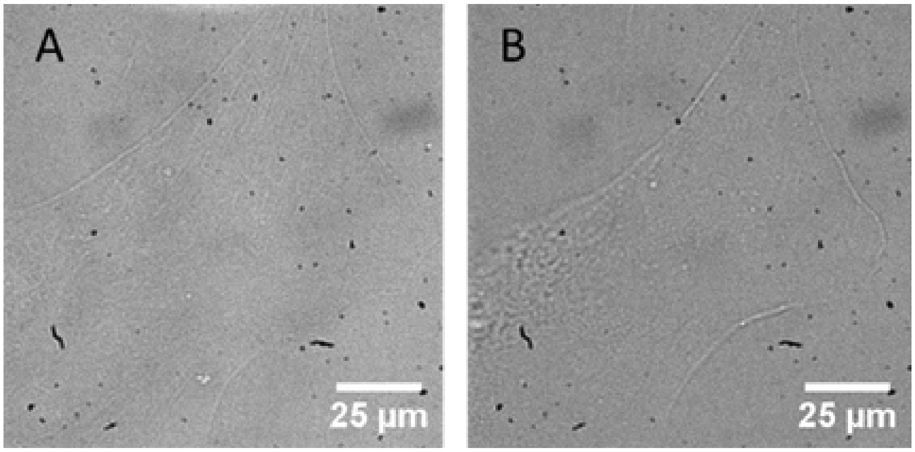

Figure 5.4: Effect of Latrunculin B treatment on a vascular smooth muscle cell (VSMC). (A) Cell before LatB treatment. (B) Same cell after 15 min of LatB treatment.

Typical trajectories for EGF receptors in VSMC are shown in figure 5.5 A. The trajectories were recorded at 37°C with an excitation intensity of 0.25 kW/cm^2 and an acquisition time of 51.3 ms (50 ms was used for photon acquisition and 1.3 ms for camera readout).

The EGF receptors are known for their important role in cell signaling and activation. It is believed that the confinement of these receptors in small domains favors their interactions and their dimerization process which is required for receptor activation. The difference in EGF receptor movements before and after drug treatments in VSMC is shown in Figure 5.5 B and C. Before drug treatment, receptors were observed to be confined in small domains without hopping outside the confinement domain while after drug treatment by cholesterol oxidase or latrunculin B, the receptors are still confined but in larger domains and start hopping from one domain to adjacent ones. They are seen to undergo free motion when they transition between two confinement domains. We first identified the confined trajectory portions manually and then analyzed them with Bayesian inference. Alternatively, in order to avoid manually deciding which portions are confined and which are free, we collaborated with Yann LANOISELEE and Denis GREBENKOV to develop an algorithm to split the trajectories into parts exhibiting confined motion and parts undergoing free motion.

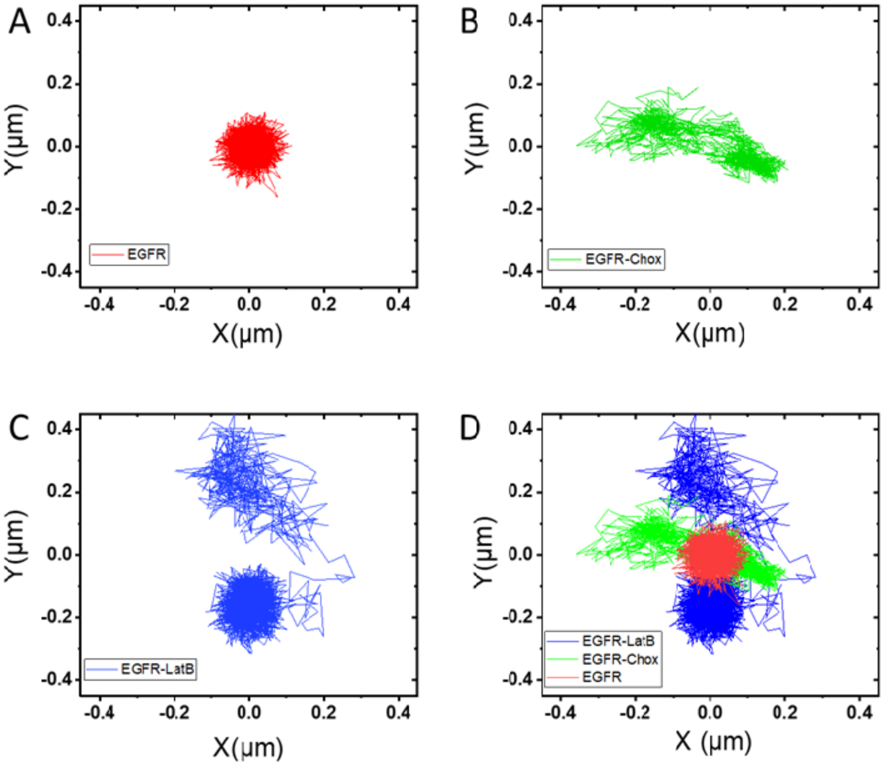

Figure 5.5: Typical EGFR trajectories in different conditions (A) The red trajectory is that of an EGFR in VSMC in normal conditions. (B) The green trajectory is the trajectory of an EGFR after 15 min incubation with cholesterol oxidase. (C) The blue trajectory shows the motion of an EGF receptor after incubating the cells with latrunculin B for 15 min. (D) Overlap of trajectories obtained in the three different conditions.

5.1.5 Analysis Methods

Baysian Inference technique

The Bayesian inference (BI) technique was adapted to the single-particle tracking field by Jean-Baptiste MASSON in collaboration with my team at LOB to extract parameters of motion inside confinement domains, including the receptor diffusion coefficient and the confining potential acting on the receptors [247]. Compared to the most popular methods based on the analysis of the Mean Square Displacement (MSD), Bayesian inference can extract more information about the confinement and be less biased. However, using BI as implemented in [247], we can only extract information from a confined trajectory portion but not for trajectories where the receptor alternates between free and confined motion. In single-molecule tracking experiments of membrane proteins, it is common to observe the hopping of the receptors between different confinement domains. Therefore, to use the Bayesian inference technique, we have to split the trajectory by clustering models such as K-means clustering or Gaussian Mixture Models. These techniques also cannot distinguish free-motion trajectory portions from confined portions but assign all the tracking points into different clusters. We therefore initially resorted to manual identification of the confined trajectory portions before implementing an automated technique developed by Yann LANOISELEE and Denis GREBENKOV.

In the framework of Bayesian inference, the receptor motion is assumed to follow the Langevin equation of motion:

$$\frac{d\mathbf{r}}{dt} = v, m\frac{d\mathbf{v}}{dt} = -\gamma\mathbf{v} - \nabla V(\mathbf{r}) + \sqrt{2D\gamma^2}\xi \tag{5.2}$$

Where $\gamma\mathbf{v}$ represents the friction term with γ, the friction coefficient, being related to the diffusion coefficient D by $\gamma = \frac{k_BT}{D}$, with k_BT being the thermal energy. The second term $\nabla V(r)$ is a force acting on the receptors due to an arbitrary potential $V(r)$. $\sqrt{2D\gamma^2}\xi$ is the noise term that leads to Brownian motion with diffusion coefficient D. The motions inside the cell membrane reach the equilibrium very fast in time scales on the order of attoseconds to picoseconds. Therefore, we assume the receptor motion is in the steady state condition with a constant velocity. Then $m\frac{dv}{dt} = 0$. Therefore, the velocity is rewritten as:

$$\mathbf{v} = -\frac{\nabla V(\mathbf{r})}{\gamma} + \sqrt{2D}\xi \tag{5.3}$$

The Fokker–Planck equation that describes the time evolution of the probability function $P(t)$of going from point (r_1,t_1) to point (r_2,t_2) is given by the following equation with $-\nabla V(r)$ being the force $\mathbf{F}$.

$$\partial_t P = -\frac{1}{\gamma}.(\mathbf{F}P) + D\Delta P \tag{5.4}$$

The equation can be solved to give the likelihood function, that is the probability to go from one space-time point (r_1, t_1) to the next point (r_2, t_2) as a function of D and **F**:

$$P(r_2, t_2|r_1, t_1) = \frac{exp(-\frac{(r_2-r_1-\mathbf{F}(t_2-t_1)/\gamma)^2}{4D(t_2-t_1)}}{4\pi D(t_2 - t_1)} \tag{5.5}$$

The trajectory being a series of consecutive points from (r_1, t_1) to (r_N, t_N), where N is the total number of trajectory points, the overall probability can be calculated by multiplying all the probabilities of the individual transitions from point (r_n, t_n) to (r_{n+1}, t_{n+1}). If D and F are known variables, we can calculate the probability of observing the trajectory T,P(T—D,**F**):

$$P(T|D, F) = \prod_{alltransitions} P(r_{n+1}, t_{n+1}, r_n, t_n) \tag{5.6}$$

We then invoke Bayes' theorem:

$$P(Q|T) = \frac{P(T|Q)P_0(Q)}{P_0(T)} \tag{5.7}$$

The Q variable represents D and F, T represents the trajectory. $P_0(Q)$ describes the prior knowledge about **F** and D, $P(Q|T)$ is the posteriori probability which is calculated from eq. (5.7). The $P_0(Q)$ is assumed to be constant for a reasonable range of values and be 0 outside of this zone. $P_0(T)$ is the probability of observing the trajectory T and is set to 1.

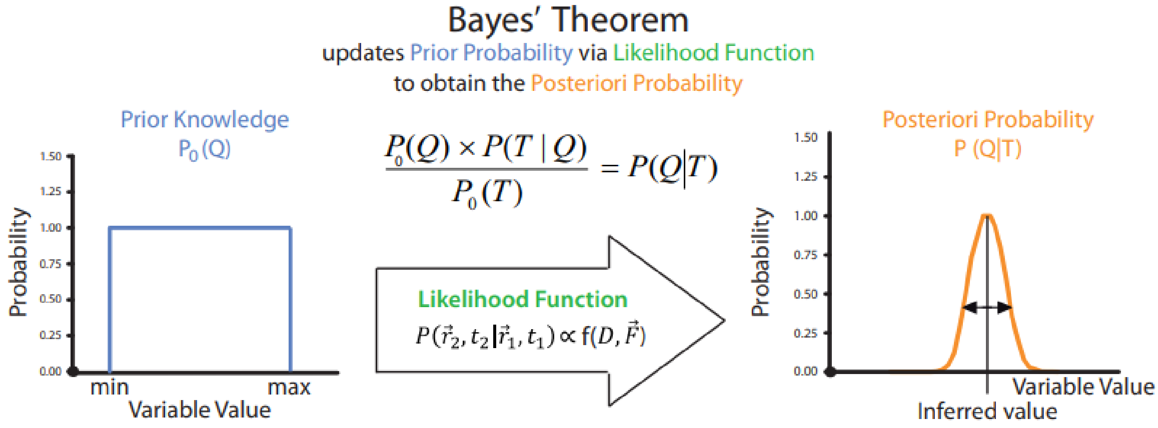

Figure 5.6: Bayes' theorem. The prior knowledge about the variable Q, $P_0(Q)$, is updated via the likelihood function $P(T|Q)$. $P(Q|T)$ is the posteriori probability and is calculated as the product of the likelihood $P(T|Q)$ with the prior distribution $P_0(Q)$ and divided by the known evidence $P_0(T)$. $P_0(Q)$ is equal to 1 in a reasonable variable value range and takes on the value of 0 elsewhere. The inferred variable value is the peak of the posteriori probability. Figure from [247].

The inferred values for the variables are taken to achieve the maximum value of the posteriori probability (MAP). We used a Quasi-Newtonian optimization with Broyden-Fletcher-Goldfarb-Shanno algorithm to optimize the maximum value of the posteriori probability. A Monte-Carlo exploration of the posteriori probability around the maximum value yields the width of the posteriori distribution. The width of the distribution yields the uncertainty of the inferred value (Figure 5.6).

Note that the solution of the Fokker-Planck equation in the form of eq. (5.5) is valid only if the force F can be considered constant. Therefore, the trajectory area is divided into small subdomains so that the force can be considered to be constant in each subdomain (Figure 5.6 A). We typically divide the trajectories in our analysis into 8x8 grids. The number of subdomains is chosen to be not too small so that the number of trajectory points inside one subdomain is high enough to contain enough information to be analyzed and yield inferred values with reasonably low uncertainty. There are two ways to determine the force acting on the receptors. In the first method, the force inside each subdomain is calculated separately. In this case, the inferred force parameters are the variables F^x_{ij} and F^y_{ij} for all subdomains ij. A polynomial fit can then be used to describe the confinement potential inside the whole domain (Figure 5.7 E). The second method is to consider the potential of the whole domain as a polynomial (Figure 5.7 B). The potential can be chosen to be a 2nd, 3rd, or 4th polynomial. We used 2nd order polynomials to analyze the trajectories of EGF receptors in VSMC, PEC, and shCD9 PEC. Indeed after checking with the experimental data, we found an insignificant difference of results when using 2nd or 4th order polynomials. The 4th order potential can be used for receptors in picket-and-fence confinement domains such as transferrin receptors [1]. The form of the 2nd order potential used in all the analyses is shown in the following equation:

$$V_{2^{nd}order} = C + C_x x + C_y y + C_{xx} x^2 + C_{xy} xy + C_{yy} y^2 \tag{5.8}$$

In this case, the inferred force parameters are C_x, C_y, $C_x y$, $C_x x$ and $C_y y$. The first order coefficient C_x and C_y are negligible compared to the 2nd order terms. The inferred potential can thus be rewritten as:

$$V_{2^{nd}order} = C_{xx} x^2 + C_{xy} + C_{yy} y^2 \tag{5.9}$$

and can then be diagonalized to yield: $V_{2^{nd}order} = \frac{1}{2} k_x x^2 + \frac{1}{2} k_y y^2$ where the spring constant of k_x and k_y in the x and y directions equals $2C_{xx}$ and $2C_{yy}$, respectively. Because the trajectories are nearly isotropic, the k_x and k_y values are similar. Therefore, we can characterize the potential by a spring constant k: $k_r = \sqrt{(k_x^2 + k_y^2)}$.

The diffusion coefficient is considered constant inside the different subdomains because the diffusion coefficients D_{ij} in each subdomain do not vary strongly [247].

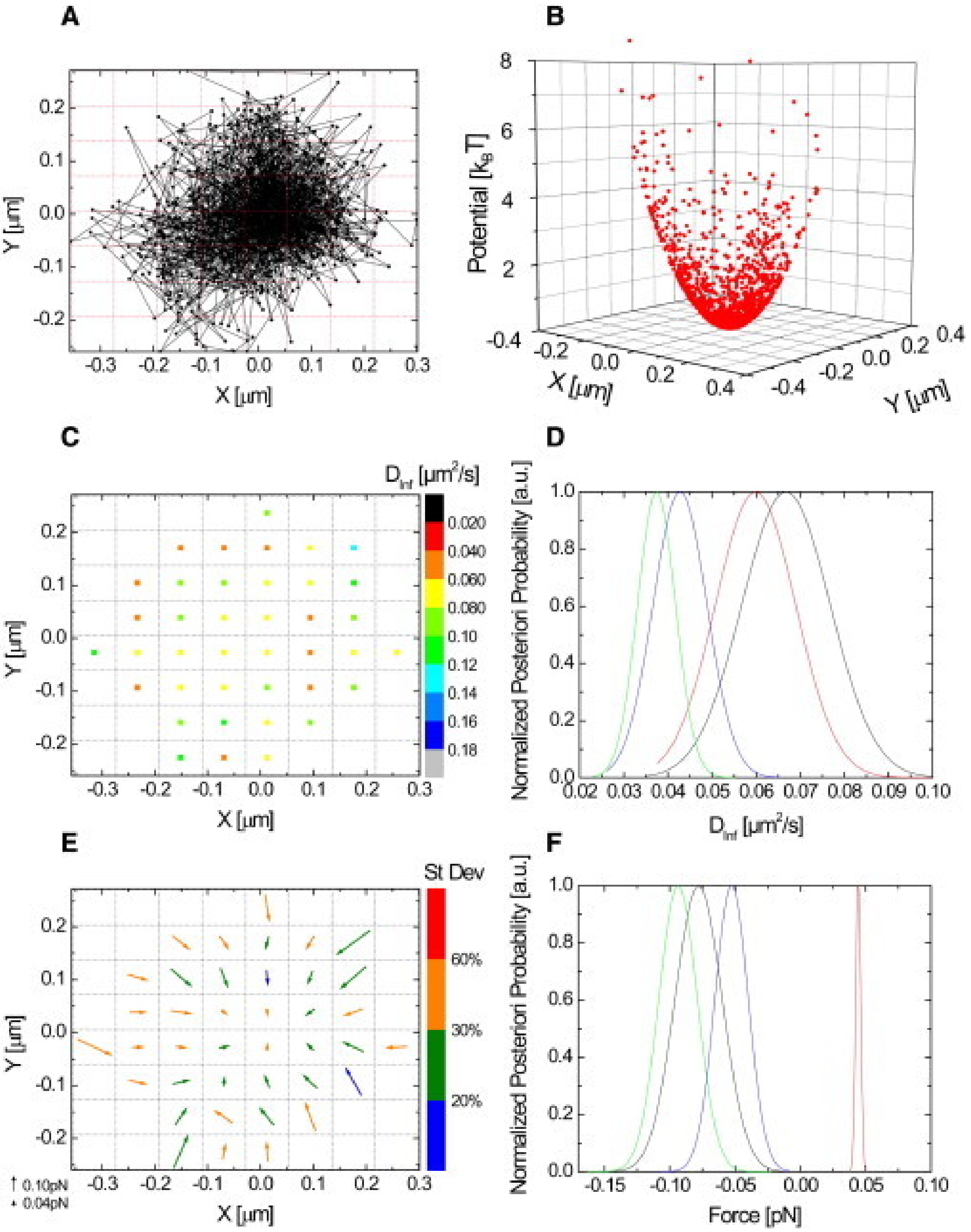

Figure 5.7: Bayesian Inference of a confining potential from a receptor trajectory. (A) The trajectory of CPϵT toxin receptor in an MDCK cell in a subdomain grid (8x8). (B) The inferred second-order potential, (C) the map of inferred diffusion coefficient values in each subdomain, (E) the inferred forces in each subdomain: the length of the arrow indicates the strength of the force and the color code of the arrows refers to the corresponding standard deviation obtained from the posteriori probability distribution. (D, F) Four representative posteriori probabilities for the diffusivities in (D), and the forces of four different subdomains, respectively. Figure from [247]

5.1.6 Detection of transient trapping by a structural approach

This approach was dabbed structural approach because it analyzes the spatial and temporal structure of the trajectory. The first step in the trajectory analysis is to split the trajectory into confined and free portions [253]. First, the distances from one point to another in the trajectory were calculated to establish a distance matrix. The matrix elements are calculated from the trajectory coordinate of the tracking trajectory as shown in equation 5.10.

$$M(i,j) = exp(-\frac{1}{2}(\frac{|r_i - r_j|}{\lambda})^2) \tag{5.10}$$

Where $|r_i - r_j|$ is the distance between two points in the trajectories, λ is the characteristic confinement length scale, and r_i and r_j are the coordinates of the trajectory points in 2D in our case. So if

$$|r_i - r_j| >> \lambda => M(i,j) \approx 0$$

while

$$|r_i - r_j| < \lambda => M(i,j) \approx 1$$

To remove the noise from the matrix M_{ij}, the matrix M is locally smoothed by convolving M with a normalized and constant square matrix $(2\mu+1)\times(2\mu+1)$, where μ is the smoothing parameter, through FFT (Figure 5.8 B), a typical value of μ being 2. The matrix M after the smoothing process is transformed into a binary matrix B by setting the matrix value equal to 1 when the values are bigger than a threshold value p_c and equal to 0 otherwise (Figure 5.8 C). We used $p_c = \exp^{-1}$ which means that two points of the trajectory are considered to be confined inside the same confinement domain if the distance between them is smaller than $\lambda\sqrt{2}$.

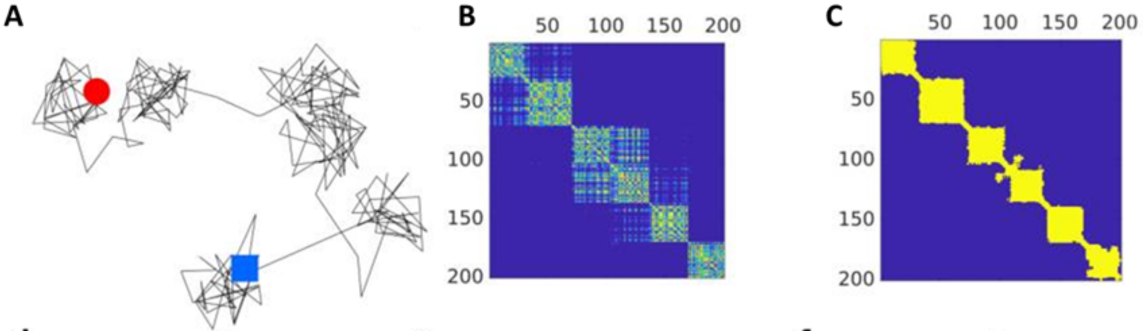

Figure 5.8: (A) Simulated 2D trajectory where the motion alternates between confined and free Brownian motion. (B) The distance matrix was created from the trajectory in (A). (C) The binary matrix was created by convolving the distance matrix with a normalized and constant square 5×5 matrix and by then applying a threshold to the matrix values. Figure extracted from [253]

In this matrix, confinement during a certain duration appears as a block across the diagonal of the matrix. Therefore, identifying a trapping event is based on identifying the presence of a block (Figure 5.8 C). A new methodology for detecting the block structure was introduced [253]. To define the trapped and the free part of the trajectory, the algorithm is based on equality observed inside a block as described below. To know if any point in the trajectory $n \in [1, .., N]$ belongs to a block or not, three parameters were constructed from the diagonal binary matrix B (Figure 5.9 A). The first parameter $l_|(n)$ is the block time, which is the approximate trapping duration seen from each $n-th$ trajectory point n. The second parameter $l_\perp(n)$ is the neighboring time, which is perpendicular to the diagonal inside the block of 1-values. The last parameter $l_{||}(n)$ is the persistence time which is parallel to the block matrix diagonal and starts from the extremity of the segment of the neighboring time $l_\perp(n)$ (see Figure 5.9 A).

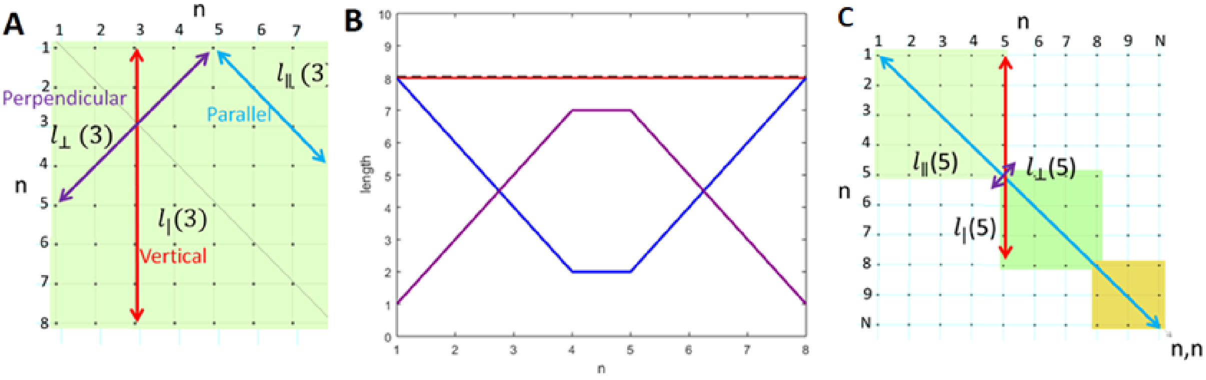

Figure 5.9: Block identification as computed in an ideal matrix of a fully trapped trajectory with only 8 points. (A) Illustration of a block time at trajectory point n = 3 with $l_|(3)$ in red, the neighboring time $l_\perp(3)$ in purple and the persistence time $l_{||}(3)$ in cyan. (B) The illustration of the equality along the diagonal of the binary matrix B_{88} for a perfect confined trajectory. (C) The binary matrix of a trajectory with three different confining domains. The equality inside the block is broken at the transition point as the persistence time takes on the value of the diagonal for the whole trajectory. Figure extracted from [253].

In ideal cases, when we assume that the trajectory is confined in only one domain without any hopping, the recurrence matrix will be a square (NxN) matrix with all the matrix elements in one block of 1. From these three parameters, an invariant quantity that is valid for any point along the matrix diagonal can be deduced as:

$$v(n) = \frac{l_|(n)}{l_{||}(n) + l_\perp(n) - 1} = 1 \tag{5.11}$$

Figure 5.9 B illustrates the equality $v(n) = 1$. This equality is an essential condition to determine if the point n belongs to a block or not. In the case of a transition between one block to another, the equality is broken at the transition point (Figure 5.9 C).

To illustrate how the invariance is broken outside blocks, we assume the extreme case of transition where there is only one transition point n between two successive matrix blocks. In this case, the transition point n will lie on the matrix diagonal. At the ending point of the first trapping block n-1 and the transition point n, there is a sharp transition between $v(n-1) = 1$ in block 1 to $v(n+1) = 1/N$ in block 2 as shown in Figure 5.9 C. Given that the total trajectory with steps N has a bigger size than the size of the two blocks (including the transition point n in the special case) $N > s_1 + s_2$, at the transition point n, the equality inside the block is broken. Indeed, the $l_{||}$ increases from $s_1 - 2$ to N while $l_{|}$ increases only from s_1 to $s_1 + s_2 - 1$ and does not compensate the increase of $l_{||}$ in the numerator.

To obtain a better visualization of the block time parameters, the values of these parameters were computed from the binary matrix in Figure 5.8 C. Because the block in practice never has a perfect square shape, we choose a $v(n)$ threshold value equal to 0.75 rather than 1. By applying a threshold value for $v(n)$, we can determine free and confined portions of the trajectory (Figure 5.10 B,C). In experimental conditions, because of the random nature of receptor motion, there are lacunarities inside the blocks. These lacunarities can make the invariant change inside the block. Therefore, these holes are filled.

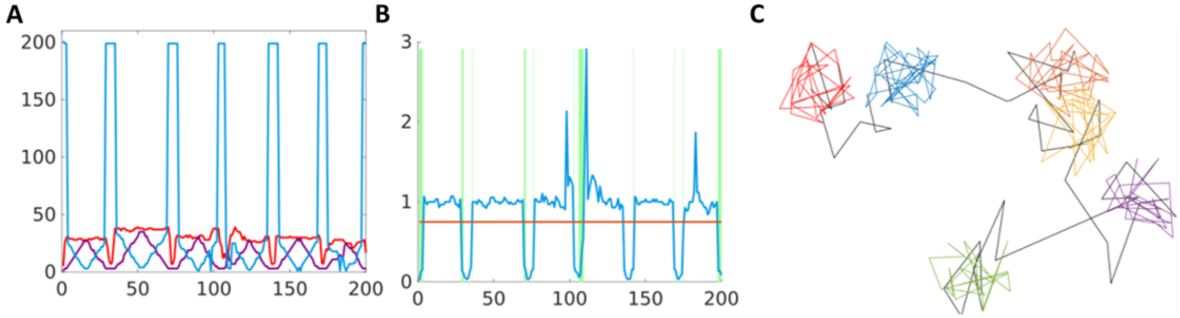

Figure 5.10: (A) The computed values of the three measures $l_{|}$ (red), $l_{\perp}$ (purple) and $l_{|}|$ (cyan) from the binary matrix of the trajectory shown in (C). (B) Calculated values of $v(n)$ as a function of n (cyan). $v(n)$ fluctuates close to 1 inside the trapping blocks and drops dramatically outside the blocks. The threshold value for $v(n)$ to determine the trapped and free portions is shown as a red line at $v(n) = 0.75$. (C) The split trajectory where black color represents the transient free parts and other colors represent the trapped portions.

We then used the time-averaged mean square displacement (TAMSD) curve, often called simply mean square displacement curve, to calculate the diffusion coefficient and the harmonic potential acting inside the trapping domain. The mean square displacement for the trapped portions of the trajectory is calculated:

$$\delta^2(\Delta, t) = \frac{1}{N - \Delta} \sum_{n=1}^{N-\Delta} (x(n + \Delta) - x(n))^2 \tag{5.12}$$

where Δ is the time interval considered.

Considering Brownian motion of the receptor inside a parabolic potential, the receptor motion can be described as:

$$dx = -lxdt + \sqrt{2D}dW_t \tag{5.13}$$

with the first term being the force term and the second the Brownian motion term, where the mean inversion time l is used to characterize the parabolic potential instead of the stiffness k and is related to k by $l = \frac{k}{\gamma} = \frac{kD}{k_B T}$.

In this case, the TAMSD can be described by the equation [254]:

$$< \delta^2(\Delta) >= \frac{2}{l} D[1 - \exp(-\Delta l)] \tag{5.14}$$

The mean reversion time $1/l$ of the harmonic potential and the diffusion coefficient can be deduced by fitting the MSD curve. Then the potential stiffness k can be calculated [254]:

$$k = \frac{l k_B T}{D} \tag{5.15}$$

The team's previous work has shown that the confinement potential inside raft domains in the case of ϵ-toxin and α-toxin receptors is parabolic [255] as well as in the case of EGFR in MDCK cells [1]. We, therefore, assume here also a parabolic confinement potential. This was confirmed by Bayesian inference analysis showing that a fourth-order confinement potential does not provide an improved description of the confinement potential as discussed above.

5.2 Tracking results in VSMC and MDCK cells

5.2.1 EGFR tracking in MDCK cells

In previous work done by Chao Yu, EGF receptors in MDCK were found to be located in cholesterol-enriched nanodomains [1]. To further examine if the domain is also enriched in sphingomyelin or not, we labeled EGF receptors with nanoparticles and applied the enzyme sphingomyelinase to remove sphingomyelin. When doing the tracking experiments, we observed that the number of labeled receptors diminishes significantly after applying sphingomyelinase.

To obtain the number of nanoparticles labeling receptors, first, I thresholded the image manually with the same threshold for all images. Then the number of nanoparticles was counted using the "Analyze Particles" tool in ImageJ [256].

The cell membrane area then was determined by using a plug-in of Fiji: Trainable Weka segmentation [257] (Figure 1.16).

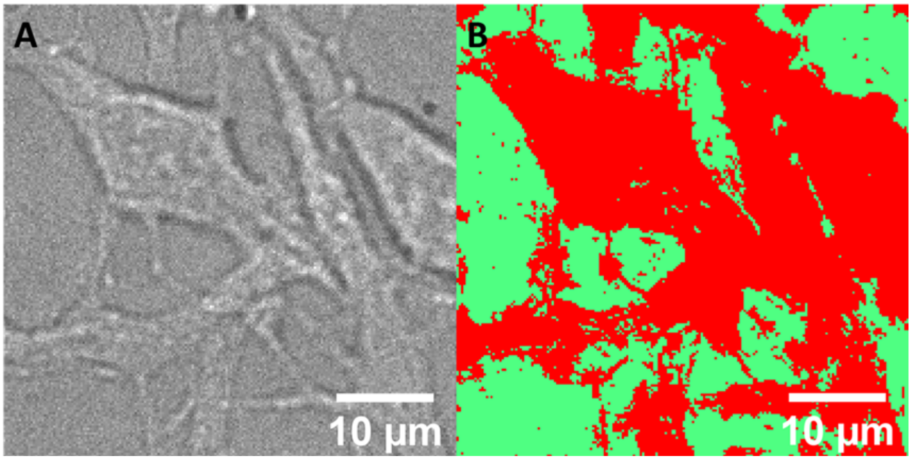

Figure 5.11: Cell segmentation: (A) Bright-field image of parietal epithelial cells. (B) Binary image of the segmented cell area (red) and background (green).

Figure 5.12 shows the number of nanoparticles per cell area in MDCK. The results were averaged from two different days of experiments. To confirm that the reduction of the number of nanoparticles labeling receptors was truly due to the sphingomyelinase treatment, different orders of sphingomyelinase treatment were performed. For the control experiment, we incubated nanoparticles bound to EGF to recognize EGF receptors without any addition of sphingomyelinase. In the first experiment with sphingomyelinase treatment, the experiment was done similarly to the control tracking experiment. The cells were first incubated for 15 min with nanoparticles then after washing three times with the imaging medium, they are incubated for 15 min with sphingomyelinase. We can see from Figure 5.12 that the number of nanoparticles labeling receptors on the cell membrane drops about 10 times after applying sphingomyelinase from 0.011± 0.001 μm^{-2} to 0.0015± 0.0003μm^{-2}. In the second experiment, the sphingomyelinase was first incubated with the cells to disrupt the rafts, then the nanoparticles bound to EGF were incubated with the cells to bind to EGF receptors. In the second case, the number of labeled receptors also decreases drastically down to 0.001± 0.0002 μm^{-2}. The results of these two experiments with sphingomyelinase treatment were not significantly different. This confirmed that EGF receptors in MDCK cells are located in raft nanodomains enriched both in cholesterol [1] and in sphingomyelin. Our interpretation of the strong decrease of observable EGF receptors, in this case, is that after raft disruption that receptors cannot find the appropriate environment in the cell membrane and are therefore internalized and degraded.

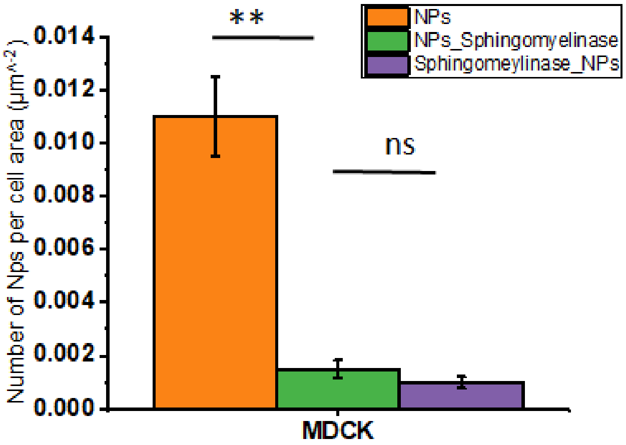

Figure 5.12: Number of NPs labeling EGFR on the cell membrane without and with sphingomyelynase treatment in MDCK cells. **:$P < 0.01, ns : P > 0.05$

5.2.2 EGFR tracking in VSMC cells

The initial analysis of the receptor trajectories was done by using Bayesian Inference, the trajectories were split manually and then analyzed with Bayesian inference. From Bayesian Inference, the diffusion coefficient and the stiffness of a harmonic confining potential are extracted. The domain size of receptors is determined by a circular domain with a radius that contains 95% of all the trajectory points.

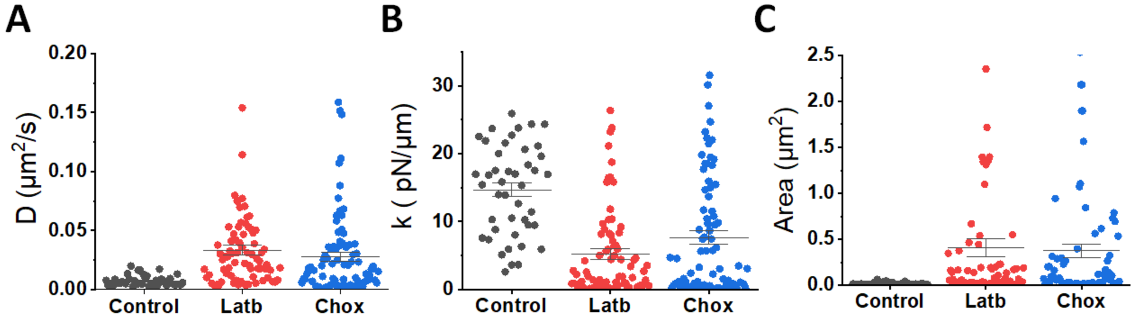

Figure 5.13: Effect of cholesterol depletion and actin depolymerisation on the movement of EGF receptors in vascular smooth muscle cells. The analysis was done by Bayesian Inference. (A) Diffusion coefficient of EGF receptors (B) spring constant and (C) area of confinement domain.

Cholesterol Depletion

In VSMC, the diffusion coefficients of EGF receptors increase after extraction of cholesterol oxidase and depolymerization of actin filaments.

The **diffusion coefficients** increase from 0.0072 ± 0.0006 $\mu m^2/s$ to 0.028 ± 0.004 $\mu m^2/s$ after treating the cells for 15 minutes with 20 U/mL cholesterol oxidase. The diffusion coefficients of receptors increase with the level of cholesterol extraction [255]. The more cholesterol is removed from the cell membrane, the less compact the confining domain and the larger the diffusion coefficients are expected to be. As a reference, around 27% of cholesterol was removed by treating MDCK cells for 15 minutes with 20 U/mL cholesterol oxidase. The distributions of the diffusion coefficients of receptors are compared by using the t-test: the obtained p-value equals 10^{-6} that is much smaller than the threshold p-value of 0.05. The diffusion coefficients increase by a factor of 3.8 after applying cholesterol oxidase.

The **spring constant** that is extracted from the second-order confining potential also shows that the confinement of receptors reduces dramatically after cholesterol extraction. The stiffness reduces from 14.6 ± 1.1 pN/µm^2 to 6.9 ± 0.9 pN/µm^2. The p-value of the student t-test of 3.5x10^{-7} is much lower than the threshold p-value. The k-value decreases 53% after cholesterol removal.

The **area** of the confinement domains also increases significantly after cholesterol removal. The domain size of EGF receptors increases from 0.018 ± 0.002 μm^2 to 0.37 ± 0.08 μm^2. The shapes of the receptor confinement domains change slightly after cholesterol oxidase treatment and the receptors also hop from one domain to other domains. The t-test gives a p-value of 0.001 that is below the threshold p-value of 0.05. The average domain size increases by a factor of 20.1 after cholesterol oxidation.

The effect of cholesterol oxidation on the confinement of EGF receptors in VSMC is found to agree with the results obtained by tracking EGF receptors in MDCK cells [1]. This result indicates that EGF receptors reside in cholesterol-rich domains, most probably rafts. To confirm that these domains are indeed cholesterol- and sphingomyelin-rich domains, i.e. rafts, experiments with sphingomyelinase treatment need to be performed.

Note that the experiments were done on different days with different batches of cells. Because of the vulnerability of VSMC, the experiments were not performed on the same coverslip. The results of two different days were combined for each experimental condition. The t-test found no significant difference in results obtained on different days of the experiment for each condition.

Actin Depolymerization

To confirm whether EGF receptors in vascular smooth muscle cells are tethered to actin filaments or not, we used latrunculin B to depolymerize the actin filaments.

Our results show that, in VSMC, the actin cytoskeleton is also involved in the confinement of EGF receptors. The **diffusion coefficient** of EGF receptors increases from 0.0072 ± 0.0006 $\mu m^2/s$ to 0.033± 0.004 $\mu m^2/s$, while **stiffness of the harmonic potential k** decreases by 65% from 14.6 ± 1.1 $pN/\mu m^2$ to 5.12 ± 0.74 $pN/\mu m^2$ and the **area** increases from 0.018 ± 0.002 μm^2 to 0.41 ± 0.09 μm^2.

Comparison between the structural/MSD analysis and the Bayesian inference analysis

We compare the results obtained by Bayesian Inference (BI) and by the structural approach (SA) followed by MSD analysis. The tracking results for EGFR in VSMC cells analyzed by the two methods are summarized in Table 5.1. Both methods give similar results for the diffusion and the spring constant of EGFR in VSMC.

Figure 5.14 shows the diffusion coefficient and the spring constant obtained by the structural approach. We can see that the diffusion coefficient increases when we applied latrunculin B or cholesterol oxidase to the cells while the spring constant decreases significantly after the drug treatments.

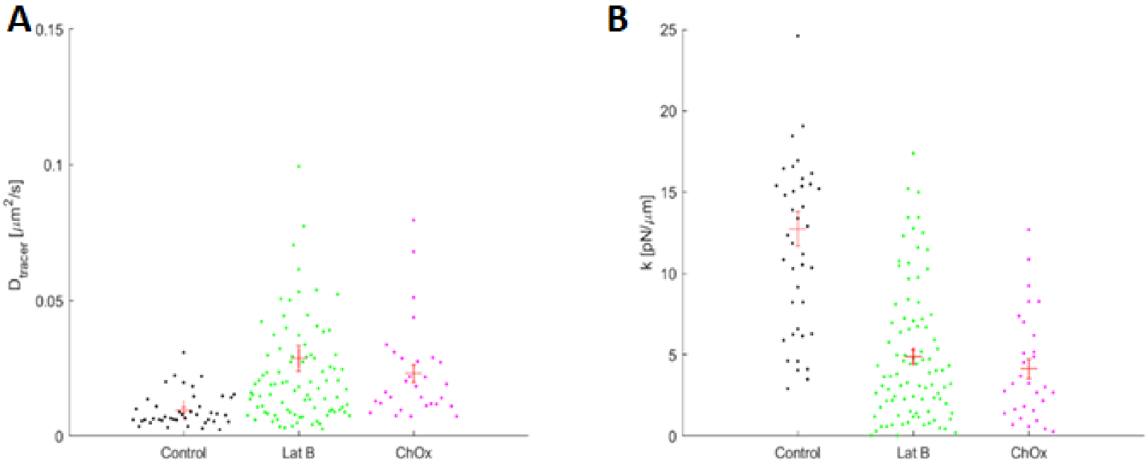

Figure 5.14: Single-particle tracking analysis by the structural approach for the same trajectories as in Figure 5.13. Effect of cholesterol depletion and actin depolymerization on the movement of EGF receptors in vascular smooth muscle cells. The spring constant k was calculated for the trapped portions. The results were obtained for $\lambda = 2.5$ and adjacent domains were merged when the trapped portions overlap by 70% or more. (A) Diffusion coefficient of EGF receptors, (B) spring constant.

By using the structural approach, we can extract information about the confinement time and free time of receptors in the cell membrane. The portion of confinement and free time is shown in Figure 5.15. In the control cells, most of the time (99.6%), receptors stay in the same confinement domain. When using drugs to disrupt the raft domain or depolymerize the actin cytoskeleton, receptors explore the membrane outside confining domains more than in the control case. After latrunculin B treatment, the receptors move freely during 9.6 % of the time. When the confining domains of cells were disrupted by cholesterol oxidase, the receptors spend around 17% of their time outside confinement domains. Note that these percentages cannot be directly compared because the durations of free and trapped portions depend on the percentage of actin cytoskeleton depolymerization and cholesterol removal.

The tracking EGF receptors in VSMC agree with the tracking results of EGF receptors in MDCK cells after applying the latrunculin B and cholesterol oxidase.

EGFR	Analysis	D ($\mu m^2/s$)	k ($pN/\mu m$)	A (μm^2)	T.P (%)
Control (N=49)	BI	0.0072 ± 0.0006	14.6 ± 1.1	0.018 ± 0.002	nd
	SA	0.0070 ± 0.0009	12.730 ± 0.969	nd	98.6
Latb (N=77)	BI	0.033± 0.004	5.12 ± 0.74	0.41 ± 0.09	nd
	SA	0.029 ± 0.005	4.894 ± 0.466	nd	90.4
Chox (N=86)	BI	0.028 ± 0.004	6.9 ± 0.9	0.37 ± 0.08	nd
	SA	0.023 ± 0.002	4.124 ± 0.355	nd	83

BI: anaysis done by Bayesian inference; SA: analysis done by structural approach and MSD, D: Diffusion coefficient, k: spring constant, A: Area, T.P: Trapped portion.

Table 5.1: EGFR confinement analysis by Bayesian inference and structural approach followed by MSD analysis in VSMC cells.

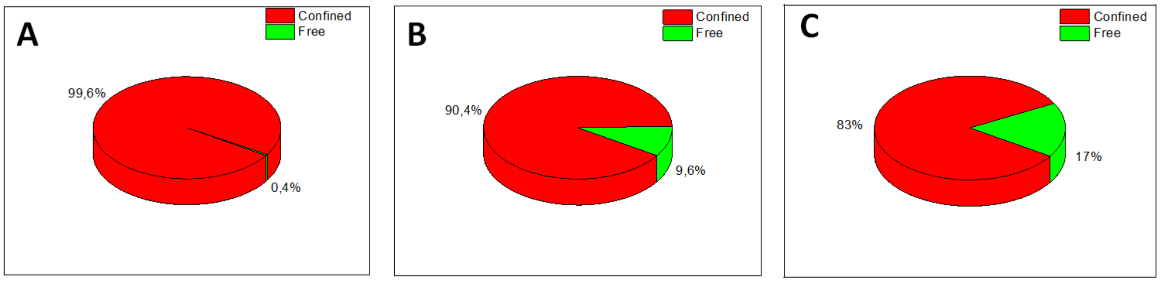

Figure 5.15: Free and trapped portion of EGFR in (A) control VSMC cells, (B) cells with latruculin B treatment and (C) cells with cholesterol oxidase treatment.

Furthermore, in recent work, C. Yu et al. tracked EGF receptors in MDCK under an external flow force in a microchannel [1]. The receptors moved in the force flow direction where the magnitude of the displacement depended on the magnitude of the applied force. The EGF receptors are believed to move while creating an elastic deformation. When the external force stops, the receptor comes back close to the initial position. By modeling the confinement of the receptors with an elastic behavior, the elastic spring constant was calculated by Hooke's law:

$$F = -k.\delta x. \tag{5.16}$$

Moreover, Chao Yu also found that EGF receptor elasticity originates from the direct binding between EGF receptors and the actin cytoskeleton. When latrunculin B was applied, the spring constant decreased significantly from 1.4 ± 0.1 pN/µm to 0.22 ± 0.04 pN/µm [1].

Based on our results, Figure 5.17 proposes a model that describes the confinement nature of EGF receptors in vascular smooth muscle cells and MDCK. The EGF receptors reside in raft domains enriched in cholesterol and sphingolipids. They also bind directly to the actin cytoskeleton via their actin-binding domain. Figure 5.17 B shows the effect of actin

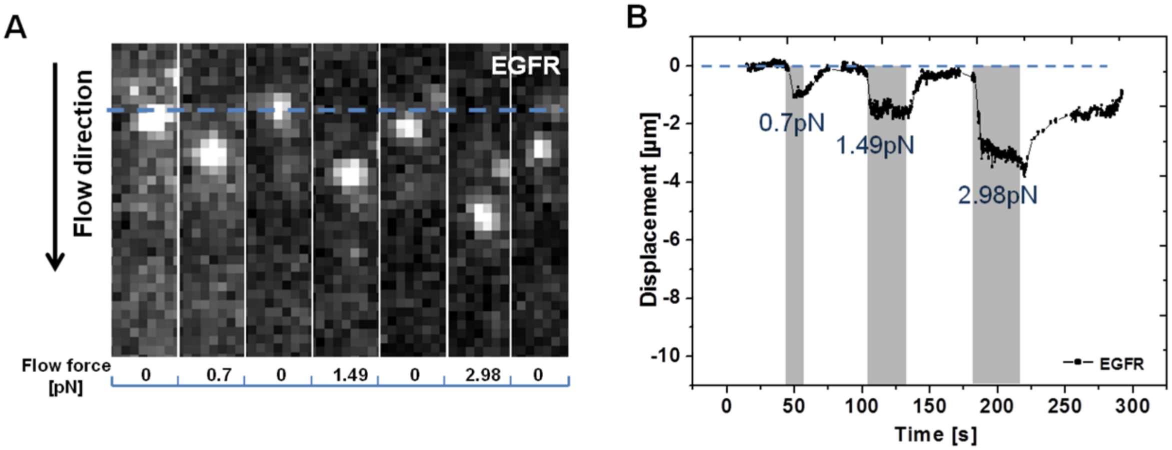

Figure 5.16: (A) The EGFR displacement under a microfluidic flow creating a force that displaces the receptor. (B) The displacement process of EGFR is an elastic behavior. The receptor moved further under larger flow force values. The forces exerted on the receptor were estimated to be 0.7 pN at 5 μL/min flow rate), 1.49 pN at 10 μ L/min flow rate, and 2.98 pN at 20 μ L/min flow rate, respectively. The receptor then comes back close to its initial position after the flow stops. Figure extracted from [1].

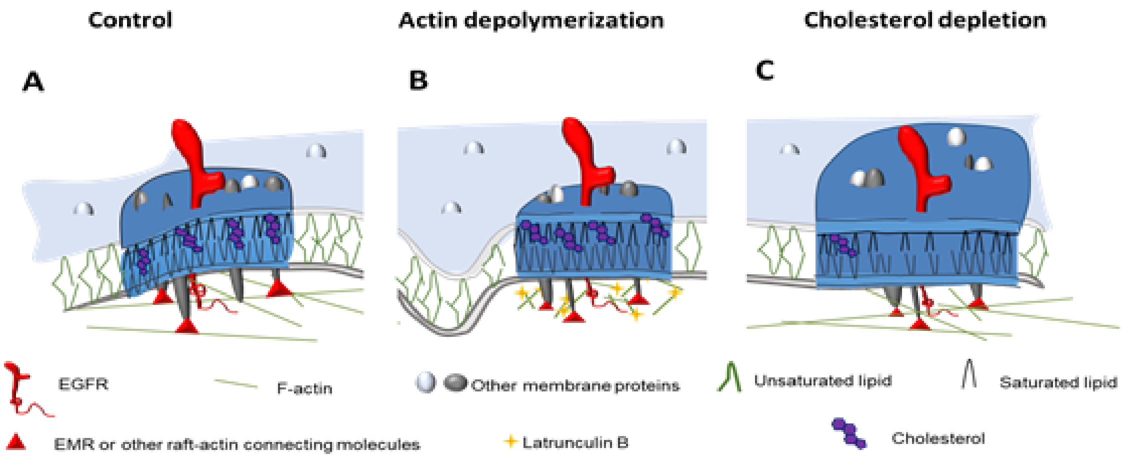

Figure 5.17: Model showing the confinement nature of EGF receptors in VSM cells and their interactions with other cell components including actin filaments and membrane lipids.

disruption on the confinement of EGF receptors, the latrunculin B treatment favors the actin depolymerization process, actin is in G-actin form or shorter actin filaments compared to the initial state. When we disrupt the actin filaments, EGF receptors still stay in the raft but now they can move freely inside the raft without the actin influence. Therefore, the stiffness of the confining potential decreases while the domain size as well as diffusion coefficient increases. Figure 5.17 C shows the EGF confinement after removal of cholesterol in the raft. The cholesterol oxidase treatment partially disrupts the raft domains enriched in cholesterol and makes the raft less compact with a more loose confining potential. The receptors confinement is now mainly due to receptors binding to the actin filaments via their actin-binding domain.

5.3 EGFR tracking in PEC and shCD9 PEC cells

In this section, we investigate the EGFR motion in other cell types: Parietal Epithelial cells (PEC) and short hairpin CD9 Parietal Epithelial cells (shCD9 PEC). From the dSTORM experiment, we already observed that the number of EGF receptors on the cell membrane diminishes in shCD9 PEC compared to PEC cells. The CD9 present in the cell membrane is essential for the EGF receptor insertion. Furthermore, the area of the EGF receptor cluster was found to be somewhat larger in shCD9PEC than in PEC cells. EGFR in PEC and shCD9PEC are mostly confined in one domain. However, the receptors also hop and jump into two or three different adjacent domains during the trajectory recording time. Therefore, to analyze trajectories of EGFR, first, the domains were split using Gaussian Model Mixture (GMM). After that, the trajectories are corrected for the mechanical drift. Then single domains are analyzed using Bayesian inference to extract the diffusion coefficient and the spring constant of the confinement potential.

5.3.1 Pre-processing trajectories

Splitting Trajectories

The Gaussian Mixture Model (GMM) was used to split the whole trajectory into separate domains. The GMM algorithm is given the determined number of clusters and then proceeds to split the whole trajectory into the defined number of clusters. GMM considers that the data points belong to different Gaussian distributions. The points are assigned into the distribution with the highest possibility. The Gaussian distribution (or normal distribution) is determined by two main parameters: mean and variance. Gaussian distribution has a bell-shaped curve, with the data points symmetrically distributed around the mean value. To find the unknown parameters (mean values, variance values) for different Gaussian distributions, the expectation-maximization (EM) algorithm is used. The EM has two main steps. E-step: For all data points, calculate the probability that they belong to different clusters. M-step: The M-step is used to update the new parameters mean and variance for Gaussian distribution. The E-step and M-step are iterated until convergence.

An example of domain clustering is demonstrated in Figure 5.18. The GMM clustering approach can identify cluster domains with different sizes and elliptical shapes. Compared to the most popular clustering model K-means which determines clusters with circular boundaries, GMM has better performance when splitting clusters with different sizes and different density of points, and it can also determine clusters with an elliptical shape. The elliptical shape of the trajectory is due to the mechanical drift. Furthermore, the Gaussian Mixture model is considered as a soft model. This means that, in GMM, the points are assigned into the cluster based on a probability value (Figure 5.18 D). Therefore, we can know the certainty with which points are assigned to a cluster.

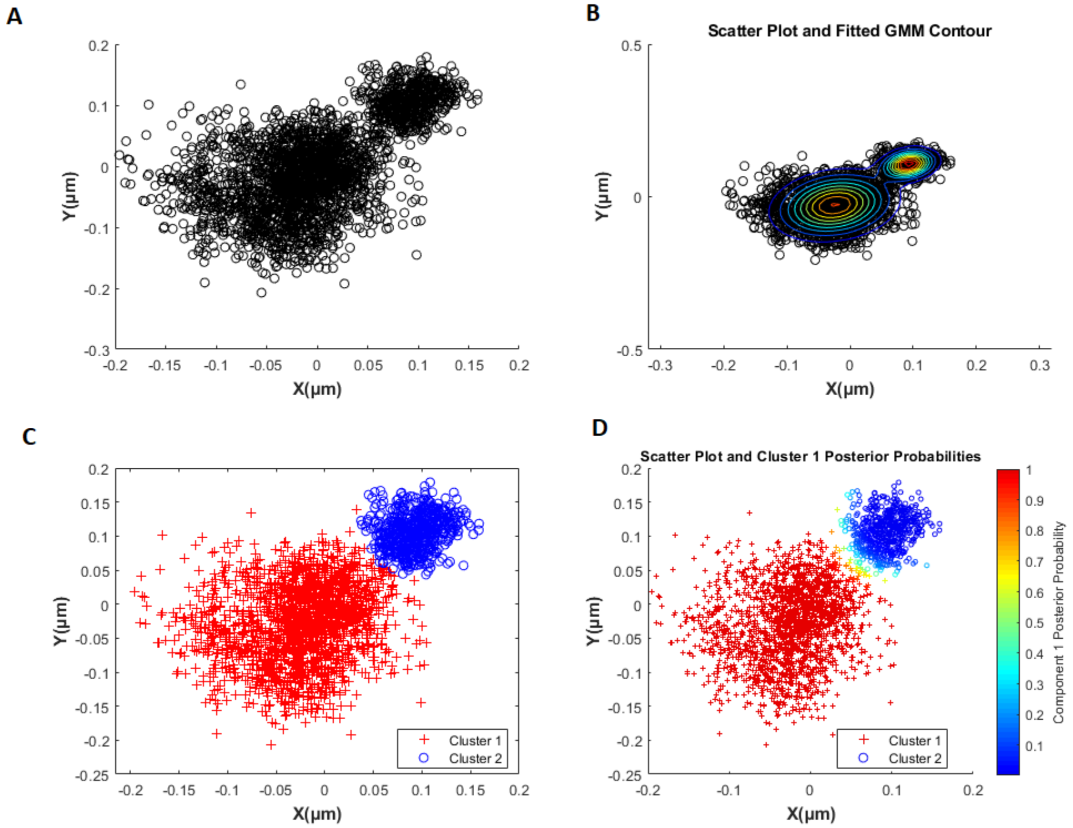

Figure 5.18: Gaussian Mixture Model to split trajectories: (A) Trajectory of EGFR in shCD9 PEC before clustering by GMM. (B) The Gaussian contours in the two clusters. (C) The trajectory is separated into two clusters. (D) The probability of points belonging to cluster 1.

Drift Correction

After splitting, if there is mechanical drift present, a linear drift is subtracted from the trajectory x(t) and y(t) values. A typical trajectory with mechanical drift is shown in Figure 5.19 A. The trajectory has the tendency to elongate in either in x or y or in both the x- and y-direction. The observed trajectory includes the confined motion of the receptors and linear drift. The mechanical drift is detected by plotting the x (or y) direction vs time (Figure 5.19 B). The plot shows a fluctuation around the center of the confinement point and a slope that indicates the value of linear drift. To eliminate the drift, we just subtracted a linear curve from the initial x(t) values. The final drift-corrected trajectory is shown in Figure 5.19 C.

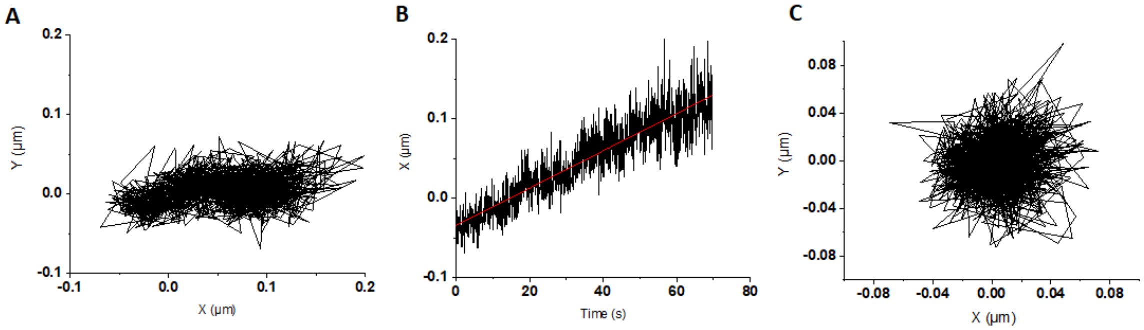

Figure 5.19: Mechanical drift correction of EGFR tracking in PEC. (A) Typical trajectory with mechanical drift. (B) The plotted x data vs time with a linear fitting line (in red). (C) The trajectory after removing the mechanical drift.

5.3.2 EGFR tracking in PEC

In this section, the EGF receptor tracking in PEC will be discussed. The EGF receptors in the cell membrane of PEC were done in three sets of conditions: control cells without any drug treatment and cells treated with sphingomyelinase or cholesterol oxidase to disrupt the confining domains.

Sphingomyelinase Treatment

To determine whether the EGF receptors in PEC are located in raft domains, we tracked the receptors after the rafts in the cell membrane were disrupted by cholesterol oxidase or sphingomyelinase. Interestingly, in MDCK cell, when applying sphingomyelinase, the number of nanoparticles labeling EGF receptors was reduced significantly compared to the control condition whereas the number of nanoparticles labeling EGF receptors remains unchanged in PEC with and without sphingomyelinase treatment (Figure 5.20). In PEC cells, the number of nanoparticles labeling EGF receptors per cell area only slightly changes from 0.0061 ± 0.0006 μm^{-2} to 0.0057 ± 0.0009 μm^{-2}. In PEC cells, the nanoparticles were incubated with cell first and the sphingomyelinase treatment was followed after. Because MDCK is a cancer cell type, the number of EGFR expressions is also expected to be higher in MDCK than in PEC. The experiments of different treatments were done on the same day as the control experiment.

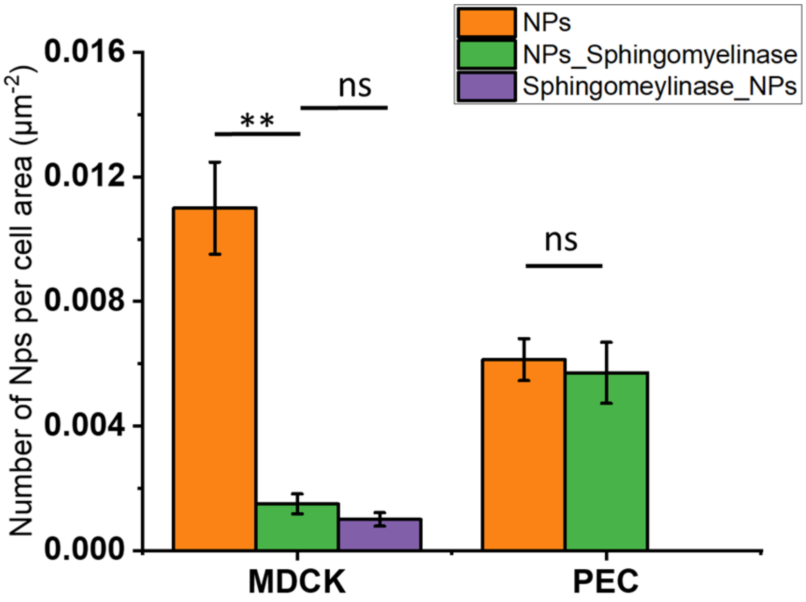

Figure 5.20: Number of NPs labeled with EGFR on the cell membrane without and with sphingomyelinase treatment in MDCK and PEC. T-test: $**: P < 0.01$, ns: $P > 0.05$

After splitting the trajectories by GMM and subtracting drift, the confined domains of the trajectories were analyzed by Bayesian inference to extract the diffusion coefficient and spring constant of a harmonic potential. Figure 5.21 shows the results of EGF receptor tracking in PEC without and with raft disruption drug treatments. There is no significant difference in the results before and after sphingomyelinase. The diffusion coefficient increases slightly from 0.017 ± 0.002 $\mu m^2/s$ to 0.02 ± 0.005 $\mu m^2/s$ while the spring constant does not change (6.9± 0.7 $pN/\mu m$ before vs. 6.6 ± 0.7 $pN/\mu m$ after treatment). The area of confinement domains of EGF receptors remains unchanged: the average domain area in the control case is 0.12 ± 0.01 μm^2 and 0.12 ± 0.02 μm^2 after sphingomyelinase treatment.

Cholesterol Oxidase Treatment

To further investigate if cholesterol oxidase treatment is related to the confinement of EGF receptors or not, we analyzed tracking experiments of EGF receptors with and without cholesterol oxidase. The result is plotted in Figure 5.21. Whereas treatment of cells with sphingomyelinase does not change the confinement domain size, the diffusion coefficient D, and the spring constant k, the cholesterol treatment does affect the receptor motion. The average diffusion D increases from 0.017 ± 0.002 $\mu m^2/s$ to 0.029 ± 0.008 $\mu m^2/s$ after cholesterol oxidase treatment, while the spring constant decreases from 6.9 ± 0.7 $pN/\mu m$ to 3.4 ± 0.6 $pN/\mu m$. The domain area of the receptor confinement also increases from 0.12 ± 0.01 μm^2 to 0.16 ± 0.02 μm^2. The receptors are still confined in domains except for the occurrence of hopping events from one domain to one or more nearby domains. To summarize, from the tracking experiments of EGF receptors in PEC cells, the receptors were found to reside in domains enriched in cholesterol but not in sphingomyelin, in contrast to what was found in MDCK cells. This finding excludes confinement in raft domains which are enriched both in cholesterol and in sphingolipids.

In PEC, the tracking experiments were done on the same days but not on the same coverslip.

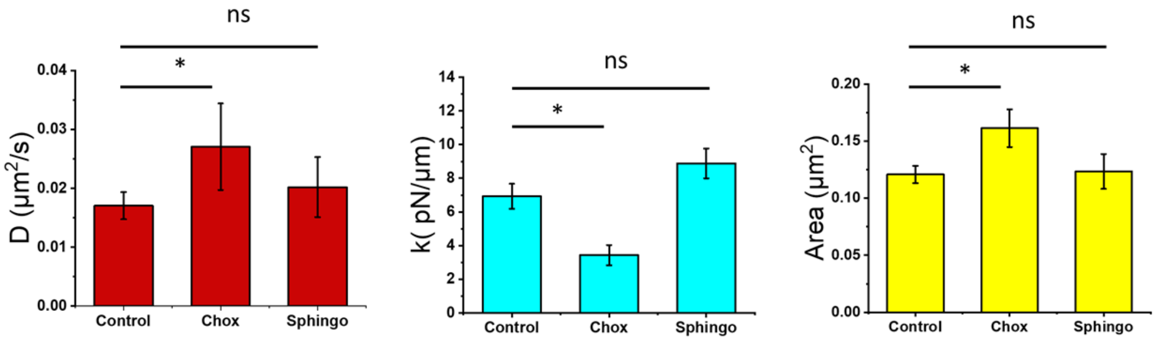

Figure 5.21: EGF receptor movement in different conditions without and with cholesterol oxidase or sphingomyelinase treatment. (A) Diffusion coefficient, (B) spring constant, (C) domain area. T-test: ns: not significant, *: $P < 0.05$.

Tracking EGFR in PEC and shCD9 PEC

To investigate the effect of depletion of CD9 proteins on EGF receptor confinement and insertion in the cell membrane, we tracked EGF receptors in shCD9 PEC cells. Figure 5.22 shows the tracking results obtained in PEC and shCD9 PEC. The confinement domains of EGF receptors are found to be larger in shCD9 PEC than in PEC. This result agrees with the result obtained by dSTORM in chapter 4. In dSTORM, the average domain size of EGF receptors is 0.0132 ± 0.0005 μm^2 (nanobody data) and in shCD9 PEC it is somewhat larger around 0.019 ± 0.002 μm^2. In the tracking experiment, the domain size was found to be in the same range as in the dSTORM experiment. The mean domain areas of EGFR are 0.012 ± 0.007 μm^2 and 0.016 ± 0.002 μm^2 in PEC and shCD9 PEC, respectively. Interestingly, the diffusion coefficients and spring constants in the confinement domains are insignificantly different in PEC and shCD9 PEC. The depletion of CD9 mainly affects the confinement domain size of EGF receptors but does not affect significantly the force acting on the receptors or the diffusivity of the receptors.

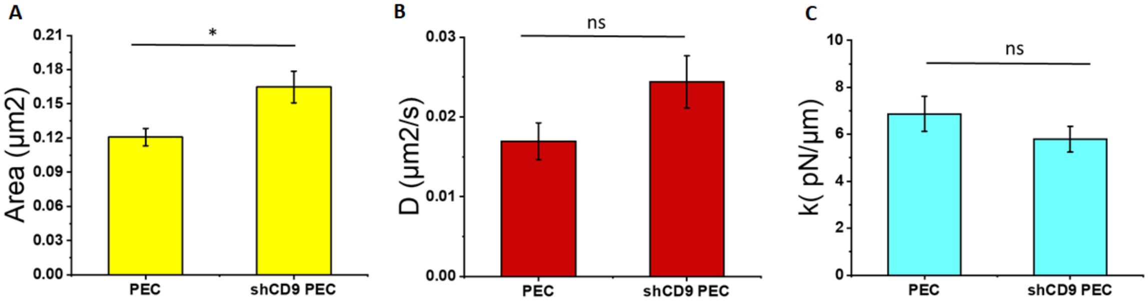

Figure 5.22: EGF receptor confinement in PEC and shCD9 PEC. (A) Confinement domain area, (B) diffusion coefficient, (C) spring constant of a harmonic potential. T-test: ns: not significant, *: $P < 0.05$.

As discussed in chapter 2, the tetraspanin-enriched membrane domains are known for the residence of tetraspanin proteins and cholesterol lipids but are not sphingolipids. The EGFR tracking results in PEC and shCD9 PEC cells confirm that EGFRs reside in domains enriched in cholesterol but not in sphingomyelin. These results, in combination with the strong reduction of receptor numbers observed in CD9-depleted cells both in dSTORM and in single-molecule tracking experiments, provide strong evidence that EGF receptors are, at least partially confined in tetraspanin-enriched domains in PEC cells.

5.4 EGFR tracking in different cell types

Figure 5.23 and table 5.2 show the single-molecule tracking results of EGF receptors in four different cell types. As we can see, the receptors in MDCK cells diffuse at the highest speed and explore the largest domain area. While EGF receptors in VSMC are confined in the smallest domain sizes and have the lowest diffusion coefficient. Even though in MDCK and VSMC, EGF receptors are confined in domains of different sizes, the stability of this domain is dependent on both cholesterol and actin. In PEC by using the STORM technique, the EGF receptors are found to be partially confined in CD9-enriched domains (Chapter 4). The tracking experiments confirm the presence of EGFR in CD9-enriched domains by showing that the EGFR motion characteristics are affected by cholesterol depletion but are independent of sphingomyelin depletion.

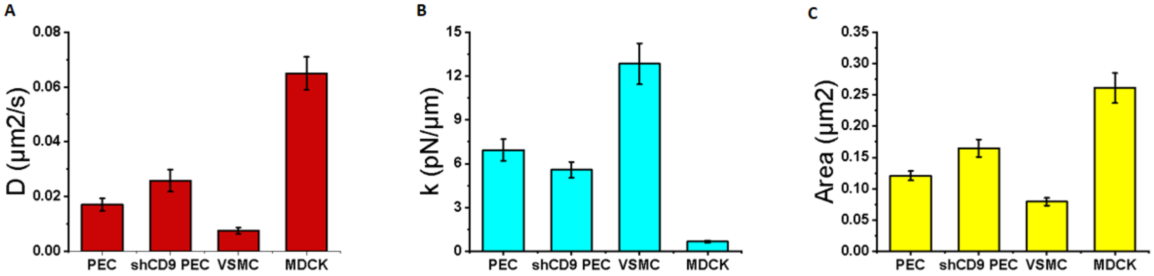

Figure 5.23: EGF receptor confinement characteristics in different cell types: in PEC, shCD9 PEC, VSMC, MDCK. (A) Diffusion coefficient, (B) Confining potential stiffness (C) confinement domain area.

Cell		D ($\mu m^2/s$)	k ($pN/\mu m$)	Area (μm^2)
PEC	Control (N= 69)	0.017 ± 0.002	6.92 ± 0.74	0.12 ± 0.007
	Latb	nd	nd	nd
	Chox (N= 20)	0.029 ± 0.008	3.4 ± 0.6	0.16 ± 0.02
	Sphingo (N=62)	0.020 ± 0.005	6.6 ± 0.7	0.12 ± 0.02
shCD9 PEC	Control (N=55)	0.025 ± 0.004	5.57 ± 0.54	0.16 ± 0.001
	Latb	nd	nd	nd
	Chox	nd	nd	nd
	Sphingo	nd	nd	nd
VSMC	Control (N=49)	0.0072 ± 0.0006	14.6 ± 1.1	0.018 ± 0.002
	Latb (N =77)	0.033± 0.004	5.12 ± 0.74	0.41 ± 0.09
	Chox (N= 86)	0.028 ± 0.004	6.9 ± 0.9	0.37 ± 0.08
	Sphingo	nd	nd	nd
MDCK	Control (N= 21)	0.065 ± 0.006	0.665 ± 0.075	0.261 ± 0.024
	Latb (N= 20)	0.091 ± 0.011	0.454 ± 0.063	0.456 ± 0.068
	Chox (N= 20)	0.215 ± 0.019	0.116 ± 0.016	1.457 ± 0.176
	Sphingo	nd	nd	nd

Note: nd: no data have been reported; D: Diffusion coefficient, k: spring constant.

Table 5.2: Table of EGFR confinement characteristics in different cell types in control cells and with the different drug treatments. Latb is treatment with latrunculin B, Chox with cholesterol oxidase, and Sphingo with sphingomyelinase.

5.4.1 Confinement Model of EGF receptors

In general, the receptors are confined in isotropic domains after subtracting systematic drift from the trajectories. Therefore, the potential determined by Bayesian k_x values is close to the k_y values. The potential can therefore be rewritten by using an average spring constant k_r:

$$u(x) = \frac{k_r r^2}{2} \tag{5.17}$$

If we assume that the thermodynamic equilibrium is reached, we can derive the probability density of observing a position of the receptor as a function of radius and spring constant:

$$P(r,\theta) = \frac{e^{-\frac{k_r r^2}{2k_B T}}}{Z} \tag{5.18}$$

with Z being defined to ensure that:

$$\int_0^{2\pi} \int_0^{+\infty} P(r,\theta)\, r\, dr\, d\theta = 1 \tag{5.19}$$

In our case, because we take 95 percent of the total trajectory points, we expect that:

$$\int_0^{2\pi} \int_0^{R} P(r,\theta)\, r\, dr\, d\theta = 0.95 \tag{5.20}$$

We set $\frac{k_r r^2}{2k_B T} = a$ and then substitute the value of $P(r,\theta)$ in equation 5.18 into the equation 5.20 which yields:

$$\int_0^{2\pi} \int_0^{+\infty} \frac{e^{-ar^2}}{Z}\, r\, dr\, d\theta = 0.95 \tag{5.21}$$

$$Z = \frac{\pi}{a} = \frac{2\pi k_B T}{k_r}$$

In order to find the effective temperature, $aZ = \pi$ is substituted in equation 5.21. After the integration step, we get:

$$\frac{1}{2} \int_0^{2\pi} \frac{e^{-ar^2}}{\pi} \Big|_0^R d\theta = 0.95$$

After solving the equation, the effective temperature of the system is found to be:

$$T = -\frac{k_r R^2}{2k_B ln(0.05)} \tag{5.22}$$

The effective temperature calculated from eq. 5.22 describes the motion of the receptors inside the parabolic potential.

The radius and spring constant relationship is given by:

$$R = \sqrt{\frac{2T k_B ln(0.05)}{k_r}} \tag{5.23}$$

Figure 5.24 shows the plot of the domain radius as a function of the reciprocal square root of the spring constant. In VSMC and MDCK, the Pearson's correlation of the domain radius to the reciprocal square root of the spring constant is presented in Table 5.3. The p-value for Pearson's correlation coefficient uses the t-distribution. For Pearson's correlation coefficient: $H_0 : \rho = 0$ vs $H_1 : \rho \neq 0$ where ρ is the correlation coefficient between a pair of variables. A small ρ is an indication that the null hypothesis can be rejected. We can conclude that a linear relationship exists between the domain radius and the reciprocal square root of the spring constant.p-value is from a t-test corresponding to the Pearson's coefficient, if p-value is larger than a threshold $\alpha = 0.05$, the null hypothesis can be rejected. The Pearson's coefficients found in PEC and shCD9 PEC are smaller than those in VSMC and MDCK cells. This is probably due to the sample sizes for PEC and shCD9 PEC being larger than those for VSMC and MDCK. From the values of Pearson's coefficient and the p-values, we can conclude that the radius is proportional to the inverse square root of the spring constant. This means that the domain radius observed from single-molecule trajectories simply reflects the stiffness of the parabolic potential. Indeed, in this framework, the observed domain size is just an apparent size determined by how far away from the center of the potential with stiffness k_r a molecule with a given thermal energy can explore the energy landscape [1].

Cell	P.C (ρ)	p-value	Effective temperature (°C)
PEC	0.944	$6.6\ e^{-42}$	322 ± 27
shCD9 PEC	0.924	$3.7\ e^{-43}$	502 ± 118
VSMC	0.971	$3.1\ e^{-13}$	488 ± 17
MDCK	0.982	$2.19\ e^{-15}$	349 ± 119

Note: P.C is Pearson's coefficient.

Table 5.3: The Pearson's coefficient, p-value of t-test and the effective temperature at the equilibrium.

The effective temperatures of EGFR in different cell types are not significantly different. The effective temperatures are also found to be much higher than the temperature of the experiment at 37 °C. This probably reflects the fact that active processes are taking place inside the confinement domain.

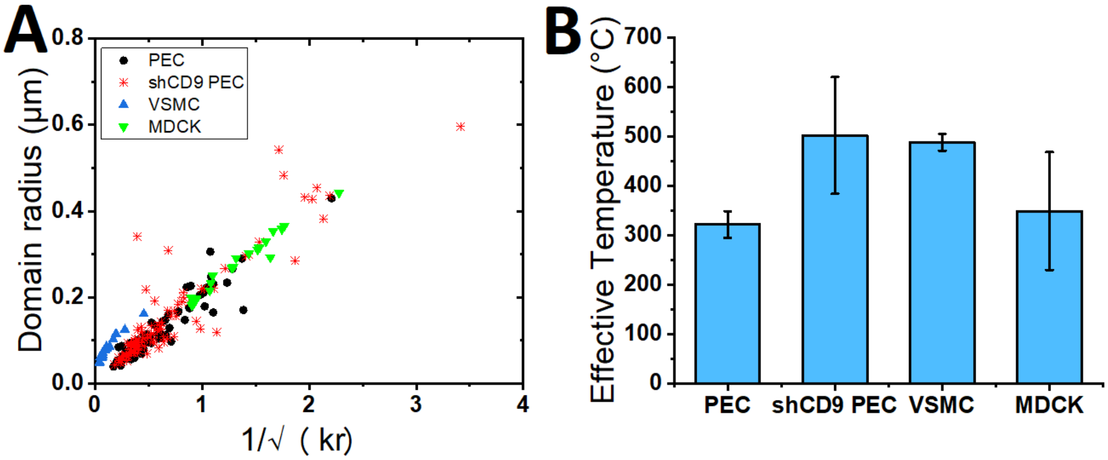

Figure 5.24: (A) The domain radius of EGF receptors in different cell types is proportional to the reciprocal square root of the spring constant of the confining harmonic potential. (B) The effective temperature of confined EGF receptors.

5.5 Discussion and Conclusion

In this chapter, we used single-particle tracking to understand the architecture and dynamics of EGF receptors in four different cell types: PEC, shCD9 PEC, VSMC, and MDCK.

The EGF receptors were labeled with Europium-doped oxide nanoparticles. Then the motions of the receptors were recorded using a wide-field microscope. The receptor position was localized by fitting the nanoparticle PSF-limited emission with a 2D Gaussian.

We introduced a new method to determine the confined and free portions of EGF receptor trajectories. EGF receptor confinement in VSMC was analyzed by two methods. In the first method, the trajectories of EGF receptors were split manually into confined and free portions. Then the confined portions were analyzed by Bayesian inference to determine the diffusion coefficient of the receptor and the spring constant of the harmonic confining energy landscape. In the second method, we used the so-called structural analysis proposed by [253] to split automatically the trajectory into portions of free and confined motion. Then the confined portions are analyzed by MSD and the model proposed by [254] for motion inside a harmonic energy landscape to extract the diffusion coefficient and the spring constant. The area of the confining domain is determined by taking the radius of a circle containing 95% of the trajectory points.

The two methods give similar results for the EGFR tracking experiment in VSMC. Using Bayesian inference, we found in control VSMC cells a diffusion coefficient D = 0.0072 ± 0.0006 $(\mu m^2/s)$ and a spring constant of the harmonic potential $k_r = 14.6 \pm 1.1$ $(pN/\mu m)$. While using the structural approach to split the trajectories and then analyze the confined portions by MSD, the diffusion coefficient of EGFR in the VSMC control cells is 0.0070 ± 0.009 $(\mu m^2/s)$ and the spring constant is 12.7 ± 1.0 $(pN/\mu m)$.

When applying cholesterol oxidase to VSMC cells to disrupt the cholesterol- and sphingolipid-rich rafts, the diffusion coefficient of EGF receptors increases while the spring constant decreases. The area of the confinement domain becomes larger after the cholesterol oxidase treatment. This means the EGF receptors are confined in domains enriched in cholesterol. When the percentage of cholesterol decreases, it leads to the partial destabilization of the confinement domains, the domain becomes less compact and the confining potential less stiff leading to the increase of the diffusion coefficient and the decrease of the spring constant. Similar to cholesterol removal, the actin depolymerization also leads to an increase in the confinement domain and the diffusion coefficient of EGF receptors in VSMC, while the spring constant decreases significantly. Therefore, by using single-particle tracking, we found that EGF receptors in VSMC are confined in a domain enriched in cholesterol and the receptors also bind to the actin cytoskeleton, the tethering contributing to the confinement of the EGF receptors. EGF receptors in VSMC behave similarly to EGF receptors in MDCK cells. They are located in membrane domains enriched in cholesterol and their confinement is, in addition, actin-cytoskeleton dependent. Moreover, I found that sphingomyelinase applied to MDCK cells leads to a strong reduction of the number of EGF receptors in the membrane indicating that EGF receptors are located in cholesterol- and sphingolipid-rich rafts in these cells.

In contrast, the EGFR confinement domains behave differently in PEC cells compared to MDCK cells. The EGFR confinement is not affected by the sphingomyelinase treatment: the diffusion coefficient, spring constant, and domain area remain unchanged. Moreover, the total number of receptors in the cell membrane does not change after the sphingomyelinase treatment. Only cholesterol removal affects the confinement characteristics of the EGFR domains. The EGF receptors in shCD9 PEC are confined in a larger domain than in PEC, however, their diffusion coefficient and spring constant of the receptors in shCD9 PEC are not significantly different from those in PEC.

These single-particle tracking results confirm those obtained by dSTORM. Both methods yield the conclusion that the number of EGF receptors in the cell membrane is much smaller in shCD9 PEC than in PEC cells. Both methods indicate that EGFRs in PEC cells are, at least partially, located in CD9-enriched domains.

Conclusion and Perspectives

In my thesis, I have investigated the EGF receptor distribution in the cell membrane of different cell types, especially the connection between EGF receptors and CD9 proteins in parietal epithelial cells (PEC) that play an important role in kidney disease.

The kidney structure and the mechanisms of inflammatory kidney diseases were introduced in the first chapter. The involvement of parietal epithelial cells in kidney function and disease were also described. The architecture of the cell membrane was then introduced. Various membrane confinement models were reviewed such as the raft model, protein tethering, the picket-and-fence model, and the tetraspanin-enriched domains. The involvement of EGFR and CD9 and their inhibition or depletion in glomerular cells in the evolution of kidney disease was also addressed in this chapter.

To understand the architecture and components of the cell membrane and other biological structures, numerous microscopic methods have been used. Conventional microscopy has a resolution limit of about 200-300 nm. Therefore, many biological organizations cannot be resolved under a conventional microscope. Electron microscopy can reach very high resolution, but it has low selectivity to detect the different cell components. Super-resolution fluorescence microscopy is a powerful technique that solves the problem of limited resolution in optical microscopy while maintaining high selectivity. Super-resolution techniques can reach a resolution of 10 nm, capable of revealing many important structures of the cell. However, super-resolution microscopy is more suitable for fixed samples. Using single-molecule tracking is, on the other hand, an ideal complementary method to study the dynamics of proteins in live cells.

By using the stochastic optical reconstruction microscopy (STORM) technique, we can lower the resolution of a microscope to about 20 nm where we can quantitatively study the distribution of EGF receptors and CD9 proteins in the cell membrane of PEC and shCD9 PEC cells. Using the tessellation clustering method, the important parameters of the EGFR and CD9 domains were revealed such as the mean domain size, the number of receptors per domain, the density of receptors inside clusters and at the whole-cell surface.

We found that in CD9-depleted cells (shCD9 PEC), the number of EGF receptors in the cell membrane is reduced significantly. Moreover, the area of the EGFR domain is larger in sh CD9 PEC than in PEC cells. This result agrees with the semi-quantitative finding obtained by Lazareth et al. (2019) that the total number of EGF receptors in the whole cell, as well as the number of phosphorylated EGFR due to HB-EGF activation, is reduced [2].

Our data show that this previously observed decrease in EGF receptor numbers per cell in Western blot data is directly reflected in the EGF receptor numbers in the cell membrane. EGFR plays an important role in the signaling processes of the cell, like proliferation. It is therefore expected that EGFR is found to be involved in cell proliferation in the Bowmann's space and in crescent formation in kidney disease [3]. However, the results of this thesis also indicate why suppression of CD9 proteins can globally improve the course of kidney disease as was demonstrated by Lazareth et al. [2].

The two-color imaging STORM results I obtained reveal the answer to the question of why CD9 depletion in PEC can reduce the number of EGFR in the membrane as well as in the whole cell: EGF receptors in PEC are, at least partially, located in tetraspanin-enriched domains. Indeed, we found partial colocalization between CD9 and EGFR membrane clusters whereas there is negligible colocalization between transferrin receptor, a reference protein located in domains delimited by the actin filaments underlying the membrane, and EGFR clusters. Further quantitative analysis of these data should confirm this result.

To further understand the confinement nature of EGF receptors in PEC and other cell types, in chapter 5, we presented the dynamics of EGF receptors by using the single-particle tracking method. We introduced a new method to analyze the molecule trajectories. By using the so-called structural method [253], we can determine the free portions and confined parts of the trajectory automatically without the human bias in the analysis. The splitting method was followed by analysis of the MSD to extract the receptor diffusion coefficient and the spring constant of a harmonic potential acting on the receptor, as in [254] describing the forces acting on the receptors inside the confinement domains. We checked that this approach yields similar result with our conventional method based on splitting the trajectory manually and analysis with Bayesian inference to find the diffusion coefficient and spring constant.

In VSMC, EGF receptors are found to be located in domains enriched in cholesterol and are also found to bind directly to the actin cytoskeleton, similar to those in MDCK cells. When applying cholesterol oxidase to disrupt these domains or using latrunculin B to depolymerize the actin filaments, we found that the receptor mean confinement area and diffusion coefficient increases while the forces acting on it due to the confining potential decrease. Whereas EGF receptor confinement in the cell membrane domains of MDCK cells is sphingomyelin-dependent, the disruption of the raft domains by sphingomyelinase does not change the EGFR domain characteristics in PEC cells. When disrupting domains in the PEC cell membrane with cholesterol oxidase, we found that the EGF receptors are still confined but in larger domains, with a higher diffusion coefficient and a lower spring constant for the confining potential. These two latter results, EGFR cholesterol-dependent and sphingomyelin-independent confinement in PEC, combined with the lower EGFR numbers in CD9-depleted cells, lead us to the conclusion that EGF receptors in PEC cells reside in tetraspanin-enriched domains, in contrast to what is observed in other cell types, like MDCK, where EGFRs reside in raft domains.

The confinement of the receptors in domains as well as the density of the receptors in the membrane are believed to directly affect the function of the receptors. To further investigate this aspect, in our group, we also measured the production of reactive oxygen species (ROS) upon EGFR activation by its EGF ligand by using the europium- doped vanadate nanoparticles as ROS nanosensors inside the cell cytosol [258]. Indeed, the activation of EGFR is known to activate ROS production through NAPDH oxidase (Nox) enzymes. The reactive oxygen species (ROS) measurements in PEC and shCD9 PEC (data not shown) done by Maxime MAUVIEL, a Ph.D. student in our group, demonstrated that the ROS produced upon EGF activation of PEC cells is much lower in CD9-depleted shCD9 PEC cells than in control PEC cells. This confirms a functional consequence of CD9 depletion on the EGF receptor activity in PEC cells.

In conclusion, this thesis investigated the molecular interaction between two proteins in the cell membrane, CD9 and EGFR. By using two single-molecule microscopy techniques, we not only mapped the distribution of two proteins by dSTORM but also explored the dynamics of EGF receptors by single-particle tracking. By disrupting the membrane nanodomains with different drugs and depolymerizing the actin cytoskeletons, we also studied the composition of the confinement domains in various cell types and found complementary evidence that EGFR are located in tetraspanin-enriched domains in PEC cells whereas previous literature data and our present data show that EGF receptors are confined in raft domains. We furthermore implemented a new method for identifying trajectory portions of confined versus free motion which allows automatic analysis of the data to avoid human bias.

To better understand how the molecular organization of these proteins in the cell membrane affects cell function and ultimately kidney disease, further research can be conducted in the future. From the single-particle tracking experiments, we found that the domain size, diffusion coefficient, and spring constant of EGF receptors in VSMC and MDCK are drastically different even though the receptors in both cell membranes are cholesterol- and actin-dependent. It is interesting to find out if the raft in VSMC is enriched also in sphingolipids like in MDCK cells.

Moreover, the size of the confinement domains in VSMC is much smaller than that in the MDCK cells raising the question: does the size of the confining domain has a functional influence on receptor activation? Therefore, it is also interesting to use STORM to determine the number of receptors in the cell membrane of VSMC and MDCK. It is expected that in the cancer cells (MDCK), EGF receptors are overexpressed. Even though the size of EGFR domains is larger in MDCK than in VSMC, the efficiency of receptor activation should depend both on the density and the total number of receptors in the domain.

In PEC and shCD9 PEC, we have shown that EGFR are localized partially in tetraspanin-enriched domains which are enriched in cholesterol but not in sphingomyelin. In a recent paper, L. FERNANDEZ and P.E. MILHIET et al. have shown that gangliosides modulate the formation of the so-called tetraspanin web [259]. It would therefore be interesting to investigate if the DL-threo-1-Phenyl-2-palmitoylamino-3-morpholino-1-propanol (PPMP) treatment that lowers the expression of gangliosides changes the CD9 and EGFR distributions and dynamics in PEC cells. Further research can be done to find out where the EGF receptors are located in CD9-depleted shCD9 PEC, whether EGFRs are located in other domain types like raft domains or if they can still be inserted in tetraspanin-enriched domains but their activation efficiency is reduced because there is lack of CD9 leading to fewer and less compact domains. The sphingomyelinase treatment can be used to answer this question. From various studies on CD9 proteins, P.E. MILHIET et al. also observed that CD9 proteins are not only confined in tetraspanin-enriched domains but also diffuse freely, alternating between confined and free motion [151, 259, 260]. In our STORM experiments, CD9 molecules in PEC cells are found to be mostly located inside clusters. We can use single-particle tracking to examine the dynamics of CD9 in PEC cells and determine the fraction of time spent in confinement domains and in free motion.

Appendix A

Experimental Setups and Protocols

During my thesis, two main methods have been used to study the dynamics and relationship between EGFR and CD9 organization: Single Particle Tracking and STORM.

Using single-molecule tracking, we investigated different EGFR confinement domains in three cell types. The tracking data were then analyzed by two main methods: Bayesian Inference (BI) on confined trajectory portions and a structural approach to split the trajectory in free-motion and confined-motion portions followed by fitting the MSD with a model of Brownian motion inside a harmonic potential to extract the diffusion coefficient D and and the stiffness of the harmonic potential k.

In single-particle tracking, we used 30-nm europium-doped oxide nanoparticles $Y_{0.6}Eu_{0.4}V0_4$ as probes with very low-concentration labeling of EGFR. See Mousseau et al. for a detailed characterization of the nanoparticles before and after functionalization for EGFR labeling [261]. Thus, we can analyze the trajectory of individual EGFR. The localization of proteins is determined by fitting the position of the nanoparticle fluorescence with a 2D Gaussian. Therefore, the localization precision is much lower than the microscope resolution which is limited by diffraction. The localization precision depends mainly on the signal-to-noise ratio and is around 30 nm in our experimental conditions when using europium-doped nanoparticles.

A.1 Single-particle tracking

A.1.1 Nanoparticle synthesis and functionalization

In our experiment, we used rare-earth-doped nanoparticles for tracking EGFR. Rare earth nanoparticles do not blink and are not photobleached, Therefore, using these nanoparticles, the tracking duration is much longer than with fluorescent dyes or proteins and is not interrupted by blinking as in the case of QDs. Furthermore, these nanoparticles also have high colloidal stability and a long radiative emission lifetime. One further advantage of these rare-earth nanoparticles compared to QDs is that they are synthesized in an aqueous solution [262]. Therefore, the synthesis and functionalization process is less complicated and less time-consuming. However, the size of rare-earth nanoparticles is relatively large compared to other probes: it ranges from 30 nm to 40 nm. To test if there is an effect of the nanoparticle labels on the movement of tracked proteins in the membrane, Silvan et al. compared the trajectory of the same proteins using organic dyes and nanoparticles and found that there is no difference in the diffusion coefficient of membrane proteins when using nanoparticles or organic dyes [255]. This is the case because the proteins are diffusing in a high-viscosity medium, the membrane, whereas the nanoparticles diffuse in water. These rare-earth doped vanadate nanoparticles do not strongly absorb outside the UV region around 280 nm where vanadate ions absorb. To avoid cytotoxicity, we excite Eu-doped nanoparticles through direct europium-ion excitation at 466 nm. This is a dipole-forbidden transition with relatively low absorption [161], lower than that of Quantum dots but on the same order as the brightest organic fluorophores [263]. The emission, centered at 617 nm, is also dipole-forbidden and is therefore long-lived and spectrally narrow allowing the use of narrow emission filters and efficient background rejection.

In our experiment, to track EGFR on the cell membrane, we used biotinylated EGF coupled to $Y_{0.6}Eu_{0.4}VO_4$ nanoparticles conjugated to streptavidin. This means that we are tracking activated receptors. The STORM experiment, on the other hand, used antibodies for the labeling and is therefore visualizing inactive receptors. The protocol of synthesis and functionalization of nanoparticles was based on previous work of D. Casanova, D. Giaume et al. [258, 264]. The nanoparticles were first coated and stabilized with silicate ions and then covered with (3-Aminopropyl)triethoxysilane (APTES). Instead of using the cross-linker Bis-(sulfosuccinimidyl)-suberate (BS3) to bind streptavidin to the APTES-coated nanoparticles, as in previous work of my team [264, 265], the amine functional group of APTES was modified to become a carboxylic group which was then activated (NHS-ester) to react with the amine groups in streptavidin molecules [261] The nanoparticle-streptavidin conjugates were then coupled to EGF-biotin with a ratio of 1:3 at 37 °C for 1 hour. Then non-reacted EGF-biotin was removed by centrifugation at 17 000 g for 15 minutes. The pellet was redispersed and potential nanoparticle aggregates formed during these steps were then removed by centrifugation at 2000 g for 5 minutes. The EGF-NPs in the supernatant were then collected for experimenting.

A.1.2 Cell culture and preparation

Parietal epithelial cells (PEC) were cultured in Endothelial Cell Basal medium with Supplement Pack endothelial Cell GM (PromoCell), 20% FBS, and 1% penicillin-streptomycin in a cell incubator (37 °C, 5% CO_2). Vascular smooth muscle cells (VSMC) were cultured in RPMI 1640 Medium (1X) [+] L Glutamine (Gibco) with 20% FBS and 1% penicillin-streptomycin in a cell incubator (37 °C, 5% CO_2). MDCK cells were cultured in DMEM, 10 % fetal calf serum (FCS), 1 % penicillin-streptomycin in a cell incubator (37 °C, 5% CO_2).

The cells were transferred in low concentration on to glass 170-µm thick coverslips. They were starved in medium without FBS from 16h to 20h before the tracking experiments. Before incubating with EGF-NPs, the cells were washed three times with minimal medium (HBSS+10mM HEPES) to avoid the autofluorescence signal from the medium. The cells were incubated with EGF-NPs for 15 minutes at 37 °C. Then the unbound EGF-NPs were removed by washing three times with minimal medium (MM). The cells were kept in MM during the microscopy measurements which lasted less than 2h. The concentration of NPs incubated with the cells is low, approximately 40 nM, to obtain optimal labeling for single-molecule tracking experiments.

For the drug treatment experiments, cells were incubated with 20 U/mL cholesterol oxidase (Calbiochem, Millipore) for 30 minutes or with sphingomyelinase 10 U/ mL (Calbiochem) before EGFR labeling with nanoparticles. In the case of latrunculin B (Calbiochem, Millipore, Billerica, MA) experiments, cells were incubated with 500 nM latrunculin B for 30 min, the nanoparticles were also placed in a 500-nM latrunculin B solution and the concentration of latrunculin B was maintained in the observation medium during the optical measurements to ensure the inhibition of actin polymerization.

A.1.3 Optical microscopy set-up

Tracking experiments were performed with a wild-field inverted microscope, Zeiss AXIOVERT 100 (Zeiss Oberkochen, Germany) or Olympus IX-81 (Olympus America, Center Valley PA, USA), equipped with a 63×, NA=1.4 oil immersion objective and a EMCCD camera (Evolve Photometrics 512). The $Y_{0.6}Eu_{0.4}VO_4$ nanoparticles are excited with a continuous diode laser emitting at 465 nm (Modulight ML6500-465). The NP emission was collected through a 617/8 filter (Chroma Technology, Bellows Falls, VT). We recorded series of images at a frame rate of approximately 20 Hz (exposure time: 50 ms; readout time: 1.3 ms) and an excitation intensity of 0.25 kW/cm2 at 37 °C. The EGF receptor position in each frame was determined from a Gaussian fit to the diffraction pattern of the nanoparticle emission with an algorithm developed by Silvan Türkcan et al. that uses MATLAB V8.2 (The Math Works, Natick, MA).

A.2 Stochastic optical resolution microscopy

The PEC cells for the dSTORM experiments were cultured in the same conditions as for the single-particle tracking experiments. The first step in dSTORM imaging is cell fixation and immunocytochemistry. The cells were first fixed with a solution containing 1% of paraformaldehyde (PFA) and 0.2% of glutaraldehyde (GA) (Sigma) during 15 minutes at 37 °C. The concentration of PFA was kept low to avoid crosslinking and bulk effects during the antibody labeling step [266]. The cells were then washed three times with a washing solution (WS; phosphate-buffered saline (PBS) 1X+ 0.125 M gelatin). The sample was then incubated with 0.1% of sodium borohydride ($NaBH_4$) (Sigma) to reduce GA and avoid background signal due to GA autofluorescence during the measurements [267]. After the cell fixation and reduction of GA, the next step is to block with blocking buffer (0.25 M gelatin in PBS 1X) to minimize non-specific interactions between the antibodies and other cell membrane components that may lead to false emission spots in the images.

In 1-color dSTORM imaging, the cells were incubated with a mouse monoclonal primary anti-EGFR antibody diluted 1/100 (Thermofisher) or a mouse monoclonal primary anti-CD9 antibody (the mAb CD9 was provided by Dr. RUBINSTEIN Eric [260]). The incubation took place at 4 °C overnight for the best labeling efficiency. After that, the cells were washed three times with WS and were then labeled with a secondary anti-mouse antibody coupled with Dylight-649 (Vertorlab DI-2649). The concentration of the secondary antibody was diluted 1/200 in PBS 1X + 0.125 gelatin. The dSTORM buffer solution used was reported in ref [179] and consists of a combination of two reducing agents β-Mercaptoethanol (BME 50mM) and mercaptoethylamine (MEA, 10 mM), cyclooctatetraene (COT, 2 mM), and sodium sulfite (30 mM) in a PBS-Tris HCl 50 mM solution with pH 8.0. The nanobodies were used in the experiment from Nanotag (FluoTag-X2 anti-Mouse IgG1).

For 2-color imaging, to label EGFR and CD9, we used a rat monoclonal primary antibody for EGFR (Abcam ICR10-ab231) and a mouse monoclonal anti-CD9 antibody coupled to Dylight 650 (provided by Dr. RUBINSTEIN Eric [260]). The secondary anti-rat antibody is coupled to CF 568. The buffer solution of 2-color STORM imaging was prepared in PBS (1X) pH 8.0 with 30 mM sodium sulfite , 30 mM dithiothreitol (DTT), and 30 mM DABCO.

In the STORM experiments, we used a wide-field inverted microscope (IX83 Olympus) with a 100x NA=1.49 objective (Olympus). The camera used in the experiment was a sCMOS camera (Orca Fusion from Hamamatsu) with 2x2 binning. The lasers used for Alexa 647 excitation, Dylight 650 excitation, and CF 568 were mounted in a 4-color laser box (Vortran). We used 150-mW excitation at 640 nm for Alexa 647 and Dylight 650, and 40-mW excitation at 532 nm for CF 568, respectively. We used filter ET (605/70 nm) and dichroic 560 (FDi01-25x36 Semrock) for CF568 and filter ET620/60x (Chroma) for excitation and T660lpxr (Chroma) and ET700/75m (Chroma) for the emission filters for Dylight 650.

Appendix B

Data analysis by ThunderSTORM

As discussed in chapter 4, we performed the post-processing process for different parameter values for EGFR using polyclonal secondary antibodies and nanobodies in PEC and shCD9 PEC cells. The results are shown in Figure B.1, Figure B.2, and Figure B.3, respectively. We also performed the post-processing filter analysis for different parameter values for CD9 proteins in PEC cells (Figure B.4). The details of the pre-processing and post-processing steps and of the parameter values chosen for the comparisons below were discussed in Chapter 4.

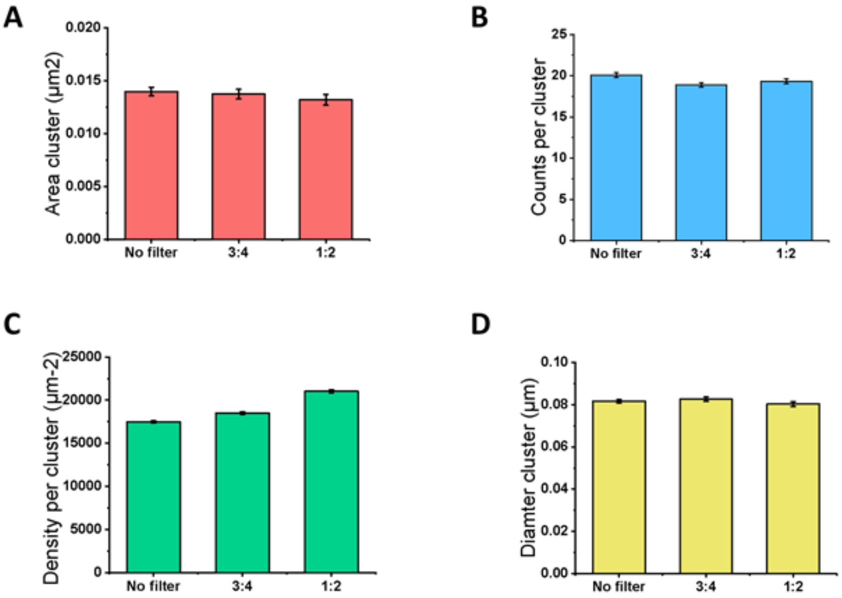

Figure B.1: EGF receptor localizations in PEC obtained by labeling with nanobodies. Analysis for different post-processing filter conditions (see Chapter 4). (A) Cluster area. (B) Number of localization counts per cluster. (C) Density of receptors per cluster area. (D) Diameter of clusters.

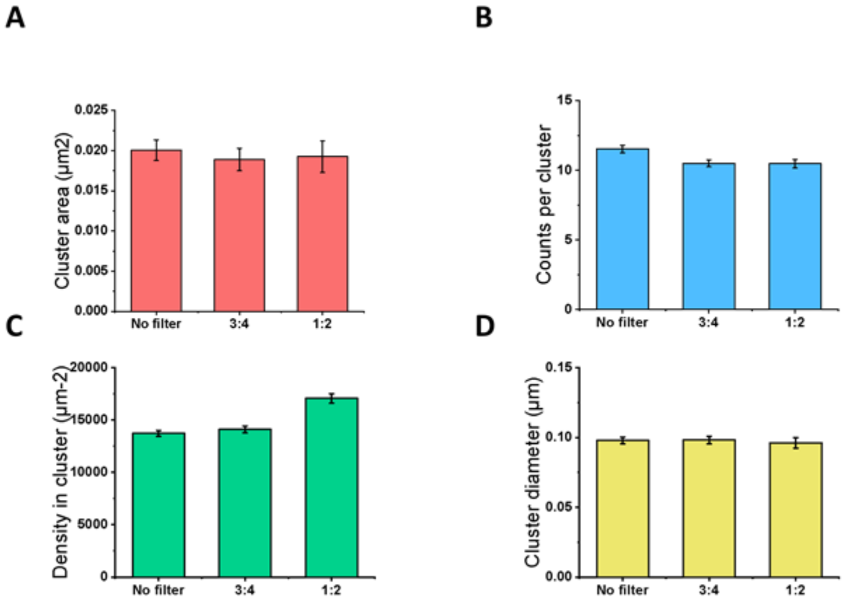

Figure B.2: EGF receptor localizations in shCD9 PEC obtained by labeling with nanobodies. Analysis for different post-processing filter conditions. (A) Cluster area. (B) Number of localization counts per cluster. (C) Density of receptors per cluster area. (D) Diameter of clusters.

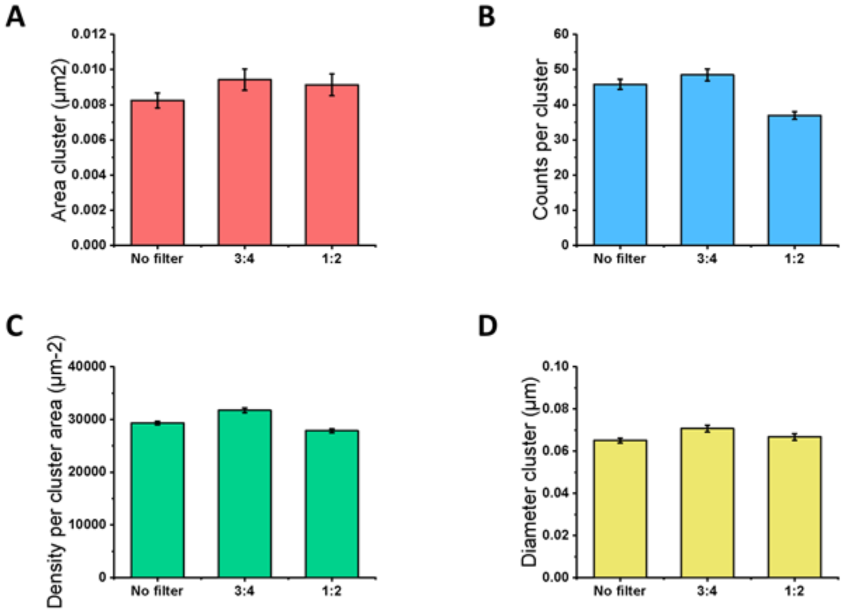

Figure B.3: EGF receptor localizations in shCD9 PEC obtained by labeling with polyclonal secondary antibodies. Analysis with different post-processing filter conditions. (A) Cluster area. (B) Number of localization counts per cluster. (C) Density of receptors per cluster area. (D) Diameter of clusters.

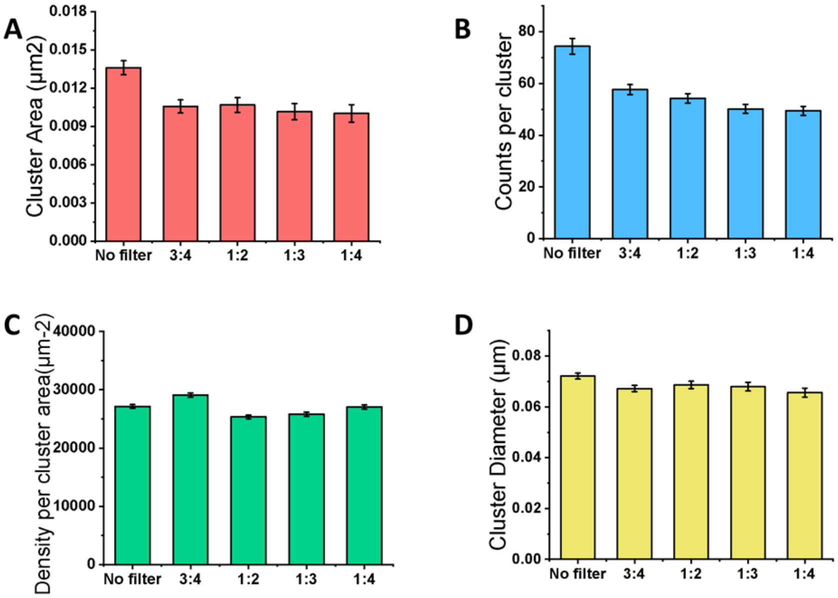

Figure B.4: CD9 localizations in PEC cells obtained by labeling with polyclonal secondary antibodies. Analysis with different post-processing filter conditions. (A) Cluster area. (B) Number of localization counts per cluster. (C) Density of receptors per cluster area. (D) Diameter of clusters.

Synthèse de thèse

Étude par imagerie de molécule unique de la régulation de la nano-organisation des récepteurs EGFR : application aux mécanismes physiopathologiques dans les maladies rénales. L'objectif de cette thèse a été d'étudier la nano-organisation membranaire des récepteurs EGFR et sa régulation, et en particulier le rôle des tétraspanines CD9 dans cette régulation, avec deux techniques optiques avancées complémentaires, la microscopie de super-résolution et le suivi de molécules uniques. Nos résultats indiquent que, dans les cellules pariétales épithéliales (PECglomérulaires les récepteurs EGFR sont, au moins partiellement, localisés dans des nanodomaines enrichis en tétraspanines CD9 et permettent ainsi de comprendre le rôle des protéines CD9 dans l'évolution de maladies rénales inflammatoires observé auparavant sur des modèles animaux. **Chapitre 1**

Dans notre vie quotidienne, nous consommons différentes substances, certaines sont toxiques, d'autres peuvent dépasser les besoins quotidiens de notre organisme. Par conséquent, pour maintenir le niveau de substances circulant dans le corps et pour éviter une accumulation de substances inutilisées ou toxiques, le rein doit filtrer les molécules solubles dans le sang, contrôler le volume des fluides corporels, équilibrer l'osmolalité sanguine à l'intérieur du corps, équilibrer les concentrations acido-basiques, ajuster les concentrations d'électrolyte et éliminer les toxines. De plus, les reins jouent également un rôle important dans la conversion de la vitamine D en sa forme activée, le calcitriol, que le corps peut ensuite utiliser.

Dans le premier chapitre, je présente un aperçu de la structure du rein et des mécanismes de certaines maladies rénales inflammatoires. Dans le rein, le néphron est la plus petite unité de filtration au sein duquel se trouve le glomérule. Le sang qui pénètre dans le glomérule par l'artériole afférente est d'abord filtré dans la barrière de filtration glomérulaire. Après cette étape de filtration, le sang circule vers les vaisseaux sanguins par l'artériole efférente tandis que l'eau et les petites molécules atteignent l'espace de Bowman. Les cellules épithéliales pariétales (PEC) qui tapissent la capsule de Bowman sont impliquées dans le processus de filtration du rein. Certains facteurs de croissance sont beaucoup plus fortement exprimés dans les PEC au cours de certaines maladies rénales que dans les PEC d'un rein sain. Après une lésion rénale, les cellules PEC sont activées et prolifèrent pour envahir l'espace de Bowman et pour former un croissant ce qui dégrade la fonction de filtration glomérulaire. L'apoptose des PEC en prolifération dans les croissants produit alors du tissu cicatriciel.

Chapitre 2

Alors que le premier chapitre présente le tableau d'ensemble des maladies rénales inflammatoires et l'implication cellulaire dans ces maladies, le deuxième chapitre résume brièvement l'organisation membranaire et les mécanismes moléculaires impliqués dans ces maladies rénales.

La membrane cellulaire est un composant essentiel de la cellule qui renferme le cytoplasme cellulaire et les autres parties de la cellule. Dans les cellules animales, il n'y a pas de paroi cellulaire. De ce fait, la membrane joue le rôle d'une barrière qui protège les autres composants cellulaires de l'environnement extérieur avec une propriété de semi-perméabilité unique qui ne permet qu'à certaines molécules de traverser la membrane tout en empêchant les autres d'entrer et de sortir de la cellule.

La membrane n'est pas une simple bicouche lipidique à l'intérieur de laquelle se déplacent les protéines membranaires librement; la plupart des protéines membranaires sont organisées en différents nanodomaines. Ces domaines peuvent être enrichis en certains types de lipides tels que le cholestérol et les sphingolipides (radeaux, où se trouvent les protéines ancrées au GPI) ou en protéines telles que la tétraspanine (domaines membranaires enrichis en tétraspanine, TEM). L'organisation de la membrane est également affectée par le cytosquelette d'actine sous-jacent et par la fixation de protéines au filaments d'actine (modèle picket-and-fence).

Les protéines de la membrane cellulaire jouent un rôle essentiel dans la signalisation cellulaire et les interactions cellulaires. Les récepteurs du facteur de croissance épidermique (EGFR) appartiennent à la famille ErbB de récepteurs tyrosine kinases (RTK).

EGFR et CD9 sont deux protéines transmembranaires impliquées dans les maladies rénales inflammatoires.

Les récepteurs à l'EGF sont impliqués dans de nombreuses activités cellulaires et dans de nombreuses maladies cancéreuses. Ainsi, ils ont été largement étudiés dans la recherche sur le cancer et la biophysique.

Le CD9 fait partie de la famille des protéines tétraspanines, il est aussi appelé Tspan 29. Similaire aux autres membres de la famille des tétraspanines, il possède quatre domaines transmembranaires traversant la membrane. La protéine CD9 est associée à différentes activités cellulaires, notamment la motilité, la prolifération, la différenciation, la fusion et l'adhésion. Comme le CD9 est impliqué dans diverses activités cellulaires, il joue un rôle essentiel dans de nombreux processus physiologiques et pathologiques, notamment la fusion spermatozoïde-ovule, la croissance des neurites, la formation de myotubes, les infections virales, la tumorigénicité et les métastases. De plus, le CD9 est également un composant de TEM et a des interactions directes ou indirectes avec d'autres protéines membranaires telles que les métalloprotéinases, les canaux ioniques, les récepteurs de facteurs de croissance, les transporteurs, les transducteurs de signal et le cytosquelette et pourrait agir comme récepteur de cytokines. Le CD9 peut potentiellement altérer l'activité de ces molécules par différents mécanismes tels que leur confinement sélectif dans les TEM, ce qui entraverait leur accès à leurs substrats ou la liaison avec leurs ligands extracellulaires ou intracellulaires.

L'inhibition de l'EGFR ou la déplétion des protéines CD9 peuvent globalement améliorer l'évolution de la glomérulonéphrite rapidement progressive (RPGN) dans des modèles murins. Par conséquent, dans ma thèse, j'ai étudié la relation entre ces deux protéines membranaires des cellules épithéliales pariétales et les mécanismes moléculaires pouvant expliquer leur rôle dans les maladies rénales. Notre hypothèse est que, bien que l'EGFR se trouve généralement confiné dans les nanodomaines membranaires de type radeau dans plusieurs types cellulaires, il peut être confiné dans des domaines enrichis en tétraspanine dans les cellules pariétales épithéliales. En effet, cela expliquerait le rôle du CD9 dans les maladies rénales.

Chapitre 3

Pour étudier la relation entre l'EGFR et la protéine CD9, nous avons utilisé deux méthodes de microscopie : le suivi de molécules uniques et la technique de microscopie à super-résolution.

Dans ce chapitre, différentes techniques de microscopie ont été abordées. Chaque méthode a des avantages et des inconvénients. Par rapport à la microscopie conventionnelle, les techniques de super-résolution peuvent donner une résolution jusqu'à 10 à 20 nm, ce qui révèle de nombreusesstructures biologiques. La microscopie à illumination structurée (SIM) fournit une résolution d'environ 100 nm tandis que la microscopie STED (Stimulated Emission Depletion) offre une résolution plus élevée que la microscopie SIM, de l'ordre de 10 à 20 nm mais nécessite un second laser intense pour l'étape de déplétion, nocive pour les cellules. La microscopie de localisation par photoactivation (PALM) et la microscopie à reconstruction optique stochastique (STORM) sont basées sur le même principe d'allumer et d'éteindre les marqueurs fluorescents : alors que dans PALM on utilise des protéines fluorescentes photoactivables pour obtenir les états "on" et "off", la microscopie STORM utilise des colorants organiques fluorescents dans un environnement réduisant les fluorophores et piégeant l'oxygène pour obtenir l'effet de clignotement désiré. DNA-PAINT est similaire à PALM et STORM mais nécessite des étapes de préparation d'échantillon plus compliquées. Dans cette thèse, nous avons choisi la méthode STORM pour étudier le récepteur EGF et la protéine CD9 et leur organisation dans la membrane cellulaire, comme décrit dans le chapitre 4. La technique STORM présente les avantages suivants : Les étapes de préparation des échantillons sont simples et les colorants organiques ont un rendement quantique et une intensité de fluorescence élevés, ce qui est bénéfique pour la précision de localisation des molécules dans l'image. De plus, la technique STORM offre une haute résolution d'environ 10 à 20 nm ce qui est beaucoup plus petit que les tailles typiques des nanodomaines membranaires d'environ 100-200 nm que nous voulons observer. Cependant, l'environnement appauvri en oxygène et réducteur utilisé dans STORM est plus approprié pour les échantillons fixés.

Dans le suivi de molécules uniques (single-particle tracking, SPT), les molécules d'intérêt sont marquées par des molécules fluorescentes ou des nanoparticules luminescentes. Les mouvements de ces molécules sont observés pendant une certaine période. En déterminant la position de toutes les molécules sur des images successives, toutes les transitions d'une position à la suivante en fonction du temps sont déduites ce qui donne la trajectoire de la molécule. La figure 1 montre le principe du SPT. A partir des trajectoires des molécules suivies, des informations sur les molécules peuvent être extraites telles que la diffusivité de la molécule, la zone de confinement, les forces et le potentiel de confinement agissant sur la molécule.

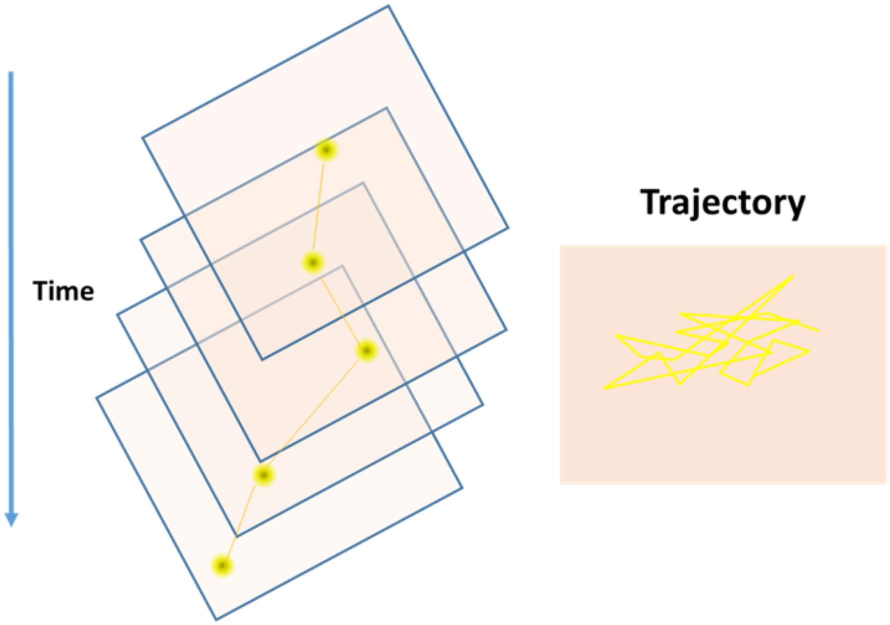

Figure B.5: Principe de la technique de suivi de molécules uniques.

Chapitre 4

Dans ce chapitre, nous avons utilisé la technique STORM pour étudier l'organisation des récepteurs EGF et des protéines CD9 dans les cellules PEC et PEC deplétées en CD9, appelées cellules shCD9 PEC. Dans nos expériences, nous avons utilisé à la fois des anticorps secondaires polyclonaux pour obtenir un signal par molécule plus élevé et des « nanobodies » comme anticorps secondaires pour minimiser l'incertitude sur le nombre de fluorophores marquant chaque protéine EGFR. Nous avons ainsi pu vérifier que les anticorps secondaires polyclonaux et nanobodies donnent des résultats similaires. Pour l'analyse, nous avons utilisé le plug-in ThunderSTORM de Fiji pour déterminer la localisation de chaque molécule. Le logiciel fournit plusieurs options pour le prétraitement et de post-traitement des images.

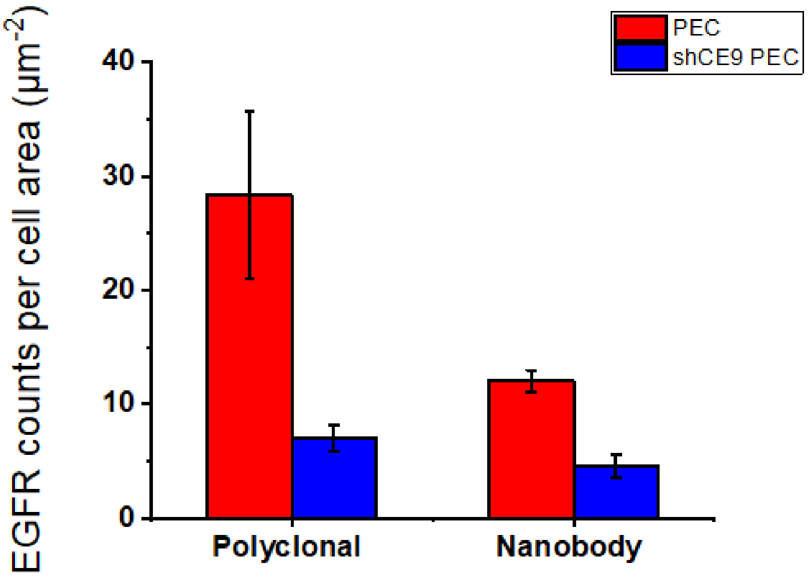

Figure B.6: Nombre de récepteurs EGF par zone cellulaire dans PEC et shCD9 PEC.

En utilisant ces étapes de pré-traitement et de post-traitement, nous pouvons éliminer les artefacts créés par la mesure qui pourraient interférer avec les résultats. Nous avons fait varier les valeurs des différents paramètres dans les étapes de pré-traitement et de post-traitement pour déterminer leurs effets sur les résultats et identifier leurs valeurs optimales. La méthode de clustering basée sur le logiciel SR-Tesseler, a ensuite été utilisée pour déterminer les clusters de protéines à partir de l'ensemble complet des points de localisation pour chaque molécule obtenus à l'issue de l'étape d'analyse des images. Bien que la technique STORM rencontre des difficultés liées à la dérive mécanique du montage expérimental, c'est une technique puissante qui offre une résolution bien au-delà de la limite de diffraction. À partir d'expériences STORM à une couleur, les distributions d'EGFR et de CD9 ont été révélées. Les récepteurs de l'EGF se trouvent principalement localisés dans des nanodomaines de taille moyenne d'environ 100 nm. Dans les cellules PEC déplétées en CD9, l'EGFR est confiné dans des nanodomaines avec une taille de domaine un peu plus grande que dans les cellules PEC. De plus, l'absence de CD9 affecte à la fois l'organisation membranaire de EGFR et sa population. Le nombre de récepteurs à l'EGF par nanodomaine diminue dans les cellules shCD9 PEC par rapport aux PEC de type sauvage (Figure 2). Par ailleurs, la densité des récepteurs EGF dans le nanodomaine ainsi que la densité moyenne dans l'ensemble de la cellule diminue avec la déplétion de CD9. Avec une distribution semblable aux récepteurs EGF, les CD9 sont situés principalement à l'intérieur de clusters, avec une densité inférieure à celle des récepteurs EGF. Notez que la protéine CD9 dans les cellules PEC de souris saines est exprimée à des niveaux inférieurs à ceux des cellules PEC des modèles murins malades.

Notre interprétation de ces résultats est que les récepteurs à l'EGF sont, au moins en partie, confinés dans des domaines enrichis en tétraspanine CD9. Lorsque CD9 est déplété dans les cellules shCD9 PEC, les récepteurs EGF ne trouvent pas l'environnement approprié pour s'insérer dans la membrane cellulaire et y sont présents en nombre et en densité inférieurs. Par ailleurs, les domaines de confinement des récepteurs EGF dans les cellules shCD9 PEC sont probablement plus grands en raison du nombre beaucoup plus faible de protéines CD9 disponibles. Par ailleurs, nos résultats expliquent aussi pourquoi Lazareth et al., Nat. Commun. 2019, ont observé un nombre d'EGFR phosphorylés plus faible dans les cellules PEC déplétées en CD9 : il y a un nombre de récepteurs EGF inférieur par cellule, un nombre de récepteurs EGF inférieurdans chaque domaine de confinement, et une plus faible densité d'EGFR à l'intérieur de chaque domaine de confinement. Comme l'activation de l'EGFR n'a lieu qu'après dimérisation, lorsque le nombre de récepteurs EGF dans la membrane cellulaire est plus faible, nous nous attendons à ce que la signalisation soit moins efficace. . Par conséquent, une densité de récepteurs plus faible dans les domaines de confinement membranaire signifie que le processus de dimérisation et d'activation sera plus lent et moins efficace. Comme l'activation du récepteur EGF conduit à la prolifération et à la migration cellulaire, cette découverte explique également pourquoi l'évolution de RPGN s'améliore après la suppression globale de CD9 chez la souris.

En utilisant l'imagerie STORM à deux couleurs, la distribution relative de l'EGFR et du CD9 dans la membrane PEC a pu être révélée. On retrouve un chevauchement partiel entre les clusters de EGFR et de CD9. Une incertitude demeure cependant car, dans notre analyse, la correction de la dérive mécanique est faite indépendamment pour les images de chaque couleur (Figure 3). Il existe donc un déplacement non nul entre les images des deux couleurs. Pour contourner ce problème, nous avons introduit des nanoparticules d'or sur les lames de microscope en tant que marqueurs fiduciaires visibles dans les images enregistrées pour chaque couleur. Une analyse approfondie de ces derniers résultats devrait confirmer et quantifier le degré du chevauchement entre les clusters CD9 et EGFR et notre interprétation de la raison pour laquelle la déplétion de CD9 affecte la population et la distribution de l'EGFR.

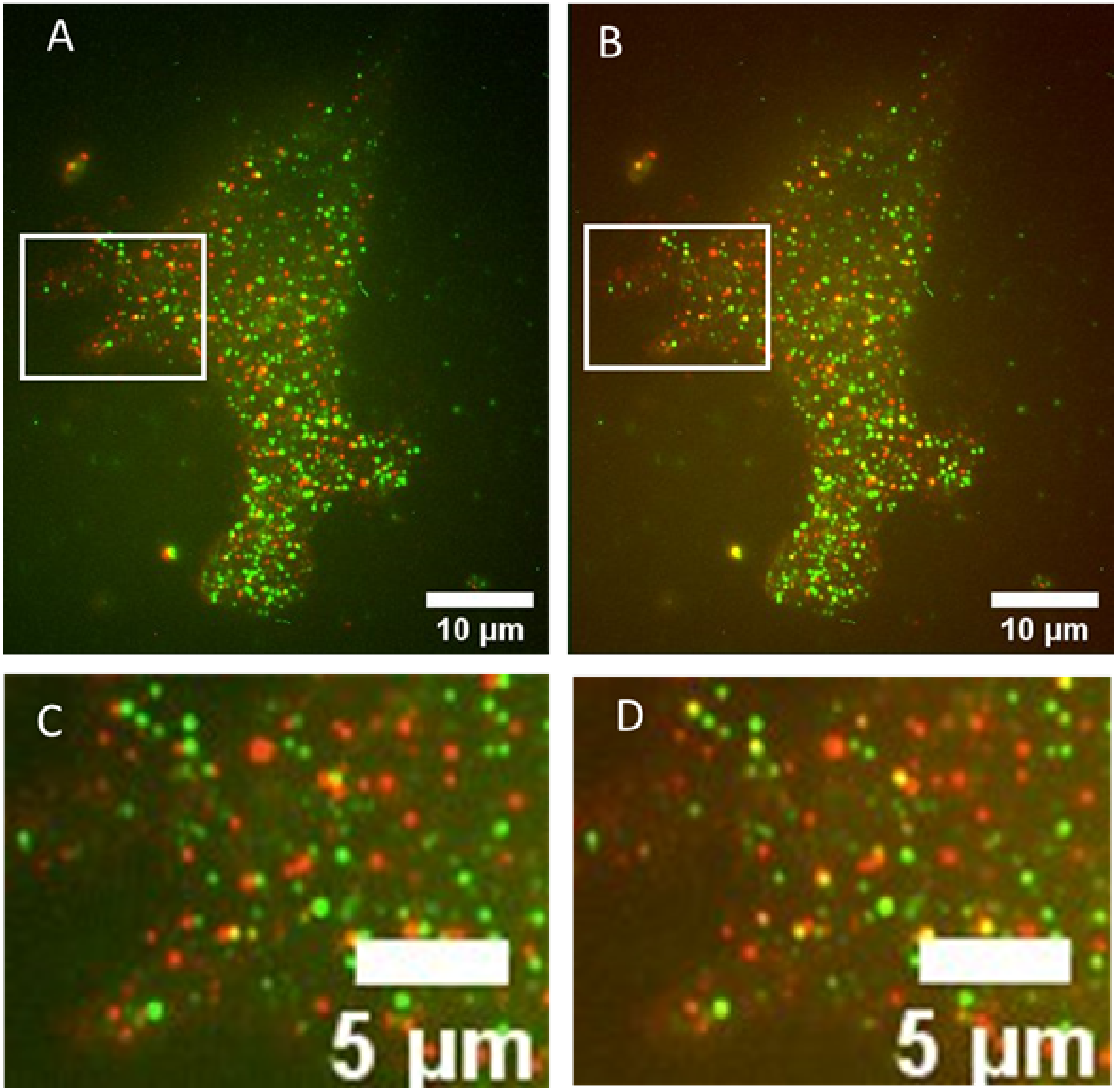

Figure B.7: Distribution de l'EGFR (rouge) et de la protéine CD9 (verte) dans une cellule PEC (A) avant la correction de la dérive mécanique, (B) après la correction de la dérive. (C), (D) Une région a été agrandie avant et après la correction de la dérive, respectivement.

Chapitre 5

Dans ce chapitre, nous avons utilisé le suivi de molécule unique pour comprendre l'architecture du confinement et la dynamique des récepteurs EGF dans quatre types cellulaires différents : PEC, shCD9 PEC, cellules musculaires lisses vasculaires (CMLV) et MDCK (cellules Madin-Darby Canine Kidney). Les récepteurs EGF ont été marqués avec des nanoparticules d'oxyde (vanadate d'Yttrium) dopées à l'Europium de taille de 30-40 nm fonctionnalisées et conjuguées au ligand EGF du récepteur EGFR. Puis lesmouvements des récepteurs ont été enregistrés à l'aide d'un microscope à champ large. La position de chaque récepteur a été déterminée en ajustant la tâche d'émission la nanoparticule limitée par la diffraction (Point Spread Function, PSF – en effet, nous pouvons considérer les nanoparticules comme des points sources de lumière) avec une gaussienne 2D. Le confinement des récepteurs à l'EGF dans les CMLV a été analysé initialement en scindant manuellement les trajectoires en portions de mouvement confiné et de mouvement libre.. Ensuite, les parties confinées ont été analysées par inférence Bayésienne pour déterminer la constante de raideur du paysage énergétique de confinement (en supposant un potentiel de confinement harmonique) et le coefficient de diffusion du récepteur. Dans un deuxième temps, nous avons introduit une nouvelle méthode, en collaboration avec Yann Lanoiselée et Denis Grebenkov, basée sur la matrice de distance entre points de la trajectoire et la détermination de blocs de confinement au sein de cette matrice pour déterminer les parties confinées et libres des trajectoires des récepteurs EGFR. Cette analyse dite structurale permet de diviser automatiquement la trajectoire en portions de mouvement libre et confiné et fonctionne plus efficacement que les approches automatisées précédentes. Puis les portions confinées ont été analysées par l'approche de ≪ mean square displacement ≫ (MSD) en supposant un mouvement Brownien confiné à l'intérieur d'un paysage énergétique harmonique pour extraire le coefficient de diffusion et la constante de raideur du paysage énergétique. L'aire du domaine de confinement est déterminée de manière empirique en prenant le rayon d'un cercle contenant 95% des points de la trajectoire.

Les deux méthodes donnent des résultats similaires pour les expériences de suivi de EGFR dans les cellules CMLV. En utilisant l'inférence Bayésienne, nous avons trouvé dans les cellules CMLV un coefficient de diffusion moyen de $D = 0{,}0072 \pm 0{,}0006$ ($\mu m^2/s$) et une valeur moyenne de la constante de raideur du potentiel harmonique de $k_r = 14{,}6 \pm 1{,}1$ (pN/µm) pour N= ????. En utilisant l'analyse structurale pour décomposer les trajectoires puis en analysant les portions confinées par MSD, nous avons trouvé un coefficient de diffusion moyen de l'EGFR dans les cellules témoins CMLV de 0,0070 ± 0,009 ($\mu m^2/s$) et une valeur moyenne de la constante de raideur du potentiel de confinement de 12,7 ± 1,0 (pN/µm). Lors de l'application de cholestérol oxydase aux cellules CMLV pour perturber les radeaux riches en cholestérol et en sphingolipides, le coefficient de diffusion des récepteurs à l'EGF augmente tandis que la constante de raideur diminue. L'aire du domaine de confinement devient plus grande après le traitement par l'enzyme cholestérol oxydase. Cela signifie que les récepteurs à l'EGF sont confinés dans des domaines enrichis en cholestérol dans les cellules CMLV. En effet, lorsque le pourcentage de cholestérol diminue, cela entraîne une déstabilisation partielle desdomaines de confinement, les domaines deviennent moins compacts et le potentiel de confinement moins raide conduisant à l'augmentation du coefficient de diffusion et à la diminution de la raideur du potentiel. De manière similaire à l'élimination du cholestérol, la dépolymérisation de l'actine entraîne également une augmentation de la taille du domaine de

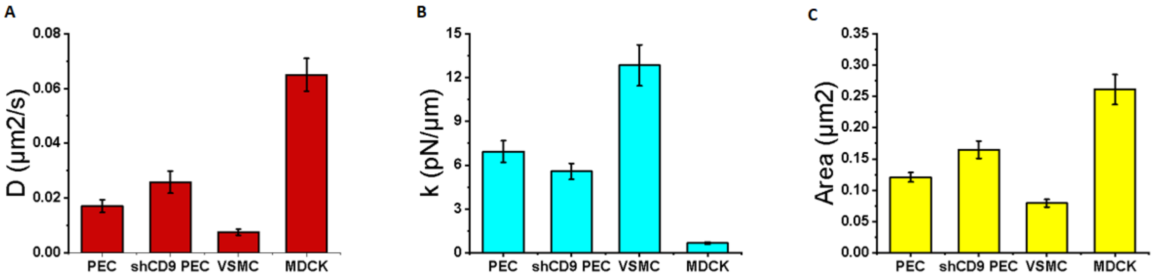

Figure B.8: Caractéristiques de confinement des récepteurs à l'EGF dans différents types cellulaires : PEC, shCD9 PEC, CLMV et MDCK. (A) Coefficient de diffusion D, (B) Raideur du potentiel harmonique de confinement k_r (C) aire du domaine de confinement.

confinement et du coefficient de diffusion des récepteurs à l'EGF dans les CMLV, tandis que la raideur du potentiel de confinementdiminue considérablement. Nous attribuons cela au fait que les récepteurs à l'EGF comportent un domaine capable de se fixer directement sur les filaments d'actine. Par conséquent, en utilisant le suivi de particules uniques marquant les récepteurs à l'EGF, nous avons constaté que ces récepteurs, dans les cellules CMLV, sont confinés dans un domaine enrichi en cholestérol et se lient également au cytosquelette d'actine, cette liaison contribuant également au confinement des récepteurs à l'EGF. Ainsi, les récepteurs à l'EGF dans les CMLV se comportent de manière similaire aux récepteurs à l'EGF dans les cellules MDCK (Chao Yu, Ph. D. thesis Ecole polytechnique, 2019). Ils sont localisés dans des domaines membranaires enrichis en cholestérol et leur confinement est dépendant du cytosquelette d'actine. De plus, j'ai découvert que l'incubation des cellules MDCK avec l'enzyme sphingomyélinase qui dégrade la sphingomyéline entraîne une forte réduction du nombre de récepteurs à l'EGF dans la membrane indiquant que les récepteurs à l'EGF sont situés dans des radeaux riches en cholestérol et en sphingolipides dans ces cellules. En revanche, les domaines de confinement des récepteurs EGFR se comportent différemment dans les cellules PEC par rapport aux cellules MDCK. Le confinement des récepteurs EGFR n'est pas affecté par le traitement avec la sphingomyélinase : le coefficient de diffusion, la raideur du potentiel de confinement et l'aire du domaine restent inchangés. De plus, le nombre total de récepteurs dans la membrane cellulaire ne change pas après le traitement de ces cellules par sphingomyélinase. Seule l'élimination du cholestérol affecte les caractéristiques de confinement des récepteurs EGFR. Les récepteurs à l'EGF dans les cellules déplétées en CD9, shCD9 PEC, sont confinés dans des domaines plus larges que dans les cellules PEC « wild type ». Cependant, leur coefficient de diffusion et la constante de raideur du potentiel confinant ces récepteurs dans les cellules shCD9 PEC ne sont pas significativement différents de ceux dans les cellules PEC (Figure 4). Ces résultats de suivi de récepteurs individuels confirment ceux obtenus par dSTORM. Les deux méthodes mènent à la conclusion que le nombre de récepteurs à l'EGF dans la membrane cellulaire est beaucoup plus petit dans les cellules shCD9 PEC que dans les cellules PEC. Les deux méthodes indiquent que les récepteurs EGFR dans les cellules PEC sont, au moins partiellement, situés dans des domaines enrichis en CD9, contrairement à ce que nous observons dans les cellules MDCK et CMLV. Ainsi, le type du domaine de confinement des récepteurs EGFR dépend du type cellulaire ce qui explique les résultats parfois contradictoires rapportés dans la littérature.

Conclusion

Dans ma thèse, j'ai étudié la distribution des récepteurs à l'EGF dans la membrane de différents types cellulaires, en particulier le lien entre les récepteurs à l'EGF et les protéines CD9 dans les cellules épithéliales pariétales (PEC) qui jouent un rôle important dans les maladies rénales inflammatoires. La structure rénale et les mécanismes des maladies rénales inflammatoires ont été introduits dans le premier chapitre. L'implication des cellules épithéliales pariétales dans la fonction rénale et les maladies rénales inflammatoires a également été décrite. L'architecture de la membrane cellulaire a ensuite été introduite. Divers modèles de confinement membranaire ont été examinés, tels que le modèle des radeaux, nanodomaines riches en cholestérol et en sphingolipides, la fixation directe de protéines sur les filaments d'actine, le modèle ≪ picket-and-fence ≫ et les domaines enrichis en tétraspanines. Le fait que l'inhibition des récepteurs EGFR ou la déplétion en CD9 dans les cellules glomérulaires induit une protection dans l'évolution des maladies rénales inflammatoires témoigne de la participation de ces protéines aux mécanismes pathophysiologiques des maladies rénales inflammatoires. . Le rôle des récepteurs EGFR dans ces maladies peut être attribué au fait que l'activation de ces récepteurs est impliquée dans les réponses cellulaires de prolifération et de migration, processus responsables de l'endommagement de l'espace de Bowman et de la capacité de filtration glomérulaire. Le rôle des protéines CD9 cependant est moins clair. Nous avons essayé de vérifier si le rôle des protéines CD9 était dicté par le fait que les récepteurs EGFR sont confinés dans des domaines enrichis en CD9. Cette hypothèse de travail permet d'expliquer l'implication de CD9 dans l'évolution des maladies rénales inflammatoires dans des modèles souris. De nombreuses méthodes microscopiques ont été utilisées pour comprendre l'architecture et les composants de la membrane cellulaire.. La microscopie conventionnelle a une limite de résolution d'environ 200-300 nm. Par conséquent, de nombreuses organisations biologiques ne peuvent pas être résolues sous un microscope conventionnel. La microscopie électronique peut atteindre une très haute résolutionmais présente une faible sélectivité pour détecter les différents composants cellulaires. La microscopie à fluorescence à super-résolution est une technique puissante qui résout le problème de la résolution limitée de lamicroscopie optique tout en conservant une grande sélectivité. Les techniques de super-résolution peuvent atteindre une résolution de 10 nm, capable de révéler de nombreuses structures importantes de la cellule. Cependant, la microscopie à super-résolution de type STORM est plus adaptée aux échantillons fixés. Ainsi, j'ai utilisé deux techniques complémentaires, la microscopie à super-résolution et le suivi de molécules uniques qui est une méthode idéale pour étudier la dynamique des protéines dans les cellules vivantes.

En utilisant la technique de microscopie à reconstruction optique stochastique (STORM), nous pouvons abaisser la résolution d'un microscope à environ 20 nm, résolution avec laquelle j'ai pu étudier quantitativement la distribution des récepteurs EGFR et des protéines CD9 dans la membrane cellulaire de cellules PEC et shCD9PEC. En utilisant la méthode de clustering par tessellation, les paramètres importants des clusters de EGFR et des domaines enrichis en CD9 ont été révélés tels que la taille moyenne des domaines, le nombre de récepteurs par domaine, la densité des récepteurs EGFR et des protéines CD9 à l'intérieur des clusters ainsi que leurs densité moyenne sur la surface de la cellule entière. Nous avons constaté que, dans les cellules appauvries en CD9 (shCD9 PEC), le nombre de récepteurs à l'EGF dans la membrane cellulaire est considérablement réduit. De plus, l'aire des domaines EGFR est plus importante dans les cellules sh CD9 PEC que dans les cellules PEC.

Nos données confirment la diminution précédemment observée du nombre de récepteurs EGFR par cellule dans des expériences de Western blot. Nos expériences indiquent de plus que ce n'est pas uniquement le nombre total de récepteurs EGFR dans une cellule qui est diminué, comme indiqué par les expériences de Western blot mais que c'est le nombre de récepteurs EGFR dans la membrane cellulaire qui est diminué. Ces résultats montrent clairement que les protéines CD9 régulent la présence des récepteurs EGFR dans la membrane cellulaire. Les résultats de l'imagerie STORM à deux couleurs que j'ai obtenus apportent la réponse à la question pourquoi la déplétion de CD9 dans les cellules PEC a pour conséquence la réduction du nombre d'EGFR dans la membrane ainsi que dans la cellule entière : les récepteurs à l'EGF dans les cellules PEC sont, au moins partiellement, localisés dans des clusters ou domaines enrichis en tétraspanine. En effet, nous avons trouvé une colocalisation partielle entre les clusters membranaires de CD9 et de EGFR tandis qu'il existe une colocalisation négligeable entre les récepteur EGFR et le récepteur de transferrine, un récepteur de référence connu pour être situé dans des domaines délimités par les filaments d'actine sous-jacents à la membrane. Une analyse quantitative plus poussée de ces données devrait confirmer ce résultat.

Pour mieux comprendre la nature du confinement des récepteurs EGFR dans les cellules PEC et dans d'autres types cellulaires nous avons étudié, dans le chapitre 5, la dynamique des récepteurs EGFR en utilisant le suivi de récepteurs uniques marqués par des nanoparticules luminescentes dopées aux terres rares.. Nous avons introduit une nouvelle méthode pour analyser les trajectoires des molécules : en utilisant la méthode dite structurale [253], nous avons pu déterminer les parties libres et confinées des trajectoires des récepteurs de manière automatique excluant tout biais humain dans l'analyse. Nous avons vérifié que cette approche donnent des résultats similaires avec notre méthode conventionnelle basée sur la division manuelle de la trajectoire. Nous avons ensuite analyser le parties confinées des trajectoires par inférence Bayésienne pour extraire le coefficient de diffusion et la constante de raideur du potentiel de confinement. Dans les cellules CMLV, les récepteurs à l'EGF se trouvent localisés dans des domaines enrichis en cholestérol et se lient également directement au cytosquelette d'actine, de manière similaire à ce qui a été observé dans les cellules MDCK. Lors de l'application de cholestérol oxydase pour perturber ces domaines ou de l'utilisation de latrunculine B pour dépolymériser les filaments d'actine, nous avons observé que le coefficient de diffusion des récepteurs augmente tandis que les forces agissant sur lui en raison du potentiel de confinement diminuent. Alors que le confinement des récepteurs EGFR dans les domaines de la membrane cellulaire des cellules MDCK est dépendante de la sphingomyéline, l'application de sphingomyélinase dans les cellules PEC ne modifient pas les caractéristiques des domaines de confinement des récepteurs EGFR . Lors de la perturbation des domaines EGFR de la membrane cellulaire des cellules PEC avec la cholestérol oxydase, en revanche, nous avons constaté que les récepteurs à l'EGF sont toujours confinés mais dans des domaines de taille plus grande, avec un coefficient de diffusion plus élevé et une constante de raideur plus faible pour le potentiel de confinement. Ces deux derniers résultats, le fait que le confinement des récepteurs EGFR est cholestérol-dépendant mais indépendant de la sphingomyéline dans les cellules PEC, combiné à l'observation de nombres inférieurs d'EGFR dans les cellules appauvries en CD9, nous amènent à la conclusion que les récepteurs EGFR dans les cellules PEC résident dans des nanodomaines enrichis en tétraspanine, contrairement à ce qui est observé dans d'autres types de cellules, comme les cellules MDCK, où les EGFR résident dans des domaines de type radeau riches en cholestérol et en sphingomyéline. Ainsi, l'organisation membranaire des récepteurs EGFR est régulée par les tétraspanines CD9 dans les cellules PEC ce qui affecte directement leur fonction et explique l'implication des protéines CD9 dans les maladies rénales inflammatoires. Pour approfondircet aspect, dans notre équipe, nous avons également mesuré la production d'espèces réactives d'oxygène (reactive oxygen species; ROS) lors de l'activation de l'EGFR par son ligand EGF en utilisant les nanoparticules de vanadate dopées à l'europium comme nanocapteurs ROS à l'intérieur du cytosol cellulaire [258]. En effet, l'activation de l'EGFR est connue pour activer la production de ROS par les enzymes NAPDH oxydase (Nox). Les mesures des espèces réactives d'oxygène (ROS) dans les cellules PEC et shCD9 PEC (données non présentées) effectuées par Maxime MAUVIEL, doctorant de notre équipe, a démontré que la concentration des ROS suite à l'activation des récepteurs EGFR dans les cellules PEC est beaucoup plus faible dans les cellules appauvries en CD9 (shCD9 PEC) que dans les cellules PEC témoins. Ceci confirme une conséquence fonctionnelle sur l'activité des récepteurs EGFR de la déplétion en CD9 dans les cellules PEC.

En conclusion, dans le cadre de cette thèse, j'ai étudié l'interaction moléculaire entre deux protéines dans la membrane cellulaire, les protéines CD9 et les récepteurs EGFR. En utilisant deux techniques de microscopie à l'échelle moléculaire, j'ai non seulement cartographié la distribution de ces deux protéines par dSTORM mais aussi exploré la dynamique des récepteurs EGFR par suivi de molécules individuelles. En perturbant les nanodomaines membranaires avec différents traitements pharmacologiques et en dépolymérisant le cytosquelette d'actine, nous avons également étudié la composition des domaines de confinement dans divers types cellulaires et avons obtenu des preuves complémentaires que les récepteurs EGFR sont situés dans des domaines enrichis en tétraspanine dans les cellules PEC alors que les données précédentes de la littérature et nos propres données montrent que les récepteurs EGFR sont confinés dans des domaines de type radeau riches en cholestérol et en sphingolipides. En outre, nous avons mis en œuvre une nouvelle méthode pour identifier les portions de trajectoire de mouvement confiné par rapport au mouvement libre ce qui permet une analyse automatique des données sans biais humains. Pour mieux comprendre comment l'organisation moléculaire de ces protéines dans la membrane cellulaire affecte la fonction cellulaire et, en fin de compte, les maladies rénales, des recherches supplémentaires peuvent être menées. À partir d'expériences de suivi de molécules uniques, nous avons constaté que la taille du domaine, le coefficient de diffusion et la constante de raideur du potentiel de confinement des récepteurs EGFR dans les cellules CMLV et MDCK sont radicalement différents même si le confinement des récepteurs dans les deux types cellulaires est cholestérol- et actine-dépendant . Il serait intéressant de savoir si le domaine de confinement des récepteurs EGFR dans les cellules CMLV est également enrichi en sphingolipides comme dans les cellules MDCK. Par ailleurs, la taille des domaines de confinement dans les cellules CMLV est beaucoup plus petite que celle dans les cellules MDCK soulevant la question : la taille du domaine de confinement joue-t-elle un rôle fonctionnel sur l'activation des récepteurs? La densité des récepteurs dans les nanodomaines est déterminée par la taille du domaine et par le nombre de récepteurs par domaine. Par conséquent, il serait également intéressant d'utiliser la technique STORM pour déterminer le nombre de récepteurs par domaine et dans la membrane cellulaire des cellules CMLV et MDCK. On s'attend à ce que, dans les cellules cancéreuses MDCK, les récepteurs à l'EGF soient surexprimés. Même si la taille des domaines de confinement des récepteurs EGFR est plus grande dans les cellules MDCK que dans CMLV, l'efficacité de l'activation des récepteurs devrait dépendent à la fois de la densité et du nombre total de récepteurs dans le domaine. Dans PEC et shCD9 PEC, nous avons montré que l'EGFR est localisé partiellement dans des domaines enrichis en tétraspanine qui sont enrichis en cholestérol mais pas en sphingomyéline.

List of Figures

Bibliography

1. Yu, C. Quantitative Study of Membrane Nano-organization by Single Nanoparticle Imaging, 162.
2. Lazareth, H. *et al.* The tetraspanin CD9 controls migration and proliferation of parietal epithelial cells and glomerular disease progression. *Nature Communications* **10,** 3303 (Dec. 2019).
3. Bollée, G. *et al.* Epidermal growth factor receptor promotes glomerular injury and renal failure in rapidly progressive crescentic glomerulonephritis. *Nature Medicine* **17,** 1242–1250 (Sept. 25, 2011).
4. Lote, C. J. in *Principles of Renal Physiology* (ed Lote, C. J.) 21–32 (Springer, New York, NY, 2012).
5. *Kidney Structure — Biology for Majors II* https://courses.lumenlearning.com/wm-biology2/chapter/kidneys/ (2021).
6. Lote, C. J. *Principles of Renal Physiology* (Springer New York, New York, NY, 2012).
7. Bertram, J. F., Douglas-Denton, R. N., Diouf, B., Hughson, M. D. & Hoy, W. E. Human nephron number: implications for health and disease. *Pediatric Nephrology (Berlin, Germany)* **26,** 1529–1533 (Sept. 2011).
8. *Nephron – Structure — BIO103: Human Biology* https://courses.lumenlearning.com/suny-dutchess-ap1/chapter/nephrons-structure/ (2021).
9. Boron, W., Boron, W. F. & Boulpaep, E. L. *Medical Physiology: A Cellular and Molecular Approach* Google-Books-ID: PwJtAAAAMAAJ. 1380 pp. (W.B. Saunders, 2003).
10. Scott, R. P. & Quaggin, S. E. The cell biology of renal filtration. *Journal of Cell Biology* **209,** 199–210 (Apr. 27, 2015).
11. Hall, J. E. & Guyton, A. C. *Guyton and Hall Textbook of Medical Physiology* Google-Books-ID: di5PtQAACAAJ. 1091 pp. (Saunders/Elsevier, 2011).
12. *Glomerular filtration (glomerulus) — Renal physiology (article) — Khan Academy* https://www.khanacademy.org/_render (2021).
13. Akilesh, S. in *Pathobiology of Human Disease* 2716–2733 (Elsevier, 2014).
14. Oddsson, Á., Patrakka, J. & Tryggvason, K. in *Reference Module in Biomedical Sciences* B9780128012383002014 (Elsevier, 2014).

15. Wartiovaara, J. *et al.* Nephrin strands contribute to a porous slit diaphragm scaffold as revealed by electron tomography. *Journal of Clinical Investigation* **114,** 1475–1483 (Nov. 15, 2004).
16. Reiser, J. & Altintas, M. M. Podocytes. *F1000Research* **5,** F1000 Faculty Rev–114 (Jan. 28, 2016).
17. Miner, J. H. The Glomerular Basement Membrane. *Experimental Cell Research* **318,** 973–978 (May 15, 2012).
18. Ohse, T. *et al.* The enigmatic parietal epithelial cell is finally getting noticed: a review. *Kidney International* **76,** 1225–1238 (Dec. 2009).
19. Kuppe, C. *et al.* Novel parietal epithelial cell subpopulations contribute to focal segmental glomerulosclerosis and glomerular tip lesions. *Kidney International* **96,** 80–93 (July 2019).
20. Kiuchi-Saishin, Y. *et al.* Differential expression patterns of claudins, tight junction membrane proteins, in mouse nephron segments. *Journal of the American Society of Nephrology: JASN* **13,** 875–886 (Apr. 2002).
21. Doné, S. C. *et al.* Nephrin is involved in podocyte maturation but not survival during glomerular development. *Kidney International* **73.** Publisher: Elsevier, 697–704 (Mar. 2, 2008).
22. Ohse, T. *et al.* Establishment of conditionally immortalized mouse glomerular parietal epithelial cells in culture. *Journal of the American Society of Nephrology: JASN* **19,** 1879–1890 (Oct. 2008).
23. Ohse, T. *et al.* A new function for parietal epithelial cells: a second glomerular barrier. *American Journal of Physiology. Renal Physiology* **297,** F1566–1574 (Dec. 2009).
24. Igarashi, P. Following the expression of a kidney-specific gene from early development to adulthood. *Nephron. Experimental Nephrology* **94,** e1–6 (2003).
25. Dijkman, H. B. P. M. *et al.* Proliferating cells in HIV and pamidronate-associated collapsing focal segmental glomerulosclerosis are parietal epithelial cells. *Kidney International* **70,** 338–344 (July 2006).
26. Smeets, B. *et al.* The parietal epithelial cell: a key player in the pathogenesis of focal segmental glomerulosclerosis in Thy-1.1 transgenic mice. *Journal of the American Society of Nephrology: JASN* **15,** 928–939 (Apr. 2004).
27. Debiec, H. *et al.* Antenatal membranous glomerulonephritis due to anti-neutral endopeptidase antibodies. *The New England Journal of Medicine* **346,** 2053–2060 (June 27, 2002).
28. Shirato, I., Asanuma, K., Takeda, Y., Hayashi, K. & Tomino, Y. Protein gene product 9.5 is selectively localized in parietal epithelial cells of Bowman's capsule in the rat kidney. *Journal of the American Society of Nephrology: JASN* **11,** 2381–2386 (Dec. 2000).

29. Diomedi-Camassei, F., Ravà, L., Lerut, E., Callea, F. & Van Damme, B. Protein gene product 9.5 and ubiquitin are expressed in metabolically active epithelial cells of normal and pathologic human kidney. *Nephrology, Dialysis, Transplantation: Official Publication of the European Dialysis and Transplant Association - European Renal Association* **20,** 2714–2719 (Dec. 2005).

30. Wiggins, J. E., Goyal, M., Wharram, B. L. & Wiggins, R. C. Antioxidant ceruloplasmin is expressed by glomerular parietal epithelial cells and secreted into urine in association with glomerular aging and high-calorie diet. *Journal of the American Society of Nephrology: JASN* **17,** 1382–1387 (May 2006).

31. Stamenkovic, I., Skalli, O. & Gabbiani, G. Distribution of intermediate filament proteins in normal and diseased human glomeruli. *The American Journal of Pathology* **125,** 465–475 (Dec. 1986).

32. Gharib, S. A. *et al.* Transcriptional Landscape of Glomerular Parietal Epithelial Cells. *PLOS ONE* **9.** Publisher: Public Library of Science, e105289 (Aug. 15, 2014).

33. Flamant, M., Bollee, G., Henique, C. & Tharaux, P.-L. Epidermal growth factor: a new therapeutic target in glomerular disease. *Nephrology Dialysis Transplantation* **27,** 1297–1304 (Apr. 1, 2012).

34. Tang, J., Liu, N. & Zhuang, S. Role of epidermal growth factor receptor in acute and chronic kidney injury. *Kidney International* **83,** 804–810 (May 2013).

35. Smeets, B. *et al.* Detection of activated parietal epithelial cells on the glomerular tuft distinguishes early focal segmental glomerulosclerosis from minimal change disease. *The American Journal of Pathology* **184,** 3239–3248 (Dec. 2014).

36. Webber, W. A. & Blackbourn, J. The permeability of the parietal layer of Bowman's capsule. *Laboratory Investigation; a Journal of Technical Methods and Pathology* **25,** 367–373 (Nov. 1971).

37. Webber, W. A. & Wong, W. T. The function of the basal filaments in the parietal layer of Bowman's capsule. *Canadian Journal of Physiology and Pharmacology* **51,** 53–60 (Feb. 1973).

38. Arakawa, M. & Tokunaga, J. A scanning electron microscope study of the human Bowman's epithelium. *Contributions to Nephrology* **6,** 73–78 (1977).

39. Yoder, B. K. Role of primary cilia in the pathogenesis of polycystic kidney disease. *Journal of the American Society of Nephrology: JASN* **18,** 1381–1388 (May 2007).

40. Volhard, F. & Fahr, T. *Die Brightsche Nierenkrankheit: Klinik, Pathologie und Atlas* (Springer-Verlag, Berlin Heidelberg, 1914).

41. Bajema, I. M. *et al.* Revision of the International Society of Nephrology/Renal Pathology Society classification for lupus nephritis: clarification of definitions, and modified National Institutes of Health activity and chronicity indices. *Kidney International* **93,** 789–796 (Apr. 2018).

42. Kitching, A. R. *et al.* ANCA-associated vasculitis. *Nature Reviews Disease Primers* **6.** Bandiera_abtest: a Cg_type: Nature Research Journals Number: 1 Primary_atype: Reviews Publisher: Nature Publishing Group Subject_term: Autoimmunity; Nephrology; Rheumatology Subject_term_id: autoimmunity; nephrology; rheumatology, 1–27 (Aug. 27, 2020).
43. Couser, W. G. Rapidly Progressive Glomerulonephritis: Classification, Pathogenetic Mechanisms, and Therapy. *American Journal of Kidney Diseases* **11,** 449–464 (June 1, 1988).
44. Charles Jennette, J. Rapidly progressive crescentic glomerulonephritis. *Kidney International* **63,** 1164–1177 (Mar. 1, 2003).
45. Jennette, J. C. & Falk, R. J. Pathogenesis of antineutrophil cytoplasmic autoantibody-mediated disease. *Nature Reviews Rheumatology* **10.** Bandiera_abtest: a Cg_type: Nature Research Journals Number: 8 Primary_atype: Reviews Publisher: Nature Publishing Group Subject_term: Immunopathogenesis;Vasculitis syndromes Subject_term_id: immunopathogenesis;vasculitis-syndromes, 463–473 (Aug. 2014).
46. Falk, R. J. & Jennette, J. C. ANCA Disease: Where Is This Field Heading? *Journal of the American Society of Nephrology* **21,** 745–752 (May 2010).
47. Goodpasture, E. W. Landmark publication from The American Journal of the Medical Sciences: The significance of certain pulmonary lesions in relation to the etiology of influenza. *The American Journal of the Medical Sciences* **338,** 148–151 (Aug. 2009).
48. McAdoo, S. P. & Pusey, C. D. Anti-Glomerular Basement Membrane Disease. *Clinical Journal of the American Society of Nephrology* **12.** Publisher: American Society of Nephrology Section: Glomerular Diseases: Update for the Clinician, 1162–1172 (July 7, 2017).
49. Scheer, R. L. & Grossman, M. A. Immune Aspects of the Glomerulonephritis Associated with Pulmonary Hemmorhage. *Annals of Internal Medicine* **60.** Publisher: American College of Physicians, 1009–1021 (June 1, 1964).
50. Dorval, G. *et al.* Syndrome de Goodpasture et maladie des anticorps anti-membrane basale chez l'enfant : revue de la littérature. *Archives de Pédiatrie* **24,** 1019–1028 (Oct. 1, 2017).
51. Jennette, J. C. Overview of the 2012 Revised International Chapel Hill Consensus Conference Nomenclature of Vasculitides. *Clinical and experimental nephrology* **17,** 603–606 (Oct. 2013).
52. McGrogan, A., Franssen, C. F. M. & de Vries, C. S. The incidence of primary glomerulonephritis worldwide: a systematic review of the literature. *Nephrology, Dialysis, Transplantation: Official Publication of the European Dialysis and Transplant Association - European Renal Association* **26,** 414–430 (Feb. 2011).
53. Guruswamy Sangameswaran, K. D. & Baradhi, K. M. in *StatPearls* (StatPearls Publishing, Treasure Island (FL), 2021).
54. Rosenberg, A. Z. & Kopp, J. B. Focal Segmental Glomerulosclerosis. *Clinical Journal of the American Society of Nephrology* **12,** 502–517 (Mar. 7, 2017).

55. Agrawal, S., Prakash, S. & Sharma, R. K. Genetic aspects of familial focal segmental glomerulosclerosis. *Clinical Queries: Nephrology* **3,** 57–72 (Apr. 1, 2014).
56. Fogo, A. B. Causes and pathogenesis of focal segmental glomerulosclerosis. *Nature Reviews Nephrology* **11,** 76–87 (Feb. 2015).
57. *Focal Segmental Glomerulosclerosis (FSGS)* UNC Kidney Center. `https://%20unckidneycenter.org/%20kidneyhealthlibrary/%20glomerular-disease/%20focal-segmental-glomerulosclerosis-fsgs/` (2021).
58. D'Agati, V. D. Focal Segmental Glomerulosclerosis. *n engl j med,* 14 (2011).
59. D'Agati, V. D., Fogo, A. B., Bruijn, J. A. & Jennette, J. C. Pathologic classification of focal segmental glomerulosclerosis: a working proposal. *American Journal of Kidney Diseases: The Official Journal of the National Kidney Foundation* **43,** 368–382 (Feb. 2004).
60. Stokes, M. B., Markowitz, G. S., Lin, J., Valeri, A. M. & D'Agati, V. D. Glomerular tip lesion: A distinct entity within the minimal change disease/focal segmental glomerulosclerosis spectrum. *Kidney International* **65,** 1690–1702 (May 1, 2004).
61. Herlitz, L. C. *et al.* Development of focal segmental glomerulosclerosis after anabolic steroid abuse. *Journal of the American Society of Nephrology: JASN* **21,** 163–172 (Jan. 2010).
62. Markowitz, G. S. *et al.* Collapsing focal segmental glomerulosclerosis following treatment with high-dose pamidronate. *Journal of the American Society of Nephrology: JASN* **12,** 1164–1172 (June 2001).
63. Markowitz, G. S., Nasr, S. H., Stokes, M. B. & D'Agati, V. D. Treatment with IFN-, -, or - Is Associated with Collapsing Focal Segmental Glomerulosclerosis. *Clinical Journal of the American Society of Nephrology* **5,** 607–615 (Apr. 2010).
64. Fatima, H. *et al.* Parietal Epithelial Cell Activation Marker in Early Recurrence of FSGS in the Transplant. *Clinical Journal of the American Society of Nephrology* **7,** 1852–1858 (Nov. 2012).
65. Roeder, S. S. *et al.* Activated ERK1/2 increases CD44 in glomerular parietal epithelial cells leading to matrix expansion. *Kidney International* **91,** 896–913 (Apr. 1, 2017).
66. Eymael, J. *et al.* CD44 is required for the pathogenesis of experimental crescentic glomerulonephritis and collapsing focal segmental glomerulosclerosis. *Kidney International* **93,** 626–642 (Mar. 1, 2018).
67. Sicking, E.-M. *et al.* Subtotal ablation of parietal epithelial cells induces crescent formation. *Journal of the American Society of Nephrology: JASN* **23,** 629–640 (Apr. 2012).
68. Smeets, B., Dijkman, H. B. P. M., Wetzels, J. F. M. & Steenbergen, E. J. Lessons from studies on focal segmental glomerulosclerosis: an important role for parietal epithelial cells? *The Journal of Pathology* **210,** 263–272 (Nov. 2006).
69. Pabst, R. & Sterzel, R. B. Cell renewal of glomerular cell types in normal rats. An autoradiographic analysis. *Kidney International* **24,** 626–631 (Nov. 1, 1983).

70. Singh, S. K. S., Jeansson, M. & Quaggin, S. E. New insights into the pathogenesis of cellular crescents. *Current Opinion in Nephrology and Hypertension* **20,** 258–262 (May 2011).

71. Boucher, A., Droz, D., Adafer, E. & Noël, L. H. Relationship between the integrity of Bowman's capsule and the composition of cellular crescents in human crescentic glomerulonephritis. *Laboratory Investigation; a Journal of Technical Methods and Pathology* **56,** 526–533 (May 1987).

72. Ophascharoensuk, V. *et al.* Role of intrinsic renal cells versus infiltrating cells in glomerular crescent formation. *Kidney International* **54,** 416–425 (Aug. 1, 1998).

73. Lan, H. Y. *et al.* Macrophage apoptosis in rat crescentic glomerulonephritis. *The American Journal of Pathology* **151,** 531–538 (Aug. 1997).

74. Shimizu, A. *et al.* Apoptosis in progressive crescentic glomerulonephritis. *Laboratory Investigation; a Journal of Technical Methods and Pathology* **74,** 941–951 (May 1996).

75. Achenbach, J. *et al.* Parietal epithelia cells in the urine as a marker of disease activity in glomerular diseases. *Nephrology Dialysis Transplantation* **23,** 3138–3145 (Oct. 1, 2008).

76. Kalluri, R. & Neilson, E. G. Epithelial-mesenchymal transition and its implications for fibrosis. *The Journal of Clinical Investigation* **112,** 1776–1784 (Dec. 2003).

77. Kalluri, R. & Weinberg, R. A. The basics of epithelial-mesenchymal transition. *The Journal of Clinical Investigation* **119,** 1420–1428 (June 1, 2009).

78. Ng, Y.-Y. *et al.* Glomerular epithelial–myofibroblast transdifferentiation in the evolution of glomerular crescent formation. *Nephrology Dialysis Transplantation* **14,** 2860–2872 (Dec. 1, 1999).

79. Fujigaki, Y. *et al.* Mechanisms and kinetics of Bowman's epithelial-myofibroblast transdifferentiation in the formation of glomerular crescents. *Nephron* **92,** 203–212 (Sept. 2002).

80. Kriz, W. *et al.* Tracer Studies in the Rat Demonstrate Misdirected Filtration and Peritubular Filtrate Spreading in Nephrons with Segmental Glomerulosclerosis. *Journal of the American Society of Nephrology* **12.** Publisher: American Society of Nephrology Section: Immunology and Pathology, 496–506 (Mar. 1, 2001).

81. Kriz, W., Gretz, N. & Lemley, K. V. Progression of glomerular diseases: is the podocyte the culprit? *Kidney International* **54,** 687–697 (Sept. 1998).

82. Appel, D. *et al.* Recruitment of podocytes from glomerular parietal epithelial cells. *Journal of the American Society of Nephrology: JASN* **20,** 333–343 (Feb. 2009).

83. Sagrinati, C. *et al.* Isolation and characterization of multipotent progenitor cells from the Bowman's capsule of adult human kidneys. *Journal of the American Society of Nephrology: JASN* **17,** 2443–2456 (Sept. 2006).

84. Ronconi, E. *et al.* Regeneration of glomerular podocytes by human renal progenitors. *Journal of the American Society of Nephrology: JASN* **20,** 322–332 (Feb. 2009).

85. Ito, Y. *et al.* Expression of connective tissue growth factor in human renal fibrosis. *Kidney International* **53,** 853–861 (Apr. 1998).

86. Ito, Y. *et al.* Kinetics of Connective Tissue Growth Factor Expression during Experimental Proliferative Glomerulonephritis. *Journal of the American Society of Nephrology* **12.** Publisher: American Society of Nephrology Section: Immunology and Pathology, 472–484 (Mar. 1, 2001).

87. Fujigaki, Y. *et al.* Cytokines and cell cycle regulation in the fibrous progression of crescent formation in antiglomerular basement membrane nephritis of WKY rats. *Virchows Archiv: An International Journal of Pathology* **439,** 35–45 (July 2001).

88. Singer, S. J. & Nicolson, G. L. The Fluid Mosaic Model of the Structure of Cell Membranes. *Science, New Series* **175,** 720–731 (1972).

89. Nicolson, G. L. The Fluid-Mosaic Model of Membrane Structure: still relevant to understanding the structure, function and dynamics of biological membranes after more than 40 years. *Biochimica Et Biophysica Acta* **1838,** 1451–1466 (June 2014).

90. Sezgin, E., Levental, I., Mayor, S. & Eggeling, C. The mystery of membrane organization: composition, regulation and roles of lipid rafts. *Nature Reviews Molecular Cell Biology* **18.** Bandiera_abtest: a Cg_type: Nature Research Journals Number: 6 Primary_atype: Reviews Publisher: Nature Publishing Group Subject_term: Membrane biophysics;Membrane lipids;Membrane proteins;Membrane structure and assembly;Membranes Subject_term_id: membrane-biophysics;membrane-lipids;membrane-proteins;membrane-structure-and-assembly;membranes, 361–374 (June 2017).

91. Steck, T. L. THE ORGANIZATION OF PROTEINS IN THE HUMAN RED BLOOD CELL MEMBRANE. *The Journal of Cell Biology* **62,** 1–19 (July 1, 1974).

92. Alberts, B. *et al.* The Lipid Bilayer. *Molecular Biology of the Cell. 4th edition.* Publisher: Garland Science (2002).

93. Harayama, T. & Riezman, H. Understanding the diversity of membrane lipid composition. *Nature Reviews Molecular Cell Biology* **19.** Bandiera_abtest: a Cg_type: Nature Research Journals Number: 5 Primary_atype: Reviews Publisher: Nature Publishing Group Subject_term: Membrane biophysics; Membrane lipids; Membrane proteins; Membrane structure and assembly; Membranes Subject_term_id: membrane-biophysics; membrane-lipids; membrane-proteins; membrane-structure-and-assembly; membranes, 281–296 (May 2018).

94. Simons, K. & Ikonen, E. Functional rafts in cell membranes. *Nature* **387.** Bandiera_abtest: a Cg_type: Nature Research Journals Number: 6633 Primary_atype: Reviews Publisher: Nature Publishing Group, 569–572 (June 1997).

95. Van Meer, G., Voelker, D. R. & Feigenson, G. W. Membrane lipids: where they are and how they behave. *Nature Reviews Molecular Cell Biology* **9.** Bandiera_abtest: a Cg_type: Nature Research Journals Number: 2 Primary_atype: Reviews Publisher: Nature Publishing Group, 112–124 (Feb. 2008).

96. Brown, D. A. & London, E. Structure and Function of Sphingolipid- and Cholesterol-rich Membrane Rafts *. *Journal of Biological Chemistry* **275.** Publisher: Elsevier, 17221–17224 (June 9, 2000).
97. De Almeida, R. F. M., Fedorov, A. & Prieto, M. Sphingomyelin/ Phosphatidylcholine/ Cholesterol Phase Diagram: Boundaries and Composition of Lipid Rafts. *Biophysical Journal* **85,** 2406–2416 (Oct. 1, 2003).
98. Lodish, H. *et al.* Membrane Proteins. *Molecular Cell Biology. 4th edition.* Publisher: W. H. Freeman (2000).
99. Chen, J. *et al.* Systemic localization of seven major types of carbohydrates on cell membranes by dSTORM imaging. *Scientific Reports* **6,** 30247 (July 25, 2016).
100. Pike, L. J. The challenge of lipid rafts. *Journal of Lipid Research* **50,** S323–S328 (Suppl Apr. 2009).
101. Hanada, K., Nishijima, M., Akamatsu, Y. & Pagano, R. E. *The Journal of Biological Chemistry* **270,** 6254–6260 (Mar. 17, 1995).
102. Schroeder, R., London, E. & Brown, D. Interactions between saturated acyl chains confer detergent resistance on lipids and glycosylphosphatidylinositol (GPI)-anchored proteins: GPI-anchored proteins in liposomes and cells show similar behavior. *Proceedings of the National Academy of Sciences of the United States of America* **91,** 12130–12134 (Dec. 6, 1994).
103. Lingwood, D. & Simons, K. Lipid Rafts As a Membrane-Organizing Principle. *Science* **327,** 46–50 (Jan. 1, 2010).
104. Shogomori, H. & Brown, D. A. Use of detergents to study membrane rafts: the good, the bad, and the ugly. *Biological Chemistry* **384,** 1259–1263 (Sept. 2003).
105. Lu, S. M. & Fairn, G. D. Mesoscale organization of domains in the plasma membrane – beyond the lipid raft. *Critical Reviews in Biochemistry and Molecular Biology* **53.** Publisher: Taylor & Francis _eprint: https://doi.org/10.1080/10409238.2018.1436515, 192–207 (Mar. 4, 2018).
106. Frisz, J. F. *et al.* Sphingolipid Domains in the Plasma Membranes of Fibroblasts Are Not Enriched with Cholesterol*. *Journal of Biological Chemistry* **288,** 16855–16861 (June 7, 2013).
107. Suzuki, K. G. N. *et al.* GPI-anchored receptor clusters transiently recruit Lyn and G alpha for temporary cluster immobilization and Lyn activation: single-molecule tracking study 1. *The Journal of Cell Biology* **177,** 717–730 (May 21, 2007).
108. Lenne, P.-F. *et al.* Dynamic molecular confinement in the plasma membrane by microdomains and the cytoskeleton meshwork. *The EMBO Journal* **25,** 3245–3256 (July 26, 2006).
109. Goswami, D. *et al.* Nanoclusters of GPI-anchored proteins are formed by cortical actin-driven activity. *Cell* **135,** 1085–1097 (Dec. 12, 2008).

110. Kusumi, A., Sako, Y. & Yamamoto, M. Confined lateral diffusion of membrane receptors as studied by single particle tracking (nanovid microscopy). Effects of calcium-induced differentiation in cultured epithelial cells. *Biophysical Journal* **65,** 2021–2040 (Nov. 1, 1993).

111. Freeman, S. A. *et al.* Transmembrane Pickets Connect Cyto- and Pericellular Skeletons Forming Barriers to Receptor Engagement. *Cell* **172,** 305–317.e10 (Jan. 11, 2018).

112. Kusumi, A., Suzuki, K. G. N., Kasai, R. S., Ritchie, K. & Fujiwara, T. K. Hierarchical mesoscale domain organization of the plasma membrane. *Trends in Biochemical Sciences* **36.** Publisher: Elsevier, 604–615 (Nov. 1, 2011).

113. Kusumi, A. *et al.* Membrane mechanisms for signal transduction: the coupling of the meso-scale raft domains to membrane-skeleton-induced compartments and dynamic protein complexes. *Seminars in Cell & Developmental Biology* **23,** 126–144 (Apr. 2012).

114. Kusumi, A. *et al.* Dynamic Organizing Principles of the Plasma Membrane that Regulate Signal Transduction: Commemorating the Fortieth Anniversary of Singer and Nicolson's Fluid-Mosaic Model. *Annual Review of Cell and Developmental Biology* **28,** 215–250 (Nov. 10, 2012).

115. Winder, S. J. & Ayscough, K. R. Actin-binding proteins. *Journal of Cell Science* **118,** 651–654 (Feb. 15, 2005).

116. Jin, S., Haggie, P. M. & Verkman, A. S. Single-Particle Tracking of Membrane Protein Diffusion in a Potential: Simulation, Detection, and Application to Confined Diffusion of CFTR Cl Channels. *Biophysical Journal* **93,** 1079–1088 (Aug. 1, 2007).

117. Gupta, N. *et al.* Quantitative proteomic analysis of B cell lipid rafts reveals that ezrin regulates antigen receptor–mediated lipid raft dynamics. *Nature Immunology* **7.** Bandiera_abtest: a Cg_type: Nature Research Journals Number: 6 Primary_atype: Research Publisher: Nature Publishing Group, 625–633 (June 2006).

118. Viola, A. & Gupta, N. Tether and trap: regulation of membrane-raft dynamics by actin-binding proteins. *Nature Reviews. Immunology* **7,** 889–896 (Nov. 2007).

119. Hemler, M. E. Tetraspanin functions and associated microdomains. *Nature Reviews Molecular Cell Biology* **6,** 801–811 (Oct. 2005).

120. Yáñez-Mó, M., Barreiro, O., Gordon-Alonso, M., Sala-Valdés, M. & Sánchez-Madrid, F. Tetraspanin-enriched microdomains: a functional unit in cell plasma membranes. *Trends in Cell Biology* **19,** 434–446 (Sept. 1, 2009).

121. Charrin, S. *et al.* A physical and functional link between cholesterol and tetraspanins. *European Journal of Immunology* **33,** 2479–2489 (2003).

122. Claas, C., Stipp, C. S. & Hemler, M. E. Evaluation of prototype transmembrane 4 superfamily protein complexes and their relation to lipid rafts. *The Journal of Biological Chemistry* **276,** 7974–7984 (Mar. 16, 2001).

123. Yang, X. *et al.* Palmitoylation of tetraspanin proteins: modulation of CD151 lateral interactions, subcellular distribution, and integrin-dependent cell morphology. *Molecular Biology of the Cell* **13,** 767–781 (Mar. 2002).

124. Berditchevski, F., Odintsova, E., Sawada, S. & Gilbert, E. Expression of the palmitoylation-deficient CD151 weakens the association of alpha 3 beta 1 integrin with the tetraspanin-enriched microdomains and affects integrin-dependent signaling. *The Journal of Biological Chemistry* **277,** 36991–37000 (Oct. 4, 2002).

125. Charrin, S. *et al.* Differential stability of tetraspanin/tetraspanin interactions: role of palmitoylation. *FEBS letters* **516,** 139–144 (Apr. 10, 2002).

126. Kovalenko, O. V., Yang, X. H. & Hemler, M. E. A novel cysteine cross-linking method reveals a direct association between claudin-1 and tetraspanin CD9. *Molecular & cellular proteomics: MCP* **6,** 1855–1867 (Nov. 2007).

127. Brown, D. A. & London, E. Functions of Lipid Rafts in Biological Membranes. *Annual Review of Cell and Developmental Biology* **14,** 111–136 (1998).

128. Foster, L. J., Hoog, C. L. d. & Mann, M. Unbiased quantitative proteomics of lipid rafts reveals high specificity for signaling factors. *Proceedings of the National Academy of Sciences* **100.** Publisher: National Academy of Sciences Section: Biological Sciences, 5813–5818 (May 13, 2003).

129. Zuidscherwoude, M. *et al.* The tetraspanin web revisited by super-resolution microscopy. *Scientific Reports* **5.** Number: 1 Publisher: Nature Publishing Group, 12201 (July 17, 2015).

130. Cohen, S. & Carpenter, G. Human epidermal growth factor: isolation and chemical and biological properties. *Proceedings of the National Academy of Sciences of the United States of America* **72,** 1317–1321 (Apr. 1975).

131. Bargmann, C. I. & Weinberg, R. A. Increased tyrosine kinase activity associated with the protein encoded by the activated neu oncogene. *Proceedings of the National Academy of Sciences* **85.** Publisher: National Academy of Sciences Section: Research Article, 5394–5398 (Aug. 1, 1988).

132. Kraus, M. H., Issing, W., Miki, T., Popescu, N. C. & Aaronson, S. A. Isolation and characterization of ERBB3, a third member of the ERBB/epidermal growth factor receptor family: evidence for overexpression in a subset of human mammary tumors. *Proceedings of the National Academy of Sciences of the United States of America* **86,** 9193–9197 (Dec. 1989).

133. Plowman, G. D. *et al.* Ligand-specific activation of HER4/p180erbB4, a fourth member of the epidermal growth factor receptor family. *Proceedings of the National Academy of Sciences* **90.** Publisher: National Academy of Sciences Section: Research Article, 1746–1750 (Mar. 1, 1993).

134. Ward, C. W., Hoyne, P. A. & Flegg, R. H. Insulin and epidermal growth factor receptors contain the cysteine repeat motif found in the tumor necrosis factor receptor. *Proteins* **22,** 141–153 (June 1995).

135. Ward, C. W. & Garrett, T. P. The relationship between the L1 and L2 domains of the insulin and epidermal growth factor receptors and leucine-rich repeat modules. *BMC Bioinformatics* **2,** 4 (July 27, 2001).

136. Lax, I. *et al.* Chicken epidermal growth factor (EGF) receptor: cDNA cloning, expression in mouse cells, and differential binding of EGF and transforming growth factor alpha. *Molecular and Cellular Biology* **8,** 1970–1978 (May 1988).

137. Bouyain, S., Longo, P. A., Li, S., Ferguson, K. M. & Leahy, D. J. The extracellular region of ErbB4 adopts a tethered conformation in the absence of ligand. *Proceedings of the National Academy of Sciences* **102.** Publisher: National Academy of Sciences Section: Biological Sciences, 15024–15029 (Oct. 18, 2005).

138. Ogiso, H. *et al.* Crystal structure of the complex of human epidermal growth factor and receptor extracellular domains. *Cell* **110,** 775–787 (Sept. 20, 2002).

139. Garrett, T. P. J. *et al.* Crystal structure of a truncated epidermal growth factor receptor extracellular domain bound to transforming growth factor alpha. *Cell* **110,** 763–773 (Sept. 20, 2002).

140. Cho, H.-S. & Leahy, D. J. Structure of the Extracellular Region of HER3 Reveals an Interdomain Tether. *Science.* Publisher: American Association for the Advancement of Science (Aug. 23, 2002).

141. Wieduwilt, M. J. & Moasser, M. M. The epidermal growth factor receptor family: Biology driving targeted therapeutics. *Cellular and molecular life sciences : CMLS* **65,** 1566–1584 (May 2008).

142. Gao, J. *et al.* Mechanistic insights into EGFR membrane clustering revealed by super-resolution imaging. *Nanoscale* **7.** Publisher: The Royal Society of Chemistry, 2511–2519 (Jan. 28, 2015).

143. Valley, C. C., Liu, S., Lidke, D. S. & Lidke, K. A. Sequential Superresolution Imaging of Multiple Targets Using a Single Fluorophore. *PLOS ONE* **10.** Publisher: Public Library of Science, e0123941 (Apr. 10, 2015).

144. Valley, C. C. *et al.* Enhanced dimerization drives ligand-independent activity of mutant epidermal growth factor receptor in lung cancer. *Molecular Biology of the Cell* **26,** 4087–4099 (Nov. 5, 2015).

145. Hemler, M. E. Specific tetraspanin functions. *The Journal of Cell Biology* **155,** 1103–1108 (Dec. 24, 2001).

146. Levy, S. & Shoham, T. Protein-Protein Interactions in the Tetraspanin Web. *Physiology* **20.** Publisher: American Physiological Society, 218–224 (Aug. 1, 2005).

147. Kitadokoro, K. *et al.* CD81 extracellular domain 3D structure: insight into the tetraspanin superfamily structural motifs. *The EMBO Journal* **20,** 12–18 (Jan. 15, 2001).

148. Knobeloch, K.-P. *et al.* Targeted Inactivation of the Tetraspanin CD37 Impairs T-Cell-Dependent B-Cell Response under Suboptimal Costimulatory Conditions. *Molecular and Cellular Biology* **20,** 5363–5369 (Aug. 2000).

149. Umeda, R. *et al.* Structural insights into tetraspanin CD9 function. *Nature Communications* **11.** Number: 1 Publisher: Nature Publishing Group, 1606 (Mar. 30, 2020).

150. Charrin, S. *et al.* Lateral organization of membrane proteins: tetraspanins spin their web. *The Biochemical Journal* **420,** 133–154 (May 13, 2009).

151. Espenel, C. *et al.* Single-molecule analysis of CD9 dynamics and partitioning reveals multiple modes of interaction in the tetraspanin web. *The Journal of Cell Biology* **182,** 765–776 (Aug. 25, 2008).

152. Feng, L. *et al.* Heparin-binding EGF-like growth factor contributes to reduced glomerular filtration rate during glomerulonephritis in rats. *Journal of Clinical Investigation* **105,** 341–350 (Feb. 1, 2000).

153. Murayama, Y. *et al.* The tetraspanin CD9 modulates epidermal growth factor receptor signaling in cancer cells. *Journal of Cellular Physiology* **216,** 135–143 (July 2008).

154. Richards, B., Wolf, E. & Gabor, D. Electromagnetic diffraction in optical systems, II. Structure of the image field in an aplanatic system. *Proceedings of the Royal Society of London. Series A. Mathematical and Physical Sciences* **253.** Publisher: Royal Society, 358–379 (Dec. 15, 1959).

155. Gibson, S. F. & Lanni, F. Diffraction by a circular aperture as a model for three-dimensional optical microscopy. *JOSA A* **6.** Publisher: Optical Society of America, 1357–1367 (Sept. 1, 1989).

156. Shen, H. *et al.* Single Particle Tracking: From Theory to Biophysical Applications. *Chemical Reviews* **117.** Publisher: American Chemical Society, 7331–7376 (June 14, 2017).

157. Clausen, M. P. & Lagerholm, B. C. The probe rules in single particle tracking. *Current Protein & Peptide Science* **12,** 699–713 (Dec. 2011).

158. Wüstner, D. Fluorescent sterols as tools in membrane biophysics and cell biology. *Chemistry and Physics of Lipids* **146,** 1–25 (Mar. 2007).

159. Alivisatos, A. P. Semiconductor Clusters, Nanocrystals, and Quantum Dots. *Science* **271.** Publisher: American Association for the Advancement of Science, 933–937 (Feb. 16, 1996).

160. Nirmal, M. *et al.* Fluorescence intermittency in single cadmium selenide nanocrystals. *Nature* **383.** Bandiera_abtest: a Cg_type: Nature Research Journals Number: 6603 Primary_atype: Research Publisher: Nature Publishing Group, 802–804 (Oct. 1996).

161. Beaurepaire, E. *et al.* Functionalized Fluorescent Oxide Nanoparticles: Artificial Toxins for Sodium Channel Targeting and Imaging at the Single-Molecule Level. *Nano Letters* **4.** Publisher: American Chemical Society, 2079–2083 (Nov. 1, 2004).

162. Mialon, G. *et al.* High Up-Conversion Efficiency of YVO4:Yb,Er Nanoparticles in Water down to the Single-Particle Level. *The Journal of Physical Chemistry C* **114.** Publisher: American Chemical Society, 22449–22454 (Dec. 30, 2010).

163. Wu, S. *et al.* Non-blinking and photostable upconverted luminescence from single lanthanide-doped nanocrystals. *Proceedings of the National Academy of Sciences* **106.** Publisher: National Academy of Sciences Section: Physical Sciences, 10917–10921 (July 7, 2009).

164. Ye, Z., Wang, X. & Xiao, L. Single-Particle Tracking with Scattering-Based Optical Microscopy. *Analytical Chemistry* **91.** Publisher: American Chemical Society, 15327–15334 (Dec. 17, 2019).

165. Hui, Y. Y. *et al.* Single particle tracking of fluorescent nanodiamonds in cells and organisms. *Current Opinion in Solid State and Materials Science. Nanodiamond Science and Technology* **21,** 35–42 (Feb. 1, 2017).

166. Saxton, M. J. & Jacobson, K. Single-particle tracking: applications to membrane dynamics. *Annual Review of Biophysics and Biomolecular Structure* **26,** 373–399 (1997).

167. Metzler, R., Jeon, J.-H., Cherstvy, A. G. & Barkai, E. Anomalous diffusion models and their properties: non-stationarity, non-ergodicity, and ageing at the centenary of single particle tracking. *Physical Chemistry Chemical Physics* **16.** Publisher: The Royal Society of Chemistry, 24128–24164 (Oct. 21, 2014).

168. Bouzigues, C. & Dahan, M. Transient Directed Motions of GABAA Receptors in Growth Cones Detected by a Speed Correlation Index. *Biophysical Journal* **92.** Publisher: Elsevier, 654–660 (Jan. 15, 2007).

169. Abbe, E. Beiträge zur Theorie des Mikroskops und der mikroskopischen Wahrnehmung. de. *Archiv für Mikroskopische Anatomie* **9,** 413–468 (Dec. 1873).

170. Gustafsson, M. G. L. Surpassing the lateral resolution limit by a factor of two using structured illumination microscopy. *Journal of Microscopy* **198,** 82–87 (2000).

171. Hell, S. W. & Wichmann, J. Breaking the diffraction resolution limit by stimulated emission: stimulated-emission-depletion fluorescence microscopy. EN. *Optics Letters* **19,** 780–782 (June 1994).

172. Huang, B., Bates, M. & Zhuang, X. Super-Resolution Fluorescence Microscopy. *Annual Review of Biochemistry* **78,** 993–1016 (2009).

173. Khater, I. M., Nabi, I. R. & Hamarneh, G. A Review of Super-Resolution Single-Molecule Localization Microscopy Cluster Analysis and Quantification Methods. *Patterns* **1,** 100038 (June 12, 2020).

174. Sharonov, A. & Hochstrasser, R. M. Wide-field subdiffraction imaging by accumulated binding of diffusing probes. en. *Proceedings of the National Academy of Sciences* **103,** 18911–18916 (Dec. 2006).

175. Jungmann, R. *et al.* Single-molecule kinetics and super-resolution microscopy by fluorescence imaging of transient binding on DNA origami. *Nano Letters* **10,** 4756–4761 (Nov. 10, 2010).

176. Schnitzbauer, J., Strauss, M. T., Schlichthaerle, T., Schueder, F. & Jungmann, R. Super-resolution microscopy with DNA-PAINT. en. *Nature Protocols* **12,** 1198–1228 (June 2017).

177. Agasti, S. S. *et al.* DNA-barcoded labeling probes for highly multiplexed Exchange-PAINT imaging. *Chem. Sci.* **8.** Publisher: The Royal Society of Chemistry, 3080–3091 (2017).

178. Jungmann, R. *et al.* Quantitative super-resolution imaging with qPAINT. *Nature methods* **13.** Edition: 2016/03/28, 439–442 (May 2016).

179. Olivier, N., Keller, D., Gönczy, P. & Manley, S. Resolution Doubling in 3D-STORM Imaging through Improved Buffers. en. *PLoS ONE* **8** (ed Sauer, M.) e69004 (July 2013).

180. Betzig, E. *et al.* Imaging intracellular fluorescent proteins at nanometer resolution. *Science (New York, N.Y.)* **313,** 1642–1645 (Sept. 15, 2006).

181. Rust, M. J., Bates, M. & Zhuang, X. Sub-diffraction-limit imaging by stochastic optical reconstruction microscopy (STORM). en. *Nature Methods* **3,** 793–796 (Oct. 2006).

182. Heilemann, M. *et al.* Subdiffraction-Resolution Fluorescence Imaging with Conventional Fluorescent Probes. *Angewandte Chemie International Edition* **47,** 6172–6176 (2008).

183. Hartwich, T. M. *et al.* *A stable, high refractive index, switching buffer for super-resolution imaging* en. preprint (Biophysics, Nov. 2018).

184. Ober, R. J., Ram, S. & Ward, E. S. Localization Accuracy in Single-Molecule Microscopy. *Biophysical Journal* **86,** 1185–1200 (Feb. 2004).

185. *Single-Molecule Super-Resolution Imaging* Nikon's MicroscopyU. `https://www.microscopyu.com/techniques/super-resolution/single-molecule-super-resolution-imaging` (2021).

186. Dempsey, G. T. *et al.* Photoswitching Mechanism of Cyanine Dyes. *Journal of the American Chemical Society* **131,** 18192–18193 (Dec. 2009).

187. Li, H. & Vaughan, J. C. Switchable Fluorophores for Single-Molecule Localization Microscopy. *Chemical reviews* **118,** 9412–9454 (Sept. 26, 2018).

188. Dempsey, G. T., Vaughan, J. C., Chen, K. H., Bates, M. & Zhuang, X. Evaluation of fluorophores for optimal performance in localization-based super-resolution imaging. *Nature Methods* **8,** 1027–1036 (Dec. 2011).

189. Bittel, A. M. *et al.* Methodology for Quantitative Characterization of Fluorophore Photoswitching to Predict Superresolution Microscopy Image Quality. *Scientific Reports* **6.** Bandiera_abtest: a Cc_license_type: cc_by Cg_type: Nature Research Journals Number: 1 Primary_atype: Research Publisher: Nature Publishing Group Subject_term: Chemical physics;Single-molecule fluorescence Subject_term_id: chemical-physics;single-molecule-fluorescence, 29687 (July 14, 2016).

190. Wiederschain, G. Y. The Molecular Probes handbook. A guide to fluorescent probes and labeling technologies. *Biochemistry (Moscow)* **76,** 1276–1276 (Nov. 1, 2011).

191. Shim, S.-H. *et al.* Super-resolution fluorescence imaging of organelles in live cells with photoswitchable membrane probes. *Proceedings of the National Academy of Sciences* **109.** ISBN: 9781201882107 Publisher: National Academy of Sciences Section: Biological Sciences, 13978–13983 (Aug. 28, 2012).

192. Lukinavičius, G. *et al.* A near-infrared fluorophore for live-cell super-resolution microscopy of cellular proteins. *Nature Chemistry* **5.** Bandiera_abtest: a Cg_type: Nature Research Journals Number: 2 Primary_atype: Research Publisher: Nature Publishing Group Subject_term: Chemical biology;Fluorescent probes Subject_term_id: chemical-biology;fluorescent-probes, 132–139 (Feb. 2013).

193. Vaughan, J. C., Jia, S. & Zhuang, X. Ultrabright photoactivatable fluorophores created by reductive caging. *Nature Methods* **9.** Bandiera_abtest: a Cg_type: Nature Research Journals Number: 12 Primary_atype: Research Publisher: Nature Publishing Group Subject_term: Fluorescent dyes;Imaging;Super-resolution microscopy Subject_term_id: fluorescent-dyes;imaging;super-resolution-microscopy, 1181–1184 (Dec. 2012).

194. Vaughan, J. C., Dempsey, G. T., Sun, E. & Zhuang, X. Phosphine Quenching of Cyanine Dyes as a Versatile Tool for Fluorescence Microscopy. *Journal of the American Chemical Society* **135.** Publisher: American Chemical Society, 1197–1200 (Jan. 30, 2013).

195. Grimm, J. B. *et al.* A general method to improve fluorophores for live-cell and single-molecule microscopy. *Nature Methods* **12.** Bandiera_abtest: a Cg_type: Nature Research Journals Number: 3 Primary_atype: Research Publisher: Nature Publishing Group Subject_term: Cellular imaging; Chemical synthesis;Chemical tools; Fluorescent dyes Subject_term_id: cellular-imaging; chemical-synthesis;chemical-tools; fluorescent-dyes, 244–250 (Mar. 2015).

196. Grimm, J. B. *et al.* Bright photoactivatable fluorophores for single-molecule imaging. *Nature Methods* **13.** Bandiera_abtest: a Cg_type: Nature Research Journals Number: 12 Primary_atype: Research Publisher: Nature Publishing Group Subject_term: Chemical tools;Fluorescence imaging Subject_term_id: chemical-tools;fluorescence-imaging, 985–988 (Dec. 2016).

197. Roubinet, B. *et al.* Fluorescent Photoswitchable Diarylethenes for Biolabeling and Single-Molecule Localization Microscopies with Optical Superresolution. *Journal of the American Chemical Society* **139.** Publisher: American Chemical Society, 6611–6620 (May 17, 2017).

198. Uno, S.-n. *et al.* A spontaneously blinking fluorophore based on intramolecular spirocyclization for live-cell super-resolution imaging. *Nature Chemistry* **6.** Bandiera_abtest: a Cg_type: Nature Research Journals Number: 8 Primary_atype: Research Publisher: Nature Publishing Group Subject_term: Chemical biology;Fluorescent probes Subject_term_id: chemical-biology;fluorescent-probes, 681–689 (Aug. 2014).

199. Deniz, E. *et al.* Photoactivatable Fluorophores for Super-Resolution Imaging Based on Oxazine Auxochromes. *The Journal of Physical Chemistry C* **116.** Publisher: American Chemical Society, 6058–6068 (Mar. 15, 2012).

200. Fernández-Suárez, M. & Ting, A. Y. Fluorescent probes for super-resolution imaging in living cells. *Nature Reviews Molecular Cell Biology* **9.** Bandiera_abtest: a Cg_type: Nature Research Journals Number: 12 Primary_atype: Reviews Publisher: Nature Publishing Group, 929–943 (Dec. 2008).

201. McKinney, S. A., Murphy, C. S., Hazelwood, K. L., Davidson, M. W. & Looger, L. L. A bright and photostable photoconvertible fluorescent protein. *Nature Methods* **6.** Bandiera_abtest: a Cg_type: Nature Research Journals Number: 2 Primary_atype: Research Publisher: Nature Publishing Group, 131–133 (Feb. 2009).

202. Paez-Segala, M. G. *et al.* Fixation-resistant photoactivatable fluorescent proteins for CLEM. *Nature Methods* **12.** Bandiera_abtest: a Cg_type: Nature Research Journals Number: 3 Primary_atype: Research Publisher: Nature Publishing Group Subject_term: Fluorescence imaging;Protein design;Scanning electron microscopy;Transmission electron microscopy Subject_term_id: fluorescence-imaging;protein-design;scanning-electron-microscopy;transmission-electron-microscopy, 215–218 (Mar. 2015).

203. Kopek, B. G. *et al.* Diverse protocols for correlative super-resolution fluorescence imaging and electron microscopy of chemically fixed samples. *Nature Protocols* **12.** Bandiera_abtest: a Cg_type: Nature Research Journals Number: 5 Primary_atype: Protocols Publisher: Nature Publishing Group Subject_term: Fluorescent proteins;Image processing;Scanning electron microscopy;Super-resolution microscopy;Transmission electron microscopy Subject_term_id: fluorescent-proteins; image-processing; scanning-electron-microscopy; super-resolution-microscopy; transmission-electron-microscopy, 916–946 (May 2017).

204. Gurskaya, N. G. *et al.* Engineering of a monomeric green-to-red photoactivatable fluorescent protein induced by blue light. *Nature Biotechnology* **24.** Bandiera_abtest: a Cg_type: Nature Research Journals Number: 4 Primary_atype: Research Publisher: Nature Publishing Group, 461–465 (Apr. 2006).

205. Durisic, N., Laparra-Cuervo, L., Sandoval-Álvarez, Á., Borbely, J. S. & Lakadamyali, M. Single-molecule evaluation of fluorescent protein photoactivation efficiency using an in vivo nanotemplate. *Nature Methods* **11.** Bandiera_abtest: a Cg_type: Nature Research Journals Number: 2 Primary_atype: Research Publisher: Nature Publishing Group Subject_term: Fluorescence imaging;Fluorescent proteins;Single-molecule biophysics;Super-resolution microscopy Subject_term_id: fluorescence-imaging;fluorescent-proteins;single-molecule-biophysics;super-resolution-microscopy, 156–162 (Feb. 2014).

206. Wang, S., Moffitt, J. R., Dempsey, G. T., Xie, X. S. & Zhuang, X. Characterization and development of photoactivatable fluorescent proteins for single-molecule-based superresolution imaging. *Proceedings of the National Academy of Sciences of the United States of America* **111,** 8452–8457 (June 10, 2014).

207. Chudakov, D. M., Lukyanov, S. & Lukyanov, K. A. Tracking intracellular protein movements using photoswitchable fluorescent proteins PS-CFP2 and Dendra2. *Nature Protocols* **2.** Bandiera_abtest: a Cg_type: Nature Research Journals Number: 8 Primary_atype: Protocols Publisher: Nature Publishing Group, 2024–2032 (Aug. 2007).

208. Habuchi, S. *et al.* Reversible single-molecule photoswitching in the GFP-like fluorescent protein Dronpa. *Proceedings of the National Academy of Sciences* **102.** Publisher: National Academy of Sciences Section: Biological Sciences, 9511–9516 (July 5, 2005).

209. Rego, E. H. *et al.* Nonlinear structured-illumination microscopy with a photoswitchable protein reveals cellular structures at 50-nm resolution. *Proceedings of the National Academy of Sciences* **109.** Publisher: National Academy of Sciences Section: PNAS Plus, E135–E143 (Jan. 17, 2012).

210. Zhou, X. X. & Lin, M. Z. Photoswitchable fluorescent proteins: ten years of colorful chemistry and exciting applications. *Current Opinion in Chemical Biology* **17,** 682–690 (Aug. 2013).

211. Brakemann, T. *et al.* A reversibly photoswitchable GFP-like protein with fluorescence excitation decoupled from switching. *Nature Biotechnology* **29.** Bandiera_abtest: a Cg_type: Nature Research Journals Number: 10 Primary_atype: Research Publisher: Nature Publishing Group Subject_term: Biotechnology;Fluorescence imaging;Fluorescent proteins Subject_term_id: biotechnology;fluorescence-imaging;fluorescent-proteins, 942–947 (Oct. 2011).

212. Jensen, N. A. *et al.* Coordinate-Targeted and Coordinate-Stochastic Super-Resolution Microscopy with the Reversibly Switchable Fluorescent Protein Dreiklang. *ChemPhys* **15,** 756–762 (2014).

213. McEvoy, A. L. *et al.* mMaple: a photoconvertible fluorescent protein for use in multiple imaging modalities. *PloS One* **7,** e51314 (2012).

214. Zhang, M. *et al.* Rational design of true monomeric and bright photoactivatable fluorescent proteins. *Nature Methods* **9.** Bandiera_abtest: a Cg_type: Nature Research Journals Number: 7 Primary_atype: Research Publisher: Nature Publishing Group Subject_term: Fluorescent proteins;Protein design;Super-resolution microscopy Subject_term_id: fluorescent-proteins;protein-design;super-resolution-microscopy, 727–729 (July 2012).

215. Subach, F. V., Patterson, G. H., Renz, M., Lippincott-Schwartz, J. & Verkhusha, V. V. Bright monomeric photoactivatable red fluorescent protein for two-color super-resolution sptPALM of live cells. *Journal of the American Chemical Society* **132,** 6481–6491 (May 12, 2010).

216. Patterson, G. H. & Lippincott-Schwartz, J. A photoactivatable GFP for selective photolabeling of proteins and cells. *Science (New York, N.Y.)* **297,** 1873–1877 (Sept. 13, 2002).

217. Dertinger, T., Colyer, R., Iyer, G., Weiss, S. & Enderlein, J. Fast, background-free, 3D super-resolution optical fluctuation imaging (SOFI). *Proceedings of the National Academy of Sciences* **106.** Publisher: National Academy of Sciences Section: Biological Sciences, 22287–22292 (Dec. 29, 2009).

218. Watanabe, T. M., Fukui, S., Jin, T., Fujii, F. & Yanagida, T. Real-Time Nanoscopy by Using Blinking Enhanced Quantum Dots. *Biophysical Journal* **99,** L50–L52 (Oct. 6, 2010).

219. Chien, F.-C., Kuo, C. W. & Chen, P. Localization imaging using blinking quantum dots. *Analyst* **136.** Publisher: The Royal Society of Chemistry, 1608–1613 (Mar. 28, 2011).

220. Zhou, J., Yang, Y. & Zhang, C.-y. Toward Biocompatible Semiconductor Quantum Dots: From Biosynthesis and Bioconjugation to Biomedical Application. *Chemical Reviews* **115.** Publisher: American Chemical Society, 11669–11717 (Nov. 11, 2015).

221. Ovesný, M., Křížek, P., Borkovec, J., Švindrych, Z. & Hagen, G. M. ThunderSTORM: a comprehensive ImageJ plug-in for PALM and STORM data analysis and super-resolution imaging. *Bioinformatics* **30,** 2389–2390 (Aug. 15, 2014).

222. Ripley, B. D. Modelling Spatial Patterns. *Journal of the Royal Statistical Society: Series B (Methodological)* **39,** 172–192 (1977).

223. Besag, J. Discussion on Dr Ripley's Paper. *Journal of the Royal Statistical Society: Series B (Methodological)* **39.** _eprint: https://rss.onlinelibrary.wiley.com/doi/pdf/10.1111/j.2517-6161.1977.tb01616.x, 192–212 (1977).

224. Ehrlich, M. *et al.* Endocytosis by random initiation and stabilization of clathrin-coated pits. *Cell* **118,** 591–605 (Sept. 3, 2004).

225. Kiskowski, M. A., Hancock, J. F. & Kenworthy, A. K. On the Use of Ripley's K-Function and Its Derivatives to Analyze Domain Size. *Biophysical Journal* **97,** 1095–1103 (Aug. 19, 2009).

226. Lukinavičius, G. & Johnsson, K. Switchable fluorophores for protein labeling in living cells. *Current Opinion in Chemical Biology. Molecular Imaging* **15,** 768–774 (Dec. 1, 2011).

227. Schnitzbauer, J. *et al.* Correlation analysis framework for localization-based superresolution microscopy. *Proceedings of the National Academy of Sciences* **115.** Publisher: National Academy of Sciences Section: Physical Sciences, 3219–3224 (Mar. 27, 2018).

228. Malkusch, S. *et al.* Coordinate-based colocalization analysis of single-molecule localization microscopy data. *Histochemistry and Cell Biology* **137,** 1–10 (Jan. 1, 2012).

229. Veatch, S. L. *et al.* Correlation Functions Quantify Super-Resolution Images and Estimate Apparent Clustering Due to Over-Counting. *PLOS ONE* **7.** Publisher: Public Library of Science, e31457 (Feb. 27, 2012).

230. Ester, M., Kriegel, H.-P. & Xu, X. A Density-Based Algorithm for Discovering Clusters in Large Spatial Databases with Noise, 6.

231. Mazouchi, A. & Milstein, J. N. Fast Optimized Cluster Algorithm for Localizations (FOCAL): a spatial cluster analysis for super-resolved microscopy. *Bioinformatics (Oxford, England)* **32,** 747–754 (Mar. 1, 2016).

232. Nino, D. F., Djayakarsana, D. & Milstein, J. N. FOCAL3D: A 3-dimensional clustering package for single-molecule localization microscopy. *PLOS Computational Biology* **16.** Publisher: Public Library of Science, e1008479 (Dec. 8, 2020).

233. Newman, M. E. J. The Structure and Function of Complex Networks. *SIAM Review* **45,** 167–256 (Jan. 2003).

234. Vecchio, F. *et al.* "Small World" architecture in brain connectivity and hippocampal volume in Alzheimer's disease: a study via graph theory from EEG data. *Brain Imaging and Behavior* **11,** 473–485 (Apr. 1, 2017).

235. Kumar, A. & Kulkarni, G. U. Evaluating conducting network based transparent electrodes from geometrical considerations. *Journal of Applied Physics* **119.** Publisher: American Institute of Physics, 015102 (Jan. 7, 2016).

236. Newman, M. E. J. *Networks: an introduction* Reprinted. 772 pp. (Oxford University Press, Oxford, 2016).

237. Cohen, R. & Havlin, S. *Complex Networks: Structure, Robustness and Function* Journal Abbreviation: Complex Networks: Structure, Robustness and Function Publication Title: Complex Networks: Structure, Robustness and Function (Aug. 23, 2010).

238. Rosen, K. H. *Discrete Mathematics and Its Applications Seventh Edition* 7th (McGraw-Hill Education, June 14, 2011).

239. Kelly, S. T. & Black, M. A. *graphsim: An R package for simulating gene expression data from graph structures of biological pathways* Company: Cold Spring Harbor Laboratory Distributor: Cold Spring Harbor Laboratory Label: Cold Spring Harbor Laboratory Section: New Results Type: article (June 30, 2020), 2020.03.02.972471.

240. Khater, I. M., Meng, F., Nabi, I. R. & Hamarneh, G. Identification of caveolin-1 domain signatures via machine learning and graphlet analysis of single-molecule super-resolution data. *Bioinformatics* **35,** 3468–3475 (Sept. 15, 2019).

241. Khater, I. M., Liu, Q., Chou, K. C., Hamarneh, G. & Nabi, I. R. Super-resolution modularity analysis shows polyhedral caveolin-1 oligomers combine to form scaffolds and caveolae. *Scientific Reports* **9.** Bandiera_abtest: a Cc_license_type: cc_by Cg_type: Nature Research Journals Number: 1 Primary_atype: Research Publisher: Nature Publishing Group Subject_term: Caveolae;Image processing;Super-resolution microscopy Subject_term_id: caveolae;image-processing;super-resolution-microscopy, 9888 (July 8, 2019).

242. Levet, F. *et al.* SR-Tesseler: a method to segment and quantify localization-based super-resolution microscopy data. *Nature Methods* **12,** 1065–1071 (Nov. 2015).

243. Muyldermans, S. Nanobodies: Natural Single-Domain Antibodies. *Annual Review of Biochemistry* **82.** Publisher: Annual Reviews, 775–797 (June 2, 2013).

244. Rothbauer, U., Zolghadr, K., Muyldermans, S., Schepers, A. & Cardoso, M. C. A Versatile Nanotrap for Biochemical and Functional Studies with Fluorescent Fusion Proteins*S, 8.

245. Ries, J., Kaplan, C., Platonova, E., Eghlidi, H. & Ewers, H. A simple, versatile method for GFP-based super-resolution microscopy via nanobodies. *Nature Methods* **9,** 582–584 (June 2012).

246. Castro, B. M., Torreno-Pina, J. A., van Zanten, T. S. & Garcia-Parajo, M. F. in *Methods in Cell Biology* (ed Conn, P. M.) 105–122 (Academic Press, Jan. 1, 2013).

247. Türkcan, S., Alexandrou, A. & Masson, J.-B. A Bayesian Inference Scheme to Extract Diffusivity and Potential Fields from Confined Single-Molecule Trajectories. *Biophysical Journal* **102,** 2288–2298 (May 16, 2012).

248. Lange, Y. Tracking cell cholesterol with cholesterol oxidase. *Journal of Lipid Research* **33,** 315–321 (Mar. 1, 1992).

249. Hannun, Y. The sphingomyelin cycle and the second messenger function of ceramide. *Journal of Biological Chemistry* **269,** 3125–3128 (Feb. 1994).

250. Hannun, Y. A. Functions of Ceramide in Coordinating Cellular Responses to Stress. *Science* **274.** Publisher: American Association for the Advancement of Science, 1855–1859 (Dec. 13, 1996).
251. Alessenko, A. V. The role of sphingomyelin cycle metabolites in transduction of signals of cell proliferation, differentiation and death. *Membrane & Cell Biology* **13,** 303–320 (2000).
252. Sawai, H. & Hannun, Y. A. Ceramide and sphingomyelinases in the regulation of stress responses. *Chemistry and Physics of Lipids* **102,** 141–147 (Nov. 1, 1999).
253. Lanoiselée, Y., Grimes, J., Koszegi, Z. & Calebiro, D. Detecting Transient Trapping from a Single Trajectory: A Structural Approach. *Entropy* **23,** 1044 (Aug. 13, 2021).
254. Cherstvy, A. G., Thapa, S., Mardoukhi, Y., Chechkin, A. V. & Metzler, R. Time averages and their statistical variation for the Ornstein-Uhlenbeck process: Role of initial particle distributions and relaxation to stationarity. *Physical Review E* **98,** 022134 (Aug. 28, 2018).
255. Türkcan, S. Investigation of the Cell Membrane Architecture by Single-Molecule Tracking of Peptidic Toxins, 205.
256. *Particle Analysis* ImageJ Wiki. `https://imagej.github.io/imaging/particle-analysis` (2021).
257. Arganda-Carreras, I. *et al.* Trainable Weka Segmentation: a machine learning tool for microscopy pixel classification. *Bioinformatics* **33,** 2424–2426 (Aug. 1, 2017).
258. Casanova, D. *et al.* Single europium-doped nanoparticles measure temporal pattern of reactive oxygen species production inside cells. *Nature nanotechnology* **4,** 581–5 (Oct. 1, 2009).
259. Fernandez, L. *et al.* CD82 and Gangliosides Tune CD81 Membrane Behavior. *International Journal of Molecular Sciences* **22.** Number: 16 Publisher: Multidisciplinary Digital Publishing Institute, 8459 (Jan. 2021).
260. Lozahic, S. *et al.* CD46 (membrane cofactor protein) associates with multiple beta1 integrins and tetraspans. *European Journal of Immunology* **30,** 900–907 (Mar. 2000).
261. Mousseau, F. *et al.* Luminescent lanthanide nanoparticle-based imaging enables ultra-sensitive, quantitative and multiplexed in vitro lateral flow immunoassays. *Nanoscale* **13.** Publisher: The Royal Society of Chemistry, 14814–14824 (Sept. 17, 2021).
262. Huignard, A., Gacoin, T. & Boilot, J.-P. Synthesis and Luminescence Properties of Colloidal YVO4:Eu Phosphors. *Chemistry of Materials* **12.** Publisher: American Chemical Society, 1090–1094 (Apr. 1, 2000).
263. Bouzigues, C., Gacoin, T. & Alexandrou, A. Biological Applications of Rare-Earth Based Nanoparticles. *ACS Nano* **5.** Publisher: American Chemical Society, 8488–8505 (Nov. 22, 2011).
264. Giaume, D. *et al.* Functionalized Luminescent Oxide Nanoparticles as Biological Probes. *MRS Online Proceedings Library (OPL)* **942.** Publisher: Cambridge University Press (2006).

265. Casanova, D. *et al.* Counting the Number of Proteins Coupled to Single Nanoparticles. *Journal of the American Chemical Society* **129.** Publisher: American Chemical Society, 12592–12593 (Oct. 1, 2007).

266. Stanly, T. A. *et al.* Critical importance of appropriate fixation conditions for faithful imaging of receptor microclusters. *Biology Open* **5,** 1343–1350 (July 27, 2016).

267. Weber, K., Rathke, P. C. & Osborn, M. Cytoplasmic microtubular images in glutaraldehyde-fixed tissue culture cells by electron microscopy and by immunofluorescence microscopy. *Proceedings of the National Academy of Sciences of the United States of America* **75,** 1820–1824 (Apr. 1978).

université
PARIS-SACLAY

ÉCOLE DOCTORALE
Interfaces:
matériaux, systèmes, usages

Titre : Imagerie à l'échelle de la molécule unique de la régulation de la nano-organisation du récepteur EGFR : application à des mécanismes pathophysiologiques dans des maladies rénales

Mots clés : EGFR, CD9, kidney disease, PEC, shCD9 PEC, VSMC, MDCK, dSTORM, SPT single-particle tracking, Bayesian inference

Résumé : Dans la première partie de la thèse, nous avons révélé la distribution des récepteurs à l'EGF (EGFR) et du CD9 dans la membrane des cellules épithéliales pariétales (PEC) impliquées dans des maladies rénales inflammatoires. Dans un premier temps, nous avons utilisé la technique dSTORM pour cartographier quantitativement la localisation de ces protéines dans la membrane cellulaire et démontrer leur colocalisation dans les cellules épithéliales pariétales. Ces protéines sont localisées dans de petits domaines d'un rayon d'environ 50 nm à 100 nm dans la membrane des cellules PEC.

Dans la deuxième partie, nous avons utilisé une technique complémentaire à dSTORM, la technique de suivi de particules uniques pour étudier la dynamique des récepteurs à l'EGF dans la membrane de différents types cellulaires. Pour analyser la trajectoire de suivi d'une seule particule, nous avons introduit une nouvelle méthode pour déterminer les parties libres et confinées des mouvements des protéines. Le confinement des récepteurs EGFR a ensuite été analysé par inférence Bayésienne pour extraire les caractéristiques de confinement, la raideur du potentiel de confinement harmonique et le coefficient de diffusion. Nous avons montré que ces caractéristiques varient d'un type cellulaire à l'autre.

Title : Single-molecule-based imaging study of EGFR receptor nano-organization regulation : application to pathophysiological mechanisms in kidney diseases

Keywords : EGFR, CD9, kidney disease, PEC, shCD9 PEC, VSMC, MDCK, dSTORM, SPT single-particle tracking, Bayesian inference

Abstract : In the first part of the thesis, we revealed the distribution of EGF receptors and CD9 in the membrane of parietal epithelial cells (PEC) that are involved in inflammatory kidney diseases. First, we used the dSTORM technique to quantitatively map the localization of these proteins in the cell membrane and demonstrate their colocalization in parietal epithelial cells. These proteins are found to be localized in small domains with a radius of about 50 nm - 100 nm in the membrane of PEC cells. In the second part, we used a technique complementary to dSTORM, the single-particle tracking technique, to study the dynamics of the proteins in the cell membrane of different cell types. To analyze the trajectory obtained from singleparticle tracking, we introduced a new method to determine the free and confined portions of the protein motions. The confinement of EGFR was also analyzed by Bayesian inference to extract the confinement characteristics, the stiffness of the harmonic confining potential and the diffusion coefficient. We showed that the confinement characteristics depend on the cell type.